Opto-phononic confinement in GaAs/AlAs-based resonators

Fabrice-Roland Lamberti

THÈSE DE DOCTORAT
DE L'UNIVERSITÉ SORBONNE PARIS CITÉ
PRÉPARÉE À L'UNIVERSITÉ PARIS DIDEROT

École doctorale n°564: Physique en Île-de-France

réalisée

au Centre de Nanosciences et de Nanotechnologies

sous la direction de Paul VOISIN

présentée par

Fabrice-Roland LAMBERTI

THÈSE DE DOCTORAT DE PHYSIQUE

Sujet de la thèse :

Opto-phononic confinement in GaAs/AlAs-based resonators

soutenue le 12 Juillet 2018

devant le jury composé de :

Présidente du Jury	Prof. VASANELLI Angela	Université Paris Diderot
Directeur de thèse	Dr. VOISIN Paul	C2N/CNRS
Rapporteur	Dr. GAYRAL Bruno	CEA-INAC
Rapporteur	Prof. RUELLO Pascal	Université du Maine
Examinatrice	Dr. BENCHABANE Sarah	Institut FEMTO-ST/CNRS
Examinateur	Dr. SCHERBAKOV Alexey	Technische Universität Dortmund
Encadrant de thèse	Dr. LANZILLOTTI-KIMURA Norberto Daniel	C2N/CNRS

On passe sa vie à romancer les motifs
et à simplifier les faits.

Boris Vian

Résumé

Ces travaux de thèse portent sur la conception et sur la caractérisation expérimentale de résonateurs opto-phononiques. Ces structures permettent le confinement simultané de modes optiques et de vibrations mécaniques de très haute fréquence (plusieurs dizaines jusqu'à plusieurs centaines de GHz). Cette étude a été effectuée sur des systèmes multicouches à l'échelle nanométrique, fabriqués à partir de matériaux semiconducteurs de type III-V. Ces derniers ont été caractérisés par des mesures de spectroscopie Raman de haute résolution.

Grâce aux méthodes expérimentales et aux outils numériques développés, nous avons pu explorer de nouvelles stratégies de confinement pour des phonons acoustiques au sein de super-réseaux nanophononiques, à des fréquences de résonance de l'ordre de 350 GHz. En particulier, nous avons étudié les propriétés acoustiques de deux types de résonateurs planaires. Le premier est basé sur la modification adiabatique du diagramme de bande d'un cristal phononique unidimensionnel. Dans le deuxième système, nous utilisons les invariants topologiques caractérisant ces structures périodiques, afin de créer un état d'interface entre deux miroirs de Bragg phononiques.

Nous nous sommes ensuite intéressés à l'étude de cavités opto-phononiques permettant le confinement tridimensionnel de la lumière et de vibrations mécaniques de haute fréquence. Nous avons mesuré par spectroscopie Raman les propriétés acoustiques de résonateurs phononiques planaires placés à l'intérieur de cavités optiques tridimensionnelles, de type micropiliers. Enfin, la dernière partie de cette thèse porte sur l'étude théorique des propriétés optomécaniques de micropiliers GaAs/AlAs. Nous avons effectué des simulations numériques par éléments finis, nous permettant d'expliquer les mécanismes de confinement tridimensionnel de modes acoustiques et optiques dans ces systèmes, et de calculer les principaux paramètres optomécaniques. Les résultats de cette étude démontrent que les micropilier GaAs/AlAs possèdent des caractéristiques prometteuses pour de futures expériences en optomécanique, telles que des fréquences de résonance acoustiques très élevées, de hauts facteurs de qualités mécaniques et optiques à température ambiante, ou encore de fortes valeurs pour les facteurs de couplage optomécaniques et pour le produit $Q \cdot f$.

Mots-clefs: Nanophononique, spectroscopie Raman, optomécanique, super-réseaux, photoélasticité, invariants topologiques, cavité adiabatique, résonateurs acoustiques, micropiliers, méthode des éléments finis.

Abstract

The work carried out in this thesis addresses the conception and the experimental characterization of opto-phononic resonators. These structures enable the confinement of optical modes and mechanical vibrations at very high frequencies (from few tens up to few hundreds of GHz). This study has been carried out on multilayered nanometric systems, fabricated from III-V semiconductor materials. These nanophononic platforms have been characterized through high resolution Raman scattering measurements.

The experimental methods and the numerical tools that we have developed in this thesis have allowed us to explore novel confinement strategies for acoustic phonons in acoustic superlattices, with resonance frequencies around 350 GHz. In particular, we have studied the acoustic properties of two nanophononic resonators. The first acoustic cavity proposed in this manuscript enables the confinement of mechanical vibrations by adiabatically changing the acoustic band-diagram of a one-dimensional phononic crystal. In the second system, we take advantage of the topological invariants characterizing one dimensional periodic structures, in order to create an interface state between two phononic distributed Bragg reflectors.

We have then focused on the study of opto-phononic cavities allowing the simultaneous confinement of light and of high frequency mechanical vibrations. We have measured, by Raman scattering spectroscopy, the acoustic properties of planar nanophononic structures embedded in three-dimensional micropillar optical resonators. Finally, in the last sections of this manuscript, we investigate the optomechanical properties of GaAs/AlAs micropillar cavities. We have performed numerical simulations through the finite element method that allowed us to explain the three-dimensional confinement mechanisms of optical and mechanical modes in these systems, and to calculate the main optomechanical parameters. This work shows that GaAs/AlAs micropillars present very interesting properties for future optomechanical experiments, such as very high mechanical resonance frequencies, large optical and mechanical quality factors at room temperature, and high values for the vacuum optomechanical coupling factors and for the $Q \cdot f$ products.

Keywords: Nanophononics, Raman scattering spectroscopy, Optomechanics, superlattices, photoelasticity, topological invariants, adiabatic cavity, acoustic resonators, micropillars, finite element method.

Remerciements

Au cours de ces trois ans et demi de thèse, j'ai cotoyé de nombreuses personnes qui ont influencé de façon significative mon travail. Je souhaiterais les remercier dans les quelques lignes qui suivent.

Je voudrais tout d'abord adresser un remerciement général au Centre de Nanosciences et de Nanotechnologies qui m'a accueilli pendant toute la durée de mon doctorat. Je souhaiterais en particulier remercier Giancarlo Faini, directeur de ce remarquable lieu de travail. Je remercie les membres du service informatique, pour leur disponibilité et leur réactivité, le service administratif pour m'avoir sorti à plusieurs reprises des méandres des ordres de missions ou des demandes d'achat, et l'atelier mécanique, pour les emprunts occasionnels de matériel au cours de l'installation de nouvelles manips'. Je remercie également le personnel de la salle blanche, dont le travail quotidien a permis (entre autre) la réalisation des échantillons étudiés dans cette thèse.

Je tiens à remercier les membres de mon jury de thèse, à qui j'ai eu l'occasion de présenter mes travaux avec beaucoup de plaisir. Je remercie en particulier Bruno Gayral et Pascal Ruello d'avoir accepté le rôle de rapporteurs, et d'avoir relu et évalué avec attention mon manuscrit. Je remercie également Sarah Benchabane et Alexey Scherbakov, dont les questions et commentaires m'ont permis de pousser encore un peu plus loin ma réflexion sur mon sujet. Je remercie en outre Angela Vasanelli pour avoir présidé ce jury et animé une séance de discussion très enrichissante.

Je souhaiterais ensuite remercier Paul Voisin qui m'a accueilli "chez les GOSS" en tant que directeur de l'équipe, et qui a supervisé ce travail jusqu'au bout, malgré son départ à la retraite. Je le remercie pour sa disponibilité et pour les conseils qu'il m'a prodigué tout au long de mon doctorat.

Je remercie bien sûr Daniel Lanzillotti Kimura, mon encadrant de thèse, pour m'avoir guidé au quotidien dans mon travail, d'abord en tant que postdoctorant, puis en tant que chercheur permanent au CNRS. Au cours de ces années j'ai pu apprécier sa grande culture scientifique, sa passion et son dynamisme. Je le remercie non seulement pour toutes nos discussions et pour tout le savoir-faire scientifique qu'il a su me transmettre, mais aussi pour ses conseils d'ordre méthodologique. Je suis sûr que les résultats présentés dans ce manuscrit ne constituent que les prémices d'une ligne de recherche qui ne cessera de se développer, et que sous son impulsion, tout ira très vite.

Je voudrais également remercier Pascale Senellart et Loïc Lanco qui ont contribué de façon significative à l'encadrement de mon travail. Je les remercie pour leur implication, pour leur investissement et pour toutes leurs remarques qui ont été cruciales au cours de ma thèse. Je tiens à remercier Pascale non seulement pour ses nombreux conseils et pour ses prises de décision avisées, mais aussi pour son soutien et pour sa bienveillance, en particulier au cours des moments difficiles. Je pense que sa rigueur

intellectuelle, son enthousiasme et l'énergie qu'elle sait dégager constituent un véritable exemple pour toute l'équipe. Je remercie Loïc Lanco pour les innombrables et passionnantes discussions scientifiques que j'ai pu avoir avec lui, qu'elles aient été liées à mon sujet ou non. Loïc est un formidable pégagogue, et j'espère un jour pouvoir expliquer avec autant de clarté des concepts complexes comme lui y parvient. Je le remercie enfin pour sa disponibilité, pour sa gentillesse, et pour toutes nos conversations au sujet de tout et de rien, qui m'ont permis de souffler au cours des journées chargées.

Je remercie Ivan Favero pour son investissement dans ce projet, et pour avoir apporté son expertise dans le domaine de l'optomécanique, que ce soit du point de vue expérimental ou théorique. Je voudrais également le remercier de m'avoir ouvert les portes de son groupe au laboratoire Matériaux et Phénomènes Quantiques (MPQ). Celà m'a permis de collaborer avec une équipe remarquable du point de vue scientifique et qui s'est toujours montrée très accueillante à mon égard.

Merci beaucoup à Aristide Lemaître, Carmen Gomez Carbonell, Abdelmounaim Harouri, et Isabelle Sagnes pour avoir fabriqué les échantillons de très grande qualité que j'ai étudié tout au long de ma thèse. Je remercie également Aristide pour les discussions/rappels/cours express sur des sujets aussi variés que la topologie, la croissance par MBE, ou le magnétisme.

Je tiens à remercier Martin Esmann et Omar Ortiz, les deux autres membres de l'équipe impliqués dans des sujets de nanophononique. Je remercie chaleureusement Martin, avec qui j'ai eu la chance de travailler en étroite collaboration pendant les deux dernières années de ma thèse. Martin est un compagnon de laboratoire extraordinaire, d'une très grande compétence scientifique et d'une très grande patience, mais également muni d'un potentiel comique insoupçonnable. Je n'ai malheureusement pas eu l'occasion de collaborer autant avec Omar, mais je suis sur que ses expériences pompe-sonde feront des étincelles à l'avenir!

Je remercie les autres chercheurs avec qui j'ai eu l'occasion de collaborer sur certains aspects de mon sujet. Je remercie Guy Aubin pour avoir développé la chaîne de mesure pour la manip' de mouvement Brownien. Je suis convaincu que même si nos efforts n'ont pas encore porté leurs fruits, son travail sera essentiel pour de futures expériences dans cette ligne de recherche. Je remercie également Guy pour ses explications détaillées sur les PSD, les NEPs, les amplis, les écoles de commerce, les plans de carrière, ou encore les gamins. Je remercie en outre Qifeng Yao, ancien postdoctorant au laboratoire MPQ, pour m'avoir expliqué avec beaucoup de patience ses simulations par éléments finis, afin que je puisse prendre la relève sur l'étude numérique des micropiliers.

Merci à Olivier Krebs qui a toujours été disponible pour m'aider et pour me conseiller toutes les fois que je l'ai sollicité. Je le remercie également d'avoir sauvé mon spectromètre d'une mort certaine, et ce de façon assez spectaculaire.

Je remercie Jacqueline Bloch, Alberto Amo, et Sylvain Ravets, la porte de leur bureau à toujours été ouverte. Je les remercie pour leur aide, pour toutes les discussions que j'ai pu avoir avec eux, et pour les emprunts occasionnels de lasers. Je tiens également à m'excuser de la pollution sonore que j'ai pu engendrer au cours de mes discussions avec Loïc.

Je remercie chaleureusement les amis thésards(des) et postdocs que j'ai eu la chance de cotoyer. Je remercie Valentin Goblot, pour nos débats enflammés sur les derniers articles du Monde, Marijana Milicevic, zdravo zdravo, sorry I couldn't

resist, Lorenzo De Santis, il mio padano preferito, Paul Hilaire, dont sa maîtrise de la physique du spin ne rivalise qu'avec ses talents de jongleur, Guillaume Coppola, pour son optimisme sans faille, Justin Demory, dont le look métalleux cache une âme sensible, Florian Pastier, pour son sérieux au bureau, Clément Millet, pour sa gentillesse et sa disponibilité, Nicola Carlon Zambon (a.k.a. Titta), pour sa curiosité scientifique insatiable et Philippe St-Jean, pour sa bonne humeur à toute épreuve. Je remercie également Hélène Ollivier et Marie Billard, les deux nouvelles (super) thésardes de l'équipe. Je remercie en outre Carlos Antón Solanas et Juan Loredo, les deux guerriers au photon unique, pour leur aide et leurs conseils au labo.

Je remercie également Valérian Giesz et Niccolo Somaschi, qui ont fondé avec Pascale la start-up Quandela, une entreprise qui tutoiera les plus grandes multinationales du CAC 40 dans un avenir proche. Je suis sincèrement admiratif du sérieux dont vous faites preuve au quotidien, et les recrutements de Marie et de Florian montrent que votre travail porte déjà ses fruits. Je vous souhaite tout le succès possible au cours de cette aventure. Je tiens à remercier Valérian pour ses conseils de vétéran au début de ma thèse, pour m'avoir mis en contact avec l'Institut Villebon-Georges Charpak afin que je puisse enseigner, mais aussi pour avoir très vite reconnu mes talents d'humoriste. Je remercie Niccolo pour avoir passé avec moi de longues journées au labo. Je pense que le rock psychédélique et le reggae ne se sont jamais aussi bien entendus qu'avec nous.

Je tiens à remercier les autres membres du C2N avec qui j'ai eu l'occasion d'échanger. Je remercie en particulier Rémy Braive, les membres de son équipe, et Julien Chaste. Leurs explications sur leurs domaines de recherche respectifs étaient très intéressantes pour moi, et j'espère que les réunions d'optomécanique continueront d'avoir lieu. Je remercie également Fabrice Raineri pour ses conseils.

Je remercie mes amis insaliens, Ben, Sarika, Tom et Joffrey, pour les soirées, les voyages et les festivals passés ensemble. Je vous remercie d'avoir toujours été là pour moi, et d'avoir fait le déplacement le jour de ma soutenance. Une pensée à la petite Télina, qui va beaucoup changer la vie des Giraudeaux. Je remercie également Gabriele, Riccardo et Agnese pour tous ces moments de détente et pour m'avoir accompagné dans ma découverte de *Paris by night*.

Je termine ces remerciements par ma famille. Je ne pourrais jamais assez remercier ma mère, mon père et ma soeur, car sans eux je n'aurais jamais pu en arriver là. Je les remercie de m'avoir toujours soutenu et suivi jusqu'au bout dans toutes mes décisions, et ce, malgré les kilomètres qui nous séparent depuis maintenant des années. Je remercie en particulier ma mère, qui a su me transmettre sa curiosité et son goût de l'effort. Je remercie enfin Ségolène, pour m'avoir plus que patiemment attendu au cours de ces derniers mois de travail intense, pour son écoute au quotidien, et pour avoir décidé de partager un bout de chemin avec moi.

Contents

Motivation **1**

1 Fundamentals of phonon engineering **6**
1.1 Periodic structures for propagation control 6
1.2 One-dimensional phononic crystals 8
1.2.1 Acoustic superlattices: a first description 8
1.2.2 Phononic band diagrams 11
1.3 Acoustic Distributed Bragg Reflectors 17
1.4 Phononic Fabry-Perot cavities 20
1.5 Conclusion 24

2 Optical measurements of acoustic phonons **25**
2.1 Raman scattering: phonon spectroscopy 25
2.1.1 The Photoelastic model 26
2.1.2 A microscopic description 29
2.1.3 Raman scattering on superlattices 30
2.2 Engineering optical fields for Raman scattering 33
2.2.1 Optical Fabry-Perot resonators 34
2.2.2 Enhancing Raman intensities 37
2.2.3 Relaxing the rules of backscattering 39
2.3 Coherent phonon generation and detection: phonon dynamics 41
2.4 Optomechanical systems 43
2.4.1 Optomechanical interaction 43
2.4.2 Probing and manipulating the mechanical motion 44
2.4.3 Optomechanical parameters 48
2.5 Conclusion 50

3 Acoustic confinement: beyond the Fabry-Perot resonator **52**
3.1 Raman scattering set-up 53
3.2 Adiabatic confinement of acoustic phonons 57
3.2.1 Design of an adiabatic cavity 58
3.2.2 Characterization of the Adiabatic Cavity 61
3.3 Topological nanocavities 70
3.3.1 Topological invariants for phononic interface states 70
3.3.2 Interface states 77
3.3.3 Characterization of the topological cavity 79
3.4 Conclusion 83

4 Three-dimensional optical confinement in acousto-optic resonators 85
4.1 Optical properties of micropillars 86
4.1.1 Confined optical modes 86
4.1.2 Probing the optical properties of micropillars 89
4.2 Confinement of light and acoustic phonons in micropillars 92
4.2.1 Optical micropillars embedding acoustic resonators 92
4.2.2 Optical probing of micropillars acoustic properties 94
4.3 Raman scattering in micropillars 98
4.4 Conclusion 103

5 Micropillars as optomechanical resonators 104
5.1 Towards three-dimensional confinement 105
5.1.1 Simultaneous confinement of light and sound in planar cavities 105
5.1.2 Opto-phononic micropillars 109
5.2 Micropillar optical and mechanical confinement, a comparison 111
5.2.1 Spatial profile of confined modes 111
5.2.2 Eigenfrequencies as a function of radius 115
5.3 Mechanical confinement mechanisms in micropillars 117
5.4 Optomechanical properties of micropillars 124
5.4.1 Mechanical quality factor 124
5.4.2 Optomechanical coupling factor 129
5.4.3 Local optomechanical properties of micropillars 132
5.5 Conclusion 134

Conclusions 136

Motivation

The mechanical motion of atoms plays an essential role in the description of basic phenomena encountered in condensed matter physics, such as ultrasound and heat transport [1]. Furthermore, phonons, the elementary quanta of mechanical vibrations, dramatically affect the behavior of other fundamental excitations in solid state physics, such as photons and electrons. Indeed, phonons play a central role in the study of electronic transport, scattering processes, and intra-band relaxation of carriers in semiconductor materials [2].

Over the last decades, the control of photons and electrons has led to major technological advances for the transfer and the manipulation of energy and information [3, 4]. The control of mechanical vibrations has also been a very active field of research over the last years, and its further development could have significant consequences over a broad range of technological applications [5–7].

The phononic spectrum that is nowadays investigated spans over a wide range of frequencies. For example, millihertz mechanical waves are relevant for the study of geological events such as earthquakes [8], while phonons with frequencies over one terahertz are of particular interest for the study of heat transport in solid state media [5, 9]. In this thesis we will focus on the control of mechanical vibrations with frequencies spanning from few tens up to few hundreds of GHz. The general objective of this work consists in investigating novel nanophononic confinement methods in one-dimension, and to move progressively toward the three-dimensional confinement of phonons and photons.

Nanostructured systems offer the possibility to engineer the behavior of phonons in the GHz-THz range. The finite dimensions of the considered systems dramatically modifies the dispersion relation of mechanical vibrations, their spatial profile, and the phononic density of states [6, 10]. The control of mechanical vibrations at the nanoscale, or nanophononics, is relevant in other research fields, such as nanoelectronics [11]. Indeed, the modification of the dispersion relation for acoustic phonons, the main carriers of heat in semiconductor materials, and the enhancement of surfaces and interfaces scattering events, leads to a reduction of the thermal conductivity in nanostructured devices [6]. Understanding the mechanisms leading to the decreasing of heat conduction in these systems is particularly interesting for the development of future efficient thermal management strategies [12]. Heat conduction at the nanoscale is also widely investigated for renewable energy harvesting. Indeed, reducing the thermal conductivity through nanopatterning would allow to fabricate materials with enhanced thermoelectric properties [10]. Simple nanophononic structures such as one dimensional superlattices [13], or more sophisticated nanostructured devices based on phononic crystals and metamaterials [14, 15] have been developed to control the propagation of heat carriers.

The development of high frequency phononic resonators at the nanoscale is crucial for the conception of future nano-electromechanical systems (NEMS). Microelectromechanical systems (MEMS) are widely used in everyday technology as sensors and actuators [16]. With the field of microelectronics which is pushing down the size of the developed devices below the sub micrometer scale, the technology of MEMS could be progressively replaced by nano-electromechanical systems [17]. These structures have promising applications, for example for the development of highly sensitive force and mass sensors [18, 19]. Nanomechanical resonators are also studied in the context of cavity optomechanics, a research field aiming to control the interactions between a confined optical mode and a mechanical degree of freedom [20]. Scaling down the size of optomechanical resonators allows to increase their mechanical resonance frequencies. Optomechanical systems presenting high frequency mechanical resonances are desirable for sensing applications, since it allows to increase the performances of optomechanical-based accelerometers and mass detectors [21]. Additionally, these systems have drawn significant attention in the context of quantum optomechanics [22, 23]. Indeed, the development of high frequency optomechanical resonators would facilitate the preparation and the manipulation of systems in their mechanical quantum ground state [24]. As a direct consequence, an increasing number of nano-optomechanical platforms with mechanical resonances in the few GHz range are nowadays investigated [20]. Well established designs in nanophononics, such as phononic cystals, are now used in cavity optomechanics for optimizing the confinement of mechanical vibrations [25, 26]. The work presented in this manuscript is relevant in this context, since we will present nanostructured cavity designs that allow to localize simultaneously light and ultra-high frequency mechanical vibrations.

The control of mechanical waves achieved in nanophononics could also be useful in the context of quantum technologies in the solid state. Mechanical vibrations have been investigated in order to couple to different quantum systems, such as nitrogen vacancy (NV) centers [27], superconducting circuits [28], or quantum dots [29]. This opens the possibility of using phonons for manipulating and exchanging quantum information between qubits. In this thesis, we study nano-mechanical oscillators that have the potential to interface qubits with confined mechanical waves.

The development of new characterization tools for the experimental study of the acoustic properties of nanophononic resonators is an active field of research. The interaction between light and phonons is a powerful tool for studying mechanical vibrations in the GHz/THz range. Indeed, several optical-based techniques can be implemented for this purpose, such as Raman scattering spectroscopy [30], optical interferometric and Brownian motion measurements [31], or pump-probe coherent phonon generation and detection [32, 33]. Picosecond acoustics is used for non-destructive testing, for the characterization of thin films and layered semiconductor structures [34, 35], and for non-invasive studies and imaging techniques of biological matter [36, 37]. In this work we focus our experimental efforts on the development of a high resolution Raman scattering set-up that allowed us to characterize the structures presented in this manuscript.

Acoustic nanometric superlattices enabled the study and the control of acoustic phonons in the GHz/THz regime [38]. The description of mechanical vibrations in these structures is usually carried out in a Bloch wave formalism, and their dispersion relations are represented through acoustic band diagrams [39]. Periodic layered media have been employed for the study of acoustic phenomena such as the Hartman effect

for phonons [38] or slow acoustic modes [40]. They are also the fundamental building block for the design of nanophononic devices such as acoustic mirrors [41], or planar cavities [42] that confine mechanical modes in the GHz/THz regime.

The confinement of mechanical vibrations in layered systems is of particular relevance in nanophononics. Indeed, these high frequency phononic cavities can be used as monochromatic acoustic generators and detectors, or as spectral filters [43]. Furthermore, layered acoustic systems and nanophononic cavities are nowadays studied for understanding the coupling mechanisms between confined high frequency phonons and electronic transitions in optoelectronic systems, such as VCSELs [44]. The interactions between acoustic waves and gain media could allow to modulate the emission properties of these nanometric lasers in the GHz regime [45]. Additionally, these nanophononic structures constitute a fundamental building block of SASERs [46], that is, sources for coherent and intense sound waves with nanometric wavelengths [47]. The confinement of acoustic phonons in superlattice based acoustic resonators constitutes the core of this thesis. So far, the localization of mechanical vibrations in layered nanophononic structures has been essentially implemented through the traditional Fabry-Perot design [48]. These acoustic cavities are fabricated by embedding an acoustic spacer between two phononic distributed Bragg reflectors (DBRs). However, acoustic superlattices offer the possibility of exploring other confinement strategies in the GHz/THz range, that are inspired from designs used in optical cavities. Proposing new strategies for the localization of acoustic phonons in the hypersonic range constituted our first research line.

The first approach that we have investigated relies on the fabrication of a nanophononic cavity by progressively perturbing the periodicity of a superlattice. In this way, we adiabatically modify the phononic dispersion relation of the periodic medium, and create a confined state that is smoothly localized.

The second addressed strategy is the development of acoustic cavities based on topological invariants. The study of topological phases has become a very active research field for the control of wave propagation. In optics, topological edge states are investigated for the creation of robust and unidirectional waveguides [49]. Similar works have been performed in macroscopic acoustics [50]. Despite the fact that theoretical studies have also been carried out in nanophononics [51], topological phases have not yet been experimentally used for engineering high frequency mechanical vibrations.

The confinement strategies discussed above enable the localization of acoustic phonons only in one dimension of space. However, current fabrication techniques allow to realize three-dimensional resonators out of these planar structures. The second line of research addressed in this manuscript is the confinement of light and mechanical vibrations in systems of higher dimensions.

The confinement of light and hypersound in one-dimensional nanophononic structures is a strategy that has already been explored. For instance, embedding a planar acoustic cavity inside an optical cavity allows to confine optical modes at the position of the nanophononic resonator. This greatly facilitate its characterization by optical means [42]. Current fabrication techniques enable the realization of micropillar resonators from these planar structures. These systems are well known for localizing optical modes in the three dimensions of space [52]. They are currently studied for fabrication of semiconductor lasers [53], single photon sources [54], or to study the dynamics of cavity polaritons [55]. However, the interactions between the mechani-

cal modes inside a nanophononic resonator and three dimensionally confined optical modes have not been studied yet. We will address this question by performing Raman scattering measurements on micropillar resonators embedding acoustic cavities.

Pump-probe coherent phonon generation and detection allowed to demonstrate that a planar GaAs/AlAs Fabry-Perot resonator can simultaneously localize acoustic phonons at resonance frequencies around 20 GHz, and optical modes in the near infrared range [56]. By fabricating micropillar cavities out of these one-dimensional structures, it is possible to obtain three-dimensional optomechanical resonators operating at unprecedentedly high mechanical frequencies compared to state-of-the-art optomechanical systems [20]. Furthermore, theoretical models have been proposed to study the behavior of tripartite systems, where a confined phonon mode is strongly coupled to a mechanical mode and an electronic two-level system [57]. The layered nanophononic systems considered here are interesting for this purpose, since they are obtained from III-V semiconductor materials in which quantum dots can be readily integrated.

The three-dimensional confinement of phonons in GaAs/AlAs micropillars having resonance frequencies around 20 GHz has been recently demonstrated through pump-probe experiments [58]. Although the optical properties of these resonators are well known, these recent experimental advances in the study of the mechanical and optomechanical properties of these systems demand theoretical investigations. We performed numerical simulations in order to understand the confinement mechanisms of acoustic phonons in these resonators and to evaluate the main optomechanical parameters.

The manuscript is organized in six chapters. Chapter 1 is dedicated to the introduction of the basic concepts that are used for engineering the behavior of mechanical vibrations in layered nanophononic systems. In particular, we will recall the working principles of one-dimensional acoustic superlattices and phononic Fabry-Perot cavities.

In Chapter 2, we will present the main optical characterization techniques that can be used for probing the acoustic properties of nanophononics resonators. We will start by presenting the physical mechanisms of inelastic light scattering from mechanical waves, and we will recall the relevant selection rules for Raman scattering spectroscopy on layered systems. We will also explain the characterization of these systems through Raman scattering can be greatly facilitated by engineering the optical environment of nanophononic resonators. Finally, we will briefly present two other experimental techniques that are widely used in nanophononics and optomechanics: pump-probe coherent phonon generation and detection, and Brownian motion measurements.

In Chapter 3, we present the work carried out for the development of novel nanophononic one-dimensional structures. We will detail the design of the first acoustic system that we have characterized, where we localize a mechanical mode by adiabatically breaking the periodicity of a superlattice. We will then move to the confinement of phonons using topological invariants. For each system, we will present the experimental results obtained by Raman scattering spectroscopy. The analysis of the probed spectra will be carried out with the help of numerical simulations based on a photoelastic model.

In Chapter 4, we will present a technique that allows the measurement of Raman signals generated by acoustic cavities embedded in optical micropillar resonators,

which confine light in the three dimensions. We will investigate the effect of the cavity finite lateral dimensions on the probed spectra.

In Chapter 5, we will present the numerical simulations that we have carried out for understanding the mechanical and optomechanical properties of micropillars. We will first recall the experimental works that allowed to demonstrate the full confinement of both mechanical and optical fields in these systems. We will then explain the main mechanisms leading to the localization of the phononic mode in a micropillar, that we have investigated through the finite element method. Furthermore, we will present the estimations of optomechanical parameters that we have determined through this numerical method.

Finally, we will terminate this manuscript with a general conclusion, where we will summarize the main advances reported in this manuscript. We will also propose future perspectives of this work.

Chapter 1

Fundamentals of phonon engineering

In this chapter we introduce the fundamentals of phonon engineering in one-dimensional structures. We present the relation between band structures and reflectivity properties of periodic systems, and the engineering of distributed Bragg reflectors and nanocavities.

1.1 Periodic structures for propagation control

In solid state physics, a crystal is a periodic arrangement of elementary constituents in space (e.g. atoms, ions or molecules) [1]. Such a periodic arrangement is described by a primitive cell (or unit cell) and a Bravais lattice. To obtain the crystalline structure, it is sufficient to know the configuration of the elementary constituents in the primitive unit cell and to translate it along the Bravais lattice.

The geometry and composition of this regular medium determines its electronic behavior. Indeed, an electron propagating in a crystal, described by its wavefunction, experiences a periodic potential caused by the elementary constituents [1, 2]. As a direct consequence, the electronic properties are described by band diagrams. This electronic dispersion relation is constituted by bands, corresponding to energy intervals for which the electrons can propagate, and gaps, i.e. intervals for which the propagation of electrons in the crystal is forbidden. Electronic band diagrams are usually represented in the first Brillouin zone, the primitive unit cell of the reciprocal crystal lattice [1, 2].

The optical analog of an electronic crystal is a photonic crystal. The periodic electronic potential is "mimicked" by introducing a modulation of the dielectric function [59, 60]. This periodic arrangement can be carried out in one, two, or three dimensions. The atoms or ions relevant in an electronic crystal are now replaced by materials with different dielectric constants and with minimal light absorption. Such a mapping between electrons and light propagating in periodically modulated media is possible because of the strong analogies between the equations governing their propagation [59–61]. In particular, due to reflections and interference processes occurring in a photonic crystal, these systems reproduce for optical waves several phenomena observed in their electronic counterpart [59]. The physical notions and vocabulary used to describe their properties are inherited from the ones used for electrons in crystals [59, 61]. For example, the optical dispersion relation of a photonic crystals

is also constituted by bands. Furthermore, it can also present frequency intervals in which light cannot propagate, i.e. optical gaps.

One significant difference between electronic and photonic crystals is the scale of the modulation, quantified by the size of the unit cell. For metals or semiconductor materials, the lattice constants are usually in the ångström range [1]. In the case of photonic crystals, in general the unit cell is comparable to the optical wavelengths for which the system is designed. For example, the optical lattice parameter is on the order of 100 nm for near infrared frequencies, whereas it can be in the cm range for microwaves.

A well known class of photonic crystals are one-dimensional periodic stacks of dielectric materials [59]. In these superlattices, the linear dispersion relation of light is folded into the photonic crystal's reduced Brillouin zone. This folding is accompanied by the opening of optical minigaps at the center and at the edges of the Brillouin zone. These multilayer systems are nowadays widely used for the fabrication of optical components such as highly reflective mirrors, Fabry-Perot interferometers and optical filters [62]. Additionally, they are also used to realize optical cavities in the solid-state, i.e. structures that allow to confine optical modes in one or more directions of space. Solid-state optical cavities are essential in optoelectronic applications. For example, they play a central role in the fabrication of vertical cavity surface emitting lasers [63] (VCSELs) or they can be interfaced with light emitting diodes [64] (LED) to improve their emission properties. Furthermore, optical cavities are also crucial in fundamental research. Indeed, since the proposition of Yablonovitch to control light emission processes with photonic crystals [60], they have been implemented to demonstrate that light-matter interactions can be dramatically modified in solid-state systems [65, 66].

The concepts developed in the field of photonic crystals can be transposed to phonons. Indeed, both light and mechanical wave dynamics are ruled by a wave equation. Therefore, the interference effects, which are at the heart of a photonic crystal's functioning, can also be obtained in an acoustic medium. The modulation in the dielectric function is now replaced by a modulation in the elastic properties of the system. Instead of considering the optical indices of refraction, a phononic crystal is obtained by stacking materials with contrasting acoustic impedances (i.e. the product of the mass density with the speed of sound), and with minimal sound absorption, in a periodic fashion. As in the case of an electronic or a photonic crystal, the dispersion relation of this phononic system is described by a band diagram, in which gaps can open, preventing the propagation of mechanical waves in the corresponding frequency intervals.

The first experimental characterizations of nano-acoustic superlattices have been carried almost 40 years ago. In 1979, Narayanamurti *et al.* first studied the acoustic transmission properties of a "dielectric phonon filter" constituted by a periodic stacking of GaAs/AlGaAs layers [67]. They observed a drop in the transmission spectrum of the superlattice, associated to acoustic Bragg reflections occuring in the phononic band gap of the system. One year later, Colvard *et al.* unambiguously evidenced the folding of acoustic phonons dispersion relation in superlattices through Raman scattering experiments [68]. Since then, the theoretical and experimental study of these systems has become a very active field of research [39, 69]. In the early 90s, the concepts of two-dimensional and three-dimensional phononic crystals presenting complete gaps were introduced, dramatically increasing the possibilities of sound ma-

nipulation [70, 71]. This was inspired by the proposition of Yablonovitch in optics, and initially motivated for the control of phonon propagation, the development of novel mechanical insulation strategies, and by the investigation of localization effects caused by disorder. Phononic crystals have been implemented in a great variety of systems, and designed to manipulate mechanical vibrations in the sonic (10^2-10^3 Hz) [72, 73], ultrasonic (10^4-10^6 Hz) [74, 75] and hypersonic (GHz) [76, 77] frequency ranges [78]. Their applications are very diverse, and span from acoustic isolators [79], phononic waveguides [80] or sound manipulation [81], to heat propagation management [82].

Recently, the simultaneous confinement of light and mechanical vibrations and their interactions has drawn significant attention. In phoxonic crystals, also called optomechanical crystals, materials and geometry are chosen in such a way that simultaneous confinement of photonic and phononic modes is possible [83, 84], leading to strong interactions between the two fields [85]. Periodically patterned media are nowadays a class of optomechanical resonators [20]. Optomechanical crystals, have been implemented, for example, for the investigation of systems approaching or reaching their quantum mechanical ground state [24], sensing [86], or optomechanically induced transparency [87].

One-dimensional superlattices are one of the simplest examples of phononic crystals. They are the fundamental building block for the realization of more complex acoustic systems. In this thesis we have explored novel confinement methods for acoustic phonons based on these layered acoustic media. Since the mechanical vibrations studied here are in the hypersonic range, the layer thicknesses involved are on the order of few nanometers. Molecular beam epitaxy (MBE) is a very well adapted fabrication technique for the growth of acoustic superlattices operating in this frequency range. Indeed, it allows to fabricate semiconductor heterostructures with layer thicknesses of few nanometers, with atomic monolayer resolution and with sharp interfaces [88], an essential requirement for nanophononic applications. Optical characterization techniques have demonstrated to be particularly well suited for probing the properties of layered nanophononic systems, operating in the GHz-THz regime.

1.2 One-dimensional phononic crystals

In this section, we present in detail the main features of one-dimensional nanophononic superlattices. We will first provide a qualitative description of their behavior. We will then introduce an analytical model, allowing to derive the acoustic dispersion relation of these systems.

1.2.1 Acoustic superlattices: a first description

The nanophononic superlattices studied in this work are obtained by stacking layers of materials with contrasting acoustic impedances in a periodic fashion [39]. The characteristic layer thicknesses involved are on the order of few nanometers. In this work, we focus on solid state systems, in which acoustic phonons in the hypersonic range can propagate.

The presence of any atomic defect with a size comparable to the considered phononic wavelengths can significantly affect the acoustic properties of the superlattice [89]. Monolayer thickness fluctuations that appear during the fabrication pro-

cess, in particular at the interface between the two different materials, can become dispersion or localization centers for the mechanical waves.

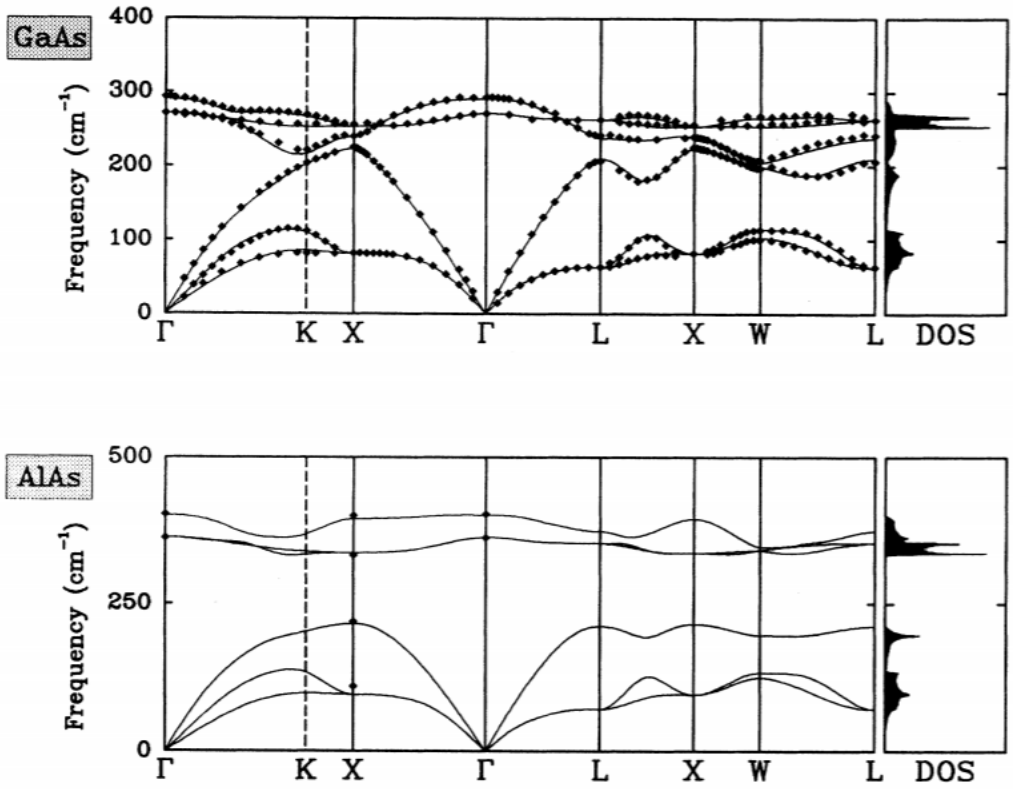

Figure 1.1 – Phonon Dispersion relations in bulk GaAs and AlAs, reproduced from [90]. The diamond symbols correspond to experimental data obtained through neutron scattering. The continuous lines correspond to ab-initio calculations. In the right panels the density of states for the two considered bulk materials are represented.

Semiconductor epitaxy fabrication techniques are well suited for the realization of high quality nanophononic structures. GaAs and AlAs are widely used in optoelectronics, and a significant know-how has been developed for the fabrication of layered systems based on these materials. Nowadays, GaAs and AlAs have become a model material combination for the realization of nanophononic structures. This is in particular due to the small lattice mismatch between these two III-V semiconductors, and to the fact that their bulk phononic properties are well known. All the samples presented in this manuscript were fabricated by MBE with alternating layers of these two materials, or of their alloys.

Figure 1.1 shows the phonon dispersion relations of GaAs and AlAs bulk materials [90]. GaAs and AlAs both have a zinc blende crystal structure, with two atoms per unit cell. The dispersion relation is therefore constituted by three acoustic phonon branches (i.e. the three low energy curves, equal to 0 at the Γ point) and three optical phonon branches. For both acoustic and optical phonons, two of the three branches are assigned to transverse phonons (i.e. the wave vector q is orthogonal to the mechanical wave polarization) and the other one is associated to longitudinal phonons.

We now provide a first qualitative description of a superlattice's acoustic behavior in order to understand its main features. It is worth noting here the hypothesis considered when studying all the planar systems presented in this manuscript. The mechanical waves that we are considering are longitudinal acoustic phonons, propagating along the [001] direction for both materials. Furthermore, we consider that the acoustic waves have linear dispersion relations in the bulk media. This is the case as long as the mechanical frequency is small, below $\approx 650\,\mathrm{GHz}$ (corresponding to $\approx 2.7\,\mathrm{meV}$) [91–93]. This condition is verified for all the systems studied here.

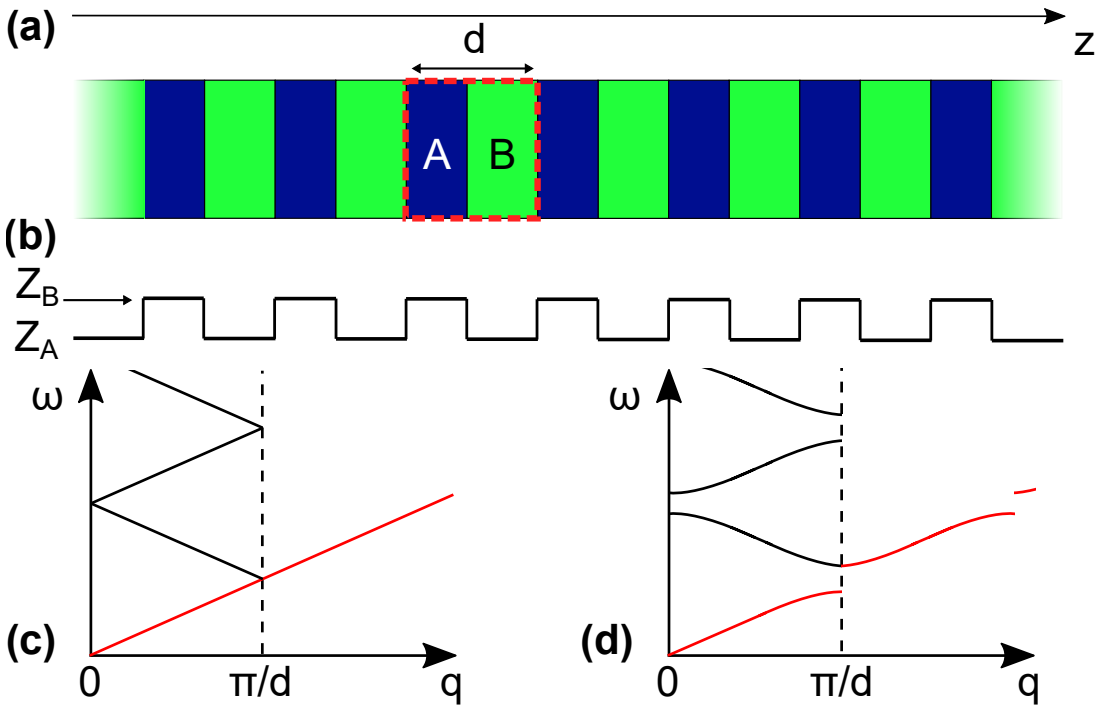

Figure 1.2 – Schematic representation of band diagram formation in an acoustic superlattice. **(a)**: Sketch of a periodic stacking of two materials A and B along the z direction. The red dashed rectangle indicates the considered unit cell, with a length d. The colors indicate layers of different materials. **(b)**: Periodic modulation of acoustic impedances in the phononic crystal. **(c)**: Dispersion relation for longitudinal mechanical waves propagating in the superlattice, when $A = B$. **(d)**: Dispersion relation for longitudinal mechanical waves propagating in the superlattice, when $A \neq B$. In Panels **(c)** and **(d)** the red curves correspond to the band diagram before being folded into the reduced Brillouin zone. The black curve indicates the folded dispersion relation. The vertical black dashed line indicates the boundary of the superlattice reduced Brillouin zone. Notice in **(d)** the opening of acoustic minigaps at the zone center and zone edge of the Brillouin zone.

We consider the infinite superlattice represented in Figure 1.2, Panel (a). The colors indicate layers of two materials A and B. They are characterized by their acoustic impendances $\mathrm{Z} = v \times \rho$, where v is the speed of sound and ρ is the material density. The red rectangle indicates the unit cell for this periodic arrangement, with a geometric size d, containing two layers of thicknesses d_1 and d_2.

Let us suppose first that all the layers are constituted by the same material, i.e. $A = B$. In this case, longitudinal acoustic phonons can propagate in a bulk medium

without any perturbation. Their dispersion relation is a straight line, and its slope corresponds to the speed of sound for longitudinal waves. Since we chose a unit cell (which in this case is somewhat arbitrary), we can fold the unperturbed acoustic dispersion in the corresponding superlattice Brillouin zone, as shown in Figure 1.2.c. As the characteristic length d of the superlattice unit cell is larger than the lattice parameters of the considered materials, the Brillouin zone associated to the phononic crystal is smaller than the ones of the bulk media. We therefore refer to it as the reduced Brillouin zone.

We now consider that $A \neq B$. Therefore, we have $\mathrm{Z_A} \neq \mathrm{Z_B}$, as plotted in Panel (b). We suppose, for this qualitative description, that the impedance contrast is weak, i.e. $\frac{Z_A}{Z_B} \approx 1$. We suppose that a longitudinal mechanical plane wave propagates inside the superlattice with a wave vector q along the z direction. Since the modulation is small, this situation is equivalent to the one described in a nearly free electron model for electronic band structures. We first consider the acoustic wavevectors that match the Bragg condition $q = n \times \pi/d$. In this case, the weak reflections occurring at the interfaces between two consecutive layers can constructively interfere. This will depend in fact also on the inner geometry of the superlattice unit cell (that is, the relative thicknesses of materials A and B). The result, in the stationary regime, is that the mechanical vibrations take the form of standing waves for these particular wavevectors. As in the case of electrons propagating in a weak electronic potential [94], this leads to the opening of *acoustic minigaps* in the band diagram, as shown in Panel (d) of Figure 1.2. No mechanical state propagating along the z direction can exist in the structure with a frequency falling inside an acoustic minigap. For wave vectors having values far from the Bragg condition, these interference effects do not occur, and the superlattice presents a linear dispersion relation characterized by an effective sound speed. The latter can be folded back in the superlattice reduced Brillouin zone, as shown in Figure 1.2.d.

The existence of acoustic minigaps is of paramount importance in this work, as we will see in the following chapters. In these frequency ranges, acoustic superlattices can be considered as perfect reflectors for longitudinal mechanical waves. Their span is determined by the acoustic impedance constrast between the constitutive materials and the layer thicknesses chosen to design the superlattice.

In this section, we have given a first description of a one-dimensional superlattice. Its main characteristics are summarized in Panel (d) of Figure 1.2. In the next section, we provide a more rigorous model, widely used in nanophononics [38, 39], that was originally derived by Colvard *et al.* [95]. It allows to calculate the acoustic band diagram of a superlattice, in a way similar to the Kronig-Penney model for electronic band structures.

1.2.2 Phononic band diagrams

In Figure 1.3 we show the calculated folded band diagram of a GaAs/AlAs superlattice, reproduced from [95]. The figure shows the dispersion relation for longitudinal acoustic waves. In this model, the superlattice is considered to be constituted by a linear chain of atoms. The GaAs and AlAs layers are constituted by 5 and 4 atomic monolayers, respectively. The folded optical branches in the two materials are separated by a wide frequency interval, preventing the propagation of optical phonons in the whole structure. For the low frequency longitudinal acoustic phonons, acoustic

minigaps open. Far from the center and the edge of the reduced Brillouin zone, the dispersion relation is linear. An effective sound speed, derived from the constituent materials and from geometrical parameters, can be calculated [39, 96].

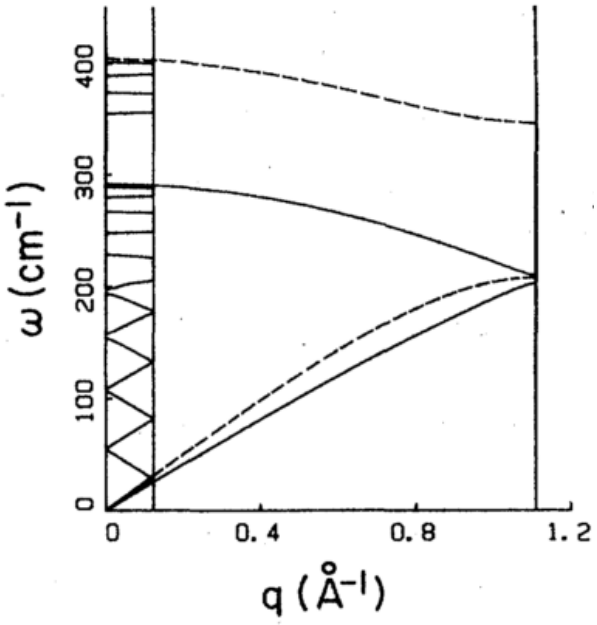

Figure 1.3 – Phononic band diagrams calculated by considering linear-chain models. The mechanical waves considered here are the longitudinal ones. The Brillouin zones represented are the ones of the bulk materials and of the superlattice (the smaller one). In the bulk Brillouin zone, the dashed lines correspond to the AlAs dispersion relation, and the solid lines show the one for GaAs. In the superlattice Brillouin zone, the solid lines correspond to the folded dispersion relation. The image is reproduced from [95].

We now derive the acoustic dispersion relation of a superlattice. We consider the structure represented in Figure 1.4, where the [001] direction is indicated by the z axis. The layers have thicknesses of d_a and d_b, respectively. The total unit cell has a length d. In the frequency ranges that we are considering, the bulk mechanical waves present a linear dispersion relation. In the model that we present below, the crystals are considered as elastic continua. The wave equation describing the propagation of mechanical vibrations reads:

$$\frac{\partial}{\partial t}\left(\rho(z)\frac{\partial u(z,t)}{\partial t}\right) = \frac{\partial}{\partial z}\left(C_{11}(z)\frac{\partial u(z,t)}{\partial z}\right) \tag{1.1}$$

where $u(z,t)$ corresponds to the displacement along the z axis, whereas ρ and C_{11} are the mass density and the stiffness constant for longitudinal modes along the [001] crystal direction, respectively. Considering that in each layer the material parameters are homogeneous, the equation becomes:

$$\rho_j \frac{\partial^2 u(z,t)}{\partial^2 t} = C_j \frac{\partial^2 u(z,t)}{\partial^2 z} \tag{1.2}$$

where the j subscripts indicate the material properties in the j^{th} layer. We are seeking harmonic solutions in time. Furthermore, the system is translation invariant in the x and y directions. For a wave that is propagating with a wavevector q along the z direction, we look for solutions having the form:

$$u(z,t) = u(z) \times e^{i\omega t} \tag{1.3}$$

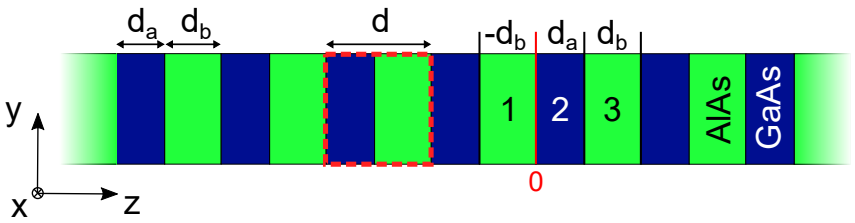

Figure 1.4 – Schematic representation of a superlattice. The dashed red rectangle corresponds to the superlattice unit cell. The colors indicate layers of different materials. The propagation axis z is indicated.

Inside a layer j, the spatial part $u(z)$ can be locally decomposed in two counter-propagating plane waves:

$$u_j(z) = A_j e^{ik_j z} + B_j e^{-ik_j z} \tag{1.4}$$

where k_j is the local wavevector of the plane wave in layer j. We now use boundary conditions at different interfaces between the layers 1,2 and 3, shown in Figure 1.4. The origin is marked by a vertical solid red line. The boundary conditions are the continuity of stress and displacement between two consecutive layers. They read as:

$$u_j(b_j) = u_{j+1}(b_j) \tag{1.5}$$

and

$$C_j \frac{\partial u_j}{\partial z}\bigg|_{b_j} = C_{j+1} \frac{\partial u_{j+1}}{\partial z}\bigg|_{b_j} \tag{1.6}$$

In the equations shown above, $\mathrm{b_j}$ indicates the interface between the layers j and $j+1$. For layers 1 and 2, Equation 1.4 becomes:

$$u_1(z) = A_1 e^{ik_1 z} + B_1 e^{-ik_1 z} \tag{1.7}$$

and

$$u_2(z) = A_2 e^{ik_2 z} + B_2 e^{-ik_2 z} \tag{1.8}$$

For layer 3 we apply the Bloch theorem. Since the system is periodic, the mechanical solution can be put in the form:

$$u(z) = e^{iqz}\phi(z) \tag{1.9}$$

$\phi(z)$ is the part of the Bloch wave with the same periodicity d as the acoustic superlattice. Therefore, the mechanical wave in layer 3 can be written as:

$$u_3(z) = e^{iqd} \times (A_1 e^{ik_1(z-d)} + B_1 e^{-ik_1(z-d)}) \tag{1.10}$$

We consider Equation 1.7, Equation 1.8, and Equation 1.10. By applying the boundary conditions at the interfaces between layer 1 and layer 2, and between layer 2 and layer 3, we find:

$$\begin{aligned} A_1 + B_1 &= A_2 + B_2 \\ C_1 k_1 (A_1 - B_1) &= C_2 k_2 (A_2 - B_2) \\ A_2 e^{ik_2 d_a} + B_2 e^{-ik_2 d_a} &= e^{iqd}(A_1 e^{-ik_1 d_b} + B_1 e^{ik_1 d_b}) \\ C_2 k_2 (A_2 e^{ik_2 d_a} - B_2 e^{-ik_2 d_a}) &= C_1 k_1 e^{iqd}(A_1 e^{-ik_1 d_b} - B_1 e^{ik_1 d_b}) \end{aligned} \tag{1.11}$$

where $k_j v_j = \omega$. The parameter v_j is the speed of sound in the material j, with $v_j = \sqrt{C_j/\rho_j}$. We find a homogeneous linear system of four equations with four unknowns. This system has a non-trivial solution if its determinant is equal to 0. By expressing this condition, we find the dispersion relation of the superlattice between ω and q [38, 39]:

$$cos(qd) = cos\left(\omega\left(\frac{d_a}{v_a} + \frac{d_b}{v_b}\right)\right) - \frac{\epsilon^2}{2} sin\left(\omega\frac{d_a}{v_a}\right) sin\left(\omega\frac{d_b}{v_b}\right) \tag{1.12}$$

with

$$\epsilon = \frac{\rho_b v_b - \rho_a v_a}{(\rho_b v_b \rho_a v_a)^{1/2}} \tag{1.13}$$

The parameter ϵ represents the phononic modulation in the superlattice due to the difference in acoustic impedances between the consecutive layers.

We now investigate the effect of each part of the dispersion relation. We first consider only the first term in Equation 1.12 [39]:

$$cos(qd) = cos\left(\omega\left(\frac{d_a}{v_a} + \frac{d_b}{v_b}\right)\right) \tag{1.14}$$

It can also be expressed as:

$$qd = \pm\omega\frac{1}{v} + 2p\pi \tag{1.15}$$

with

$$v = \frac{v_a v_b}{(1-\beta)v_b + \beta v_a} \tag{1.16}$$

and

$$\beta = \frac{d_b}{d} \tag{1.17}$$

In Equation 1.15, p is an integer. This expression describes a linear dispersion relation folded in the first Brillouin zone (as the one represented in Figure 1.2.c), with a slope, that is, an effective group velocity, given by v. The folded dispersion relation crosses the Brillouin zone center and edge for the frequencies:

$$\Omega_m = \frac{m\pi v}{d} \tag{1.18}$$

where m is an even (odd) integer number for the crossings at the center (edge) of the Brillouin zone. The effect of the second term in Equation 1.12, corresponding to the acoustic impedance modulation, is to open acoustic minigaps centered at the frequencies Ω_m. The amplitude of the acoustic minigaps can be approximately determined as [39]:

$$\Delta\Omega_m = 2\epsilon\frac{v}{d}sin\left(\frac{m\pi}{2}\frac{(1-\beta)v_b - \beta v_a}{(1-\beta)v_b + \beta v_a}\right) \tag{1.19}$$

Notice that the absolute value of Ω_m and the width of the acoustic minigaps are inversely proportional to d. Therefore, by decreasing the period thickness of the system, we increase the span and the central frequency of the minigaps. Choosing material combinations with a large ϵ value also allows to widen the forbidden frequency intervals.

The choice of the individual layer thicknesses determines both the spectral position of the acoustic minigaps and their span. It is worth noting that for any fraction of constitutive materials in the unit cell (that is $\forall\beta \in]0,1[$) there will always be open acoustic minigaps in a one-dimensional superlattice. This is in particular true for the acoustic minigap located at Ω_1, that is, the first forbidden frequency interval at the zone edge of the reduced Brillouin zone [97]. Nevertheless, some minigaps can be closed, depending on the design of the system, as can be deduced from Equation 1.19.

In Figure 1.5, we show the calculated dispersion relation for a GaAs/AlAs $(\frac{\lambda}{4}, \frac{\lambda}{4})$ superlattice. It was determined by implementing a transfer matrix method for acoustic waves and by considering the Bloch wave character of the eigensolutions. The design frequency considered here is $f_0 = 350\,\text{GHz}$. The parameter λ in the $(\frac{\lambda}{4}, \frac{\lambda}{4})$ nomenclature describing the design of the superlattice corresponds to the wavelength of a mechanical plane wave propagating at a frequency f_0 in the considered materials. The layers thicknesses in the unit cell are therefore $d_{GaAs} = \frac{\lambda_{GaAs}}{4} = 3.414\,\text{nm}$ and $d_{GaAs} = \frac{\lambda_{GaAs}}{4} = 4.043\,\text{nm}$. The material parameters used for the numerical calculations (both mechanical and optical) are shown in Table 1.1.

Materials	Density g/cm^3	Speed of sound (m s^{-1})	Index of refraction
GaAs	5.35	4780	3.54
AlAs	3.77	5660	2.96

Table 1.1 – Mechanical and optical properties of GaAs and AlAs [38, 98].

In Fig. 1.5.a we observe that the two first zone edge (ZE) acoustic minigaps are open, whereas the two zone center (ZC) ones are closed. This is evidenced in Panels (b) and (c), where we plot a detailed view of the first zone center and zone edge minigaps, respectively. The design frequency f_0 is located at the center of ZE[1], that is, $2\pi f_0 = \Omega_1$. The $(\frac{\lambda}{4}, \frac{\lambda}{4})$ design is in fact the one that maximizes the span of the first zone edge minigap. Note that this is a standard choice in photonics. For the superlattice considered here, this forbidden frequency interval has a span of $\approx 40\,\text{GHz}$.

As we mentioned before, for a frequency value located in an acoustic minigap no Bloch modes with a real value of q can be found. Nevertheless, Bloch wave eigenstates can still be determined inside the acoustic minigaps, but with complex q values, i.e. the modes are evanescent waves. The imaginary part of the wave vector corresponds to the decay length κ^{-1} of the state. In a semi-infinite system, we can consider a

longitudinal mechanical plane wave that is incident on an acoustic superlattice, with a frequency falling inside an acoustic minigap. Since its propagation is forbidden inside the layered periodic medium, the mechanical amplitude exponentially decays in a spatial region given by $1/\kappa$. κ is maximal for frequency values located at the center of the acoustic minigaps, and increases with the acoustic impedance contrast between the constitutive materials. The incident mechanical wave is completely reflected by the acoustic superlattice, which behaves as a perfect acoustic mirror.

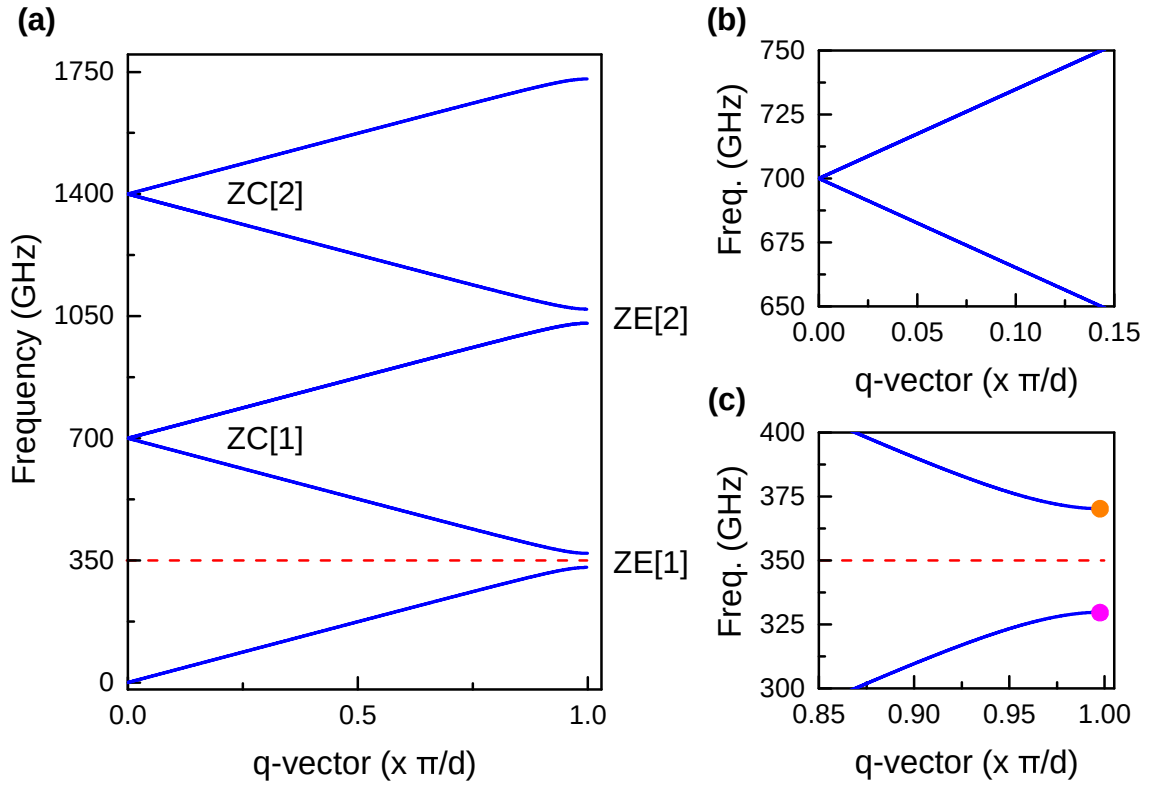

Figure 1.5 – **(a)**: Calculated band diagram of a $(\frac{\lambda}{4}, \frac{\lambda}{4})$ GaAs/AlAs superlattice, folded in the reduced Brillouin zone. The dashed line indicates the spectral position of the design frequency f_0. The ZE[i] and ZC[i] indicate the zone edge and zone center acoustic minigaps, respectively. **(b)**: Detailed view of the closed ZC[1] minigap, around 700 GHz. **(c)**: Detailed view of the open ZE[1] minigap, around 350 GHz. The orange and magenta dots indicate the first zone edge upper and lower eigenmodes, respectively.

In Panel (c) we can see that when q approaches the zone edge, the two visible bands progressively flatten. When the wave vector reaches the value $\frac{\pi}{d}$, the group velocity becomes $\frac{\partial \omega}{\partial q} = 0$. The two corresponding eigenmodes are standing waves and do not transport energy. They are marked by an orange and a magenta dot in the dispersion relation. The high frequency and low frequency modes have resonance frequencies of 370 GHz and 330 GHz, respectively.

We plot their spatial displacement field profiles in Figure 1.6, where we can see the position of their nodes and antinodes. In the figure we also defined a centrosymmetric unit cell for the superlattice indicated by the red rectangle, with a central AlAs

layer. The two modes have similar local wave vectors. However, they have different spatial distributions since they are orthogonal eigenmodes. In particular, they need to respect the symmetry properties of the superlattice, that is, they are symmetric or antisymmetric with respect to the mirror symmetry plane (black vertical line) located at the center of the defined unit cell. Therefore, there are only two possible spatial profiles. One standing wave presents a node in the middle of the unit cell (Panel (b)), whereas the other one presents an antinode (Panel (a)).

The existence of eingenmodes with a standing wave spatial profile that bound acoustic minigaps will play an important role for the design of topological acoustic cavities, as we will see in Chapter 3. Indeed, the topological phase of a superlattice can be deduced from the symmetry properties of these modes.

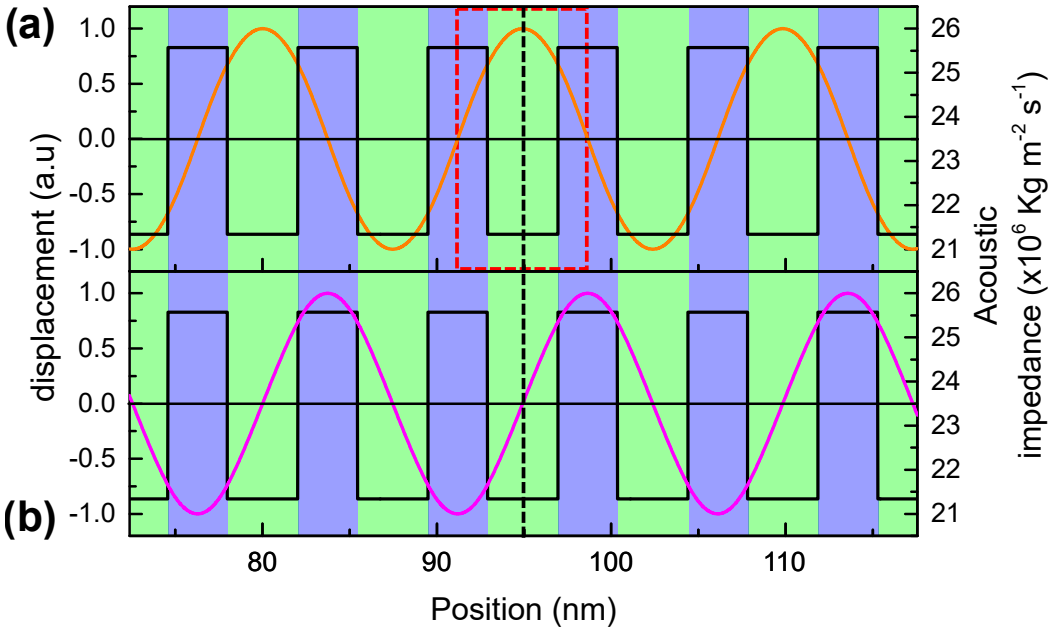

Figure 1.6 – Displacement fields of the high frequency (Panel (a), orange curve) and low frequency (Panel (b), magenta curve) standing wave modes bounding the first zone edge acoustic minigap. The amplitudes of normalized displacement are indicated by the left axis. The square black lines show the profile of the acoustic impedances in the layers (right axis). The colors indicate the layers of AlAs (green) and GaAs (blue). The red square corresponds to the chosen symmetric unit cell. The black vertical line indicates the mirror symmetry plane mentioned in the main text.

1.3 Acoustic Distributed Bragg Reflectors

Acoustic superlattices are idealized one-dimensional crystals with infinite spatial extent. Therefore, these systems cannot be realized experimentally. Nevertheless, structures presenting an acoustic periodic modulation over a finite region of space can be fabricated. A schematic representation is given in Figure 1.7, where the layered medium is embedded in bulk GaAs.

Since the system is of finite size along z, we can study its acoustic transmission and reflection properties. Indeed, we can send an incident acoustic wave, for example from

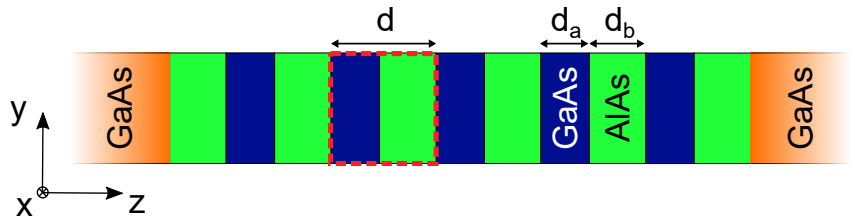

Figure 1.7 – Diagram of an acoustic distributed Bragg reflector embedded in bulk GaAs. The structure is constituted by 5.5 layer pairs.

the left GaAs substrate, and measure the reflected and transmitted field intensities as function of frequency. Since the structure is one-dimensional, the propagation of the incident acoustic waves can be simulated by using an implementation of the transfer matrix method.

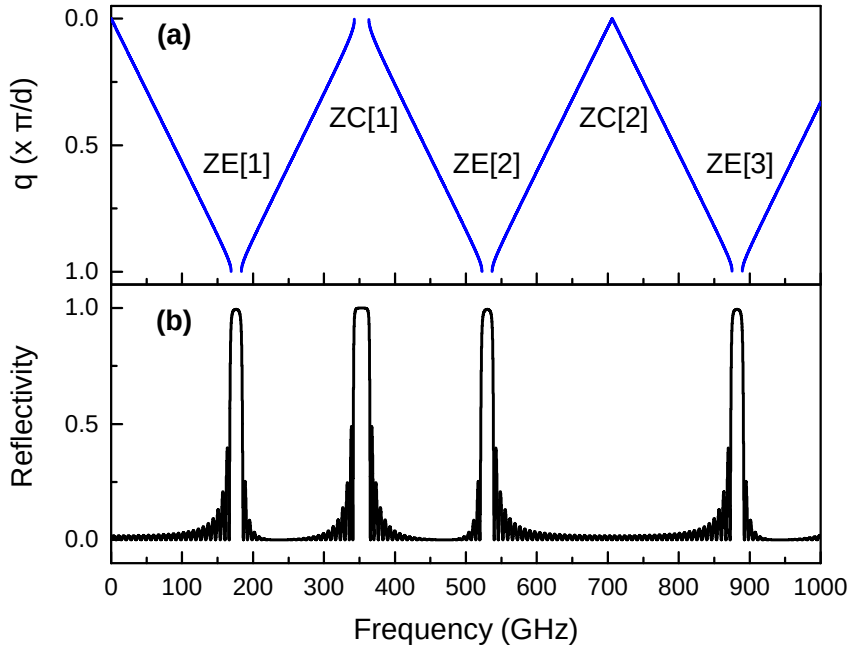

Figure 1.8 – **(a)**: Acoustic band diagram of a $(\frac{\lambda}{4}, \frac{3\lambda}{4})$ superlattice. The design frequency $f_0 = 350\,\text{GHz}$ is located at the center of ZC[1]. **(b)**: Acoustic reflectivity spectrum of the corresponding $(\frac{\lambda}{4}, \frac{3\lambda}{4})$ acoustic superlattice. Each acoustic stop band can be associated to an acoustic minigap in the superlattice band diagram.

In Figure 1.8.b we show the calculated reflectivity spectrum for a structure constituted by 24.5 GaAs/AlAs layers pairs embedded in a bulk matrix, as represented in Figure 1.7. The layer thicknesses are 12 nm and 3.4 nm for the AlAs and GaAs layers, respectively. This geometry corresponds to a $(\frac{\lambda}{4}, \frac{3\lambda}{4})$ periodic stack for a design frequency $f_0 = 350\,\text{GHz}$. The band diagram of the corresponding infinite superlattice is plotted in Figure 1.8.a. The frequency f_0 is located at the center of the ZC[1] acoustic minigap. The $(\frac{3\lambda}{4}, \frac{\lambda}{4})$ design is in fact the one that maximizes the span of this particular forbidden frequency interval [97]. In this minigap, a maximal value of the

acoustic reflectivity is reached at its center and it can be approximated by Equation 1.20 for a large number of periods [99]:

$$R = 1 - 4Z^{2N} + O(Z^{4N}) \tag{1.20}$$

with $Z = \frac{Z_{AlAs}}{Z_{GaAs}}$, which corresponds to the acoustic impedance contrast. For a DBR constituted by 10 layer pairs, the DBR reflectivity is around 0.9. By doubling the layer pair number, it reaches a value of 0.998.

The high reflectivity frequency intervals visible in Panel (b), also called stop bands, can be associated to the acoustic minigaps generated in the corresponding infinite periodic structure. They are due to constructive interferences between the successive back reflections occurring at the interfaces between the different semiconductor layers. These finite size structures operate as acoustic distributed Bragg reflectors for longitudinal mechanical waves, in strong analogy with their optical counterpart.

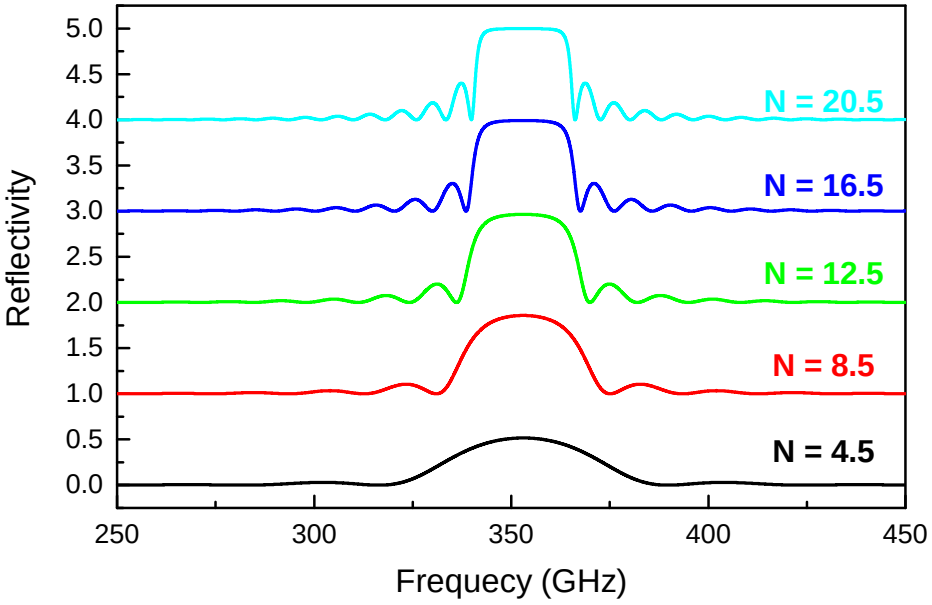

Figure 1.9 – Acoustic reflectivity of a DBR as function of increasing pair number around ZC[1]. The curves have been vertically shifted for clarity. The parameter N indicates the number of layer pairs inside the simulated DBR.

Outside of these frequency regions, the reflectivity spectrum drops significantly and presents fast oscillations, called Bragg oscillations. Their number between two acoustic stop bands increases with the number of bilayers in the DBR.

In Figure 1.9, we plot the acoustic reflectivity around the first ZC for a $(\frac{\lambda}{4}, \frac{3\lambda}{4})$ DBR with different number of layer pairs N. As expected from Equation 1.20, the acoustic reflectivity at the center of the stop band increases with N and the number of Bragg oscillations increases. Finally, the reflectivity values in this frequency interval progressively converge to one. For a sufficiently large number of layer pairs, an acoustic DBR becomes a highly reflective phononic mirror over frequency ranges corresponding to the acoustic stop-bands. This property is extremely useful for the conception of other phononic systems, such as acoustic cavities.

1.4 Phononic Fabry-Perot cavities

Because of the existence of stop bands, acoustic DBRs can be used to control the propagation of longitudinal mechanical waves. In particular, by introducing a defect inside such a periodic stack, we can realize an acoustic Fabry-Perot resonator, such as the one represented in Figure 1.10. The system can also be considered to be constituted by two DBRs enclosing a spacer layer. Such phononic resonators confine a discrete set of mechanical modes in one direction with resonance frequencies falling in the acoustic stop bands of the implemented DBRs.

An acoustic cavity can be fabricated from two $(\frac{\lambda}{4}, \frac{3\lambda}{4})$ DBRs designed at a frequency f_0. As mentioned before, this geometry maximizes the span of the acoustic stop band associated to the first ZC minigap centered at f_0. We can then introduce a spacer between the two acoustic mirrors that verifies the standard resonance condition for a Fabry-Perot cavity:

$$d_{spacer} = p\frac{f_0}{2v_{spacer}} \tag{1.21}$$

where p is an integer. The confined mode eigenfrequency is in this case located at the center of the considered stop band. This resonant state has the form of a standing wave, and its mechanical energy is spatially concentrated at the spacer position.

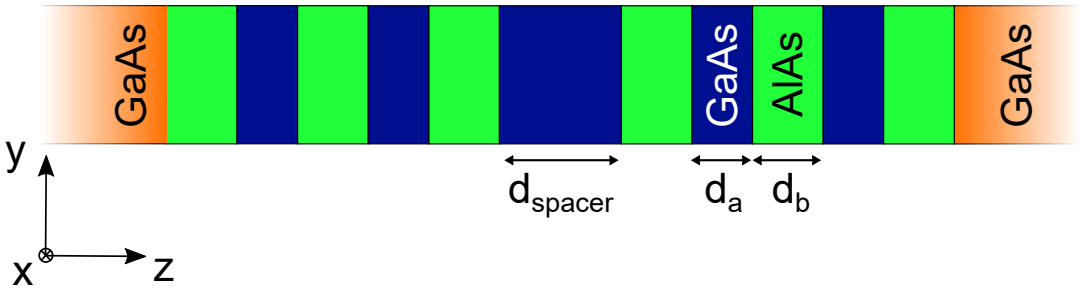

Figure 1.10 – Schematic diagram of an acoustic cavity embedded in a GaAs matrix. The number of layer pairs in the DBRs is arbitrary here and has been chosen for clarity.

In Figure 1.11.a, we show the simulated spatial profile of a confined mechanical mode, calculated through the transfer matrix method. The plotted quantity is the modulus of the displacement field $|u(z)|$ inside the structure. The amplitude of the displacement is normalized to the amplitude of the field inside the bulk matrix. The system is constituted by two $(\frac{\lambda}{4}, \frac{3\lambda}{4})$ AlAs/GaAs DBRs designed for $f_0 = 350\,\text{GHz}$, embedding a $\frac{\lambda}{2}$ GaAs spacer (that is, $p = 1$ in Eq. 1.21). Each DBR contains 17.5 layer pairs. The displacement amplitude is greatly enhanced inside the spacer and the mode exponentially decays inside the two DBRs. Its spatial profile $|u(z)|$ presents two maxima in the spacer of the cavity.

In Figure 1.11.b, we can see that the confined mode eigenfrequency is falling at the center of the first ZC acoustic minigap of the associated superlattice. This is indicated by the dashed green line. In the reflectivity curve (Figure 1.11.c), we observe a sharp dip located in the middle of the stop band. This feature marks the existence of the confined mode at a resonance frequency of $f_0 = 350\,\text{GHz}$ (corresponding to an energy of 1.45 meV).

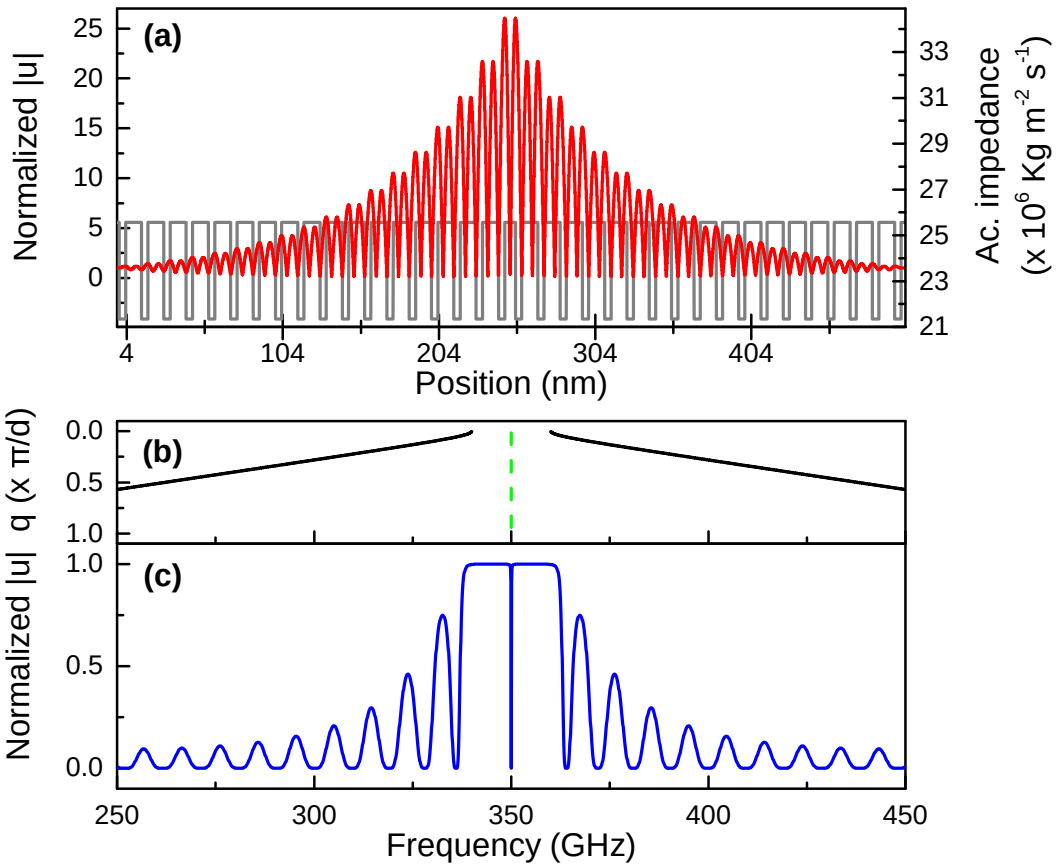

Figure 1.11 – Confined mechanical mode spatial profile and reflectivity curve of a $\frac{\lambda}{2}$ cavity. The mirrors have a $(\frac{\lambda}{4}, \frac{3\lambda}{4})$ geometry. **(a)**: Confined mechanical mode spatial profile (red curve, left axis) and acoustic impedance (grey curve, right axis) as function of the position in the structure. The GaAs spacer is at the center of the plot. **(b)**: Acoustic band diagram of the $(\frac{\lambda}{4}, \frac{3\lambda}{4})$ superlattice, without any spacer. The vertical green dashed line indicates the spectral position of the corresponding confined cavity mode inside the first ZC minigap. **(c)**: Cavity acoustic reflectivity, between 250 GHz and 450 GHz. The sharp dip in the acoustic stop band marks the existence of the confined mechanical mode at a resonance frequency of 350 GHz.

The mechanical field confinement strength of a cavity is quantified by its mechanical quality factor (Q_m). It corresponds to the ratio $Q_m = 2\pi \times E_{mech}/\Delta E_{mech}^{cycle}$. E_{mech} and ΔE_{mech}^{cycle} are the resonator mechanical energy and the mechanical energy lost *per* cycle of field oscillation, respectively. Furthermore, the quality factor value is proportional to the maximal field intensity, when the cavity is excited with a monochromatic plane wave resonant with the confined mode. Therefore, it quantifies the intensity enhancement obtained inside an acoustic resonator. The quality factor can be calculated from the reflectivity curve of the acoustic structure. By considering the resonance frequency f_0 and the full width half maximum (FWHM) Γ of the Lorentzian reflectivity dip, it is given by $Q_m = \frac{f_0}{\Gamma}$.

In the case represented in Figure 1.11, we find $Q_m = 5600$. The considered FWHM decreases when either the reflectivity or the spacer thickness d_{spacer} are increased. This is clearly visible in the following equation [99, 100]:

$$\Gamma = -\frac{v_s \times ln(\sqrt{R_L R_R})}{d_{spacer} + l_{DBR}} \tag{1.22}$$

where R_L and R_R are the reflectivities of the right and left DBRs. The parameter v_s is the speed of sound in the spacer and l_{DBR} corresponds to the penetration depth of the confined mode inside the DBRs. The lifetime of the confined phonons is given by $1/\Gamma$.

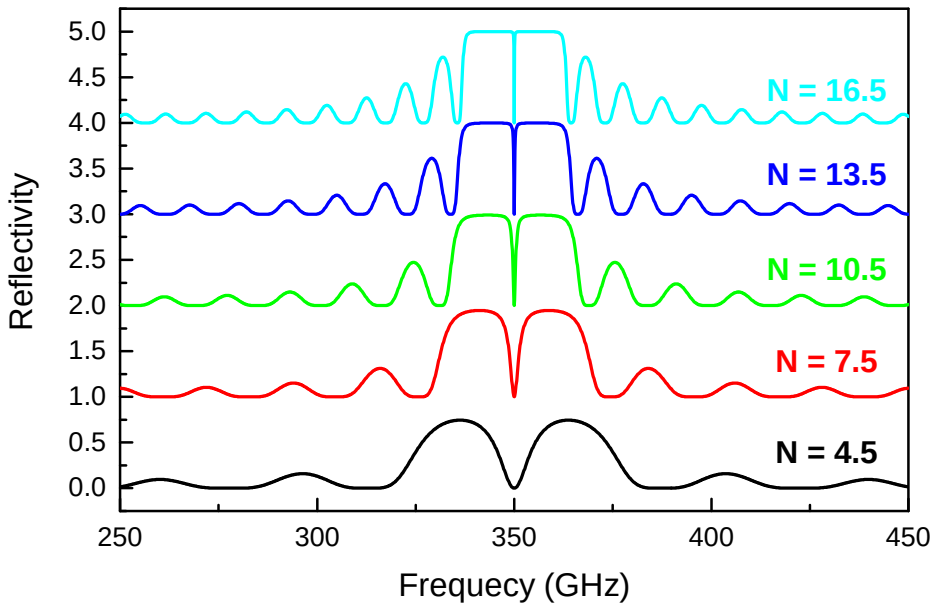

Figure 1.12 – Acoustic reflectivity curves for a $\frac{\lambda}{2}$ cavity with increasing layer pairs number (N) in each DBR. The curves have been shifted vertically for clarity.

In Figure 1.12 we plot the simulated reflectivity curves for a $\frac{\lambda}{2}$ cavity when the number of DBR layer pairs is increased. We observe that the reflectivity dip FWHM in the stop band decreases. This is due to the fact that we are increasing the reflectivity of the acoustic mirrors at the confined mode resonance frequency. Similarly to what

we observed for the case of a bare acoustic DBR in Figure 1.9, the acoustic stop band boundaries get better and better defined and the number of Bragg oscillations around the stop band increases.

The resonance frequency of the confined mechanical mode can be tuned by varying the thickness of the spacer. In Figure 1.13 we show the evolution of the resonance frequency as a function of this parameter, starting from a $\frac{\lambda}{2}$ cavity. The mechanical mode is red-shifted, since the overall size of the resonator increases, whereas the acoustic stop-band remains unaltered, since it depends solely on the DBRs' geometry. When the reflectivity dip disappears into the Bragg oscillations, a second dip, associated to the first order cavity mode, appears in the stop band and progressively reaches its center. When represented by its displacement modulus $|u(z)|$, the spatial profile of this confined mode presents three maxima inside the spacer. In this plot, the Fabry-Perot resonance condition smoothly changes from $d_{cav} = \frac{\lambda}{2}$ to $d_{cav} = \lambda$.

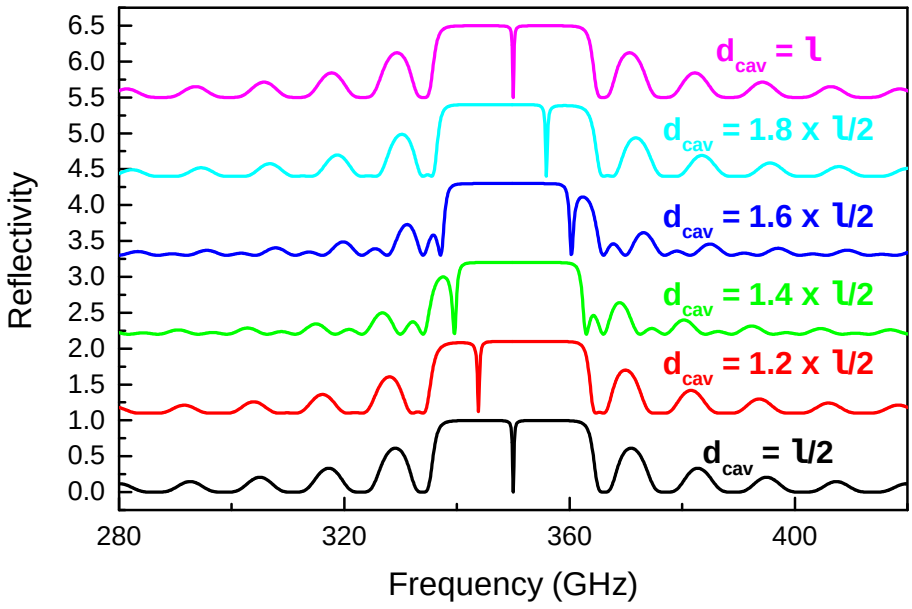

Figure 1.13 – Acoustic reflectivity curves for an acoustic cavity when changing the spacer size. d_{cav} is indicated next to each reflectivity curve. The layer pairs number is of 13.5 in each DBR.

Acoustic Fabry Perot resonators have been extensively studied in the field of nanophononics for the confinement of acoustic phonons in the hypersonic range. Nevertheless, other confinement methods have been explored in layered media. One example are mechanical modes that are spatially confined at the interface between a DBR and air. In particular, if the periodic stacking is terminated by the layer with the weaker acoustic impedance, surface modes can appear [101, 102]. They are spectrally located inside the acoustic DBR stop bands. Therefore, these modes exponentially decay in the periodic semiconductor medium, and because their mechanical frequency are in the hundreds of GHz range, they cannot propagate in air. Furthermore, since a DBR/air interface acts as a perfect reflector with zero stress boundary condition, asymmetric Fabry-Perot cavities can be designed. By placing an acoustic spacer be-

tween a DBR and air, confined mechanical modes can be generated and have been experimentally investigated [103]. Finally, the localization of acoustic phonons has also been demonstrated in Tamm plasmon resonators. In this case, the studied cavity was constituted by a DBR on which a thin gold layer was deposited. The optical and the mechanical modes were simultaneously confined at the interface between the metal and the dielectric structure [104].

As we will see in Chapter 3, we investigated novel localization strategies for high frequency phonons. The Fabry-Perot design presented here is completely analogous to the one that can be used for the fabrication of optical dielectric cavities. In this work we will take further advantage of the recent designs proposed for localization of photons to develop novel mechanical resonators.

The lack of trivial transducers to generate and detect acoustic phonons in the hypersonic range has motivated the development of optical methods to study the dynamics of these mechanical vibrations. For example, measuring the Raman spectra generated by confined acoustic phonons allows us to study the properties of nanophononic resonators. In fact, it is this experimental technique that we have implemented for the investigation of new confinement methods in planar systems, presented in Chapter 3. In the next chapter, we will introduce the main experimental methods allowing to probe mechanical vibrations in the temporal and spectral domain, by interfacing acoustic and optical fields.

1.5 Conclusion

In this chapter, we introduced the main concepts for acoustic waves manipulation in the hypersonic range with one-dimensional layered systems. We first introduced the working principles of acoustic superlattices, by providing an intuitive description and a more quantitative theoretical model. We have then studied how we can take advantage of concepts such as acoustic band diagrams and minigaps to design basic nanophononic devices, that is, acoustic DBRs and nanocavities. These notions will constitute the building blocks for the structures studied along this thesis. In Chapter 3 we will use them for the development of novel one-dimensional confinement strategies. In Chapters 4 and 5, we will study three-dimensional resonators fabricated from DBR based nanophononic resonators. In the next chapter, we will describe the main experimental techniques used in order to probe the confinement properties of nanophononic cavities.

Chapter 2

Optical measurements of acoustic phonons

Optical measurements are particularly useful for the characterization of nanophononic systems. This is due to the fact that the properties of light propagating in a solid-state medium can be affected by the presence of a mechanical wave. By measuring the signatures of this interaction, it is possible to study the acoustic properties of nanophononic systems. In this chapter we introduce the main experimental optical techniques that are relevant for the characterization of layered nanophononic resonators. We will first start by recalling the physical mechanisms leading to the inelastic scattering of light induced by phonons. We will then present how, by performing Raman scattering experiments, we can probe the acoustic properties of nanophononic layered systems. We will also see that, by confining the incident and the scattered optical fields, these measurements can be greatly facilitated. We will then introduce the working principles of two other experimental methods particularly useful for the study of phononic systems in the hypersonic range. The first one is pump-probe coherent phonon generation and detection, and the second one is Brownian motion measurements. The latter experimental technique is widely used in cavity optomechanics. We will provide a brief presentation of this research field in the last sections of this chapter.

2.1 Raman scattering: phonon spectroscopy

Spectroscopic optical measurements have been implemented for the study of high frequency mechanical systems since the early days of nanophononics. The inelastic scattering of light induced by acoustic phonons in a periodic medium generates characteristic spectral features [95]. They can be interpreted by comparing them to the acoustic band diagram of the associated superlattice. Furthermore, Raman scattering has also demonstrated to be useful for probing the confinement of acoustic cavities operating in the GHz/THz range [42]. The measurements on planar structures reported in this manuscript have been obtained through this technique.

In this section, we will review the basic concepts on which this experimental technique is based. In particular, we will provide a description of the interactions between light and mechanical vibrations, based on a photoelastic model. We will then explain how to enhance and relax the Raman scattering selection rules by engineering the optical environment of an acoustic structure.

2.1.1 The Photoelastic model

The experimental characterization of the systems presented in this manuscript relies on the interactions between light and mechanical vibrations. When a semiconductor sample is illuminated, part of the incident electromagnetic radiation is reflected at the surface of the solid state medium. The rest is transmitted and propagates inside the semiconductor material, and several light-matter interactions take place. For example, if the energy of the incident photons is higher than the fundamental electronic gaps, they can induce electronic transitions from the filled valence band up to the conduction band. Part of the incident light is absorbed, and can be dissipated as heat, or re-emitted through photoluminescence.

Light can also be scattered by inhomogeneities present in the medium. If the scattered photons have the same energy as the incident ones, this process is elastic scattering, or Rayleigh scattering [105]. On the contrary, if there is a change in the optical frequencies, it corresponds to an inelastic scattering process. In particular, the propagation of mechanical waves inside a material provokes inelastic scattering of light. It is this interaction, which tends to be weaker than photoluminescence or light reflection, that we will use for characterizing our acoustic systems. To explain its origin, we start this section by providing a macroscopic description of Raman scattering in a bulk solid-state medium, adapted from reference [2].

We consider an electromagnetic wave propagating in a semiconductor material. The associated electric field can be written as:

$$\overrightarrow{E}(r,t) = \overrightarrow{E}_i(\omega_i, \overrightarrow{k_i}) \times cos(\overrightarrow{k_i} \cdot \overrightarrow{r} - \omega_i t) \tag{2.1}$$

with k_i and ω_i the incident optical wavevector and angular frequency, respectively. The propagation of light in the solid state medium induces a polarization wave. The polarization field and the electric field are linked by the electric susceptibility tensor of the material:

$$\overrightarrow{P_i}(\omega_i, \overrightarrow{k_i}) = \chi(\omega_i, \overrightarrow{k_i})\overrightarrow{E_i}(\omega_i, \overrightarrow{k_i}) \tag{2.2}$$

The mechanical modes inside the bulk material can be put in the form of plane waves. Atomic displacements can be expressed as:

$$\overrightarrow{u}(r,t) = \overrightarrow{u}(\omega_0, \overrightarrow{q}) \times cos(\overrightarrow{q} \cdot \overrightarrow{r} - \omega_0 t) \tag{2.3}$$

The mechanical waves in the solid-state medium will affect the dielectric tensor. By assuming an adiabatic approximation, i.e. the electrons adiabatically follow the displacement of the crystal atoms, the dielectric tensor can be expressed as a function of $\overrightarrow{u}(r,t)$. Furthermore, the mechanical displacements present in the crystal are considered to be small. Therefore, the crystal electric susceptibility can be Taylor expanded as:

$$\chi(\omega_i, \overrightarrow{k_i}, \overrightarrow{u}) = \chi_0(\omega_i, \overrightarrow{k_i}) + \left.\frac{\partial \chi}{\partial \overrightarrow{u}}\right|_0 \overrightarrow{u} + ... \tag{2.4}$$

where the label 0 indicates the situation where no phonons are propagating. We keep only the first term in the previous expansion, which represents the electric susceptibility modulation induced by the mechanical wave where only one phonon is involved. By considering Equations 2.2 and 2.4, and by expressing the wave equation for the electric field, we find [105]:

$$\nabla^2 \overrightarrow{E} - \frac{n^2}{c^2}\frac{\partial^2 \overrightarrow{E}}{\partial^2 t} = \frac{1}{\epsilon_0 c^2}\frac{\partial^2 \overrightarrow{P}_{ind}(\overrightarrow{r}, t)}{\partial^2 t} \tag{2.5}$$

Where c, ϵ_0 and n are the speed of light in vacuum, the vacuum permittivity and the material refractive index, respectively. The polarization term in the previous equation $\overrightarrow{P}_{ind}$ can be expressed as:

$$\begin{aligned} \overrightarrow{P}_{ind}(\overrightarrow{r}, t, \overrightarrow{u}) = \frac{1}{2}\frac{\partial \chi}{\partial \overrightarrow{u}}\Big|_0 \overrightarrow{u}(\omega_0, \overrightarrow{q})\overrightarrow{E}_i(\omega_i, \overrightarrow{k_i})\times \\ \Big\{cos[(\overrightarrow{k_i} + \overrightarrow{q})\cdot\overrightarrow{r} - (\omega_i + \omega_0)t] + cos[(\overrightarrow{k_i} - \overrightarrow{q})\cdot\overrightarrow{r} - (\omega_i - \omega_0)t]\Big\} \end{aligned} \tag{2.6}$$

This term corresponds to a polarization field induced by the optical wave in the presence of the mechanical vibration. It is due to the perturbation of the material optical properties induced by the mechanical wave, as expressed in Equation 2.4.

In the second line of Equation 2.6 there are two plane wave terms: one oscillating at an angular frequency $\omega_i + \omega_0$ and the other one at a frequency $\omega_i - \omega_0$. The two oscillating terms contained in $\overrightarrow{P}_{ind}$ behave as two source terms of scattered optical fields [105], verifying the *energy and wavevector conservation*. One generates an optical plane wave with a scattered frequency $\omega_s = \omega_i + \omega_0$ and with a wavevector $\overrightarrow{k}_s = \overrightarrow{k}_i + \overrightarrow{q}$. This is called the anti-Stokes component. The other one generates a Stokes component with a scattered frequency $\omega_s = \omega_i - \omega_0$ and with $\overrightarrow{k}_s = \overrightarrow{k}_i - \overrightarrow{q}$.

The intensity of the scattered fields depends on the scattered radiation polarization $\overrightarrow{e}_s$ as $\left|\overrightarrow{P_{ind}}\cdot\overrightarrow{e}_s\right|^2$ [2]. If we consider an incident wave having a polarization $\overrightarrow{e}_i$, the scattered intensity is proportional to [2]:

$$I_s \propto \left|\overrightarrow{e}_s \cdot \frac{\partial \chi}{\partial \overrightarrow{u}}\Big|_0 \overrightarrow{u}(\omega_0)\cdot\overrightarrow{e}_i\right|^2 \tag{2.7}$$

The scattered light intensity is proportional to the squared mechanical vibration amplitude. Furthermore, the result of the previous equation is that for some particular choices of light polarizations and experimental configurations, the scattered field intensities might vanish [2]. These are called the Raman scattering selection rules.

The generation of inelastically scattered light is therefore due to a modulation of the material dielectric properties. This is caused by the atomic displacements occurring inside the considered system, in the presence of a mechanical wave. The description provided above is valid for optical phonons [38, 106]. In the case of acoustic phonons, the interaction between light and mechanical vibrations is mainly mediated by the photoelastic effect [39]. We follow here the description of this process for layered acoustic systems as described in He *et al.* [107]. It is worth noting that in the literature, several conventions exist to describe the photoelastic effect. In this work, we choose the one used in the aforementioned reference. We introduce the dielectric tensor $\epsilon_{ij} = \chi_{ij} + \delta_{ij}$, with δ_{ij} the Kronecker delta. The change in the susceptibility tensor, or equivalently in the relative dielectric tensor, is in this case induced by the strain fields associated to the acoustic wave. Considering the components of the displacement $\overrightarrow{u}$ in a $(\overrightarrow{x}_1, \overrightarrow{x}_2, \overrightarrow{x}_3)$ reference frame, the strain tensor is defined as:

$$\eta_{ij} = \frac{1}{2}\left(\frac{\partial u_i}{\partial x_j} + \frac{\partial u_j}{\partial x_i}\right) \tag{2.8}$$

The effect of mechanical strain is quantified by the photoelastic fourth rank tensor, and can be expressed as a change in the inverse dielectric tensor (also called the impermeability tensor), given by [108]:

$$\Delta\epsilon_{ij}^{-1} = \sum_{kl} p_{ijkl}\eta_{kl} \tag{2.9}$$

For materials with a cubic crystal structure such as AlAs and GaAs, we can directly write the change of the dielectric tensor as (n is the material's scalar index of refraction) [109–111]:

$$\Delta\epsilon_{ij} = -n^4 \sum_{kl} p_{ijkl}\eta_{kl} \tag{2.10}$$

We now consider a layered periodic medium. As mentioned before, we focus on longitudinal acoustic phonons propagating along the [001] direction in AlAs/GaAs structures. We therefore have purely longitudinal scalar strain fields $\frac{\partial u(z)}{\partial z}$. Furthermore, the incident external optical field is perpendicular to the sample surface, as represented in Figure 2.1. Additionally, in our experiments we will collect the scattered field in a backscattering configuration. The relevant photoelastic component is in this case p_{1133} for each material [107]. In a superlattice the photoelastic constants depend on the z direction since we have alternating layers of different materials. We introduce the photoelastic parameter $p(z) = -n^4 p_{1133}(z)$ [107, 111].

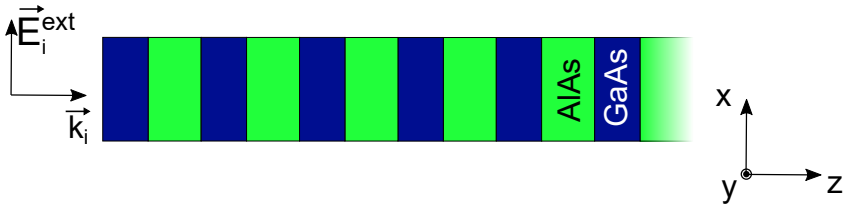

Figure 2.1 – Schematic diagram of the electromagnetic incident field during a Raman scattering experiment on a semi infinite superlattice.

In this configuration, the polarization field that is induced by the interaction with acoustic phonons through the photoelastic effect will be parallel to the orientation of the incident electric field $\overrightarrow{E_i}^{ext}$ (the x direction in Figure 2.1). Also in this case, the inelastic scattering of light is generated by a modulation of the materials dielectric properties due to the presence of acoustic phonons. We can write for example the polarization component source term giving rise to anti-Stokes Raman signals. We denote the complex incident electric field $E_i(z,t) = e^{-i\omega_i t}E_i(z)$ and the complex displacement field $u(z,t) = e^{-i\omega_0 t}u(z)$ inside the layered structure. The anti-Stokes polarization component can be written as [107]:

$$P(z,t) = p(z)\frac{\partial u(z)}{\partial z}E_i(z,t) \tag{2.11}$$

Finally, it is possible to calculate the Raman scattering cross section by performing the sum [69, 107]:

$$\sigma(\omega) \propto \left| \int E_i(z) \times p(z) \times \frac{\partial u(z)}{\partial z} \times E_s^*(z)\,\mathrm{d}z \right|^2 \tag{2.12}$$

Equation 2.12 expresses the spatial overlap integral of the incident optical field, the scattered optical field, the strain induced by the longitudinal mechanical waves and the photoelastic constant of each layer in the periodic medium. The quantity $E_s^*(z)$ corresponds to the complex conjugate of the optical scattered field spatial profile.

Equation 2.12 is central in this work, since it can be used to calculate the Raman cross sections of all the one-dimensional systems studied here. Throughout this manuscript we will compare the experimental results to theoretical Raman spectra.

2.1.2 A microscopic description

A microscopic description is useful to understand the different steps involved in Raman scattering. In particular it shows that three types of particles are involved: the incident and the scattered photons, the absorbed or emitted phonons, and the semiconductor electrons. Since the successive interactions are weak, we can find the scattering probability by applying a perturbation theory [2, 112]. We will consider here a Stokes process in a bulk medium. The scattering probability is given by the following equation, when the energy of the involved transitions are close to electronic resonances [2, 113]:

$$P_{scatt}(\omega_s,\omega_i) = \left(\frac{2\pi}{\hbar}\right)\left|\sum_{nn'}\frac{\langle i|\hat{H}_{e-R}(\omega_s)|n'\rangle\,\langle n'|\hat{H}_{e-latt}(\omega_{phon})|n\rangle\,\langle n|\hat{H}_{e-R}(\omega_i)|i\rangle}{[\hbar\omega_i-(E_n-E_i)]\,[\hbar\omega_i-\hbar\omega_{phon}-(E_{n'}-E_i)]}\right|^2 \times\,\delta(\hbar\omega_i-\hbar\omega_{phon}-\hbar\omega_s) \tag{2.13}$$

The previous equation describes a process that can be divided in three steps:

- An incident photon excites the semiconductor from an initial state $|i\rangle$ to an intermediate state $|n\rangle$ by creating an electron-hole pair. This coupling is described by the electron-radiation Hamiltonian $\hat{H}_{e-R}$ (step 1) in Figure 2.2).
- The electron hole pair undergoes a transition from the state $|n\rangle$ to the state $|n'\rangle$, *via* its coupling to the lattice. The electron-phonon interaction is described by $\hat{H}_{e-latt}$. During this process, one phonon is emitted or absorbed (step 2)).
- The exciton recombines radiatively by emitting the scattered photon. The final electronic state is the same as the initial one (step 3)). The electron-photon interaction Hamiltonian is again involved in this transition.

The electrons play an essential role, since they mediate the interaction between photons and phonons. Nevertheless, their final state is the same as their initial one. The electromagnetic radiations in the visible range have an associated wavevector that is very small ($\approx 10^5\text{cm}^{-1}$) with respect to the typical Brillouin zone sizes for semiconductor materials ($\approx 10^8\text{cm}^{-1}$). Therefore, the states that are involved in the Raman scattering process are usually located at the center of the crystal Brillouin zone.

For the electron-photon interaction, the Hamiltonian can be expressed in the simplified form [2]:

$$\hat{H}_{e-R} = \frac{e}{mc}\overrightarrow{A}\cdot\overrightarrow{\hat{p}} \tag{2.14}$$

The quantities e, m and c are the charge of the electron, its mass, and the velocity of light, respectively. $\overrightarrow{A}$ is the vector potential of the electromagnetic field and $\overrightarrow{\hat{p}}$ is the electron momentum operator.

For the electron-phonon coupling, since we are interested here in longitudinal acoustic phonons, we can consider a deformation potential interaction. In this case, the perturbation of the electronic bands eigenenergies is due to the strain field induced by the mechanical wave.

The microscopic description or Raman scattering also implies in a bulk material the conservation of energy and wavevector for the *overall* process. However, this is not the case for *each* step. In particular, the successive electronic transitions can be virtual, i.e. they can occur without conservation of energy, as represented in Figure 2.2. Nevertheless, the wavevector conservation is verified at each step.

The denominators in Equation 2.13 can become resonant if the energies of the incident or scattered photons matches the one of an electronic transition. The intensity of the Raman signal is in this case greatly enhanced. Increasing the Raman signals can also be achieved by engineering the system's photonic environment, for example by placing the system inside an optical cavity. In this case it is the electron-photon terms that become resonant, as we will see in the next sections.

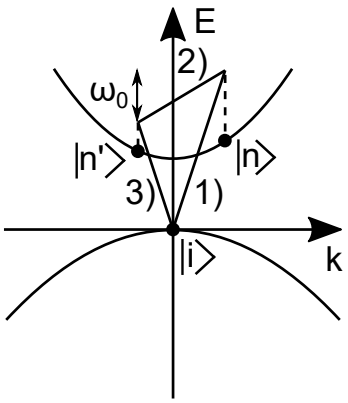

Figure 2.2 – Schematic diagram of the Stokes Raman scattering process as explained in the main text. Image adapted from reference [114]. The upper an lower parabolic curves show the electronic conduction and valence bands, respectively. The plain lines correspond to involved transitions and are labeled by 1), 2) and 3). The relevant states are also marked. The vertical arrow indicates the frequency of the scattered phonon. Notice that the transitions occur without conservation of energy. The states involved in the process are located close to the center of the crystal Brillouin zone.

2.1.3 Raman scattering on superlattices

The calculation of the Raman scattering cross sections will be performed by using Equation 2.12 obtained with a photoelastic model, in Section 2.1.1.

The Raman scattering experiments presented in this manuscript have been carried out with optical fields in the near infrared range (NIR). Inside a material with an index of refraction $n \approx 3$, this corresponds to a wavelength around 300 nm. The semiconductor layers for phononic systems operating at 300 GHz have thicknesses in

the range of few nanometers. Since the optical wavelength is here much larger than the characteristic acoustic unit cells, we will consider the acoustic structures as effective bulk media for light in the NIR range. The effective bulk dielectric constant is given by [107]:

$$\epsilon_{eff} = \epsilon_{GaAs}\frac{L_{GaAs}}{L_{tot}} + \epsilon_{AlAs}\frac{L_{tot} - L_{GaAs}}{L_{tot}} \tag{2.15}$$

where L_{GaAs} corresponds to the total length of GaAs layers and L_{tot} is the full length of the system. We define the effective index of refraction as $n_{eff} = \sqrt{\epsilon_{eff}}$. Therefore the incident and the scattered optical fields can be taken as plane waves in this effective medium. We consider that they will propagate perpendicular to the layers, that is:

$$E_{i/s}(z) \propto e^{zk_{i/s}} \tag{2.16}$$

Furthermore, the energy of a longitudinal phonon with a frequency of 300 GHz is around 1.2 meV, that is much smaller than the one of a NIR photon (≈ 1.2 eV). Hence, the incident and scattered fields verify $|k_i| \approx |k_s|$. We consider two experimental geometries: the backscattering (BS) and the forward scattering (FS) configurations. They are represented in the diagram below:

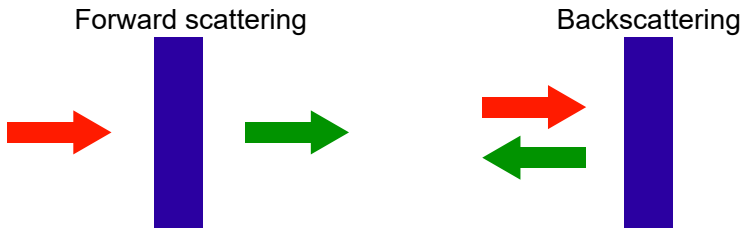

Figure 2.3 – Schematic diagrams of forward scattering and backscattering configurations. The red and green arrows indicate the incident laser and the scattered field, respectively.

We can replace in Equation 2.12 the electric field spatial profiles by Equation 2.16. In a forward scattering geometry, the Raman cross section becomes ($k_i = k_s$):

$$\sigma(\omega) \propto \left| \int p(z) \times \frac{\partial u(z)}{\partial z}\, \mathrm{d}z \right|^2 \tag{2.17}$$

and in a backscattering geometry ($k_i = -k_s$):

$$\sigma(\omega) \propto \left| \int p(z) \times e^{2ikz} \times \frac{\partial u(z)}{\partial z}\, \mathrm{d}z \right|^2 \tag{2.18}$$

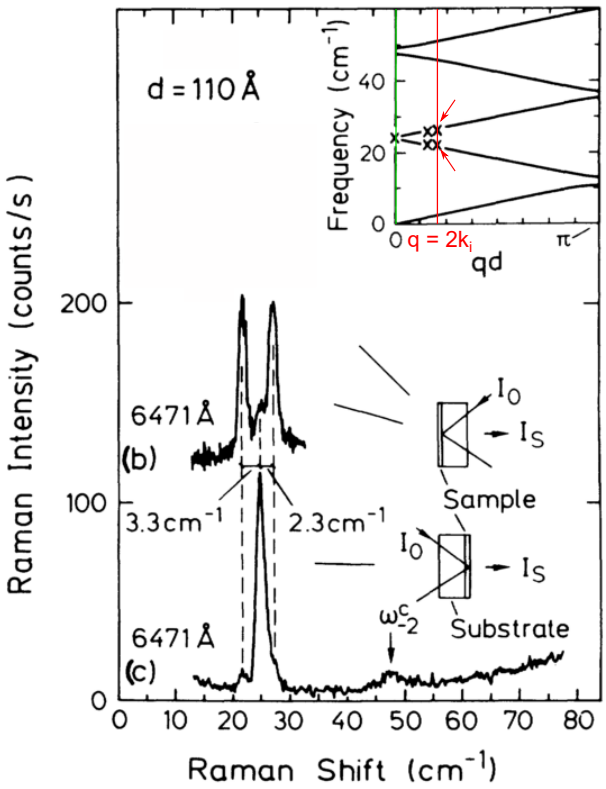

Figure 2.4 – Experimental Raman spectra reproduced from [115]. The red and green symbols have been added to the original figure for clarity. **(b)**: Raman spectrum probed in backscattering geometry. **(c)**: Raman spectrum probed in forward scattering geometry. The experimental configurations are schematically represented next to each curve and the laser wavelength is indicated. The inset shows the calculated dispersion relation of the superlattice. The red and green lines indicate the modes verifying $q = 2k_i$ and $q = 0$ respectively.

The photoelastic integrals expressed above allow to determine the acoustic modes that will be Raman active in a superlattice. For a backscattering geometry they verify $q = 2k_i = \frac{4\pi n_{eff}}{\lambda_{laser}}$, where q is the phonon wave vector and λ_{laser} is the laser wavelength in vacuum. For a forward scattering geometry, the Raman active modes are the ones matching the condition $q = 0$. These are the usual wave vector conservation conditions found for Raman scattering on bulk materials (for processes verifying $k_i \approx k_s$). However, because we have reduced the system's translation invariance by stacking layers of different materials, they are now applied to the folded superlattice dispersion relation. This is illustrated in Figure 2.4, reproduced from [115]. This figure shows experimental results obtained on an a-Si:Ha-SiN_x:H amorphous DBR sample, with unit cell length of $d = 110$ Å. Two experimental Raman spectra measured around the open first ZC acoustic minigap are reported: one was measured in a BS configuration (spectrum (b)) and the other one in FS (spectrum (c)). The inset shows the dispersion relation of the sample. The crossings between the dispersion relation and the vertical red line ($q = 2k_i$) correspond to the modes that are Raman active in a backscattering geometry. The modes generating the Raman peaks shown in Figure 2.4.b are indicated with red arrows. The two crosses next to them evidence other mechanical modes studied through Raman scattering by changing the wavelength of the laser (not shown here). By changing k_i it is therefore possible to access different parts of the acoustic

dispersion relation. The green line shows the Raman active modes that can be Raman active in FS geometry ($q = 0$). The corresponding probed spectrum is shown in Figure 2.4.c. One Raman peak is visible, associated to one of the two standing wave eigenmodes bounding the ZC[1] minigap. However, the other does not induce any Raman peak. This can be understood by considering that these two modes have different spatial symmetries, as explained in section 1.2.2. By calculating the photoelastic overlap integral, the Raman cross section vanishes for one of the two modes.

As we have seen in Section 1.4, by introducing a defect inside a DBR, we can fabricate a phononic resonator. The system can be designed in such a way that the confined state appears in a Brillouin zone center minigap, as it will be the case for all the planar systems studied here. The wave vector conservation shows that this mode will be Raman active in a forward scattering configuration.

In Raman scattering experiments it is very important to minimize the collection of unwanted signals. Indeed, Raman cross sections are generally weaker than the ones of other light-matter interactions, such as photoluminescence or Rayleigh scattering [2, 116]. The latter are in fact sources of unwanted spectral features in the measurements. Furthermore, the stray light induced by the excitation laser is a major source of noise in the experimental data.

A technique that is widely used in nanophononics in order to dramatically enhance the intensity of the measured Raman peaks is to modify the optical environment of the acoustic structure. This greatly facilitates the measurement of the Raman spectra. Furthermore, this allows to access simultaneously the BS and FS signals in a backscattering configuration, as presented in the next section.

2.2 Engineering optical fields for Raman scattering

Layered structures can be used in optics for the fabrication of optical cavities that confine modes in one or more directions of space [117, 118]. One method developed over the years in nanophononics to facilitate Raman scattering spectroscopy experiments is to embed the acoustic structure inside a one-dimensional optical cavity [42]. Indeed, this design has two consequences:

- The strong enhancement of the Raman signals generated inside the acoustic superlattice. The presence of the photonic microcavity shapes the optical density of states. If the incident and scattered fields are resonant with the optical cavity, their intensity is greatly increased. This leads to an enhancement of the Raman scattering cross sections.

- Relaxing the selection rules of backscattering and forward scattering geometries. In particular, this configuration allows to simultaneously probe the Raman peaks associated to mechanical modes with $q = 0$ and $q = 2k_i$ in a backscattering geometry configuration ($q = 0$ is the wavenumber of the phonons and k_i the one of the laser).

In the following sections we will review the main features of the optical Fabry-Perot cavity. We will then describe the physical mechanisms that lead to the enhancement

of the probed Raman spectra intensities and the relaxation of the Raman scattering selection rules.

2.2.1 Optical Fabry-Perot resonators

The optical Fabry-Perot cavities used in this work are realized with semiconductor materials. A fundamental building block to realize these systems are optical DBRs, obtained by periodically stacking semiconductor layers with contrasting optical indices of refraction. It is worth noting that the working principles of these systems are completely analogous to the ones of their acoustic counterpart, presented in section 1.3.

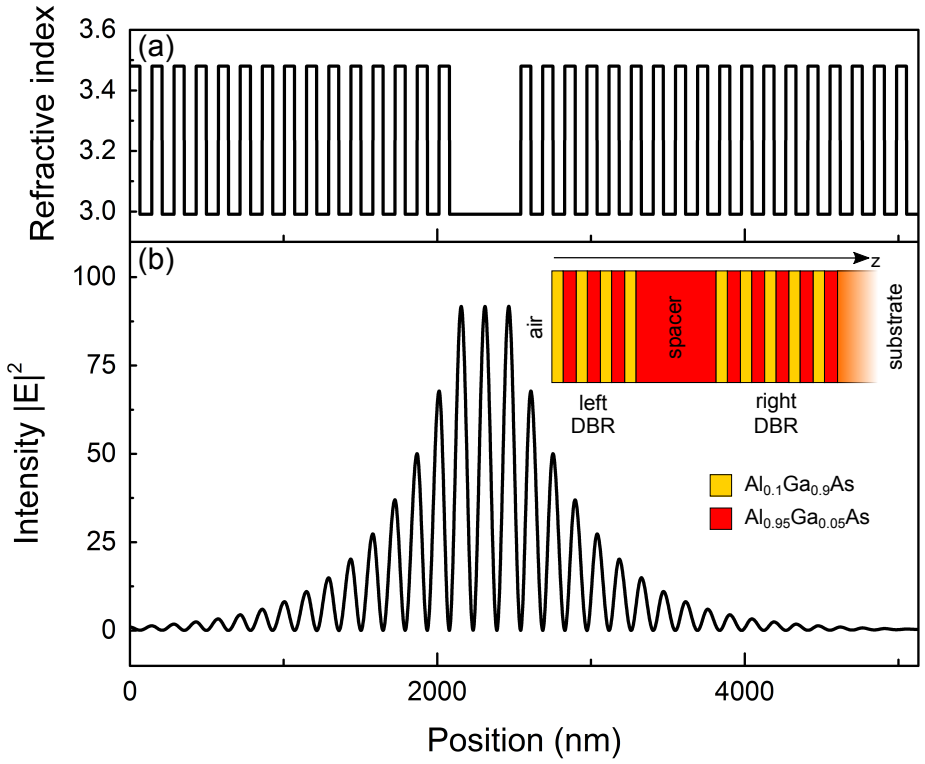

Figure 2.5 – Optical DBR-based Fabry-Perot cavity. **(a)**: Structure of the considered optical resonator. **(b)**: Simulated intensity of the electric field for the confined mode as function of the position in the system. Maximal values are reached inside the spacer. The resonance wavelength is at 925 nm. Inset: schematics of the simulated structure, showing its spatial asymmetry (see main text). The color legend indicates the composition of the layers. The number of layers represented in the DBRs is arbitrary.

Optical DBRs are widely used as high reflectivity dielectric mirrors [119]. In the frame of this work we implemented them by fabricating multilayer heterostructures based on GaAs/AlAs alloys. The two materials have refractive indices of 3.48 and 2.99, respectively. As in the case of nanophononic reflectors, optical stop-bands appear in the optical reflectivity curve of these structures. They can be identified with the

optical minigaps of the corresponding photonic infinite superlattices. In our systems, we used the stop-band related to the first ZE optical minigap. The design maximizing the span of this high reflectivity interval is the $(\frac{\lambda}{4}, \frac{\lambda}{4})$ geometry. Therefore, for the fabrication of a DBR with a stop band centered at a vacuum wavelength λ_0, we chose layer thicknesses given by:

$$d_i = \frac{\lambda_0}{4n_i} \tag{2.19}$$

where d_i and n_i correspond to the layer thickness and index of refraction for the two considered materials.

By enclosing a spacer between two optical $(\frac{\lambda}{4}, \frac{\lambda}{4})$ DBRs we obtain an optical Fabry-Perot cavity. At normal incidence, to optimize the confinement of a mode at a resonance vacuum wavelength λ_0, the thickness of the spacer d_{spacer} has to match the Fabry-Perot resonance condition $d_{spacer} = p\frac{\lambda_0}{2n_{spacer}}$ where p is an integer number. Figure 2.5 shows the simulated spatial profile of a confined mode inside an optical Fabry-Perot cavity. These calculations are performed by using a transfer matrix method. In Figure 2.5.a, we show the structure of the considered cavity, represented by using the indices of refraction of the semiconductor materials. The cavity consists of a $(\frac{3\lambda}{2})$ $Al_{0.95}Ga_{0.05}As$ spacer enclosed between two $(\frac{\lambda}{4}, \frac{\lambda}{4})$ DBRs. The size of the spacer has been chosen to confine an optical mode at $\lambda_0 = 925\,\text{nm}$. The electric field intensity for the confined optical mode is shown in Figure 2.5.b. We can see that the mode is localized inside the optical spacer.

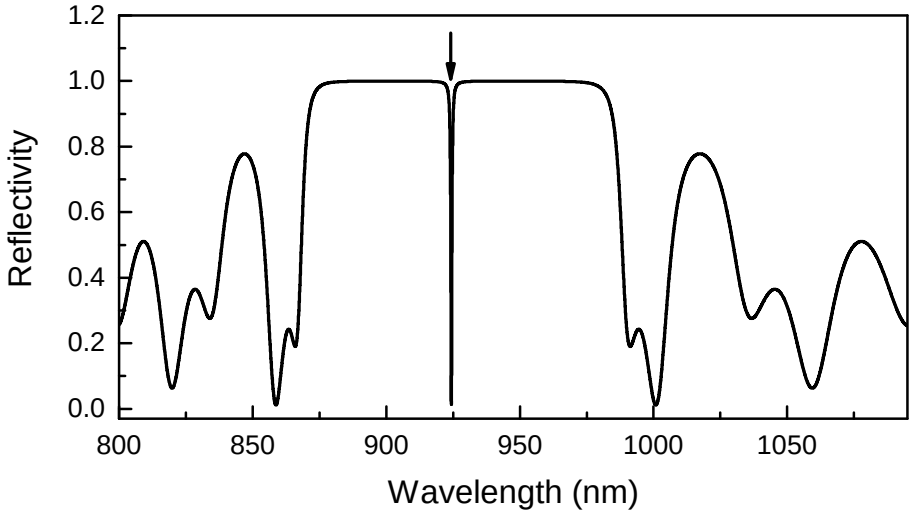

Figure 2.6 – Simulated reflectivity of an optical cavity. The system is constituted by two $(\frac{\lambda}{4}, \frac{\lambda}{4})$ $Al_{0.1}Ga_{0.9}As/Al_{0.95}Ga_{0.05}As$ DBRs separated by a $(3\frac{\lambda}{2})$ $Al_{0.95}Ga_{0.05}As$ spacer. The resonance wavelength is at 925 nm, indicated by the vertical arrow.

The inset to Figure 2.5.b shows a sketch of the system. Notice that the structure is asymmetric. The left DBR is in contact with air, whereas the other one is in contact with the GaAs substrate. To compensate the weaker impedance mismatch at the $Al_{0.95}Ga_{0.05}As$/substrate interface with respect to the one between $Al_{0.1}Ga_{0.9}As$ and air the left DBR has 14 layer pairs, whereas the right one has 18. Figure 2.6 shows

the corresponding reflectivity curve of this structure. The sharp dip in the stop band marks the presence of the confined optical mode.

The optical field intensity enhancement is quantified by the optical quality factor (Q) of the cavity. It can be determined from the reflectivity curve, by calculating the ratio between the resonance frequency f_0 and the FWHM δf of the reflectivity dip. In the case of the considered structure, we find $Q = 1970$.

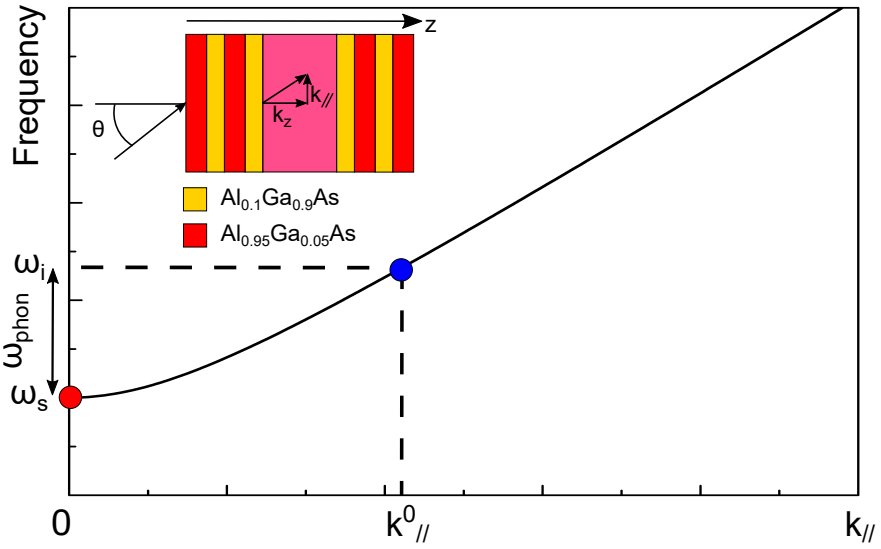

Figure 2.7 – Schematic in-plane dispersion relation of an optical cavity, as a function of the in-plane wavevector component $k_{//}$. The red and blue dot indicate the condition of Double Optical Resonance for which the intensities of the Stokes Raman signals are maximal (see Section 2.2.2). Inset: Diagram showing the incidence angle θ and the components $k_{//}$ and k_z inside the spacer. The color legend indicates the composition of the layers. The $Al_{0.95}Ga_{0.05}As$ spacer is represented in pink for clarity.

In a more general way, the optical resonance frequency is dependent on the incidence angle θ of the incoming wave. If the incidence angle is different from 0 (as shown in the inset to Figure 2.7), the wavenumber $\vec{k}$ of the confined mode inside the cavity spacer is not purely oriented along the z axis. We can decompose $\vec{k} = \vec{k_z} + \vec{k_{//}}$, where $\vec{k_{//}}$ is the component parallel to the surface of the structure, that we call the in-plane component, and $\vec{k_z}$ is the normal one. The more we increase θ, the more $\vec{k_{//}}$ increases. The optical field is resonant with the cavity if the z component of the wavevector complies with the condition [120]:

$$k_z = p\frac{\pi}{n_{spacer}d_{spacer}} \tag{2.20}$$

The total wavevector satisfying the dispersion relation of light:

$$(c/n_{spacer})\sqrt{k_z^2 + k_{//}^2} = \omega \tag{2.21}$$

c being the speed of light and ω the angular frequency of the confined mode. We find that ω as function of $k_{//}$ is given by:

$$\omega(k_{//}) = (c/n_{spacer})\sqrt{\left(p\frac{\pi}{n_{spacer}d_{spacer}}\right)^2 + k_{//}^2} \tag{2.22}$$

The more we increase the incidence angle θ, the more the confined mode resonance frequency increases. The dispersion relation in Equation 2.22 is schematically represented in Figure 2.7. This property of optical Fabry-Perot cavities is very useful, as we will see below, to enhance Raman scattering signals.

An optical cavity allows to enhance the intensity of a resonant optical field inside the spacer. An acoustic structure can play the role of an optical spacer between two $(\frac{\lambda}{4}, \frac{\lambda}{4})$ $Al_{0.1}Ga_{0.9}As/Al_{0.95}Ga_{0.05}As$ optical DBRs. Indeed, as explained in section 2.1.3, the wavelengths of NIR optical modes are much larger than the layer dimensions of acoustic cavities operating in the hundreds of GHz range. The phononic structure can be approximated as an effective homogeneous optical spacer, with a dielectric constant given by Equation 2.15. We suppose that the acoustic system total length matches the condition $L_{tot} = p\lambda_0/(2n_{eff})$. In this case, we obtain a structure where the phonons inside the acoustic system interact with strongly enhanced optical fields. Such a configuration is schematically shown in Figure 2.8. Each layer of material in the acoustic structure "sees" a constant amplitude of the confined electric field. Raman intensities can be calculated by considering the standing wave character of the incident and scattered fields in the photoelastic overlap integral (Equation 2.12).

Placing acoustic structures inside an optical resonator enhances the intensity of the Raman signals and enables the observation of Raman peaks associated to phonons with $q = 0$ in a BS configuration. In Chapter 3, the samples that will be presented have all been fabricated in this configuration. In the two following sections we will detail how the presence of the optical cavity affects the Raman cross section and the selection rules.

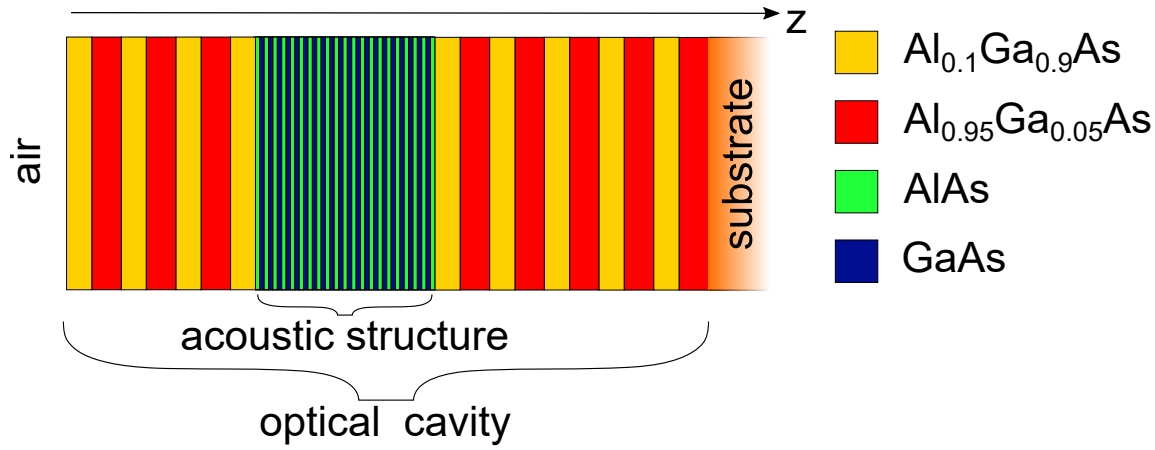

Figure 2.8 – Diagram of an acoustic structure embedded inside an optical Fabry-Perot resonator. This design is the one used for all the systems presented in this chapter. Notice the asymmetry in the number of layers between the left and right DBRs to balance their reflectivities (see main text). The color scale in the figures indicate the materials used in each layer.

2.2.2 Enhancing Raman intensities

The enhancement of the Raman signal intensities for acoustic structures embedded in an optical cavity can be explained by considering the equations describing the inelastic scattering of light, as given by Equation 2.13. We recall below the probability

of Raman scattering for a Stokes process, i.e. emission of a phonon. We denote, as before, ω_i and ω_s the angular frequencies of the incident and scattered fields:

$$P_{scatt}(\omega_s,\omega_i) = \left(\frac{2\pi}{\hbar}\right)\left|\sum_{nn'}\frac{\langle i|\hat{H}_{e-R}(\omega_s)|n'\rangle\,\langle n'|\hat{H}_{e-latt}(\omega_{phon})|n\rangle\,\langle n|\hat{H}_{e-R}(\omega_i)|i\rangle}{[\hbar\omega_i-(E_n-E_i)]\,[\hbar\omega_i-\hbar\omega_{phon}-(E_{n'}-E_i)]}\right|^2 \times\,\delta(\hbar\omega_i-\hbar\omega_{phon}-\hbar\omega_s) \tag{2.23}$$

In Equation 2.23 the incident and scattered optical fields play a role in the terms $\langle n|\hat{H}_{eR}(\omega_i)|i\rangle$ and $\langle i|\hat{H}_{eR}(\omega_s)|n'\rangle$, respectively. They correspond to the virtual transitions in which an exciton is created by absorbing an incoming photon of energy $\hbar\omega_i$, and to the re-emission of an outgoing scattered photon of energy $\hbar\omega_s$.

We suppose that the optical resonator optimally confines two optical modes having resonances at ω_e and ω_c, respectively. Furthermore, we consider that $\omega_e = \omega_i$ and $\omega_c = \omega_s$. Under this condition, Equation 2.23 presents two resonant terms for the optical fields, that is, an incoming and an outgoing resonance. The incident photons and the scattered ones being resonant respectively with an excitation and a collection mode, we call this condition the Double Optical Resonance (DOR) [121].

It is possible to simultaneously reach both resonances in a planar system using a DBR based cavity. In order to find this condition we use here the dispersion relation of the Fabry-Perot resonator as function of $k_{/\!/}$, as represented in Figure 2.7. We are considering a Stokes process, i.e. $\omega_s = \omega_i - \omega_{phon}$, with ω_{phon} the angular frequency of the considered phonons involved in the scattering process. We suppose that $\omega_s = \omega_c$ occurs at the bottom of the dispersion relation, i.e. for $k_{/\!/} = 0$ (normal collection, $\theta_0 = 0$). To find this condition, the samples that we have studied are fabricated with an in-plane thickness gradient. The optical resonance frequencies depend on the position at which the laser impinges on the sample. When displacing the laser spot on the surface of the structure, the whole dispersion relation shown in Figure 2.7 is translated vertically. For a given ω_i and ω_{phon}, we can therefore find a position for which $\omega_s = \omega_c$. Furthermore, we can find an incidence angle $\theta_0 \neq 0$, i.e. a mode with a in-plane component $k_{0/\!/}$, for which $\omega_i = \omega_e$. This allows us to be in DOR. The blue and red dots in Figure 2.7 schematically mark the spectral position of the excitation and collection modes, respectively.

The frequency shift induced by a mechanical mode resonant at 300 GHz is small with respect to the optical frequency of NIR optical fields (≈ 300 THz). Hence, the DOR incidence angle θ_0 is small for the experiments described here, around 10°. Therefore, we consider that we are almost at normal incidence also for the excitation field. As a consequence, if we couple to the excitation or the collection mode a resonant plane wave with an electric field amplitude of 1 V/m, we get the same standing wave for the two modes inside the spacer (i.e. the acoustic cavity) given by:

$$E_{inc}(z) = E_{max}\,(\exp(ikz) + \exp(-ikz)) \tag{2.24}$$

where E_{max} corresponds to the amplification factor of the electric field inside the cavity. k is the wavenumber respecting the resonance condition $k = p \times \frac{\pi}{L_{tot}}$. Finally, $|E_{max}|^2$ being proportional to Q, we consider that the excitation and the collection mode have the same Q-factor in DOR condition.

In Equation 2.23, we can calculate the $\langle n|\hat{H}_{eR}(\omega_i)|i\rangle$ matrix term by considering a dipolar interaction for $\hat{H}_{eR}$ [69]. The excitation mode has the form given by Equation 2.24. The value of $\langle n|\hat{H}_{eR}(\omega_i)|i\rangle$ is proportional to E_{max}, and the scattering probability becomes proportional to $|E_{max}|^2$. Therefore, the Raman scattering cross section is multiplied by a factor of Q [69]. Additionnally, the confinement of the resonant scattered field further increases the scattering probability [69]. By taking into account the enhancement of the two confined modes, the Raman scattering cross section is enhanced by a factor of Q^2 [69, 122]. By maximizing the confinement of the excitation and collection modes, the Raman scattering cross section is greatly increased with respect to the case where no optical cavity is present. Typical experimentally achieved values of Raman scattering signal enhancement are of the order of $10^4 - 10^6$. [123–125]

By retaking the spatial profile of the confined optical modes, as expressed in equation 2.24, and inserting it in the photoelastic overlap integral (see Section 2.1.1, Equation 2.12), the Raman scattering cross section can be written as [38]:

$$\sigma_{Raman} \propto Q^2 \times \left| \int (2 + exp(2ikz) + exp(-2ikz)) \times p(z) \times \frac{\partial u(z)}{\partial z} \, \mathrm{d}z \right|^2 \tag{2.25}$$

In this expression the Q^2 term corresponds to the enhancement factor due to optical confinement. The first term in the overlap integral (i.e. the term between brackets) corresponds to the product of the incident and the scattered field spatial profiles. A we will see in the next section, it is the standing wave character of these two fields that will allow us to probe the acoustic modes with $q = 0$ in a backscattering configuration.

2.2.3 Relaxing the rules of backscattering

We now investigate the effect on the Raman signals of having the acoustic cavity interacting with a standing wave optical mode. Equation 2.25 can be rewritten in the form [38]:

$$\sigma_{Raman} \propto Q^2 \times |A_{BS} + A_{FS}|^2 \tag{2.26}$$

with

$$A_{BS} = \int (\exp(2ikz) + \exp(-2ikz)) \times p(z) \times \frac{\partial u(z)}{\partial z} \mathrm{d}z$$

and

$$A_{FS} = \int 2 \times p(z) \times \frac{\partial u(z)}{\partial z} \mathrm{d}z$$

On one hand, in A_{BS} we observe that the optical field gives rise to oscillatory terms inside the overlap integral. It is this A_{BS} term that gives rise to Raman peaks related to mechanical modes with $q \approx 2k_i$ for an acoustic superlattice, with q being the wavevector of the mechanical mode and k_i the one of the incident laser. As already mentioned in the introduction, these Raman peaks are usually visible in a backscattering configuration for a bare acoustic structure. These modes are still Raman active in this configuration if the system is embedded in a Fabry-Perot resonator. On the other

hand, we can see that in A_{FS}, the optical field generates a constant term (the factor of 2). According to the description of the photelastic model given in the introduction, this overlap integral shows that mechanical modes with $q \approx 0$ are also Raman active. These Raman peaks that are only measurable in a forward scattering geometry for a bare acoustic cavity are now also visible in a backscattering configuration.

An intuitive picture to explain that backscattering and forward scattering Raman signals are now simultaneously visible is to consider that the incident and the scattered photons are "trapped" in the Fabry-Perot resonator. Therefore, they are reflected back and forth several times by the optical mirrors before escaping. Since the scattered photons can tunnel through any of the two DBRs, we are able to observe both the backscattering and forward scattering Raman signals in both measurement configurations [69].

The experimental configuration allowing to reach the double optical resonance condition for Stokes Raman signals is shown in Figure 2.9. The red arrow indicates the incident optical field with a frequency ω_i, which is resonant with the excitation mode. The green vertical arrow indicates the scattered light with a frequency ω_s, which is resonant with the collection mode. It is collected at normal incidence with respect to the sample surface. In the first section of Chapter 3, we will present in detail the experimental Raman set-up that we have implemented in order to fully take advantage of the DOR condition. This was carried out for characterizing the planar nanophononic resonators studied in this manuscript.

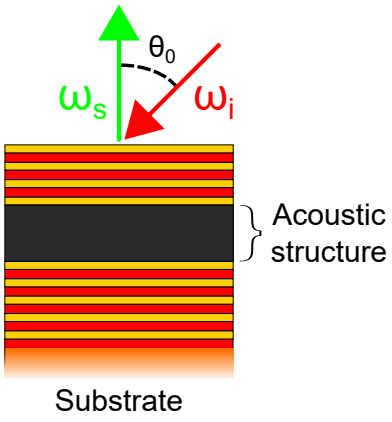

Figure 2.9 – Experimental configuration allowing to reach the DOR condition in a backscattering geometry, for Stokes Raman signals. The acoustic structure embedded in the optical cavity is indicated. The incident field (red arrow) and the scattered field (green arrow) are resonant with the optical cavity excitation mode and the collection mode, respectively. The Raman signals are collected at normal incidence. The incidence angle θ_0 has been exaggerated with respect to real experimental conditions, for clarity.

Embedding acoustic systems in an optical cavity therefore greatly facilitates the measurement of confined phonons, since Raman signals are enhanced, and the FS and BS components can be probed simultaneously in a backscattering geometry experimental configuration. The design presented in Figure 2.8 has been systematically implemented for all the samples characterized in this work.

Raman scattering spectroscopy is a powerful technique for probing the mechanical properties of acoustic layered systems. Nevertheless, other experimental methods can be used for this purpose. For example, pump-probe coherent phonon generation and detection has been widely implemented for the study of these structures. The first experimental demonstration of phononic three-dimensional confinement in AlAs/GaAs micropillars has been obtained through this experimental technique, as detailed in Chapter 5. This was the result of a collaboration between our group and the team of Alejandro Fainstein at the Centro Atómico Bariloche & Instituto Balseiro in Argentina.

2.3 Coherent phonon generation and detection: phonon dynamics

Pump-probe experimental techniques for the generation and detection of acoustic phonons were inroduced by the group of Humphrey J. Maris in the 80's [126, 127]. This method involves the use of ultrafast pulsed lasers to create and measure coherent mechanical oscillations in the hypersonic range. This is in contrast to Raman scattering experiments, where the probed mechanical vibrations are induced by thermal fluctuations inside the sample.

The principle of the experiment is represented in Figure 2.10. A pulsed laser emits picosecond (ps) or femtosecond (fs) light pulses with a repetition rate in the range of tens of MHz. Each pulse passes through a beam splitter which divides it into two beams: a strong pump pulse and a weak probe. Each one takes a different path in the set-up and plays a different role.

- The pump pulse reaches the sample first, at a time t_1. Light induces the generation of a mechanical pulse. This light-matter interaction can be mediated by several mechanisms, such as thermoelasticity, deformation potential, electrostriction, or piezoelectricity [128]. The strain pulse propagates, and eventually decays after some time. While the acoustic waves are present inside the sample, they modulate the optical properties of the system, for example through the photoelastic effect as explained in Section 2.1.1.

- The weaker probe pulse is delayed in the set up, as represented in Figure 2.10. It reaches the studied system at a time $t_2 = t_1 + \Delta t$, where Δt is the delay between the two pulses. Part of it is reflected, and its intensity is measured with a photodetector. The probe pulse probes the instantaneous optical reflectivity $R(t_1 + \Delta t)$ [128]. We can continuously change Δt between the pump and the probe, by using a mechanical delay line. Therefore, we can reconstruct the temporal evolution of the optical reflectivity ($\frac{\Delta R}{R} = \frac{R(t)-R_0}{R_0}$) induced by the strain pulse. The changes in this parameter induced by acoustic phonons are usually weak, and a lock-in synchronous detection scheme is usually implemented to improve the signal-to-noise ratio.

By following the optical reflectivity time trace, we can probe the evolution of the mechanical waves generated by the pump pulse. We present some typical experimental results obtained through pump probe measurements on a GaAs/AlAs phononic DBR, reproduced from [129]. The DBR was designed in order to have the first ZC

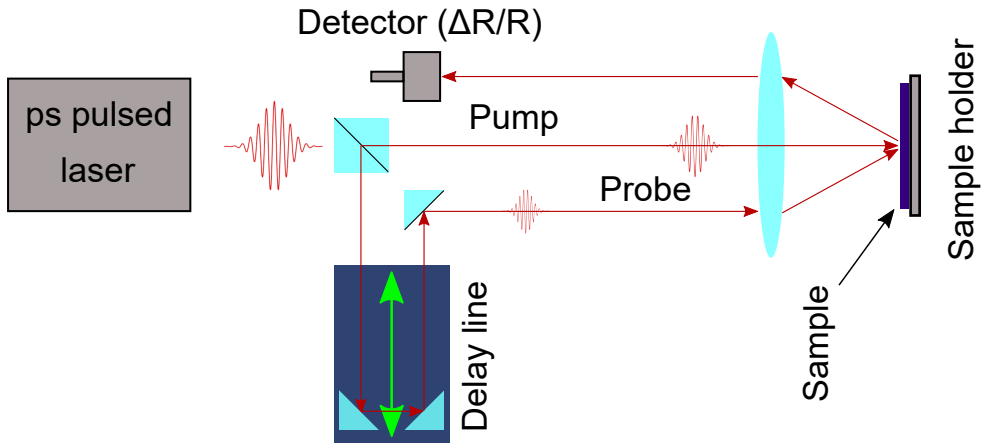

Figure 2.10 – Schematic diagram of a pump-probe experimental set-up.

acoustic minigap centered at a frequency of $\approx 1\,\mathrm{THz}$. The evolution of the optical reflectivity time trace is shown in Figure 2.11.a. The measurement was carried out with a femtosecond pulsed laser at a wavelength of 740 nm.

The pump reaches the sample at $t = 0$, where a strong reflectivity variation can be observed. This is associated to the electronic excitation of the sample, and the slow variation in the time evolution is related to temperature change and electron-hole recombination processes inside the sample [129]. On top of this low frequency evolution, we observe rapid oscillations which are provoked by the coherently generated acoustic phonons. After having removed the slow frequency components and the part of the time trace where the electronic contributions dominate the temporal evolution, the signal is Fourier transformed, as shown in Figure 2.11.b. Several sharp peaks are visible, and can be associated to mechanical modes verifying $q = 2k_i$ and $q = 0$, as indicated in the band diagram represented in the inset to Figure 2.11.b. Notice the similarities with peaks usually observed in Raman scattering experiments, as presented in Section 2.1.3.

In the presented measurements, coherent mechanical oscillations verifying $q = 2k_i$ and $q = 0$ have been simultaneously generated and probed in a DBR. Furthermore, pump probe experiments are a powerful technique for studying nanophononic resonators. Indeed, from the decay of the measured temporal traces, it is possible to measure the mechanical damping rates of the studied confined modes [43]. In a more general way, this technique is a powerful tool for studying the dynamics of mechanical vibrations in complex nanophononic layered systems [38].

In this section we have introduced pump-probe coherent phonon generation and detection, usually implemented in the context of picosecond ultrasonic experiments and in nanophononics for the study of phonon dynamics. In the next section, we describe another technique that allows to probe the mechanical motion of a system by using the simultaneous confinement of an optical and acoustic mode. This method was developed in the context of cavity optomechanics.

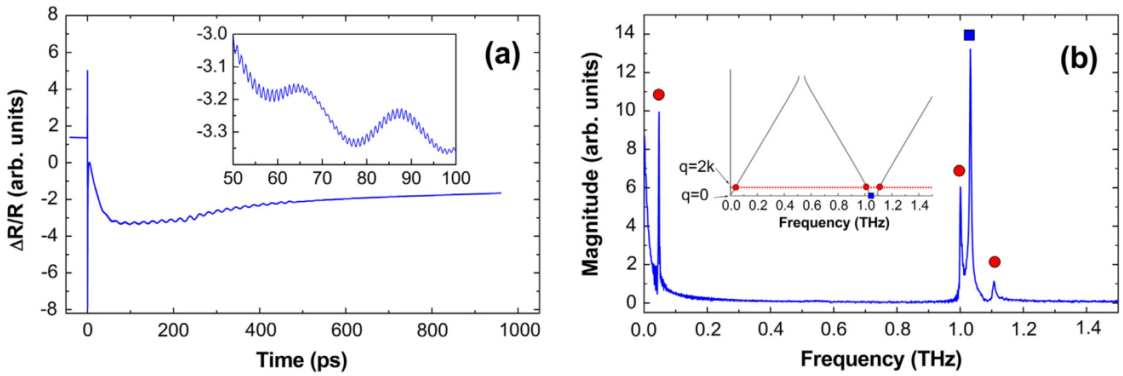

Figure 2.11 – Pump-probe measurements on an acoustic superlattice. Images reproduced from [129]. **(a)**: Time trace of optical reflectivity measured on a superlattice. The inset shows a detailed view of the reflectivity oscillations. **(b)**: Fourier transform of the reflectivity temporal evolution, after having removed the low frequency components. The red circles and blue rectangle indicate the peaks associated to mechanical modes verifying $q = 2k_i$ and $q = 0$, respectively. The inset shows the band diagram of the associated superlattice.

2.4 Optomechanical systems

If a system constitutes simultaneously a mechanical and an optical resonator, it is possible to study how one resonant mechanical vibration couples to an optical confined field. As we will see in Chapter 5, GaAs/AlAs planar systems can be etched into micropillars, which constitute three-dimensional optomechanical resonators. Three-dimensional optomechanical platforms have been widely studied in cavity optomechanics, in particular for probing and manipulating the mechanical motion associated to a confined acoustic mode [20]. In this section, we will introduce the fundamental concepts that will allow us to optimize and engineer micropillar optomechanical resonators, based on a Fabry-Perot design.

2.4.1 Optomechanical interaction

The simplest example where an optomechanical interaction takes place is represented in Figure 2.12. The considered Fabry-Perot resonator is constituted by two metallic mirrors separated by a distance L, that confine an optical mode at a frequency ω_{cav} with a quality factor given by $Q_{cav} = \frac{\omega_{cav}}{\Gamma_{cav}}$. One of the two mirrors is attached to a spring and can oscillate at a mechanical resonance frequency ω_m. Its mechanical damping rate is given by Γ_m. In this simple picture, the mechanical and optical degrees of freedom are not independent. For example, the mechanical oscillation will change the optical resonance frequency by modifying the size of the cavity. This will modulate the intensity of the optical field stored in the resonator in time. Reciprocally, this modification of the light field inside the resonator will induce a dynamic backation on the mechanical motion [130]. Indeed, the change in the intracavity power induces a delayed variation in the optical forces exerted on the movable mirror. As in the case of pump-probe experiments, these optical forces can have multiple origins, such

as radiation pressure [131], electrostriction [132] or photothermal effects [133]. The mechanical oscillation is therefore affected by the backaction of the optical field. This bi-directional interaction is quantified by the optomechanical coupling factor g_{om} [130].

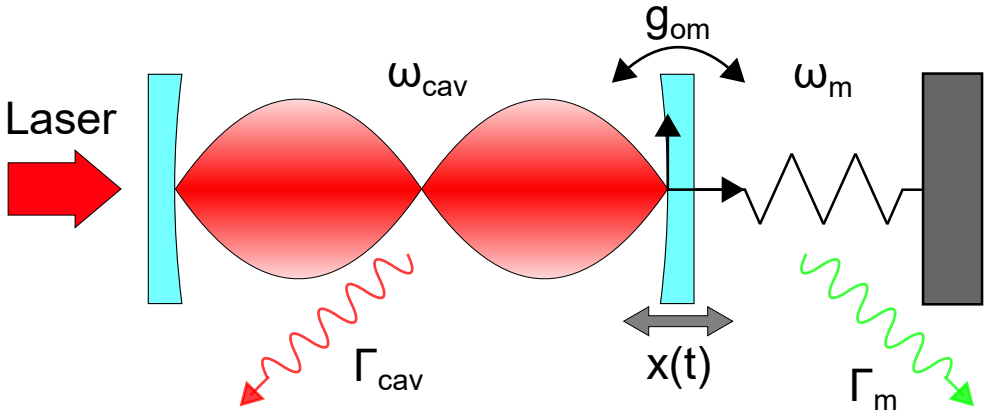

Figure 2.12 – Schematic diagram of an optomechanical resonator. The optical and mechanical resonance frequencies are noted ω_{cav} and ω_m, respectively. The quantities Γ_m and Γ_{cav} are the mechanical and optical dampings. The grey arrow indicates the mechanical motion of the resonator, coupled to the light field through g_{om}.

Optomechanical coupling between light and mechanical vibrations has been studied in a great variety of three-dimensional resonators. Their scale ranges from macroscopic objects such as macroscopic mirrors of few kilograms used in gravitational interferometers [134], down to ultracold atom ensembles trapped inside optical cavities [135]. The development of micro- and nano-fabrication techniques has allowed the realization of a plethora of solid state optomechanical systems. Among these micro- and nano-resonators, some frequently used architectures are microdisks [136] and microtoroids [137], one-dimensional [138, 139] and two-dimensional photonic crystals [140], membranes [141], nanobeams [142], clamped mirrors [143] or nanorods [144], to name a few.

2.4.2 Probing and manipulating the mechanical motion

The existence of an interaction between the optical and mechanical fields allows to precisely read the mechanical motion of the system through optical measurements. We consider the previous Fabry-Perot resonator case. The equation of motion of the mechanical harmonic oscillator (i.e. the mirror attached to the spring) is:

$$m\frac{\mathrm{d}^2x(t)}{\mathrm{d}^2t} + m\Gamma_m\frac{\mathrm{d}x(t)}{\mathrm{d}t} + m\omega_m^2x(t) = F_{ext}(t) \tag{2.27}$$

where m is the mass of the mechanical harmonic oscillator, $x(t)$ is the mechanical displacement, and F_{ext} is the sum of forces applied to the system. Expressing equation 2.27 in the frequency space ($x(\omega) = \chi(\omega)F_{ext}(\omega)$) allows to write the mechanical susceptibility of the harmonic oscillator as:

$$\chi(\omega) = [m(\omega_m^2 - \omega^2) - i\Gamma_m\omega m]^{-1} \tag{2.28}$$

In the absence of externally applied forces, the system is still subjected to thermal fluctuations represented by a force $F_{th}(t)$ which is a random variable [20]. To characterize the Brownian motion of the system, one can measure the noise power spectral density (PSD) $S_{xx}(\omega)$ of $x(t)$. The Wiener-Khinchin theorem states that the PSD can be found by performing the Fourier transform of the signal autocorrelation function [145]. In the classical limit, the fluctuation-dissipation theorem relates the PSD to the imaginary part of the oscillator susceptibility as [20]:

$$S_{xx}(\omega) = \frac{2k_bT}{\omega}\mathrm{Im}(\chi(\omega)) \tag{2.29}$$

where k_b is the Boltzmann constant and T is the resonator temperature.

One way to probe the optomechanical system's motion is to take advantage of the coupling between light and the mechanical vibration, as represented in Figure 2.13. The fluctuation $x(t)$ (Figure 2.13.a) changes the optical resonance frequency $\omega_{cav}(x)$. We denote ω^0_{cav} as the optical eigenfrequency when $x = 0$. Assuming a small mechanical motion, this is quantified by the optomechanical coupling term:

$$g_{om} = -\frac{\partial\omega^0_{cav}}{\partial x} \tag{2.30}$$

The optomechanical coupling is here due to the motion of the oscillating mirror, which changes the length of the optical cavity. This corresponds to a geometrical deformation of the system, and results in $g_{om} = \frac{\omega^0_{cav}}{L}$. Notice that we have introduced here the term g_{om} by considering the effect of the mechanical motion on the optical mode. In order to illustrate the bi-directional nature of this interaction, we can express the optical radiation pressure force acting on the movable mirror as a function of g_{om} as $F_{opt} = N_{phot}\hbar g_{om}$ [132]. N_{phot} is the number of photons stored in the cavity. From this expression, it is also clear that one way to neglect the effect of the optical forces in order to probe the Brownian motion is to keep the optical laser power low.

The mechanical motion modulates the spectral position of the optical reflectivity curve (Figure 2.13.b) in time by a quantity $\partial\omega(x(t))$ that is proportional to g_{om}. This temporal dependence of the optical reflectivity $R(t)$ can be monitored by sending an incident laser with an intensity I_0 and by measuring the reflected intensity. To maximize the sensitivity, the laser frequency is set so that it falls on the flank of the reflectivity curve, where the slope is maximal. We denote with $\Delta = \omega_{cav} - \omega_l$ the detuning between the incident laser ω_l and the cavity resonance frequency. The fluctuations of mechanical motion are transduced into fluctuations of optical intensity $I(t) = R(t)I_0$. Without considering the shot noise or other noises introduced by the laser, the power spectral density of the reflected optical intensity S_{pp} is related to the one of the mechanical resonator as [146, 147]:

$$S_{pp}(\omega) = a(I_0, g_{om}, \Delta, \Gamma_{cav})S_{xx}(\omega) \tag{2.31}$$

The factor a indicates the optomechanical transduction. One can then measure the PSD of $I(t)$, which reveals the noise spectrum of the mechanical oscillator. From this measurement, it is possible to probe the mechanical properties of the optomechanical resonator, such as its mechanical eigenfrequency and the mechanical damping rate (Figure 2.13.c). This experimental technique allows to perform very precise displacement measurements. For example, Brownian motion measurements performed on GaAs microdisks operating at mechanical resonance frequencies around 3 GHz

reached sensitivities of $\approx 10^{-16}\mathrm{m}/\sqrt{\mathrm{Hz}}$ [147] down to $\approx 10^{-17}\mathrm{m}/\sqrt{\mathrm{Hz}}$ [136]. These values are determined by the experimental noise introduced during the measurement and by the optical, mechanical, and optomechanical parameters of the considered resonator.

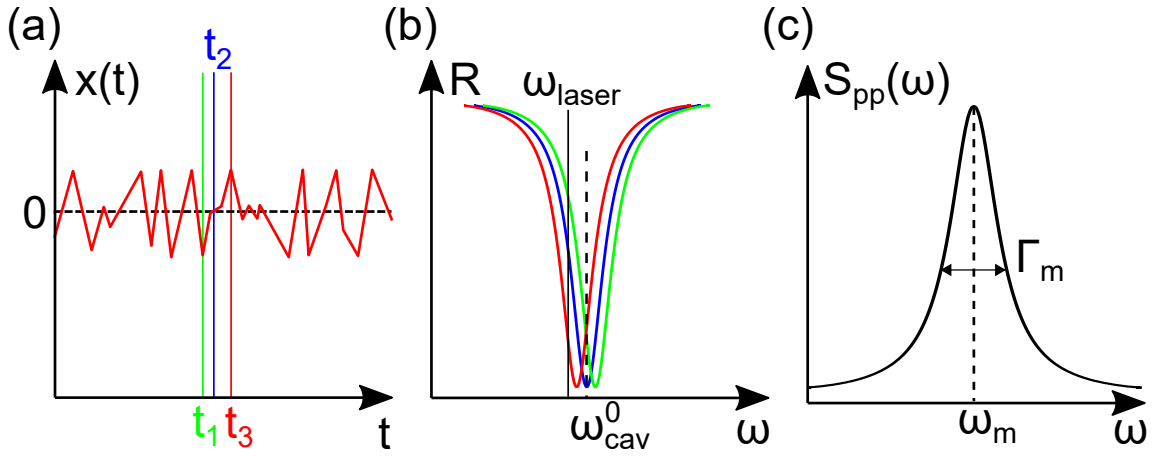

Figure 2.13 – Schematic sequence of Brownian motion measurement. **(a)**: temporal evolution of the mechanical oscillator fluctuations $x(t)$. We consider that the oscillator is at rest when $x = 0$. The vertical colored lines indicate the value of $x(t)$ at three different instants t_1, t_2, and t_3. **(b)**: Optical reflectivity curves of the optomechanical system at the three different times t_1, t_2, and t_3. Their colors indicate the corresponding times shown in Panel (a). The laser is spectrally located on the flank half minimum of the blue reflectivity curve (i.e. $x(t_2) = 0$). The reflected intensity is modulated in time by the mechanical motion. **(c)**: PSD of the measured optical reflected signal from the mechanical oscillator. This reveals the mechanical properties of the system.

The Brownian motion can be monitored through optical measurements. Notice however that the laser beam probes the mechanical fluctuations as long as its power is kept low. Indeed, by increasing this parameter, the optical forces become more and more important, inducing a modification in the mechanical behavior of the system. The dynamical effects of the optical forces have two major consequences on the mechanical oscillator properties, which can be quantitatively described by different theoretical models [20, 148, 149].

The first one is a modification of the oscillator spring constant. The mechanical frequency of the system will be increased (hardening of the spring) or decreased (softening), depending on the detuning Δ. This is called the "optical spring effect" [130].

The second one is a modification of the oscillator damping rate. A "thermodynamic" description can be provided by considering the delay between the mechanical motion $x(t)$ and the temporal evolution of the optical forces [149]. For example, the optical forces do not respond instantaneously to a geometrical change of the resonator, since the photons are trapped inside the cavity for a given lifetime τ [148]. The effect of this temporal delay is that the optical force can provide (i.e. positive work) or extract (i.e. negative work) mechanical energy from the oscillator. This effect is quantified by the effective damping rate $\Gamma_{tot} = \Gamma_m + \Gamma_{opt}$ and by the mechanical mode effective temperature [20, 148]:

$$T_{eff} = \frac{\Gamma_m}{\Gamma_{tot}} T_0 \tag{2.32}$$

where T_0 is the bath temperature. The sign of the optomechanical damping rate Γ_{opt} depends on the detuning Δ. In particular, for $\Delta < 0$, $\Gamma_{opt} < 0$ [20]. The overall damping rate is therefore decreased and the mechanical motion amplitude is increased by work provided through the optical forces. Eventually, by increasing the optical power of the pump laser, $\Gamma_{tot} = 0$ and we reach the power threshold for the onset of mechanical self oscillations [149]. On the contrary, when $\Delta < 0$, $\Gamma_{opt} > 0$ [20]. In this case, the mechanical oscillator is cooled by the optomechanical interaction. Eventually, the system is cooled down to very low effective temperatures (i.e. there are few phonons in the mechanical mode). In this case, a quantum description of the system is necessary, in particular for describing the minimal phononic population that can be reached inside the confined mechanical mode [150].

The manipulation of the mechanical mode can also be interpreted in terms of inelastic light scattering induced by the confined mechanical mode [151, 152]. The process is represented in Figure 2.14 for a cooling configuration. The laser is represented by a black vertical line, spectrally positioned at a wavelength $\omega_l = \omega_{cav} - \omega_m$. As we have seen before, the Raman process induced by the confined vibration produces both a Stokes and an anti-Stokes component, corresponding to the blue and red line in Figure 2.14, respectively. However, in this case the photons will preferentially scatter into the component of higher energy since they are resonant with the confined optical mode. Scattering a photon to a higher frequency implies the absorption of a phonon from the mechanical resonator. Since the rate of the anti-Stokes process is higher than the one of the Stokes process, this leads to an overall sideband cooling of the confined mechanical mode.

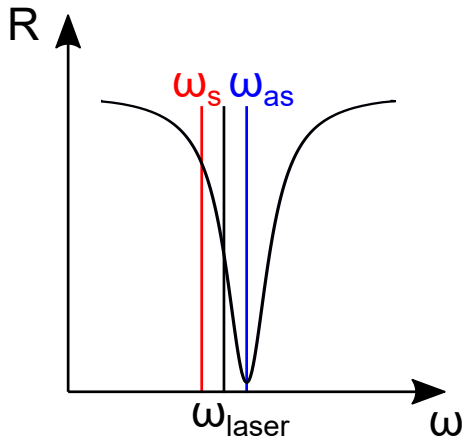

Figure 2.14 – Schematic principle of optomechanical cooling of a resonator. The laser (black vertical line) is on the red detuned flank of the optical reflectivity. The antistokes component is resonant with the confined optical mode. This enhances the anti-Stokes scattering rate with respect to the Stokes one.

In this section, we have introduced the principles of Brownian motion measurement and the manipulation of mechanical motion through optomechanical interactions. In the next section, we present the main parameters that are relevant in the previously described experiments.

2.4.3 Optomechanical parameters

We will start this section by addressing the question of the reduction point. In the previous example, the motion of the mechanical resonator could be simply described by a parameter $x(t)$, that is, the displacement of the movable mirror with respect to its resting position. In particular, the optomechanical coupling factor g_{om} could be calculated by considering this displacement. The situation is however different in several optomechanical systems, where the displacement magnitude depends on the position inside the resonator. This will be the case when we will study the optomechanical properties of micropillars (Chapter 5). The spatial profile $\overrightarrow{u}(\overrightarrow{r})$ can take different values depending on the position $\overrightarrow{r}$ in the resonator. The necessity of defining a reference displacement at a given reduction point is clear, in order to describe the mechanical motion of the system. It is worth noting that the reduction point is an arbitrary choice. In this work we will consider the point with maximal displacement, located at a position $\overrightarrow{r}_0$ in the resonator. Since we have defined a reference displacement for the mode, the g_{om} can be determined with respect to the motion at this reduction point.

The choice of the reduction point leads to the definition of the effective mass m_{eff}. We consider an optomechanical resonator with a mechanical frequency ω_m and with maximal amplitude displacement U_{max}. The effective mass is found by equating the mechanical energy stored in the optomechanical oscillator to the energy of an harmonic oscillator having a motion $x(t)$ with an amplitude U_{max}, a frequency ω_m and a mass m_{eff} [147]. The effective mass, with the current choice of the reduction point, is given by:

$$m_{eff} = \frac{\int \frac{1}{2}\omega_m^2 \| \overrightarrow{u}(\overrightarrow{r})\|^2 \rho(\overrightarrow{r}) \mathrm{d}V}{\frac{1}{2}\omega_m^2 U_{max}^2} \tag{2.33}$$

where the spatial integral is defined over the full optomechanical resonator, and ρ is the local mass density.

The quantum description of an optomechanical resonator allows to define the vacuum optomechanical coupling factor g_0. This parameter is particularly useful since it quantifies the strength of the optomechanical interaction independently of the choice of the reduction point. To introduce it, we express the Hamiltonian of the system as:

$$\hat{H} = \hbar\omega_{cav}(\hat{x})\hat{a}^\dagger\hat{a} + \hbar\omega_m\hat{b}^\dagger\hat{b} \tag{2.34}$$

where $\hat{a}^\dagger$ ($\hat{b}^\dagger$) and $\hat{a}$ ($\hat{b}$) are respectively the photon (phonon) creation and annihilation operators. Notice that here we are considering an isolated optomechanical system (no coupling to the environment). The term ω_{cav} can be expanded with respect to the motion of the reduction point as $\omega_{cav} = \omega_{cav}^0 - g_{om}\hat{x}$. By considering that $\hat{x} = x_{zpf}(\hat{b} + \hat{b}^\dagger)$, the previous expression becomes [20]:

$$\hat{H} = \hbar\omega_{cav}^0\hat{a}^\dagger\hat{a} + \hbar\omega_m\hat{b}^\dagger\hat{b} - \hat{a}^\dagger\hat{a}g_{om}x_{zpf}(\hat{b} + \hat{b}^\dagger) \tag{2.35}$$

The last term corresponds to the interaction Hamiltonian. We have introduced the zero point fluctuation amplitude, that is, the spread in position for a mechanical state with zero phonons ($\langle 0|x^2|0\rangle = x_{zpf}^2$). This can be found as:

$$x_{zpf} = \sqrt{\frac{\hbar}{2\Omega_m m_{eff}}} \tag{2.36}$$

From the previous expression, it is clear that x_{zpf} is also "point dependent", as it is the case for g_{om}. However, the product of the two does not depend on the displacement magnitude at the reduction point [147]. This parameter is the vacuum optomechanical coupling factor $g_0 = x_{zpf} \times g_{om}$. It therefore quantifies the optomechanical coupling strength in an unambiguous way, in contrast to g_{om}.

An optomechanical resonator is a system that presents simultaneously optical and mechanical resonances. In the frame of this work, the considered optomechanical systems are micropillars, that is, structures presenting mechanical resonances in the GHz range and optical eigenfrequencies in the NIR. Optomechanical system presenting GHz mechanical resonances are particularly suitable for both fundamental and applied studies.

Optomechanical system can be prepared close to their mechanical ground state, with an average phonon number $\bar{n} < 1$. This regime can be reached [153], or approached [24, 154], by placing the mechanical resonator in a cryogenic environment. The optical forces can then be used to further cool down the mode and reach $\bar{n} < 1$ [24, 152, 154]. Furthermore, optomechanical interactions allow to probe the average phonon number. Optomechanical systems with mechanical resonances in the MHz range have been used to cool down a mode close to its ground state [152, 154]. However increasing the mechanical frequencies, by reaching the GHz range, is desirable. Indeed, since the initial average phonon number satisfies $n_{th} = [e^{\frac{\hbar\omega_m}{k_b T}} - 1]^{-1}$, increasing the mechanical frequency allows to reach $\bar{n} < 1$ at higher temperatures. This facilitates the experimental preparation of optomechanical resonators in their quantum regime of mechanical motion.

High mechanical frequencies are also relevant for metrology applications. For example optomechanical resonators can be used as mass sensors[155]. In this context, one possibility is to track the change in resonance frequency induced by the adsorption of an analyte to be probed [156]. Increasing the mechanical resonance frequencies is desirable since it allows to increase the sensitivity of the detector, i.e. the smallest detectable mass change [17, 157]. Optomechanical systems have also been implemented for the fabrication of force sensors and accelerometers [158]. In this case, a high mechanical resonance frequency increases the frequency bandwidth of the detector [86].

The optical resonance frequency is of particular relevance in the systems considered in this work, since its design value will dramatically alter the optomechanical coupling strength. We will consider that in our systems the optical resonance frequency can be affected by the mechanical motion through geometrical and photoelastic effects, that is [132]:

$$\begin{aligned} g_{om} = -\frac{\partial \omega^0_{cav}(\epsilon, G)}{\partial x} &= -\frac{\partial \omega^0_{cav}(\epsilon, G)}{\partial x} \\ &= \underbrace{-\frac{\partial \omega^0_{cav}(\epsilon, G)}{\partial G}\frac{\partial G}{\partial x}}_{g^{geo}_{om}} \underbrace{-\frac{\partial \omega^0_{cav}(\epsilon, G)}{\partial \epsilon}\frac{\partial \epsilon}{\partial x}}_{g^{photo}_{om}} \end{aligned} \tag{2.37}$$

In the above equation the parameter G represents the geometry of the system, whereas ϵ indicates the dielectric constant. The parameters g_{om}^{geo} and g_{om}^{photo} correspond to the optomechanical coupling factors due to geometrical deformation and variation in the dielectric tensor induced by strain. The systems considered in this manuscript are constituted by GaAs and AlAs, and the optical mode is confined in a solid-state environment. The nature of the used materials can give rise to significant photoelastic contributions. In particular, the energy of the electronic gap at room temperature in GaAs is at 1.42 eV, corresponding to an optical wavelength of 870 nm. Designing our systems with an optical resonance energy close to the electronic transition allows to dramatically enhance the photoelastic effect [159], and therefore g_{om}^{photo}. This can be understood from the Raman scattering picture, in which the inelastic scattering probability becomes resonant under these conditions [121].

The optomechanical system is coupled to its mechanical and optical environment. These couplings are quantified by the resonator quality factors: Q_m and Q_{opt}.

As already mentioned before, the optomechanical interactions allow to cool down the mechanical confined mode. Lowering the phonon population of the mode relies on an effective insulation of the system from the mechanical bath, in order to create an energy gradient between the resonator and the environment. Maximizing Q_m is therefore crucial for preparing mechanical resonators in their quantum ground state. This parameter is in fact also relevant in the opposite regime, where the mechanical motion is amplified. Indeed, increasing Q_m allows to decrease the optical power threshold for which mechanical self oscillations occur [149]. Furthermore Q_m is involved in the calculation of the $Q \cdot f$ product. Maximizing this figure of merit is relevant in quantum optomechanical applications, since it is related to the number of coherent mechanical oscillations that the system can undergo in the presence of thermal decoherence induced by the environment [20].

The optical quality factor Q_{opt} is another crucial parameter for both mechanical motion detection and manipulation. In the frame of Brownian motion measurements, its role can be understood from Figure 2.13.b. The optical quality factor sets the slope of the reflectivity curve. Therefore, increasing this parameter enhances the optomechanical sensitivity. This facilitates the measurement of the mechanical oscillator noise spectrum.

In the context of cooling the mechanical mode, maximizing the optical quality factor increases the value of the optomechanical damping rate, allowing to reach lower effective temperatures. In the opposite regime, it reduces the threshold laser power for self oscillations [149]. These effects can be intuitively understood from the Raman scattering picture (Figure 2.14), since increasing the optical quality factor enhances the imbalance between the Stokes and anti-Stokes components.

2.5 Conclusion

In this chapter, we described the interactions taking place between acoustic phonons and photons. The inelastic scattering of light induced by mechanical waves is of paramount importance in this work, since it is this process that we have experimentally studied through Raman scattering spectroscopy. We also have recalled the main selection rules that are relevant for Raman scattering on superlattices and on nanophononic cavities. Furthermore, we have explained how, by engineering the op-

tical environment of acoustic structures, we could dramatically enhance the intensity of the Raman signals and relax the selection rules on layered systems. This design has been implemented in all the samples presented in this work, and allowed to greatly facilitate their characterization.

In the following sections, we briefly presented two other experimental techniques that are widely used to characterize mechanical resonators through optical means. The first one is pump-probe coherent phonon generation and detection. This experimental technique is particularly relevant in the context of this work, since the first experimental demonstration of mechanical confinement in micropillars was obtained through this method.

Pump-probe coherent phonon generation and detection is a complementary technique with respect to Raman scattering spectroscopy. In particular, it allows to characterize systems in the few GHz range, frequencies that are very challenging to access by Raman scattering spectroscopy. The Raman peaks would be spectrally located very close the excitation laser line, making the stray light rejection difficult to carry out. Notice however that in real experiments the pulse length used in pump-probe experiments is not infinitesimally short. This limits the eigenfrequencies that can be excited, which typically goes up to few THz with fs lasers. For probing the acoustic properties of nanophononic resonators above this frequency range, Raman scattering experiments are best suited.

Furthermore, pump-probe experiments can be used to measure the damping rates of acoustic resonators, as explained before. Measuring these parameters is more difficult by Raman scattering, since the linewidth of the Raman peaks is often determined by the resolution of the spectrometer. In the case of pump-probe experiments, this measurement is only limited by the maximum delay between the pump and the probe.

The last technique that we introduced is Brownian motion measurements. This method has been widely implemented in the context of cavity optomechanics. We first presented the basic concepts of optomechanical interactions. We then explained how to take advantage of the coupling between the confined optical and mechanical modes in order to probe the thermal fluctuations of the mechanical resonator. We have also briefly presented how to control the mechanical motion of the system through optical forces. Finally, we have introduced some general parameters that are relevant for the characterization of optomechanical resonators. In Chapter 5 we will present numerical simulations that allowed us to estimate the magnitude of these quantities for three-dimensional optomechanical resonators, that is, GaAs/AlAs micropillars.

Chapter 3

Acoustic confinement: beyond the Fabry-Perot resonator

The design of acoustic periodic media at the nanoscale enables the engineering of acoustic wave propagation in the GHz/THz range. In particular, it allows the development of novel confinement strategies in one dimension. Phononic Fabry-Perot cavities nowadays constitute the canonical resonator used in nanophononics. In fact, with few exceptions, no other confinement methods have been explored for GHz/THz waves.

In this Chapter we present two structures that we have developed to control the confinement of nano-mechanical vibrations. These designs provide additional knobs to engineer the propagation of acoustic phonons in layered systems.

The first resonator relies on the fine control of a superlattice band structure. It is inspired by cavity designs developed in optics to optimize the confinement of electromagnetic modes. In this system we adiabatically break the spatial periodicity of a superlattice. This allows to mimic the effect of a phononic potential and to generate confined states.

For the second confinement method presented in this Chapter, we take advantage of the topological properties of an acoustic periodic medium. In this case, we concatenate two acoustic superlattices in different topological phases, in order to create an interface state between the two structures.

We will demonstrate the feasibility of these systems. In particular, we have fabricated acoustic nanocavities based on the concepts introduced before, and we have experimentally probed the existence of confined phononic states through Raman scattering spectroscopy. All the samples presented in this section were realized at C2N by Aristide Lemaître and Carmen Gomez Carbonell.

The Chapter is organized as follows:

- In Section 3.1 we will describe the Raman scattering spectroscopy experiment that we have implemented in order to perform the measurements discussed in this chapter.
- In Section 3.2, we will introduce the design of the adiabatic structure. The experimental results are shown and compared to the photoelastic model, clearly demonstrating the presence of a confined mode in our system.
- In Section 3.3 we will present the concepts used to create an interface state between two acoustic superlattices, based on topological invariants. The exper-

imental Raman scattering spectra obtained on this system are again compared to numerical simulations.

- Finally, we will close this Chapter by some conclusive remarks.

3.1 Raman scattering set-up

The Raman scattering measurements discussed in this chapter were carried out using the experimental set-up represented in Figure 3.1. The configuration of this experiment has been designed to probe Stokes Raman peaks, as explained below.

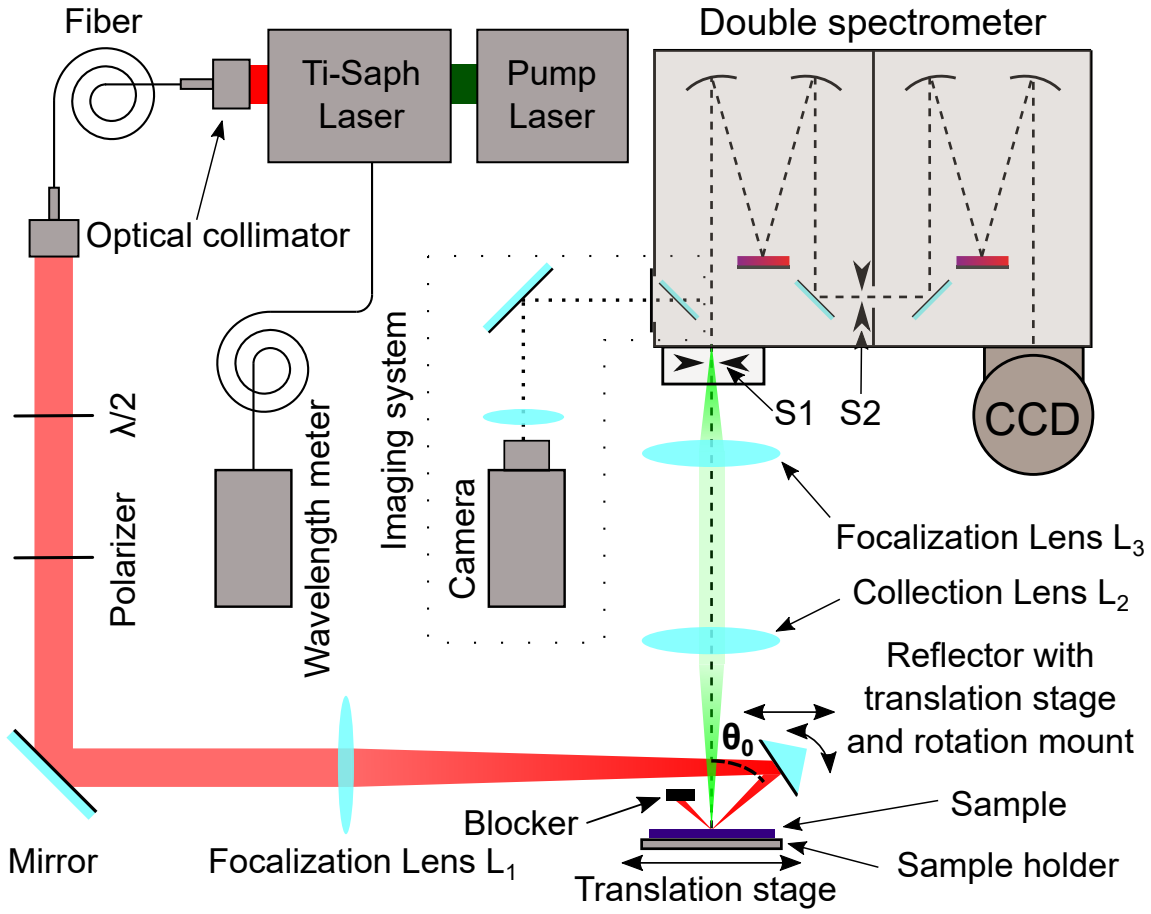

Figure 3.1 – Raman scattering experiment diagram in Stokes configuration. The excitation beam is represented in red. The angle of incidence θ_0 is indicated and exaggerated with respect of real experimental conditions for clarity of the diagram. The scattered light is represented in green. The dashed line in the spectrometer represents the path of the light when it is used in its measurement configuration. The short dotted line represents the path of the light when the entrance slit imaging system is used.

The sample is excited by a tunable continuous wave (CW) NIR Ti:Sapph laser (SolsTiS M-Squared, or Mira 900 Coherent used in CW), with a wavelength tuning range going from 700 nm up to 1050 nm. The linewidth of the laser is smaller than 5 MHz, and the maximal output power is $\approx$ 400 mW. The wavelength of the laser

is measured by a fibered wavelength meter (W5-5 HighFinesse GmbH). The SolsTiS laser can be locked to the wavelength meter, in such a way that a wavelength drift of the laser can be actively corrected. The power of the laser is controlled by a zero order $\lambda/2$ waveplate combined with a linear polarizer.

The incident beam is focalized through a lens L_1 having a focal length of 20 cm. The size of the spot on the sample is of the order of 150 µm. The laser is incident on the sample with an angle θ and the scattered light is collected at normal incidence. The set-up is optimized to measure Stokes Raman signals under double optical resonance (see Section 2.2), to enhance Raman signals at frequency shifts of ≈ 300 GHz.

The characterized structures are fabricated with a thickness gradient. This enables to find a position in which the resonance frequency ω_c of the collection mode at normal incidence matches the frequency of the scattered photons $\omega_s = \omega_i - \omega_{phon}$. The parameters ω_i and ω_{phon} are the frequencies of the incident laser and of the mechanical mode that we are probing, respectively.

Before being focalized on the sample, the beam is deviated by a reflector also mounted on a translation stage and a rotation mount. This reflector allows to carefully choose the incidence angle θ of the excitation beam. As explained by Figure 2.7 of Section 2.1, the setting of the incidence angle allows to find $\omega_e = \omega_i$, where ω_e is the frequency of the excitation mode. Controlling the incidence angle and the spatial position at which the laser impinges the sample allows to set the DOR condition for a given frequency shift in the Raman spectrum.

The inelastically scattered light is collected by a lens L_2 with a focal distance of 10 cm, in order to be analyzed by a spectrometer. The collimated beam is focalized at the entrance of a double monochromator (HRD 2 Jobin Yvon), in the plane of the entrance slit S_1. The focal length of L_3 is 12.5 cm. The double monochromator is equipped with a liquid N_2 cooled Charge Coupled Device (CCD) (LN 100BR Detector Excelon Princeton instruments).

In order to maximize the resolution of our measurement apparatus, the numerical aperture of L_3 has been chosen to match the one of the spectrometer such that the surfaces of the gratings are fully illuminated. Furthermore, the width of the entrance slit S_1 ranges between 20 µm and 30 µm. Under optimal experimental conditions the resolution measured for our spectrometer, taken as the full width half maximum of a sharp laser line, is ≈ 7 GHz, corresponding to $\approx 0.2\,\mathrm{cm}^{-1}$ (i.e. ≈ 0.019 nm), at 900 nm.

We have implemented an imaging system that is essential for performing a first alignment of the set-up. Indeed, we are collecting very weak Raman intensities. The inelastically scattered light is measured at normal incidence from the sample. The Raman signals spatially overlap the laser light that is elastically scattered at the sample surface. An aperture can be used in the first monochromator stage for sliding in a small mirror. This mirror is then used to image the plane of the slit S_1. The imaging system is constituted by a lens and a camera, and it allows to verify that we are collecting the scattered light from the sample through the entrance slit. This procedure enables us to get a first Raman spectrum that we can then further improve by correcting the set-up alignment. Maximizing the stray light rejection is a crucial step in high resolution Raman scattering experiments. In particular, remaining light coming from the excitation laser is inevitably collected.

The double spectrometer is a major asset for minimizing the stray light collection, since it allows to eliminate the spectral peak associated to the laser before it can reach

the second stage and the CCD. Indeed, as a first spectrum is formed at the plane between the two stages, the intermediate slit S_2 can be used as a narrow bandpass filter. By closing S_2, the slit spectrally blocks the light directly coming from the excitation laser (as represented in Figure 3.2.b). This filtering process is therefore a powerful tool to improve the signal to noise ratio of our measurements and to get spectrally closer to the excitation laser line.

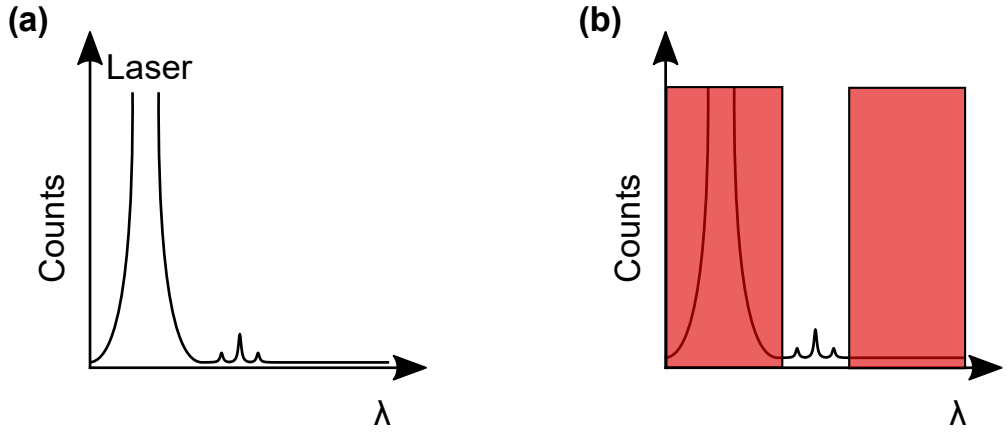

Figure 3.2 – **(a)**: Schematics of the unfiltered Raman spectrum obtained at the plane of the intermediate slit. The saturated signal represented on the left correponds to the excitation laser. The three small peaks correspond to the Raman signals of the acoustic cavity. **(b)**: Schematics of the filtered Raman spectrum. The two red rectangles indicate the action of the two intermediate slit blades when S_2 is closed. As explained in the main text, S_2 acts as a bandpass filter, letting only the Raman signal pass into the second stage of the spectrometer and be measured by the CCD.

The Stokes configuration of the set-up allows to spatially filter out the direct reflection of the laser occurring at the sample surface. Indeed, being incident with a small angle θ_0 enables to block this reflection without preventing the collection of the scattered light, as shown in Figure 3.1.

Figure 3.3 shows the Stokes Raman spectrum that we measured on an acoustic Fabry-Perot resonator embedded in an optical cavity. The acoustic system is designed to confine a mode around 250 GHz (corresponding to an energy of $\approx$ 1 meV). It is made of two $(\frac{\lambda}{4}, \frac{3\lambda}{4})$ AlAs/GaAs DBRs and a $(\frac{\lambda}{2})$ GaAs spacer. This corresponds to thicknesses of 14.6 nm and 5.75 nm for the GaAs and AlAs layers in the DBRs, respectively. The spacer thickness is 9.75 nm. As explained in Chapter 2 (Section 2.2), both forward scattering and back scattering Raman peaks are accessible with our set-up due to the design of the sample.

The Raman spectrum presented here spans over several hundreds of GHz. In real experimental conditions, in order to minimize the experimental noise, the intermediate slit is closed so that frequency intervals on the order of 50 GHz can be accessed in one measurement. Raman spectra such as the one shown in Figure 3.3 are reconstructed from several subsequent measurements, for which the laser wavelength and power are kept constant.

Panel (a) of Figure 3.3 shows the calculated acoustic reflectivity spectrum of the structure. It was simulated by considering the nominal values of the resonator layer

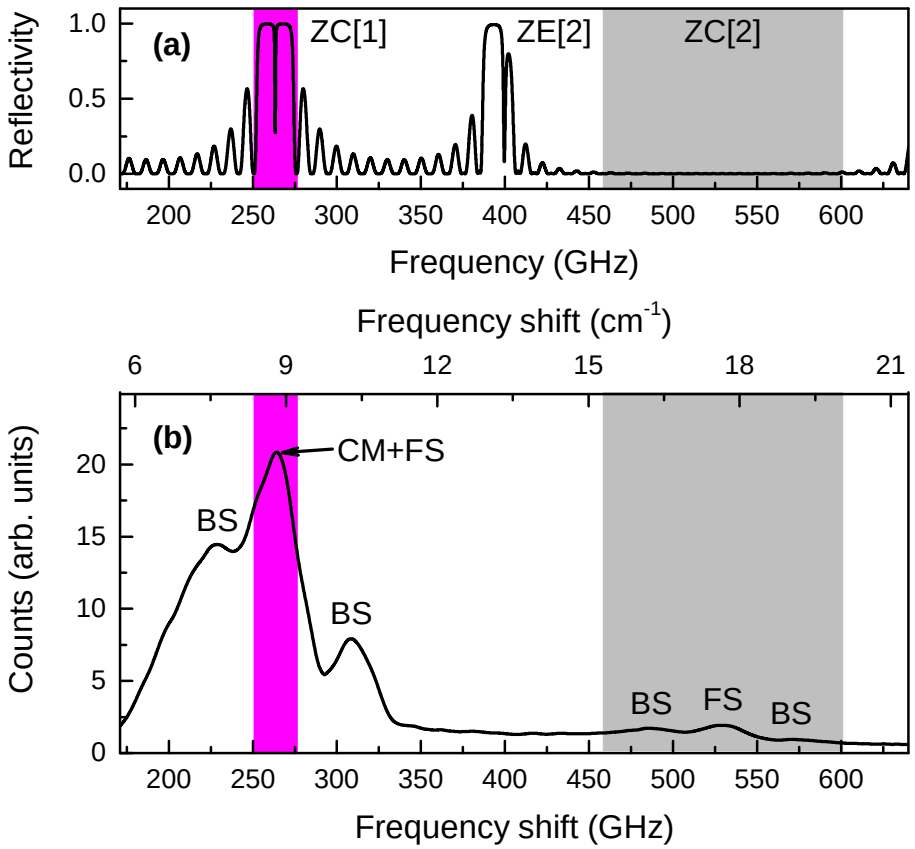

Figure 3.3 – Raman scattering spectrum measured on an acoustic Fabry-Perot resonator embedded in an optical cavity. **(a)**: Simulated reflectivity of the Fabry-Perot acoustic cavity as function of frequency. The labels ZC[1] and ZC[2] stand for first and second Brillouin zone center acoustic minigaps. ZC[2] indicates the second Brillouin zone edge minigap. **(b)**: Experimental Stokes Raman spectrum. The frequency axes are shown both in GHz and cm^{-1}. The counts numbers are normalized by the power of the laser and by the integration time. The magenta region highlights the spectral position of the first Brillouin zone-center acoustic minigap. The light grey region marks the frequency interval where a second group of Raman peaks is visible. The Raman peaks marked with the labels (BS) and (FS) correspond to phononic modes that would be Raman active in a backscattering and forward scattering geometry, respectively, in the absence of optical confinement. The peak labeled by (CM+FS) corresponds to the Raman signal generated by the confined acoustic mode and the Raman active extended mode with $q = 0$.

thicknesses. The reflectivity frequency axis has been rescaled by a global proportionality factor, to account for the sample thickness gradient. The magenta area highlights the spectral position of the first stop band at the Brillouin zone center. The existence of a confined mode in this frequency interval is evidenced by the presence of a sharp dip in the high reflectivity region.

The spectrum shown in Figure 3.3, Panel (b), was obtained for an excitation laser wavelength of 892 nm and an incident power of 4.5 mW at room temperature. The incidence angle θ_0 was set to obtain a DOR condition for Raman peaks located at a frequency shift Δf around 250 GHz. In this spectrum two groups of peaks are visible: a first triplet is observable at $\Delta f \approx 260$ GHz and another one at $\Delta f \approx 520$ GHz. The observed Raman peaks widths are determined by the experimental resolution. From the description of the Raman scattering selection rules for acoustic superlattices that we recalled in Chapter 2, we can deduce the origin of the measured Raman peaks. The first group corresponds to Raman signals located around the first ZC acoustic minigap, as it can be seen in Panel (a). The two backscattering Raman peaks are located outside of the ZC[1] acoustic stop band. They correspond to propagative mechanical modes inside the structure, verifying the scattering condition $q \approx 2k_i$. The main Raman peak (marked by the label CM+FS), well inside the ZC[1] acoustic stop band, marks the presence of the confined acoustic mode (CM). Furthermore, as explained in Chapter 2, there is also a Raman active extended mode located at $q \approx 0$, bounding the acoustic minigap. The forward scattering signal of this mode also contributes to the probed Raman main peak. A measurement with higher resolution would be required to distinguish the two signals.

The second group of peaks is located at twice the frequency shift of the first one, in a frequency interval highlighted in grey in both panels. Similarly to what is observed for the Raman peaks located around ZC[1], the central peak is associated to mechanical modes verifying $q \approx 0$, whereas the two others are generated by acoustic phonons with $q \approx 2k_i$. In this case, the ZC[2] acoustic minigap is closed, due to the choice of the layers thicknesses in the designed structure, and no acoustic stop band is visible in the grey region of Panel (a). Assuming that the actual layer thicknesses inside the sample correspond to their nominal values, the central peak is not generated by a confined mode, but only by an extended mode located at $q \approx 0$ in the acoustic band diagram.

We have shown how a confined mode can be measured by means of Raman scattering spectroscopy. The reported spectrum presents the Raman features predicted by the photoelastic model. We used this set-up to probe the Raman spectra of samples presenting novel acoustic cavity designs, and to demonstrate the confinement of mechanical vibrations in these systems.

3.2 Adiabatic confinement of acoustic phonons

In this section we describe the design of an acoustic cavity based on the local engineering of band structures to confine an acoustic mode. The development of this structure was inspired from works related to the confinement of light in defects introduced within photonic resonators [160].

3.2.1 Design of an adiabatic cavity

The realization of optical resonators that "smoothly" confine light takes place in the framework of developping cavities with modal volumes of optical-wavelength dimensions and maximal optical quality factors [161–163]. It was demonstrated that the confinement in these devices is limited by the coupling of the localized state inside the defect to radially propagative modes [164, 165]. This can be either caused by the geometry of the system, or by the presence of unwanted imperfections in the fabricated sample. One efficient design to overcome these issues in the optical domain consists in introducing tapered regions where the periodicity of the photonic crystal is progressively/adiabatically changed [165]. Such an adiabatic breaking of a photonic crystals periodicity locally changes the optical band structure of the system, leading to the creation of a confined state [160]. This approach allows for reduced optical losses, hence increased optical quality factors, when going to three-dimensional confinement. Such band engineering of optical periodic structures has been adopted in several optical systems, such as two-dimensional photonic crystal membranes [166], nanobeams [167], waveguides [168] and micropillars [160, 169].

In this work, we take advantage of the possibility to create localized states by adiabatically breaking the periodicity of an acoustic superlattice. In the structures studied here, we progressively change the layer thicknesses in an acoustic DBR. The effect of this transformation can be described by an adiabatic change of the system's local acoustic band diagram. This generates a confined mechanical state located where the perturbation is introduced, usually at the center of the structure. Furthermore, by changing the maximum thickness deviation from the periodic case, we can significantly transform the spatial profile of the confined mode, leading to major variations in its mechanical quality factor and Raman scattering cross section.

We start the conception of the adiabatic cavity by considering an acoustic AlAs/GaAs DBR constituted by 28.5 layer pairs (i.e. 57 layers). The layer thicknesses of AlAs and GaAs are $t^0_{AlAs} = 12\,\text{nm}$ and $t^0_{GaAs} = 3.4\,\text{nm}$, respectively. By choosing these thicknesses, we obtain a $(\frac{3\lambda}{4}, \frac{\lambda}{4})$ acoustic DBR, with a maximally opened Brillouin zone center acoustic minigap centered at a frequency of $\approx 350\,\text{GHz}$.

We now introduce the adiabatic perturbation by gradually changing the layer thicknesses in the central region of the DBR. The process is illustrated by the color map in Panel (a) of Figure 3.4, where we have represented the structure of the adiabatic cavity. The green and blue layers indicate the AlAs and GaAs materials, respectively.

We consider the represented system from the left side of the figure to the right side. We leave the first 16 layers of the DBR unaltered. We then progressively change the successive layer thicknesses. The envelope of the perturbation has the shape of a sin^2 function and a maximum amplitude of 7%. The adiabatic perturbation is applied to the successive $n_{adiab} = 25$ layers. We denote p as the index of the p^{th} layer in the perturbed part on the DBR. The parameter p is an integer number, going from 1 for the first perturbed layer up to n_{adiab} for the last one. The thickness t_p of the p_{th} layer in the perturbed region is given by the relations:

$$t_p^{AlAs} = t_0^{AlAs}\left(1 + 0.07 \times sin^2\left((p-1) \times \frac{1}{n_{adiab}-1} \times \pi\right)\right) \tag{3.1}$$

if the p_{th} layer is an AlAs layer, and:

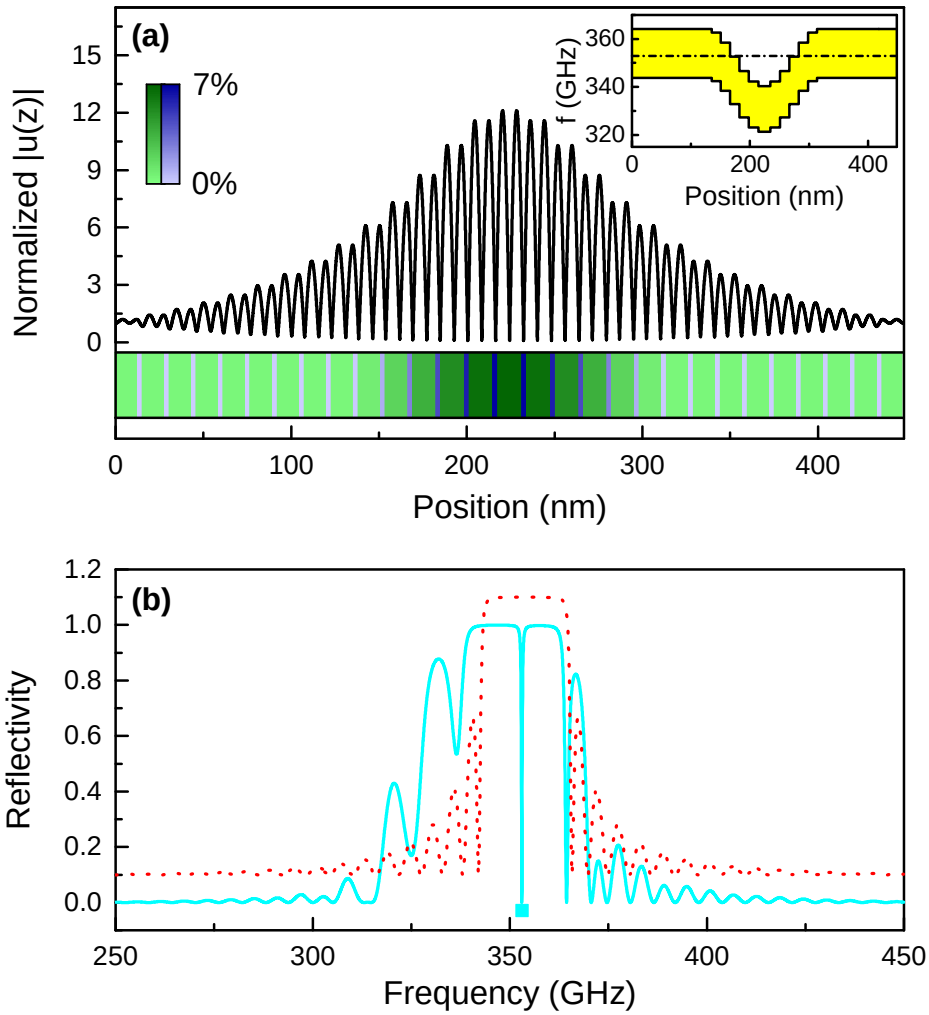

Figure 3.4 – **(a)**: Displacement profile of the confined acoustic mode inside the adiabatic structure. The color map shows the layers thicknesses adiabatic perturbation inside the structure. Green and blue regions correspond to AlAs and GaAs layers, respectively. The Inset shows the evolution of the local acoustic minigap as function of the position in the sample. **(b)**: Acoustic reflectivity for the adiabatic nanocavity (cyan curve). The spectral position of the confined mode plotted in (a) is marked by a cyan square. The acoustic reflectivity of the unperturbed DBR is shown by the red dotted line.

$$t_p^{GaAs} = t_0^{GaAs}\left(1 + 0.07 \times sin^2\left((p-1) \times \frac{1}{n_{adiab}-1} \times \pi\right)\right) \tag{3.2}$$

if the p_{th} layer is an GaAs layer. From the two equations presented above, the magnitude of the adiabatic perturbation progressively increases with p, reaches a maximal value at the center of the structure, and then decreases again. Finally, after the adiabatically perturbed region, the rest of the structure is constituted by 16 unaltered layers, represented in the rightmost part of the color map represented in Figure 3.4.a.

Since the maximal value of the adiabatic change is only of 7%, the perturbation is implemented in such a way that the change in size between two consecutive unit cells is small with respect to the nominal layer thicknesses of the initial DBR.

The presence of a confined state can be explained by locally applying the Bloch mode formalism in the aperiodic part of the sample, and in particular for one period of alternating AlAs/GaAs layer pairs [160, 170, 171]. We calculate for every pair of AlAs/GaAs layers a local acoustic band diagram. The latter is obtained by calculating the dispersion relation of an acoustic superlattice with layer thicknesses corresponding to the ones of the considered unit cell. Therefore, local acoustic minigaps can be determined for each layer pair, in particular in the adiabatically perturbed region [171]. In the inset of Figure 3.4.a, we show the evolution of the first Brillouin zone center band gap (yellow) as function of the position in the sample. The eigenfrequency of the confined mode is represented by the dashed horizontal line. By progressively increasing the thicknesses of the layers, we gradually redshift the position of the local acoustic bandgap of the system. At the center of the perturbed region, the confined mode is outside the bandgap and is therefore allowed to propagate. However, by moving away from the center, the mode enters adiabatically into the bandgap and is progressively reflected by the DBRs, leading to its confinement.

We compute the reflectivity of the system embedded in a GaAs matrix, as shown with the cyan curve in Figure 3.4. We note the presence of a sharp dip inside the stop band at 353 GHz (i.e. at ≈ 1.45 meV), corresponding to a confined mode. The dashed red line represents the simulated reflectivity spectrum of a DBR without any adiabatic perturbation. The calculated spatial profile of the confined mode (Figure 3.4, black curve) is obtained through transfer matrix calculations. The displacement has been normalized to the displacement amplitude in the GaAs substrate. This was carried out in order to show the enhancement of the acoustic displacement amplitude induced by the phononic resonator. The mode is confined at the center of the structure and decays exponentially over ≈ 150 nm, beyond the adiabatically perturbed region.

The progressive transformation of the acoustic DBR band diagram enables the "smooth" confinement of an acoustic mode. In fact, other examples of such band engineering in acoustics can be found in the literature. Previous works report on controlling the local phononic band diagram in the context of coupled acoustic resonators, i.e. structures where multiple Fabry-Perot-like cavities are coupled to mimic the formation of bands [172]. These phononic molecules are well described by a tight binding model, where each Fabry-Perot plays the role of an atom evanescently coupled to its neighbors through the acoustic mirrors. Effective potentials can be introduced by changing the resonance energy of the consecutive cavities [173]. In these cases confined states can appear and they are distributed along several resonators. These structures allowed to observe phenomena such as Wannier-Stark ladders, Bloch oscillations, and confined phononic states in parabolic potentials [171, 174].

The cavity designed here is also based on controlling the local band structure, but its working principle can be mapped to a nearly-free electron model [1]. The semiconductor interfaces reflect a small fraction of the incident acoustic wave, analogous to the atoms of a crystal for electronic wavefunctions. We can therefore design acoustic potentials without the need of concatenating several resonators separated by DBRs. As in the case of optics, this new way of localizing mechanical modes with tapered regions could lead to the development of three-dimensional mechanical resonators with confinement properties overcoming the ones currently achieved with standard Fabry-Perot designs [58, 175].

3.2.2 Characterization of the Adiabatic Cavity

We fabricated an adiabatic cavity structure by MBE, and we characterized it through the Raman scattering spectroscopy set-up presented before (Figure 3.1). The sample was fabricated on a (001) GaAs substrate. The design of the AlAs/GaAs acoustic cavity follows the structure shown in Figure 3.4. The phononic system is embedded between two $(\frac{\lambda}{4}, \frac{\lambda}{4})$ optical DBRs. The optical mirror in contact with air is constituted by 14 $Al_{0.1}Ga_{0.9}As/Al_{0.95}Ga_{0.05}As$ layer pairs, whereas the one in contact with the substrate is made of 18 pairs. The adiabatic cavity confining a mode at $\approx 353\,\mathrm{GHz}$ constitutes a $3\lambda/2$ optical spacer of a Fabry-Perot cavity at a vacuum resonance wavelength of $\approx 925\,\mathrm{nm}$. The sample is fabricated with a thickness gradient enabling us to tune the optical resonance in the ≈ 0.8 to $1\,\mu\mathrm{m}$ wavelength range by moving the laser spot on the sample.

We first address the effect of the double optical resonance condition, as illustrated in Figure 3.5. We performed an experiment where the DOR condition was optimized for frequencies shifts of $\approx 350\,\mathrm{GHz}$ (Figure 3.5.a). The incidence angle was $\theta \approx 11°$. We then moved the laser spot on the structure by translating the sample. The power of the laser and its wavelength were kept constant. For each position, we acquired a Raman spectrum for a frequency shift interval centered at 360 GHz. As shown in Figure 3.5.a, a group of Raman peaks is visible. When we move on the sample, we observe a progressive increase in the intensity of the Raman signals. We then reach a position where the spectrum is maximally enhanced, indicated by a red arrow, and we then observe a progressive decrease of the signals when we further displace the spot. The DOR condition is therefore matched when we measure maximal signal intensities.

We repeated the same experiment for a second group of Raman peaks, as shown in Figure 3.5.b, which was probed on the same sample. The incidence angle was increased to get a DOR condition at $\Delta f \approx 700\,\mathrm{GHz}$. The evolution of the Raman spectra as function of the position of the laser spot is similar to the one observed in Figure 3.5.a.

Figure 3.5 shows that by changing the experimental conditions, we can selectively enhance the intensity of the probed Raman peaks in different frequency shift intervals [121]. In particular, the frequency regions located around 360 GHz and 700 GHz present several Raman spectral features. In order to further analyze our sample, we have measured two Raman spectra on a larger frequency interval, ranging from 260 GHz up to 1170 GHz. They are plotted in Panel (b) of Figure 3.6.

We first consider the Raman spectrum represented by a black curve in Figure 3.6. For this measurement, the laser wavelength was at 913.4 nm and the incident power was 15.5 mW. This spectrum was obtained after having established a DOR around

350 GHz through the incidence angle. The Raman peaks visible around this frequency shift correspond to the ones shown in Figure 3.5.a.

The Raman peaks located around 350 GHz are enhanced by the DOR condition. In contrast, out of resonance signals poorly couple to the collection mode, and their intensities are strongly reduced. However, Raman features far from 350 GHz are visible at higher frequency shifts. In particular, weak Raman signals are visible around $\Delta f \approx 700$ GHz. They correspond to the Raman peaks already shown in Panel (b) of Figure 3.5. This is due to the relatively low quality factor of the optical Fabry-Perot ($Q = 1948$). A small fraction of these out of resonance Raman signals can therefore couple to the collection mode and appear in the spectrum.

The second Raman spectrum, plotted in red in Panel (b) of Figure 3.6, was measured after having reached the DOR condition around ≈ 700 GHz. By comparing the signal magnitudes measured in the black and red curves, we find that by changing the DOR condition, we enhanced the main peak located around $\Delta f \approx 700$ GHz by a factor of 15. As expected, the relative intensities between the first and second group of peaks are inverted with respect to the black curve discussed before. Furthermore, by shifting the DOR condition at ≈ 700 GHz, a third group of peaks becomes visible as shown by the inset to Panel (b).

In Panel (a) of Figure 3.6, we have represented the simulated reflectivity curve of the adiabatic cavity. In this curve, the acoustic stop bands are clearly visible. They present complex features due to the introduction of the adiabatic defect. However, by comparing them to the unperturbed DBR, we can associate them to Brillouin zone center or zone edge acoustic minigaps, as indicated by the labels. ZC[i] (ZE[i]) indicates that the stop band corresponds to the ith folded Brillouin zone center (zone edge) minigap. In particular, we observe the ZC[1] acoustic stop band, already shown in the Panel (b) of Figure 3.4, in which the sharp dip associated to the confined mode is located. ZC[2] is closed, as for the case of a standard $(\frac{\lambda}{4}, \frac{3\lambda}{4})$ acoustic DBR. ZC[3] is located around ≈ 1050 GHz.

We can now compare the reflectivity curve to the experimental Raman data. We first consider the black curve. A very intense Raman peak is visible at 353 GHz (marked by the label CM). Notice that this frequency corresponds to the confined mode, as shown in Panel (a). This is evidenced by the dashed red line in Figure 3.6. This very intense Raman peak marks the presence of the confined mode, demonstrating the existence of the adiabatically localized state described in Figure 3.4.

The other Raman features which are around the CM peak are associated to propagative and extended modes along the structure. This can be understood from the fact that they are spectrally located outside the ZC[1] acoustic minigap. In the absence of an optical cavity, some of them would be Raman active in a backscattering geometry whereas others would be visible in a forward scattering geometry. This point will be addressed by comparing the experimental data to numerical simulations.

The red spectrum can be used to assign the second group of peaks. In particular, we notice that no high reflectivity region in Panel (a) is present around these frequencies. This evidences the fact that these Raman peaks are associated to extended modes in the acoustic structure. Finally, the Raman peaks shown in the inset to Figure 3.6 are associated to both extended mechanical modes and higher order confined modes in the ZC[3] acoustic minigap of the structure.

We now compare the acquired experimental data to the results obtained through numerical simulations. In Figure 3.7.a we show the calculated acoustic band diagram

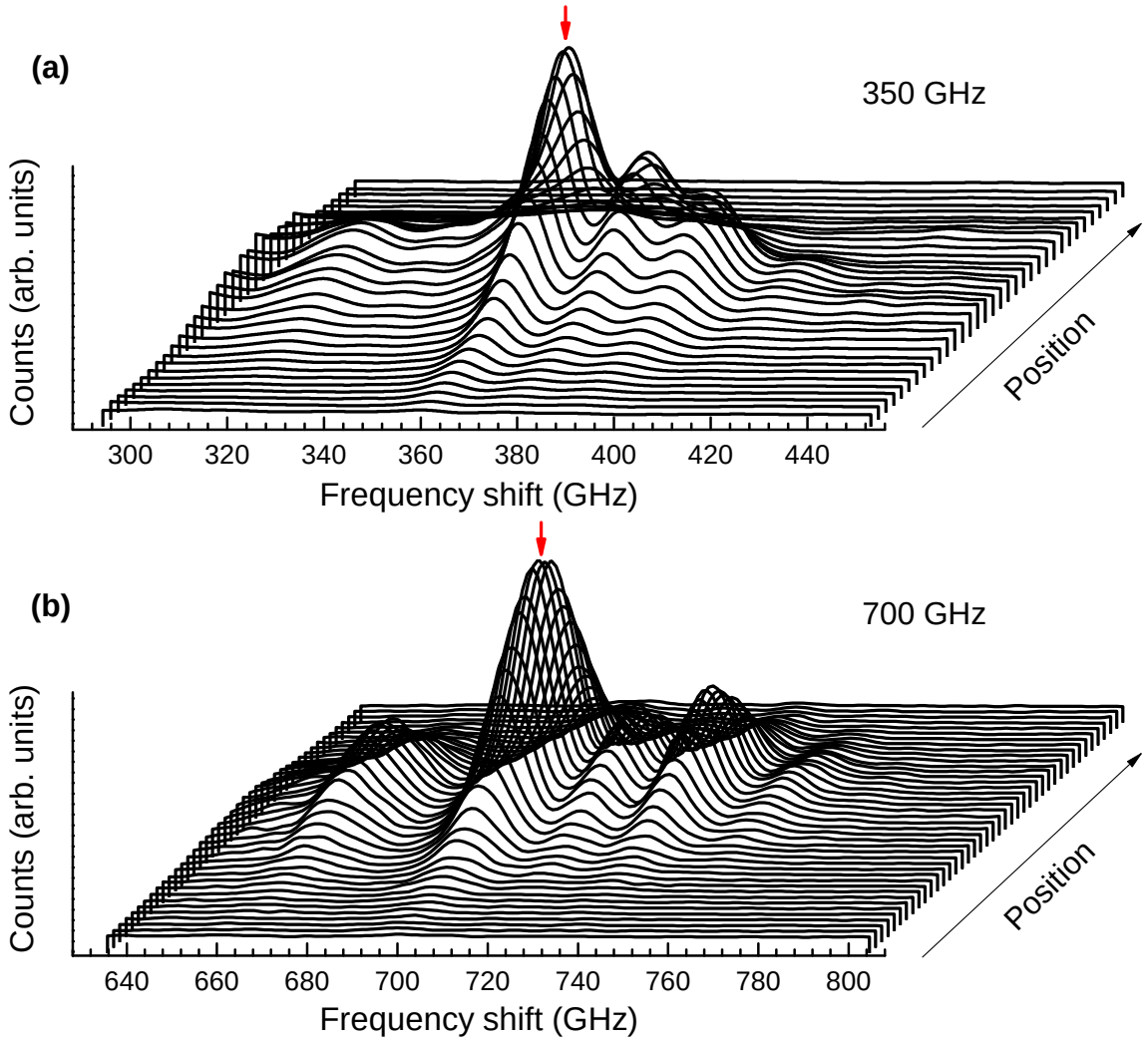

Figure 3.5 – Evolution of the Raman signal intensities when the laser spot is translated on the sample. **(a)**: First group of Raman peaks in Figure 3.6, located around the first Brillouin zone center acoustic minigap. **(b)**: Second group of Raman peaks in Figure 3.6, located around the second Brillouin zone center acoustic minigap. Panels **(a)** and **(b)** show this evolution at incidence angles θ optimized for signals located at a frequency shift of $\approx 350\,\mathrm{GHz}$ and $\approx 700\,\mathrm{GHz}$, respectively. The red arrows indicate the position with maximal intensity for the Raman spectra.

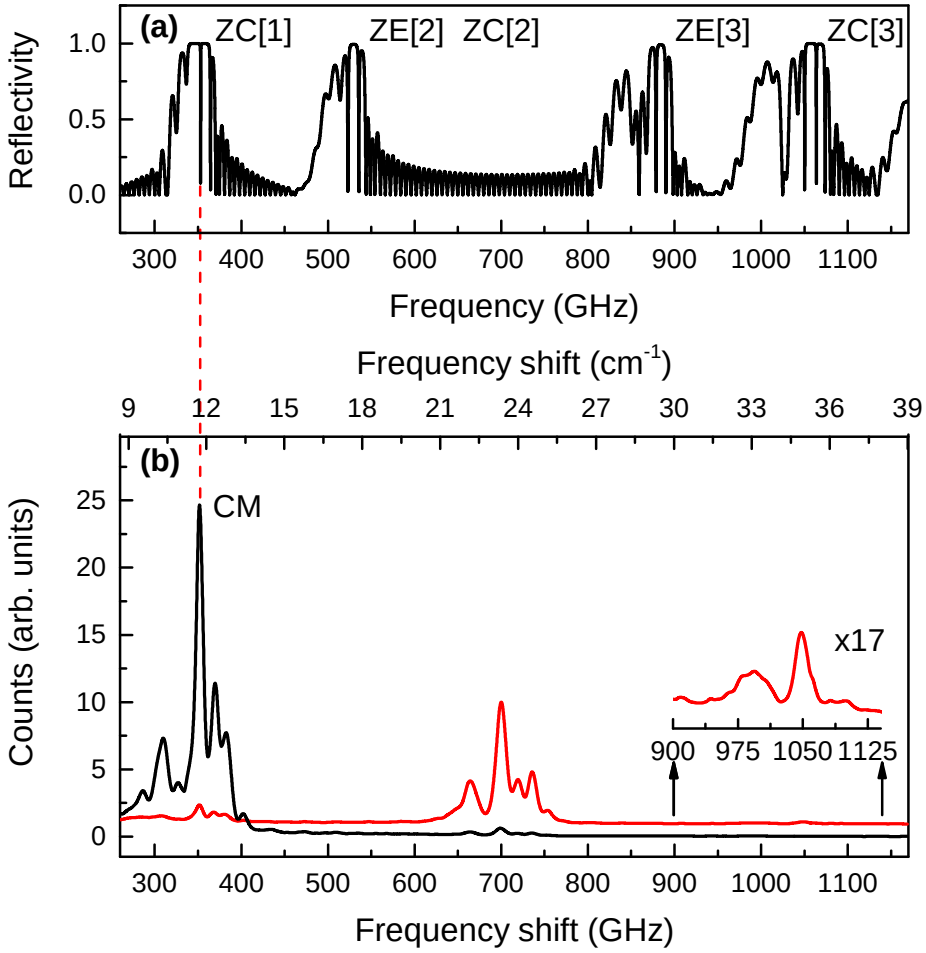

Figure 3.6 – **(a)**: Simulated acoustic reflectivity spectrum of the adiabatic cavity. The labels ZC[i] and ZE[i] indicate if the acoustic stop-band corresponds to a Brillouin zone center or zone edge minigap. **(b)**: Raman spectra measured on the adiabatic cavity. The black and red curves show the spectra obtained when the double optical resonance condition was optimized for signals located at ≈ 350 GHz and ≈ 700 GHz, respectively. CM indicates the Raman peak associated to the adiabatically confined phononic mode. The red curve has been vertically translated for clarity. Inset: detailed view of the red spectrum for frequency shifts around 1000 GHz, where Raman peaks are also visible. They are associated to the third zone center acoustic minigap (ZC[3]). The vertical axis of the inset has been magnified a factor of 17.

(black curve) of the DBR used during the conception of our sample, without any adiabatic defect. The orange line shows the spectral position of the confined mode and the acoustic minigap highlighted in grey corresponds to ZC[1]. In Panel (b), the black curve shows a detailed view for the first group of peaks when the DOR was optimized for $\Delta f \approx 350\,\mathrm{GHz}$ (black curve in Panel (b) of Figure 3.6). The main peak (CM) is the Raman signal corresponding to the confined phononic mode that we highlighted in Figure 3.6. We observe that it is spectrally well located in the ZC[1] acoustic minigap of the unperturbed DBR, also marked by a grey area.

The simulated spectrum is shown in 3.7.b (magenta curve). Transfer matrix calculations are performed to find the spatial profiles of the optical mechanical modes within the adiabatic cavity. We then compute the overlap integral of the photoelastic model (Equation 2.12 in Chapter 2). The inset to the panel shows a detailed view of this simulation in the frequency range indicated by the black arrows. The resolution of the measurement is high enough to observe the different spectral features theoretically predicted, and each theoretical Raman peak can be assigned to an experimental one. In particular, the very sharp and intense Raman peak observed in the simulated spectrum is generated by the adiabatically confined acoustic mode. The measured (CM) Raman peak is originated by the confined acoustic state. Notice that in this plot, the calculated Raman spectrum does not take into account the experimental resolution of our set-up. Furthermore, we are considering only the photoelastic contribution $p(z)$ of GaAs, that we consider constant in each layer. This is due to the fact that we have carried out the experimental measurements at a wavelength of 913.4 nm and that photoelastic constants present a resonant behavior when approaching electronic transitions in the materials [121]. The energy of the excitation laser is much closer to the electronic transition of GaAs layers (occuring at $\approx 1.46\,\mathrm{eV}$) than to the ones of AlAs, occuring at higher energies. We can therefore neglect the photoelastic contribution of AlAs layers.

These simulations allow us to determine which mechanical modes would be Raman active in a forward or backscattering geometry for a bare acoustic cavity. In our numerical simulations, we can set the A_{BS} term of Equation 2.26 (see Section 2.2.3 of Chapter 2) equal to 0. In this case, part of the peaks visible in the magenta curve of Figure 3.7 disappear. Through this technique we can assign the BS and FS labels to the experimental peaks as shown in Figure 3.7. The mode at 369 GHz is Raman active with no optical confinement in a forward scattering geometry. The peaks located at 310 GHz and 380 GHz would normally be observed in a BS geometry. They correspond to propagative mechanical modes essentially located in the DBRs. The vertical dashed lines in Panel (a) and (b) of Figure 3.7 indicate the condition $q = 2k_i$, corresponding to the mechanical modes usually Raman active in BS for a superlattice. We observe that the measured BS Raman peaks are red shifted with respect to these frequencies. The introduction of an adiabatic defect therefore also affects the spectral position of Raman peaks associated to extended modes, since it increases the average thickness of the layers located at the center of the structure.

We can further compare the numerical simulations with the experimental data by taking into account the experimental resolution of the set-up. In Figure 3.8, Panel (a), we convoluted the simulated Raman spectrum with a Gaussian curve ($2\sigma = 7\,\mathrm{GHz}$, magenta curve) and we compared it to the experimentally measured Raman peaks (black curve) located at $\Delta f \approx 350\,\mathrm{GHz}$. In Panel (b), we carried out the same comparison of the second Raman peaks group at $\approx 700\,\mathrm{GHz}$. We notice that by taking

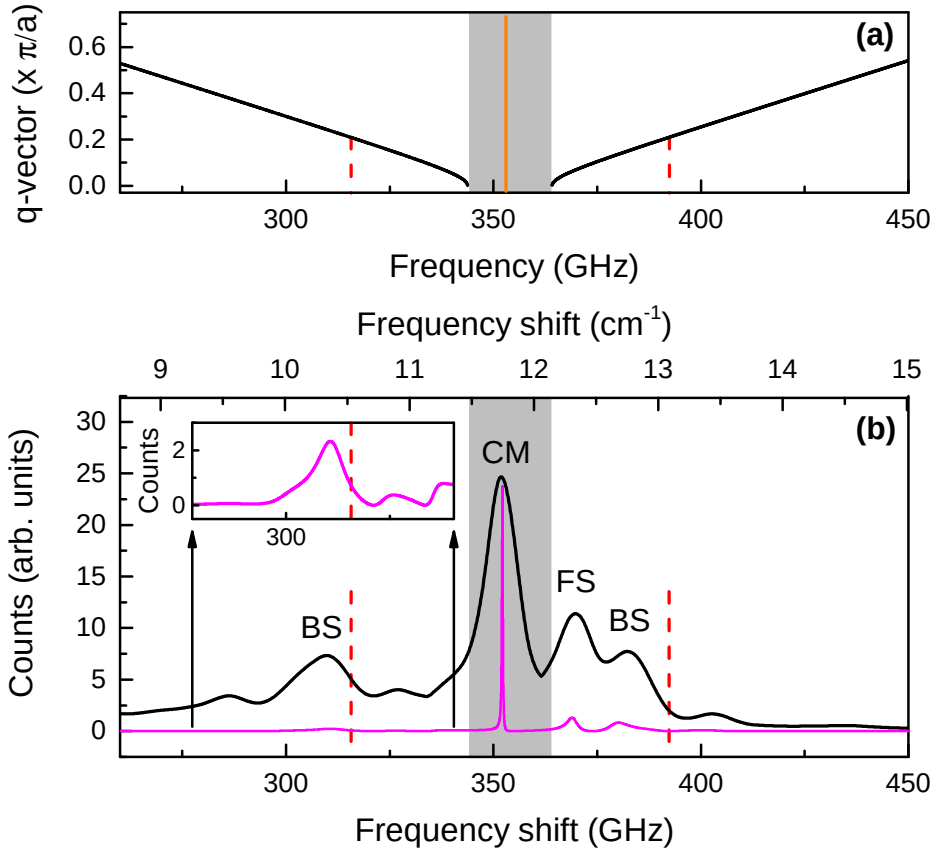

Figure 3.7 – Comparison between theoretical photoelastic model and experimental results. **(a)**: The black curve shows the acoustic band diagram of the unperturbed DBR calculated using the transfer matrix method. The orange line indicates the spectral position of the confined mode. **(b)**: The black curve is the experimental data for the first group of peaks, located around the first minigap at the Brillouin zone center. The magenta curve indicates the simulated Raman spectrum without any convolution. The inset shows a detail of such a simulated curve, as indicated by the arrows. The labels FS and BS indicate if the measured Raman peaks would be active in a forward or backward scattering geometry in the absence of the optical cavity. In both panels, the dashed red lines indicate the frequencies of the modes verifying $q = 2k_i$.

into account the experimental resolution, the simulated spectra very well reproduce all the features of the measured data. We stress the fact that for calculating the theoretical spectra, we only used the sample design parameters. No further fitting parameters were used apart from the FWHM of the convolution Gaussian curve and global rescaling factors to account for the sample thickness gradient and the absolute values of the Raman peak intensities. Such a good agreement accounts for the good quality of the sample growth [176], and the validity of the design.

Small differences between the experiments and simulations are nevertheless visible in the relative intensities of the peaks. Among the possibles reasons, we can mention the DOR condition that we are using in our experiments. Indeed, the FWHM of the optical collection mode is approximately 150 GHz. Different parts of the spectra present different optical enhancements. This effect has not been taken into account in our simulations. Furthermore, for the calculated spectrum we considered that all the GaAs layers have the same photoelastic constant. However, this parameter is intimately related to the electronic transitions and therefore to the thicknesses of the layers [177]. This results in differences in the value of this parameter, and therefore in the contributions to the Raman cross sections originating from different parts of the structure [121]. Finally, a non-constant stray-light background is present in the measurements.

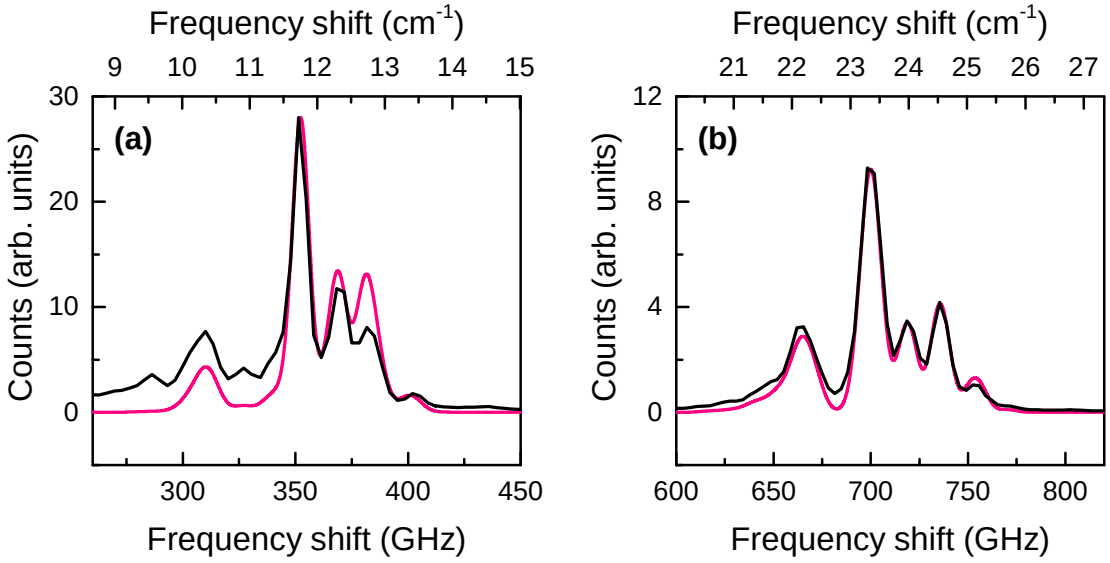

Figure 3.8 – Comparison between the convoluted numerical simulations and experimental data. **(a)**: Raman peaks centered around 350 GHz. **(b)**: Raman peaks centered around 700 GHz. In both panels, the black curves correspond to the experimental data and the pink ones to the simulated spectra calculated through the photoelastic model. For the two experimental curves, the DOR conditions where optimized for frequency shifts of ≈ 350 GHz (Panel **(a)**) and ≈ 700 GHz (Panel **(b)**).

Having observed such a good agreement between the experimental data and the theoretical results, we can perform numerical simulations to study the effect of the design parameters on the cavity confinement properties. The results are shown in Figure 3.9. We numerically investigated the confinement properties of the adiabatic

cavity by studying the effect of the sin^2 deformation of the thickness distribution. We define α as the maximum adiabatic transformation in the system. For instance, in the case of the experimentally studied structure that we described above, $\alpha = 7\%$. In Panel (a) of Figure 3.9 the color map shows the evolution of reflectivity spectra of the adiabatic cavity as a function of α. The white regions correspond to the ZC[1] acoustic stop band centered at $\approx 350\,\mathrm{GHz}$. Starting from a perfect DBR, we increase α. A sharp dip appears and gradually red shifts inside the stop band from the high energy side, reaching its center for $\alpha = 7\%$ (cyan dashed line). By further increasing α, a second sharp dip in the ZC[1] stop band appears, evidencing the presence of a second confined mode. Both dips are clearly visble for $\alpha = 11\%$ (dashed green line). Eventually, by increasing α up to 15% (red dashed line), the first mode disappears in the lower energy Bragg oscillations and the second one reaches the center of the acoustic stop band.

The spatial profiles of the first and second confined mode are plotted in the insets to Panel (b) (Figure 3.9). They have been calculated for $\alpha = 7\%$ and $\alpha = 15\%$, respectively. The eigenfrequencies of both modes are spectrally positioned at the center of the stop band. Note that in terms of spatial profiles, the second mode presents two maxima in the envelope of its displacement pattern. By changing the magnitude of α it is possible to tune the value of the mechanical cavity eigenfrequency and the spatial profile of the confined mode.

To characterize the mechanical resonator performance, in Panel (b) we studied the evolution of the confinement properties of the two considered modes, as function of the parameter α. We observe that the values of the mechanical quality factors progressively increase when the mechanical eigenfrequencies approach the center of the acoustic minigap. Maximal values for the mechanical quality factors of the first and second mode are reached for $\alpha = 7\%$ ($Q_{mechanical} = 1520$, cyan square) and $\alpha = 15\%$ ($Q_{mechanical} = 1220$, red triangle), respectively.

We compare this design to a standard Fabry-Perot resonator composed of 14 $(\frac{\lambda}{4}, \frac{3\lambda}{4})$ GaAs/AlAs layer pairs for each DBR, and one $\frac{\lambda}{2}$ AlAs spacer. The standard cavity contains the same number of layers as the adiabatic structure. The quality factor is $Q_{mechanical} = 1570$, very close to the value obtained for an adiabatic cavity with $\alpha = 7\%$. For the acoustic Fabry-Perot resonator, the effective length of the confined mode is $L_{eff}^{FP} = 92\,\mathrm{nm}$. For the adiabatic cavity with $\alpha = 7\%$, the effective length is $L_{eff}^{Adiab} = 133\,\mathrm{nm}$. This difference can be explained by considering that for an adiabatic cavity the Bragg condition is reached in a smooth way when moving away from the center of the structure, leading to a spatially extended mode. This is in strong contrast with a standard Fabry-Perot resonator, where a localized mode is generated by abruptly introducing a defect.

In Panel (c) of Figure 3.9 we plot the simulated Raman spectra around 350 GHz for cavities with $\alpha = 7\%$ (cyan curve), $\alpha = 11\%$ (green curve) and $\alpha = 15\%$ (red curve). These theoretical spectra have been Gaussian convoluted as it has been done in Figure 3.8 to account for the experimental resolution of the set-up. The resonance frequencies of the first and second mode are marked in the three curves by a square and a triangle, respectively. For $\alpha = 7\%$ the first confined mode is clearly Raman active (as already shown in Figure 3.7). For $\alpha = 11\%$ both the first and the second mode are present. However, as shown by the green curve, the only Raman active mode is the first one. For $\alpha = 15\%$, the only existing confined mode is the second one. Also in this case, no particular feature in the Raman spectrum indicates its presence. The

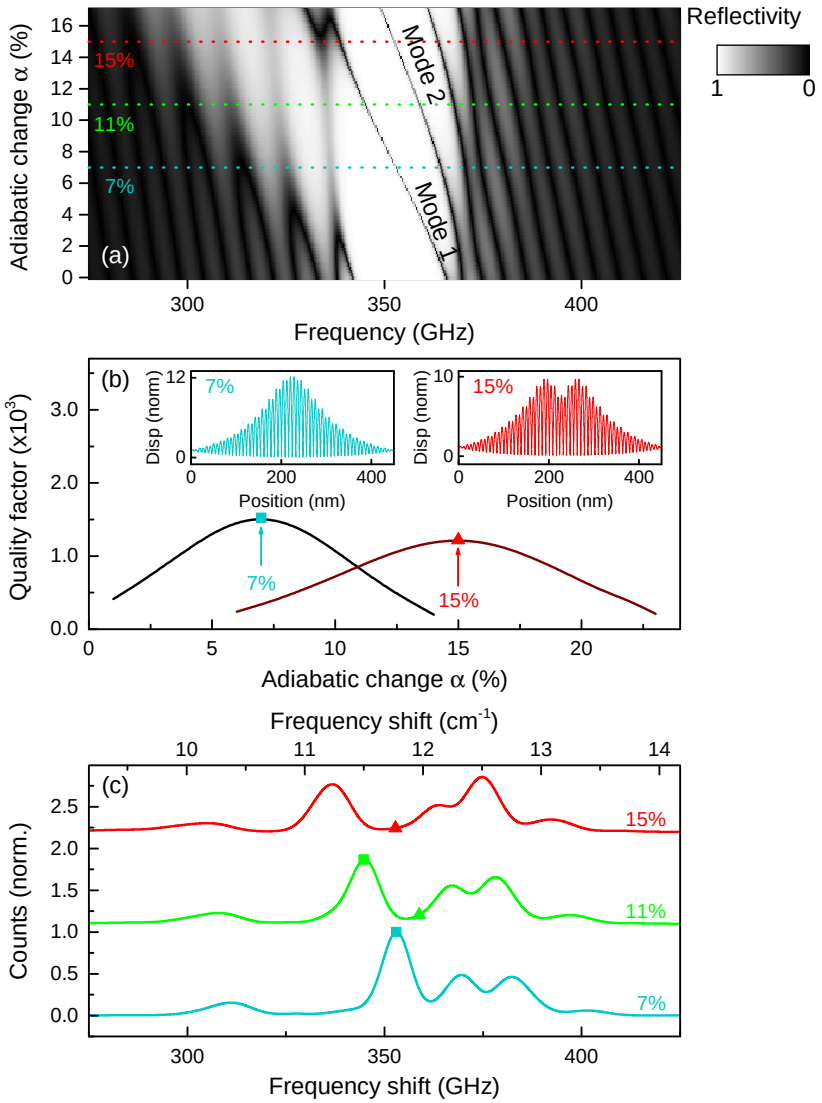

Figure 3.9 – **(a)**: Color map showing the evolution of the acoustic reflectivity spectra for the adiabatic cavity as a function of α. The dashed cyan, green and red lines mark the values of α corresponding to 7%, 11% and 15% adiabatic changes respectively. **(b)**: Evolution of the mechanical quality factor of the first and second confined mode as a function of the adiabatic transformation. The points corresponding to $\alpha = 7\%$ and $\alpha = 15\%$ are marked by a cyan square and a red triangle, respectively. Insets: spatial profiles of the first (cyan curve) and second (red curve) confined mode for $\alpha = 7\%$ and $\alpha = 15\%$, respectively. **(c)**: Simulated Raman spectra for $\alpha = 7\%$ (cyan curve), $\alpha = 11\%$ (green curve) and $\alpha = 15\%$ (red curve). An offset between the spectra has been introduced for clarity. The square and triangle symbols indicate the resonance frequencies of the first and second mode, respectively.

second mode presents a different spatial symmetry in strain along the z direction with respect to the first one. If we take the second confined mode, the overlap integral of the photoelastic model gives a Raman scattering cross section equal to 0, resulting in a Raman inactive mode. By tuning the parameter α it is thus possible to tailor the spatial profile of the adiabatic confined mode and select its symmetry.

3.3 Topological nanocavities

In the previous section, we have presented a confinement strategy for acoustic phonons based on the adiabatic transformation of a superlattice's acoustic band diagram. In fact this design follows a "traditional" approach used in nanophononics for confining acoustic phonons and creating more complex devices. Indeed, the design of the system is based on the dispersion relation of a periodic medium, and no other information than the eigenenergies of the system is used.

In this section, we propose the design of another structure where an interface state is created between two DBRs by taking advantage of the topological properties of acoustic superlattices.

The study of topological phases has allowed to develop a new set of tools to describe periodic media, providing information that goes beyond the one contained in the eigenenergies of the system, represented by band diagrams. It enabled the description of new states of matter [178], and an in-depth understanding of physical effects in electronics related to the creation of edge states between topologically inequivalent media. Examples of their applications can be found in the study of the Quantum Hall Effect [179–183], or in the development of conducting polymers [184, 185]. These principles have also been applied in optical [186–188] and in acoustic [189–193] periodic media, for the study of interface states and for the investigation of topological unidirectional edge states. In this section we present the conception and characterization of topological acoustic cavities at the nanoscale.

3.3.1 Topological invariants for phononic interface states

The existence of the confined states studied in this section is predicted through topological invariants, which describe the topological phase of the system. Since the building blocks of the systems studied here are planar acoustic superlattices, we consider the Zak phase [194, 195], a topological invariant relevant for one-dimensional periodic systems, that we briefly introduce below.

Let us consider an excitation in a periodic potential, such as an electron propagating along a direction z in a one-dimensional crystal having a lattice parameter a. The electron eigenstates can be put in the form of Bloch waves $\psi_{n,k}(z) = e^{ikz}u_{n,k}(z)$, where $u_{n,k}(z)$ corresponds to the periodic part of the wavefunction, k is the wavevector and n is the n^{th} band. We now consider an isolated band in the Brillouin zone, i.e. a band that does not cross other bands. The Zak phase of this n^{th} band is defined as a one-dimensional Berry phase [196], that is [197]:

$$\theta_n^{Zak} = i\int_{-\pi/a}^{\pi/a} \langle u_{n,k}|\partial_k|u_{n,k}\rangle \, \mathrm{d}k \tag{3.3}$$

where ∂_k is the partial derivative of a state with respect to k. To calculate the Zak phase, we consider the scalar product $A(q) = \langle u_{n,k}|\partial_k|u_{n,k}\rangle$, called the Berry connection, for the periodic part of each state represented in the band and we integrate it over the full Brillouin zone.

Phonons propagating in one-dimensional periodic media are also described by band diagrams. Zak phases can therefore be calculated for every band. As proposed by C.T. Chan and co-workers, the Berry connection for an acoustic wave propagating in a periodic medium can be found by calculating the overlap integral [192]:

$$\int_{unit\ cell} \frac{1}{2v^2(z)\rho(z)} u^*_{n,q}(z)\partial_q u_{n,q}(z)\,\mathrm{d}z \tag{3.4}$$

where q is the wavevector of the phononic Bloch modes, whereas $v(z)$ and $\rho(z)$ correspond to the sound velocity and to the mass density in the respective materials. Here the spatial integral is carried out over one unit cell of the system and $u_{n,q}$ indicates the periodic part of the displacement field expressed in the Bloch formalism. Zak phases of acoustic superlattices are relevant in this context since it is possible to relate their values to a general condition determining the existence of an interface state between two periodic structures. We state below such a general condition.

We consider two concatenated semi-infinite DBRs. We aim at creating a confined state at the interface between the two structures, at a resonance frequency f_{res}. In order to have such a localized state, f_{res} must fall in an acoustic minigap for each of the two periodic media. In such a way, the state evanescently decays in both acoustic mirrors. Furthermore, in order to get a localized mode, the reflection phases from the individual reflectors require to fulfill a particular condition [198]. We denote $r = e^{i\phi(f)}$ the complex amplitude reflection coefficient inside an acoustic minigap of the semi infinite DBR. The parameter $\phi(f)$ corresponds to the reflection phase of the system, which depends on the frequency f of the incident wave. To get a confined state inside the considered minigap, the reflection phases of the two acoustic mirrors must add up to a multiple of 2π at the resonance frequency of the designed mode. If we call ϕ_{left} and ϕ_{right} the reflection phases of a left and a right semi infinite DBRs, the condition to get a confined state between the two mirrors is [199]:

$$\phi_{left}(f_{res}) + \phi_{right}(f_{res}) = 2m\pi \tag{3.5}$$

with m an integer. Notice that the condition described above is general to get an interface state. It has been used to localize surface plasmons [200], electromagnetic fields and electronic waves[201]. What we take advantage of here is the intimate relation between the DBRs reflection phases and the Zak phases of the corresponding infinite superlattices.

To illustrate that, let us start by an acoustic superlattice constituted by $(\frac{\lambda_0}{4}, \frac{\lambda_0}{4})$ GaAs/AlAs layer pairs, designed to maximize the span of the first Brillouin zone ***edge*** gap centered at a frequency $f_0 = 175\,\mathrm{GHz}$. λ_0 indicates the corresponding acoustic wavelengths in the considered materials. The layer thicknesses fulfilling the $(\frac{\lambda_0}{4}, \frac{\lambda_0}{4})$ geometry are:

$$\begin{aligned} d_{GaAs} &= \frac{v_{GaAs}}{4f_0} \\ d_{AlAs} &= \frac{v_{AlAs}}{4f_0} \end{aligned} \tag{3.6}$$

The total acoustic path length of one superlattice unit cell is half a phonon wavelength, i.e. the thicknesses d_{GaAs} and d_{AlAs} obey:

$$\frac{d_{GaAs}}{v_{GaAs}} + \frac{d_{AlAs}}{v_{AlAs}} = \frac{1}{2f_0} \tag{3.7}$$

We now perturb the acoustic superlattice by modifying both d_{GaAs} and d_{AlAs}. However, we do it in such a way that the first Brillouin zone edge minigap stays centered at the same f_0, i.e. the two thicknesses verify Equation 3.7 for $f_0 = 175\,\text{GHz}$. The perturbations of the two layers in one unit cell are therefore linked, and the layer thicknesses after the perturbation can be written as:

$$\begin{aligned} d_{GaAs} &= \frac{v_{GaAs}}{4f_0}(1+\delta) \\ d_{AlAs} &= \frac{v_{AlAs}}{4f_0}(1-\delta) \end{aligned} \tag{3.8}$$

Where δ quantifies the perturbation of the two layers in the unit cell. For $\delta = 0$, we find the unperturbed $(\frac{\lambda_0}{4}, \frac{\lambda_0}{4})$ case. Notice that, according to Equation 3.8, $-1 < \delta < 1$. Indeed, $\delta = 1$ and $\delta = -1$ correspond to pure GaAs and AlAs slabs, respectively. In Figure 3.10, we plot the band diagrams for three superlattices with $\delta = -0.1$, $\delta = 0$ and $\delta = 0.1$ (here we show these dispersion relations for $q \in [-\frac{\pi}{a}, \frac{\pi}{a}]$). We observe that for $\delta = -0.1$ and $\delta = 0.1$, they look identical. By just considering the dispersion relations of the two perturbed superlattices with $\delta = -0.1$ and $\delta = 0.1$ no difference in the acoustic behavior of these structures can be noted.

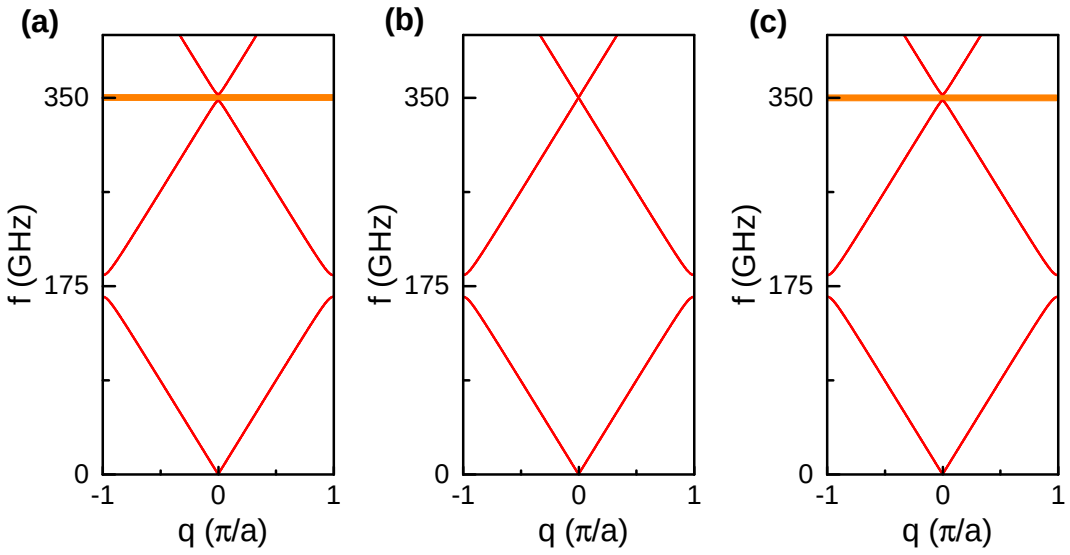

Figure 3.10 – Acoustic band diagrams for $\delta = -0.1$ (Panel (a)), $\delta = 0$ (Panel (b)) and $\delta = 0.1$ (Panel (c)). Notice that the first Brillouin zone center acoustic bandgap closes for $\delta = 0$. In the other two panels, this bandgap is highlighted by an orange region.

We now focus on the first Brillouin zone ***center*** minigap, located at a frequency $2f_0 = 350\,\text{GHz}$, and highlighted in Figure 3.10 by orange regions. For the $(\frac{\lambda_0}{4}, \frac{\lambda_0}{4})$

case (i.e. $\delta = 0$), this gap is closed. We can follow the evolution of the spectral width of this Brillouin zone center acoustic minigap when we vary the value of δ. This is what is shown in Figure 3.11. The black and the red lines indicate the frequencies of the two band edges enclosing the considered gap at $q = 0$. The frequency interval between the black and red curves therefore corresponds to the span of the minigap. The short dotted lines indicate the values of δ for which we plotted a band diagram in the previous figure.

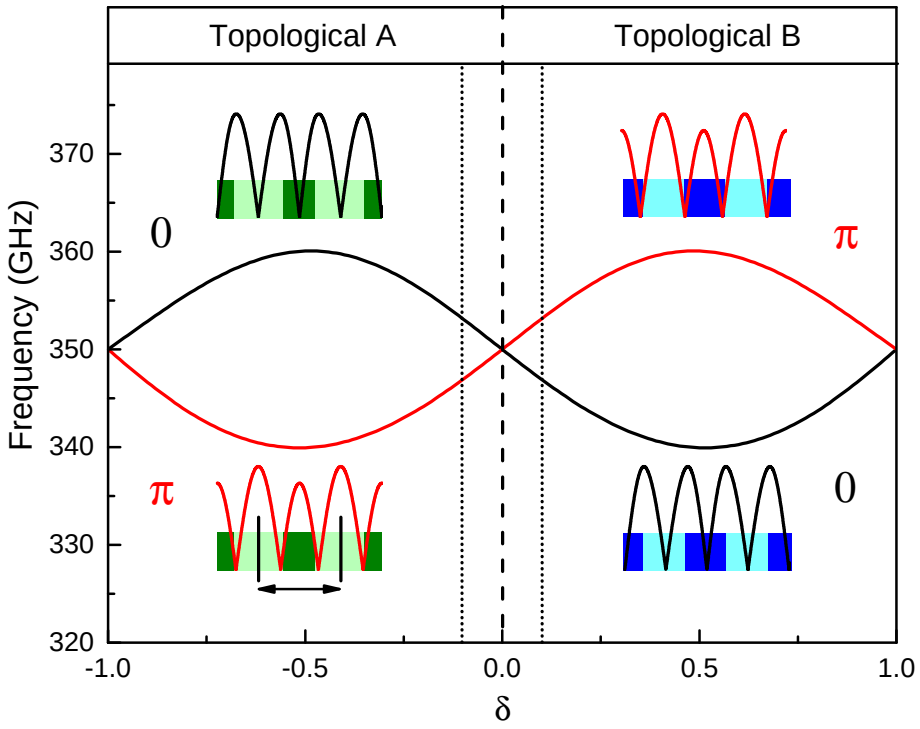

Figure 3.11 – Band inversion of the second acoustic minigap around 350 GHz. We plot the frequencies of the band edges bounding the minigap (red and black) as a function of parameter δ, which describes the relative material composition of the superlattice (see text). The insets show the evolution of the edge modes' spatial profiles for $q = 0$ inside the superlattice. Green colors indicate a SL with $\delta < 0$. Blue colors indicate $\delta > 0$. Dark (light) shades correspond to GaAs (AlAs) layers. The inset to the Figure on the bottom left shows the choice of a centro-symmetric unit cell with the black lines and the double arrow. A sign change in δ marks the transition between the topological phases A (green layers) and B (blue layers) of the DBR. The transition is characterized by an exchange in the symmetries of the Bloch modes at the upper and lower band edge (shown in the insets), and is indicated by the vertical dashed line. Accordingly, the Zak phases (0 and π values) of the two bands bounding the gap exchange. The vertical dotted lines show the particular case of $\delta = \pm 0.1$, chosen in Figure 3.10.

The values of the Zak phase for the two bands located above and below the first Brillouin zone center acoustic minigap are indicated in Figure 3.11. For $\delta < 0$, the

value of the Zak phase for the lower band is 0, whereas for the upper band it is π. The Zak phases of the considered bands are here topological invariants in the sense that by changing the value of δ, the considered bands are deformed in the Brillouin zone, but the associated Zak phases do not change. The only way to change the values of these parameters is to subject the system to a drastic transformation such as a band inversion, where we close and reopen the gap located between the two considered bands. This is indeed what we observe: after the band crossing, the values of the Zak phases are inverted for the lower and upper bands. For $\delta < 0$ we are in a given topological phase. For $\delta > 0$ we are in another one. For $\delta = 0$, where the black dashed line crosses the two curves, the Zak phase is not defined for neither of the two bands. Therefore, we can say that for the particular case of $\delta = -0.1$ and $\delta = 0.1$, even though the acoustic band gaps look the same, the two systems are not equivalent since the only way to obtain one structure from the other is through band inversion and therefore to change the topological phase of the system.

The relation between the reflection phases for a semi-infinite DBR terminated by a centro-symmetric unit cell and the Zak phases of the corresponding superlattice can be expressed in a formal way. In particular, it has been shown that sign of the reflection phase for the first Brillouin zone centre acoustic minigap is given by [192, 193]:

$$sgn(\phi) = e^{(i(\theta_0^{Zak} + \theta_1^{Zak}))} \tag{3.9}$$

In the previous equation θ_0^{Zak} and θ_1^{Zak} are the Zak phases of the lowest acoustic band (the one starting at $f = 0$) and of the band just below the first ZC acoustic minigap, respectively. In other words, the reflection phase sign of a given acoustic minigap is determined by the Zak phases of the bands that are below this frequency interval.

In the case discussed before, for any value of δ, the Zak phase θ_0^{Zak} of the lowest band does not change. This can be understood from the fact that the first Brillouin zone edge minigap always remains open. From these considerations, it is now clear that we will have opposite signs for the reflection phases when $\delta < 0$ and when $\delta > 0$, since the value of θ_1^{Zak} will be different in these two conditions.

A key aspect of this topological transition is the fact that there is an associated change in the spatial symmetries of the mechanical Bloch modes bounding the considered band gap, i.e. the edge modes represented at $q = 0$ in the lower and upper bands. We have seen in Chapter 1 (see Section 1.2.2) that these modes are mechanical standing waves. It has been shown in previous works that the symmetry properties of these modes remain unaltered in a given topological phase [192, 193]. Considering a centro-symmetric unit cell such as the one represented by the black lines in the bottom left inset to Figure 3.11, for $\delta < 0$ the Bloch mode at the lower (upper) band edge has a symmetric (antisymmetric) displacement pattern. These symmetries exchange for $\delta > 0$. The band inversion is therefore accompanied by an inversion in the symmetry properties of the edge modes located at $q = 0$. The red curve therefore indicates edge modes having a symmetric spatial profile, and the black one modes having an antisymmetric profile with respect to the center of a centro-symmetric unit cell (see insets to Figure 3.11).

The link between the topological properties of a superlattice and the reflectivity property of the associated semi-infinite DBR now becomes clear. Let us suppose that we terminate an infinite superlattice on one side to fabricate a semi-infinite DBR. Furthermore, we consider that we terminate the superlattice at the interface

between two consecutive unit cells. For a centro-symmetric unit cell this would mean to terminate the superlattice by half a layer of GaAs. As a consequence, for $\delta < 0$ the lower energy edge state has an antinode at its end, and the reflection phase is 0. For the upper state, the node indicates that the reflection phase is π. As a consequence, the reflection phase evolves from 0 up to π accross the minigap. Correspondingly, for $\delta > 0$, the reflection phase goes from $-\pi$ to 0, since the reflection phase is a monotonically increasing function of the mechanical frequency [193]. The reflection phases have opposite signs in the case of $\delta > 0$ and $\delta < 0$, as predicted by Equation 3.9.

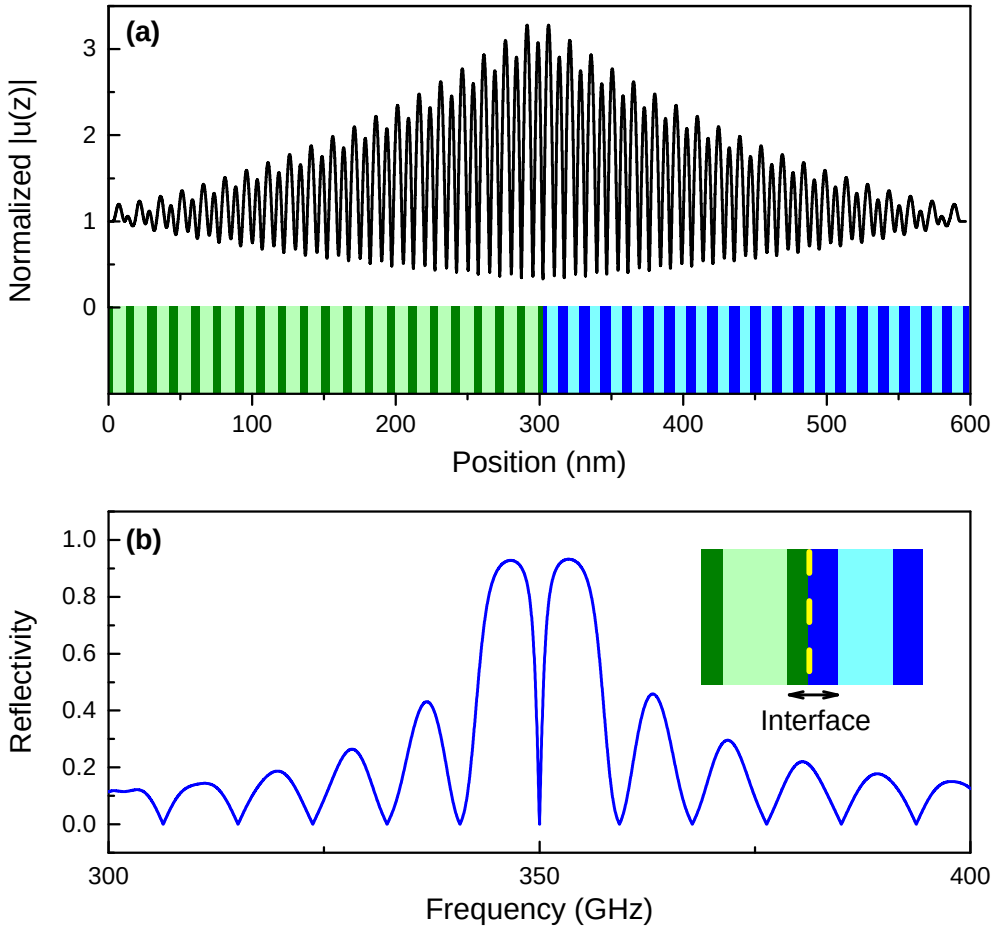

Figure 3.12 – **(a)**: Spatial profile of the interface mode inside the topological structure. The color map schematically shows the structure of the system. The black curve shows the spatial profile of the confined mode. Notice that the envelope of the mode is maximal at the interface between the two DBRs. The green colors indicate the layers of the DBR with $\delta = -0.1$, the blue colors indicate the layers of the DBR with $\delta = +0.1$. Dark colors are layers of GaAs, light colors correspond to layers of AlAs. **(b)**: Simulated acoustic reflectivity curve computed by a transfer matrix method. The sharp dip inside the high reflectivity region is spectrally located at the frequency of the interface mode plotted in Panel (a). The inset to the Panel highlights the centro-symmetric unit cell chosen to terminate the semi-infinite DBRs. The yellow line show the frontier separating the two structures. The black arrow marks the interface layer between the DBRs.

By concatening two DBRs with inverted bands and terminated by centro-symmetric unit cells, we can create an interface state. An example of such a structure is given in Figure 3.12, Panel (a), where we have concatenated two DBRs, the left one with $\delta = -0.1$ and the right one with $\delta = +0.1$. The green and blue colors indicate the DBRs in different topological phases. The dark colors indicate layers of GaAs, whereas the light colors correspond to layers of AlAs. Because of the phase evolution described before, by concatening two of these acoustic superlattices terminated by a centro-symmetric unit cell, Equation 3.5 is automatically fulfilled at the center of the considered bandgap. Indeed, the sum $\phi_{left} + \phi_{right}$ is negative for the low frequency edge of the bangap, and positive in the upper edge. Necessarily, this sum is equal to 0 inside the gap.

Figure 3.12, Panel (b), shows the calculated acoustic phonon reflectivity spectrum around the first Brillouin zone center acoustic minigap for the concatenated system. The inset to Panel (b) highlights the termination of the two DBRs, where centro-symmetric units cells have been used to terminate the structures. Clearly, a sharp dip is present in the reflectivity curve, indicating an interface state at a resonance frequency of 350 GHz. The spatial profile of the associated confined mode is plotted in Figure 3.12, Panel (a). The envelope of the state has a maximum at the interface between the two DBRs in different topological phases. This mode disappears if the bands of the two DBRs are not band inverted according to Figure 3.11. We illustrate that in Figure 3.13, where we plot the calculated acoustic reflectivity curve for a system constituted by two DBRs, one with $\delta = -0.1$ and the other one with $\delta = -0.3$. No dip in the high reflectivity region is visible. This shows that in this case we did not generate an interface state between the two mirrors. Notice that the reflectivity curve is not completely flat in the calculated acoustic stop band. This is due to the fact that the DBR with $\delta = -0.3$ presents a larger first ZC acoustic stop band than the one with $\delta = -0.1$. Therefore, if at the center of the stop band both DBRs present high reflectivity values, on its edges the only efficient mirror is the one with $\delta = -0.3$.

The design described above is an efficient way to create an interface state between two DBRs. However, the notion of "interface" state used here is only true in terms of the structures that are directly concatenated. Indeed, one could consider the system described above solely for its materials. The interface layer indicated by the black arrow in the inset of Figure 3.12 is constituted by GaAs. This layer between the two DBRs can be considered as a $\frac{\lambda}{2}$ spacer for a mechanical wave with a frequency of $2f_0 =$ 350 GHz. Indeed, for an acoustic wave propagating at a frequency $f_0 = 175$ GHz, the left and right acoustic mirrors are $(\frac{\lambda_0}{4}(1-\delta), \frac{\lambda_0}{4}(1+\delta))$ and $(\frac{\lambda_0}{4}(1+\delta), \frac{\lambda_0}{4}(1-\delta))$ GaAs/AlAs DBRs, respectively. Hence, for a mode at twice the frequency $2f_0$, for which we denote λ the corresponding acoustic wavelength in the considered materials, the mirrors constitute $(\frac{\lambda}{2}(1-\delta), \frac{\lambda}{2}(1+\delta))$ and $(\frac{\lambda}{2}(1+\delta), \frac{\lambda}{2}(1-\delta))$ DBRs. The interface layer when we concatenate the two systems has a total thickness of $\frac{\lambda}{2} = 1/2(\frac{\lambda}{2}(1-\delta) + \frac{\lambda}{2}(1+\delta))$. By stacking two DBRs terminated with centro-symmetric unit cells, one can consider that we are obtaining a Fabry-Perot resonator between two different mirrors.

Nevertheless, we can still take advantage of the link established in this section between the evolution of the reflection phases of the DBRs and the topological phases in which these structures are. In particular, in the next subsection, we present how from the concatenated system described above we create a localized state at the interface of two DBRs, where the mode is confined between layers of different materials.

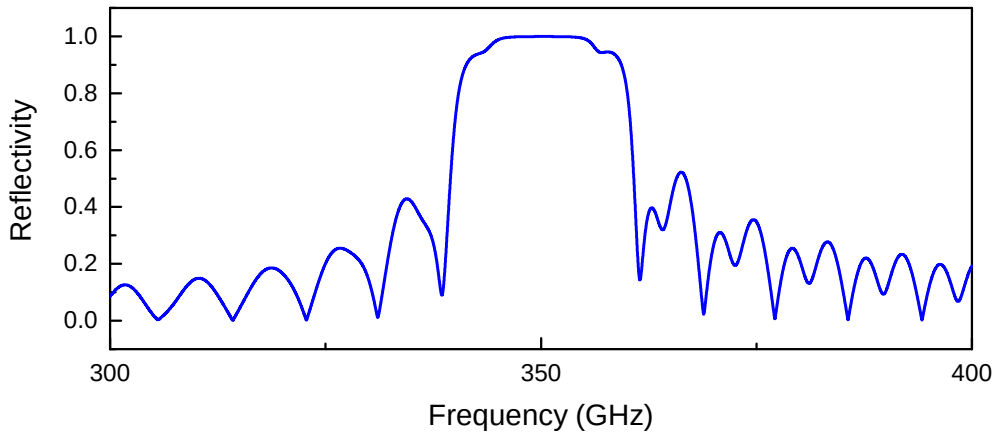

Figure 3.13 – Acoustic reflectivity curve of a system constituted by two acoustic DBRs, one with $\delta = -0.1$ and the other one with $\delta = -0.3$. Notice that in this case, no confined mode is visible in the acoustic stop band of the structure.

3.3.2 Interface states

The resonance frequency of a topological interface state can be tuned across the acoustic minigap by redefining the last unit cell of each DBR. The procedure is described on the left side of Figure 3.14. We start from centro-symmetric unit cells as represented by the sketch labelled (I). As explained before, the interface is formed by a dark green layer and dark blue layer, both representing GaAs. Overall, the interface layer behaves as a $\frac{\lambda}{2}$ spacer for phonons with a frequency of 350 GHz. We consider for example a system containing 20 unit cells in each DBR with $\delta_{left} = -0.1$ on the left phononic mirror and $\delta_{right} = +0.1$ for the right DBR. The corresponding acoustic reflectivity spectrum is shown Figure 3.14 by the red curve. This is the same system as the one studied in Figure 3.12. As before, the topological interface state appears at the center of the acoustic minigap at 350 GHz.

Next, we introduce a slight perturbation at the interface by adding an additional thin layer of GaAs in the last layer of the left DBR (black layer), as shown by the sketch (II). A particular situation is reached if the thickness of this thin layer is set to $\Delta_{GaAs} = (\delta_{right} - \delta_{left})v_{GaAs}/(8f_0)$. Together, the additional layer and the last GaAs layer of the left DBR bounding the interface add up to the same thickness as the last GaAs layer of the right DBR. In the sketch (II), at the interface, the dark green and the thin black layer together thus equal the dark blue one. The relevance of this particular perturbation is illustrated at the bottom of the figure, in sketch (III). By redefining the position of the interface between the two topologically different DBRs, the perturbation is equivalent to a change from centro-symmetric unit cells to a standard GaAs/AlAs bilayer unit cell. In other words, in order to obtain the semi-infinite DBRs contained in the cavity, the corresponding superlattices have been terminated on one side by a bilayer unit cell. For a finite size system, the cavity can therefore be considered as two concatenated DBRs, each one containing an integer number of bilayer unit cells. As a consequence, the interface now directly connects layers of different materials.

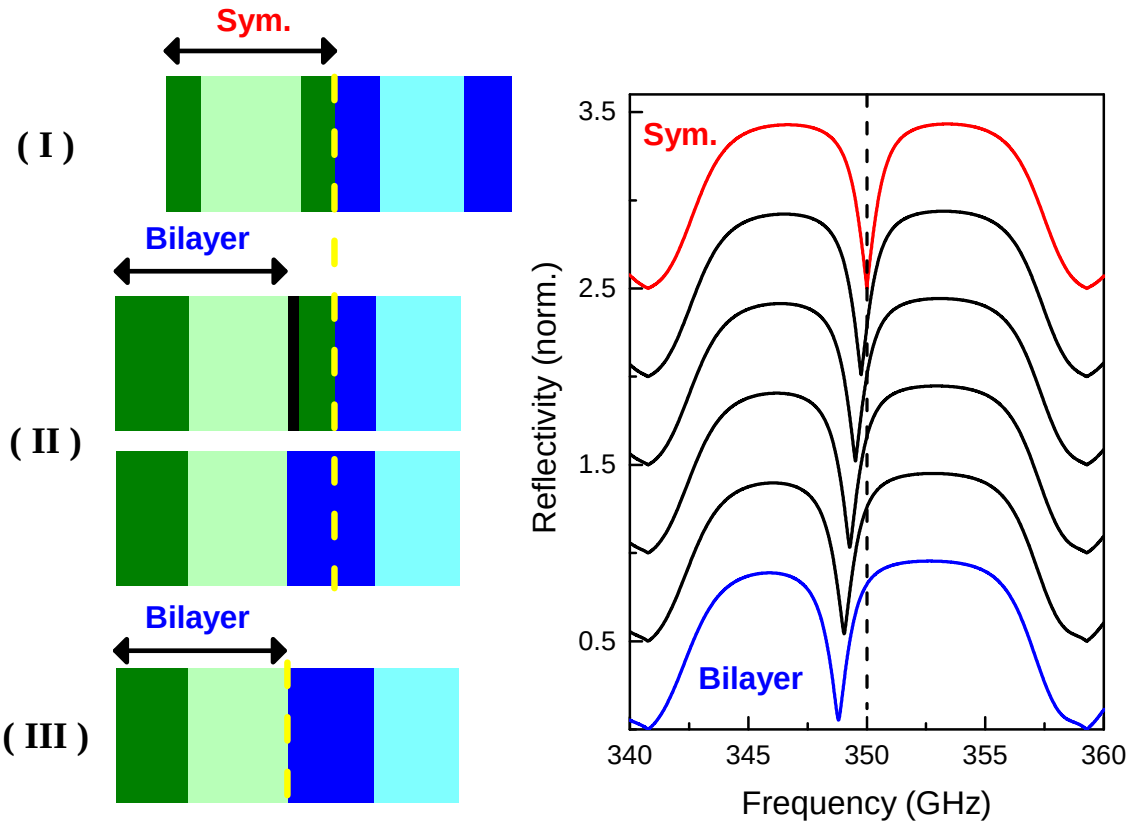

Figure 3.14 – **Left side**: (I) Interface between two topologically different DBRs terminated by centro-symmetric unit cells. (II) We add a thin layer of GaAs at the interface (black), such that the rightmost layer of the left DBR becomes as thick as the leftmost layer of the right DBR (i.e. we replace a dark green by a dark blue layer). (III) This slight perturbation is equivalent to redefining the unit cell in which we terminate the DBRs. The interface between the two DBRs now coincides with the interface between two different materials. The latter presents the experimental configuration. The yellow line shows how we define the interface between the DBRs. **Right side**: Corresponding phonon reflectivity spectra of two concatenated DBRs from different topological phases with 20 unit cells each ($\delta = -0.1$ on the left and $\delta = +0.1$ on the right). From top to bottom we gradually tune the unit cells from centro-symmetric (red) to bilayers (blue) by adding GaAs at the interface. Notice the smooth redshift of the confined state inside the acoustic minigap. For better visibility subsequent curves are vertically offset by 0.5.

The corresponding reflectivity spectrum of the shifted system is shown by the blue curve represented in Figure 3.14 and corresponds to our experimental implementation. The topological interface mode appears red-shifted from the bandgap center as a consequence of the additional propagation phase introduced by the additional perturbation layer.

Following this line of reasoning, it is possible to continuously tune the choice of the terminating superlattice unit cells (i.e. the length of the thin black layer) through intermediate cases. We show some of these intermediate cases in Figure 3.14 (black curves) and observe that the resonance frequency indeed smoothly decreases from the center of the acoustic bandgap to the red-shifted bilayers unit cell case.

In essence, by changing the unit cell symmetry we tuned the confined state eigenfrequency inside the bandgap. This enables us to create an interface state that is spatially localized between layers of different materials, and that cannot be considered as a confined acoustic mode in a Fabry-Perot resonator. In the next section, we present the Raman scattering measurements that we performed on a sample fabricated according to the design presented in this section. This allows to experimentally demonstrate the existence of such topologically engineered interface states.

3.3.3 Characterization of the topological cavity

The phononic system that was experimentally characterized is constituted by two δ-perturbed $(\frac{\lambda}{4}, \frac{\lambda}{4})$ acoustic DBRs, each one containing 20 pairs of GaAs/AlAs layers. One mirror has been perturbed with $\delta = -0.1$ and the other one with $\delta = +0.1$. The sample was designed to confine a mechanical mode at a resonance frequency of 354 GHz. The confined mode presents a maximum in its envelope at the interface between two layers of different materials (i.e. bilayer unit cell). With the parameters described above, the predicted mechanical quality factor for the interface state is of the order of 1200. As in the case of the adiabatic structure, the sample was fabricated by MBE on a (001) GaAs substrate. We characterized it by Raman scattering spectroscopy at room temperature. The whole acoustic system is enclosed between two optical DBRs. The two optical mirrors have the same structures as the ones for the adiabatic cavity: the mirror in contact with air is made of 14 layer pairs of $Al_{0.1}Ga_{0.9}As/Al_{0.95}Ga_{0.05}As$ and the one in contact with the substrate of 18 layer pairs. The acoustic structure constitutes a 2λ optical spacer, for a resonance optical vacuum wavelength of 940 nm. The sample is also fabricated with a thickness gradient, allowing to tune the resonance wavelength of the collection mode over a wavelength span of ≈ 0.83 to 1.05 µm.

Also for this sample, we first found the DOR condition for Raman peaks located at frequency shifts of ≈ 350 GHz, as shown in Figure 3.15. Therefore, these Raman spectra were obtained around the theoretical resonance frequency of the interface state. We measured the intensity of the Raman signals when we change the laser spot position on the structure. The result is similar to the one already observed for the adiabatic cavity. The intensity of the Raman spectrum is maximal for one particular position on the sample, as indicated by the vertical red arrow, due to the thickness gradient of the system.

Once the double optical resonance was found for frequency shifts around 350 GHz, we measured a Stokes Raman spectrum on a larger range of frequency shifts. The experimental curve is shown in Figure 3.16. The laser was at a wavelength of 915 nm.

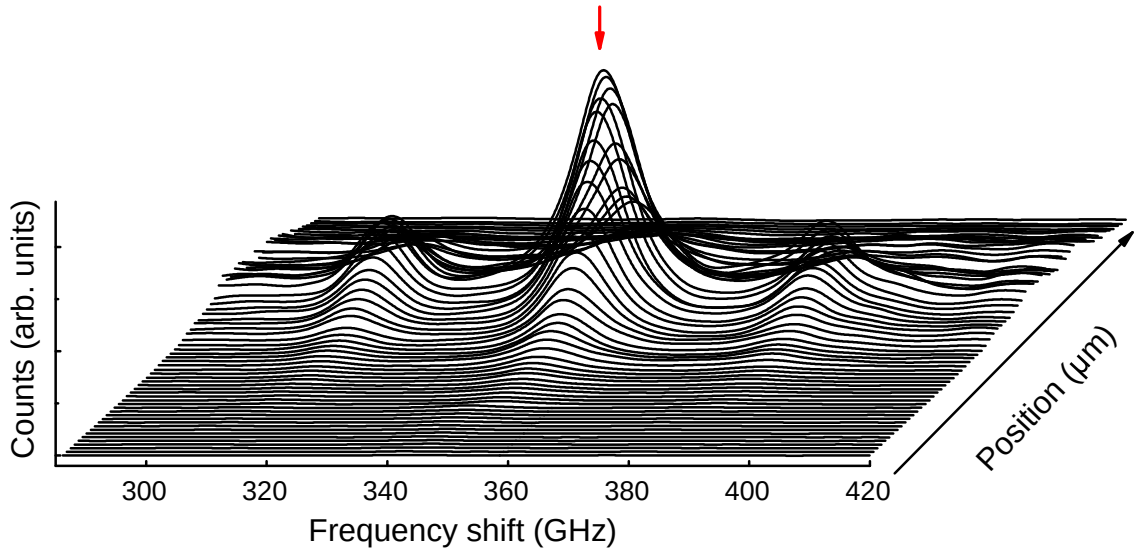

Figure 3.15 – Evolution of the Raman signal intensities when the laser spot is translated on the sample. When the Raman intensities are maximal, we are at DOR condition for frequencies around 350 GHz. The red arrow indicates the spectrum measured in DOR condition.

The power of the incident laser was ≈ 20 mW. We observe that three groups of Raman peaks are visible. The insets to the figure show detailed parts of the plot as indicated by the black arrows. We compared this spectrum to simulations of the Raman scattering cross section, to determine the spatial profile of the modes that are Raman active. The signals measured for frequency shifts of ≈ 720 GHz and ≈ 1075 GHz (insets) correspond to extended modes. We will therefore focus on the first triplet of peaks, highlighted by the red region in Figure 3.16. They correspond to the Raman peaks already shown in Figure 3.15.

In Figure 3.17 (Panel (a), black curve), we plot a detailed view of the Raman peaks highlighted in Figure 3.16.

In Panel (a) of Figure 3.17, we observe that the measured spectrum is constituted by a main peak located at $\Delta f = 360$ GHz, labeled (B), and by two satellite peaks located at frequency shifts of 323 GHz (labeled (A)) and 397 GHz (labeled (C)). As before, to attribute these peaks to extended or confined modes we compare the experimental spectrum to the simulated acoustic reflectivity curve obtained for the structure, which is represented in Panel (b) of Figure 3.17. Peaks labelled (A) and (C) fall outside the band gap of the acoustic DBRs and therefore correspond to extended phonon modes. Their spatial profile is shown in Figure 3.17 (Panel (c) and (e)), superimposed with the structure of the system. The peak labelled (B) falls in the high reflectivity interval, where the sharp dip associated to the confined mode is located. This Raman peak is generated by the interface mode confined in the structure. The spatial profile of this confined mode is shown in Figure 3.17, Panel (d). It presents a characteristic profile exponentially decaying into the DBRs.

The conclusive proof that the interface mode has been probed through Raman scattering is achieved by calculating the Raman scattering cross section with a pho-

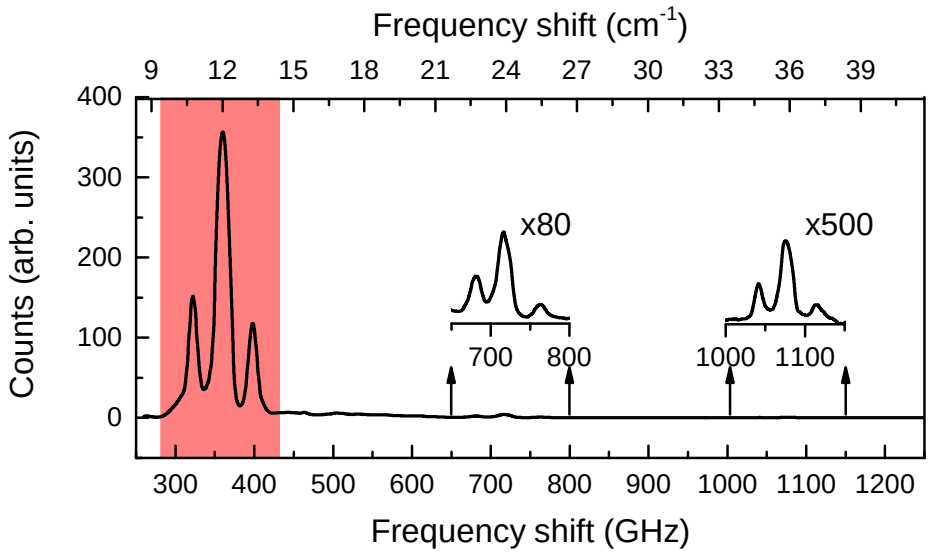

Figure 3.16 – Raman spectrum measured on the topological structure. The two insets show detailed regions of the measured plot, as indicated by the arrows. The vertical axes of the insets have been magnified by factors of 80 and 500, as indicated in the figure. The red region indicates the first triplet of Raman peaks. We will focus our analysis on this part of the spectrum (see text).

toelastic model. As in the case of the adiabatic sample, due to the wavelength of the excitation laser and the energies of the electronic transitions for GaAs and AlAs, only the photoelastic contribution of the GaAs layers is considered. As in the case of the adiabatic cavity, we stress that for this model we only used design parameters of the sample. The result of these simulations are shown in Figure 3.17, Panel (a). The solid magenta curve corresponds to the simulated data without any convolution. Under the experimental curve (in black), the main simulated Raman peak is generated by the interface state present inside the structure. We can see that other minor Raman peaks are present around the main peak, and are associated to extended modes. They are not resolved in the experimental curve.

To account for the experimental resolution, we convoluted the theoretical curve with a Gaussian distribution with $2\sigma = 13\,\mathrm{GHz}$. In this case, the FWHM of the convolution is larger than the one used for the adiabatic cavity. This difference in experimental resolution can be explained by considering a different alignment of the set up for the measurements carried out here. The result of the convolution is shown by the dashed red line in Figure 3.17, Panel (a). Evidently, the model captures all features of the measured data. In particular, the relative heights and spectral positions of the three peaks are in very good agreement.

In this section, we have shown that we are able to create a confined state inside an acoustic layered structure by taking advantage of the Zak phases, which are describing the topological phase of a superlattice. Furthermore, by tuning the choice of the unit cell describing the two concatenated semi-infinite DBRs, we can engineer the mechanical resonance frequency of the interface state. This allowed us to fabricate an acoustic cavity where the localized state lies between layers of different materials. The implemented high resolution Raman scattering set-up and the experimental

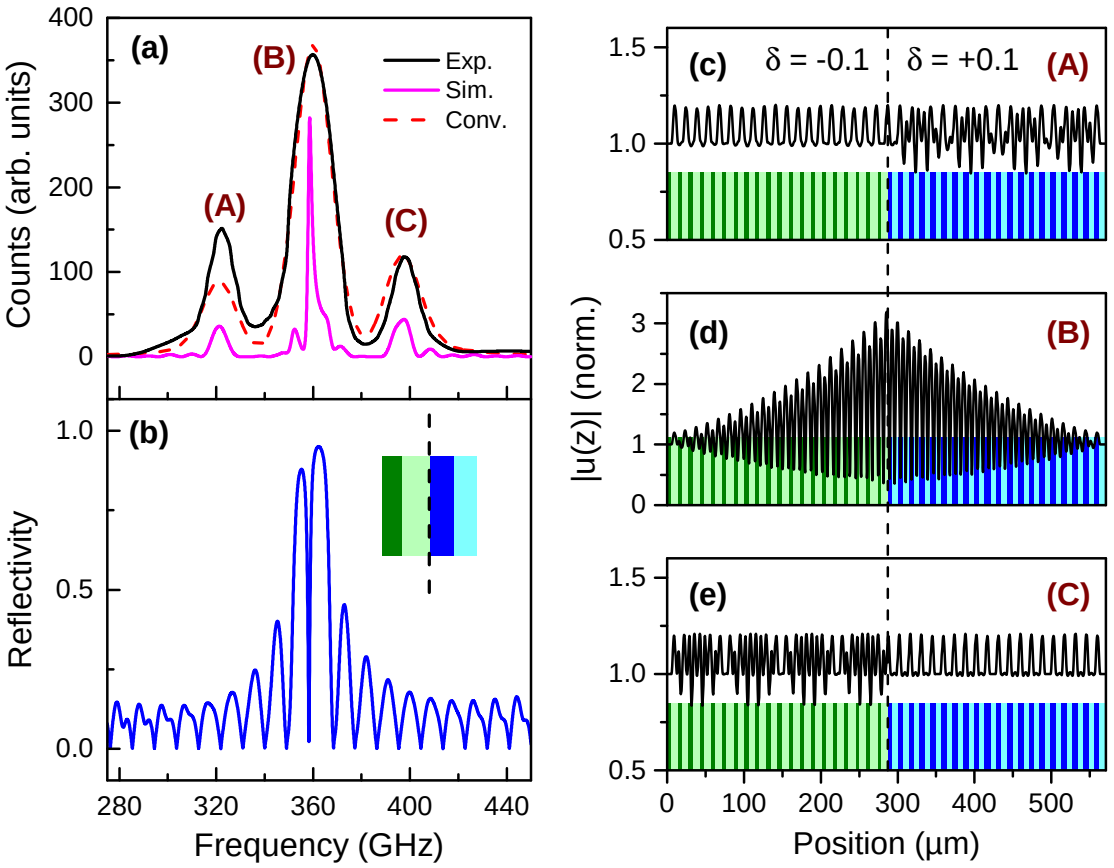

Figure 3.17 – **(a)**: Experimental Raman spectrum (solid black) together with photoelastic model calculation (solid magenta). The model calculation is convoluted with a Gaussian ($2\sigma = 13\,\mathrm{GHz}$) to account for the finite experimental resolution (dashed red). (A), (B) and (C) label the experimentally observed Raman peaks. The topological interface mode at 360 GHz corresponds to peak (B) in the Raman spectrum. **(b)**: Simulated acoustic reflectivity of the sample calculated by a transfer matrix method. Inset: schematic detail of the interface showing the asymmetric choice of the unit cell. **(c)**, **(d)** and **(e)**: The color maps show the structure of the acoustic system. The black curves show the calculated mechanical mode profiles corresponding to the peaks marked by the labels (A) (Panel **(c)**), (B) (Panel **(d)**) and (C) (Panel **(e)**) in Panel **(a)**. Peak (B) originates from the topological interface mode, peaks (A) and (C) are extended modes in the structure.

techniques presented above allowed us to successfully probe the presence of such a confined state.

The creation of such a topologically engineered confined state goes beyond the modification of a bare dispersion relation to obtain a confined mode. By just considering the eigenfrequencies contained in the acoustic band diagrams, it is not possible to predict the presence of this interface state between the concatenated systems. Topological invariants such as the Zak phase can therefore be used as a supplementary degree of freedom to control the dynamics of acoustic phonons and to describe the symmetry properties of the mechanical modes propagating inside layered systems.

3.4 Conclusion

In summary, in this chapter we have presented our experimental and theoretical work on the development of novel confinement strategies for longitudinal acoustic phonons in the GHz/THz range, going beyond the well established Fabry-Perot design used in nanophononics.

To experimentally characterize these systems, we have implemented a high resolution Raman scattering experiment. We performed an engineering of the optical environment in which the acoustic structure is probed. This enabled us to greatly enhance the intensity of the measured Raman signals and to probe the full Raman spectrum in a backscattering configuration.

Two systems have been studied in this work. The first one relies on the adiabatic confinement of longitudinal acoustic phonons at a resonance frequency of 350 GHz by progressively breaking the periodicity of an acoustic superlattice. We measured the Raman spectrum of this system in different experimental configurations, in particular by varying the DOR condition.

We determined theoretical Raman scattering cross sections of the considered systems by means of transfer matrix calculations and by using a photoelastic model, that we have compared to the experimental data. This process allowed us to understand in detail the origin of the different measured Raman peaks, and in particular to demonstrate the existence of confined states in the considered system. We then investigated the effect of the adiabatic transformation on the confinement properties of the structure, in particular on the evolution of the mechanical quality factor and on the spatial profile of the confined mode. A change in the adiabatic transformation magnitude has major effects on the Raman activity of the confined state, as shown through theoretical calculations.

In optics, the progressive transformation of a photonic crystal's periodicity allows to optimize the quality factor of three-dimensional resonators. The adiabatic confinement of acoustic modes could be used for the development of future optomechanical systems. Indeed, this strategy could be adopted in the prospect of maximizing the confinement properties of three-dimensional mechanical resonators based on phononic crystals.

The second system that has been investigated relies on the creation of a nanophononic interface state based on the engineering of topological invariants. This system was also experimentally characterized by high resolution Raman scattering spectroscopy. We showed that corresponding photoelastic model calculations perfectly account for all major features of the measured Raman spectra, in particular

the signature of the localized interface state at 360 GHz. Finally, by engineering the interface between the two DBRs constituting our topological structure, we are able to tune the frequency of the confined mode across the acoustic minigap. This work is a first example where topological invariants are used as an additional knob to control the dynamics of acoustic phonons in periodic layered media.

These new concepts for the manipulation of acoustic phonons extend the toolbox of nanoscale phonon engineering. Moreover, the GaAs/AlAs based platforms presented in this work are naturally compatible with previously studied optical structures, and can host quantum wells and quantum dots. The study of these confined acoustic phonons open further possibilities for the study of the interaction between quantum emitters and localized mechanical vibrations.

Chapter 4

Three-dimensional optical confinement in acousto-optic resonators

We have seen that one-dimensional layered systems can be implemented for the development of novel confinement methods for high frequency acoustic phonons. Furthermore, the optical environment of acoustic resonators can be engineered. This is particularly useful in the framework of Raman scattering experiments, since the measured signals can be enhanced by confining the incident laser light and the scattered field. This can be realized by fabricating an optical cavity around the acoustic resonator.

Planar GaAs/AlAs hetero-structures can be etched into micropillars, presenting lateral sizes in the range of few micrometers. In this case, we obtain a system with optical modes simultaneously confined both in the vertical and in the radial direction.

Micropillar cavities are widely used in non-linear optics, taking advantage of the strong optical non-linearities in GaAlAs alloys [202, 203]. Furthermore, they have also been employed for the study of light-matter interactions with electronic excitations both in the strong and weak coupling regime. The confined optical mode can be strongly coupled to excitonic systems such as quantum wells, for the realization of optical simulators based on cavity polaritons [204], or for the development of polariton lasers [205]. Furthermore, micropillars are used in solid state quantum optics for the fabrication of highly efficient sources of indistinguishable single photons [206, 207].

In this chapter, we investigate the possibility of performing Raman scattering experiments on these three-dimensional resonators. GaAs/AlAs micropillars have been etched from a planar sample constituted by a topological acoustic cavity embedded between two optical DBRs. We have carried out experiments that demonstrate the feasibility of measuring the Raman scattering spectra produced by the acoustic resonator, through the discrete set of optical resonances of the micropillar. We also show that, under particular conditions, the confinement of the optical mode induces a heating of the sample, which leads to a non-linear dependence of the Raman scattering intensity as a function of the incident laser power. This observation is a first example of the effect of three-dimensional optical confinement on Raman scattering measurements.

The chapter is organized as following:

- In Section 4.1 we introduce the main properties of GaAs/AlAs micropillars as optical resonators.
- In Section 4.2 we describe the heterostructure micropillar sample that we have characterized and the experimental set-up that we have implemented for this end.
- In Section 4.3 we present the experimental results that we obtained on these resonators through Raman scattering spectroscopy.
- Finally, in Section 4.4 we summarize the concepts addressed in this chapter.

4.1 Optical properties of micropillars

In this section, we present a theoretical model allowing to describe the optical behavior of a micropillar. We then investigate the optical properties of these systems numerically by performing finite element simulations, and experimentally through optical reflectivity measurements.

4.1.1 Confined optical modes

The optical properties of micropillars can be studied both through analytical approaches and by performing numerical simulations. An analytical description, such as the one given in reference [208] is particularly useful for understanding the confinement mechanisms in these resonators. We briefly recall this approach. For simplicity, we consider micropillars with circular section, as illustrated in Figure 4.1.a.

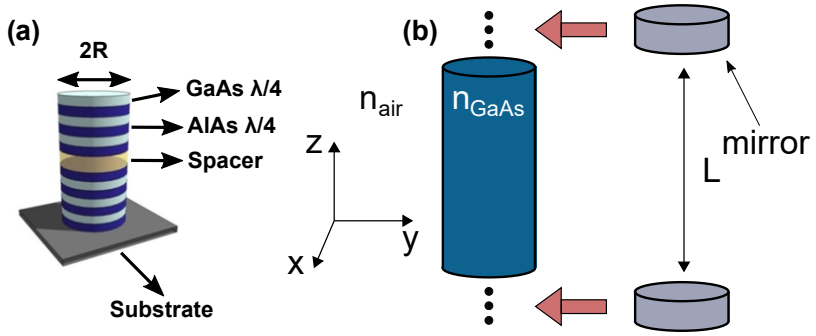

Figure 4.1 – **(a)**: Schematic diagram of a micropillar. **(b)**: Principle of the analytical derivation of the confined optical cavity modes. We first solve the propagations of guided optical waves along an infinite GaAs cylinder. We then insert two mirrors at the end of the cylindrical structure

The first step consists in finding the guided modes propagating inside an infinite GaAs dielectric waveguide having a circular section, as schematically represented in Figure 4.1.b. This is similar to the standard problem of waveguiding in fiber optics [209]. The modes are found by solving Maxwell's equations inside and outside the optical waveguide. The solutions for each component of the electric and magnetic field can be put in the form:

$$\begin{aligned} E_i(r,\phi,z) &= \psi_i^E(r)e^{i(\omega t+l\phi-\beta z)} \\ H_i(r,\phi,z) &= \psi_i^H(r)e^{i(\omega t+l\phi-\beta z)} \end{aligned} \tag{4.1}$$

where i indicates the considered spatial coordinate, β is the propagation constant along the cylinder axis, and l is an integer number. To each mode, we can associate an effective refractive index $n_{eff} = \frac{\beta c}{\omega}$, where c is the speed of light in vacuum. Notice that no weak-guidance approximation is used [208]. By applying the boundary conditions between air and the semiconductor material, we find a discrete set of guided modes for which an optical wave with a frequency ω can propagate. For a given l, several discrete solutions can be found, and they are indexed by n, a second integer value. The modes present electric and magnetic components E_z and H_z along the z direction. For some of them, the dominant field component along this axis will be the magnetic one, whereas for others it will be the electric one. The first type of modes are called the $HE_{l,n}$ modes, whereas the second ones are the $EH_{l,n}$ modes. For instance, $HE_{1,1}$ corresponds to the "monomode" solution, that is, the guided solution that always exists in the cylinder, for any frequency and waveguide radius [208].

The second step is to introduce three dimensional confinement. This can be obtained by "cutting" the infinite waveguide at two ends, and by placing two metallic mirrors, as represented in Figure 4.1.b. The confined modes are localized between the two mirrors because of the constructive interferences between counter-propagating guided modes having the same radial profile. The resonance condition is the one of a Fabry-Perot cavity, that can be expressed as

$$\omega = \frac{p\pi c}{n_{eff}L} \tag{4.2}$$

where p is an integer number characterizing the longitudinal order of the confined mode, and n_{eff} is the effective refractive index of the guided mode at the resonance frequency of the confined mode. It represents the effect of the radial confinement in the waveguide [120].

Finally, the metallic mirrors can be replaced by GaAs/AlAs DBRs, in order to obtain a micropillar cavity. The intensity of the confined optical mode decays exponentially along the z direction in the dielectric mirrors, similar to the case of a planar Fabry-Perot system. Notice that this description holds because the transverse spatial profiles of the optical modes in GaAs and AlAs waveguides are similar. Furthermore this model is also valid because the values of the effective refractive indices are similar than the ones found in the bulk materials[120, 208].

We obtain a three-dimensional resonator with a discrete set of optical resonances. The fundamental optical mode is found from the guided mode $HE_{1,1}$. The radial profile of the electric field intensity for this mode is similar to a zeroth-order Bessel function $J_0(r)$. Its resonance frequency increases when the radius of the micropillar is decreased. This is shown in Figure 4.2.a, where the eigenenergies of the fundamental optical mode and higher order harmonics have been calculated through the method described above. The vertical axis of the plot indicates the energy difference between the confined modes in the three dimensional case and the localized mode in the corresponding planar Fabry Perot cavity. For large radii, the optical eigenfrequencies converge toward this value.

In this work we have numerically simulated the optical properties of micropillars using the Finite Element Method (FEM). This method allows to find numerical approximations for the exact solutions of a partial differential equation (PDE). An introduction to this method can be found in reference [210], for which we briefly recall the basic principles here. We consider a physical problem described by a PDE defined on a domain (such as a micropillar), with a given set of boundary conditions. Instead of looking for u, the exact solution of the physical problem (for example the solution of the Helmholtz equation), we search an approximate solution u_H. In order to find it, we discretize the domain by defining a mesh on the system. We then introduce a set of basis functions ψ_i. We can define the i^{th} basis function ψ_i as being "peaked" around the node i of the mesh and being equal to zero for the other nodes. The approximate solution can be written as a linear combination of the basis functions as $u_H = \sum_i u_i \psi_i$. The coefficients u_i are then found by using this expression of u_H in the variational formulation (also called the weak formulation) of the considered problem. The finer the mesh, the closer the approximate solution will be to the exact one.

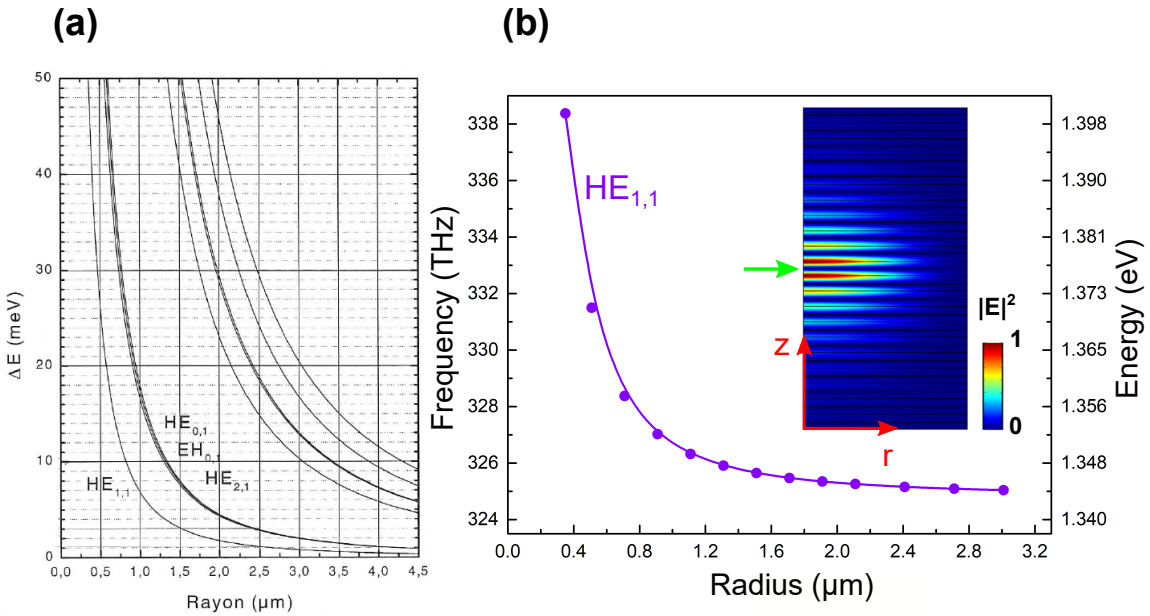

Figure 4.2 – **(a)**: Calculated resonance frequency of the confined optical modes in a micropillar as a function of the micropillar radius using the analytical model. The vertical axis shows the energy difference between the micropillar confined modes eigenfrequencies and the localized mode in the corresponding planar Fabry Perot cavity. Figure reproduced from [208]. **(b)**: fundamental optical mode resonance frequency as a function of radius, calculated by FEM. The violet line is a guide to the eye connecting the simulated resonance frequencies. The inset shows the spatial profile of the fundamental confined mode. The green arrow indicates the position of the spacer.

In this work, we used a commercial software (COMSOL, Radio Frequency Module, Eigenfrequency study) to perform numerical simulations based on FEM. The spatial

profile of the fundamental optical mode ($HE_{1,1}$) calculated through this technique is shown in the inset to Panel (b) of Figure 4.2. The micropillar is constituted by two DBRs ($\frac{\lambda}{4}, \frac{\lambda}{4}$), containing 10 GaAs/AlAs layer pairs in each mirror, enclosing a $\frac{\lambda}{2}$ GaAs spacer. The z axis indicates the revolution axis of the cylindrical structure. The plotted quantity is the intensity of the electric field. We find the Bessel-like spatial profile of the mode in the radial direction, and the exponential decay along the z axis.

In the same panel, we plot the evolution of the fundamental mode eigenfrequency as a function of radius, obtained through the same numerical method. Similarly to what was obtained with the analytical method, the resonance frequency blueshifts when the radius is decreased.

In this section, we have presented the optical properties of a micropillar, that can be found with an analytical model or by performing a finite element analysis. In the next section, we briefly show how the confinement properties of these optical resonators can be put in evidence by performing reflectivity experiments.

4.1.2 Probing the optical properties of micropillars

The properties of micropillars introduced in the previous section can be put in evidence experimentally by studying how light couples to the discrete set of optical resonances. This can be carried out by performing reflectivity measurements on these resonators.

In this case, we use a lens to focalize a collimated laser beam on the micropillar's top mirror. We measure the reflected light intensity while varying the incident laser wavelength. When the laser is resonant with a confined optical mode, a sharp dip appears in the reflectivity curve. An example of such a measurement is shown in Figure 4.3.a. The inset to the figure schematically shows the configuration of the measurement. The purple beam indicates the incident and the reflected laser beams. Notice that in order to efficiently couple the laser to a given mode, the spatial profile of the incident beam must match its radiation pattern in the free space. For the fundamental mode, it corresponds approximately to a divergent Gaussian beam. In the inset of Figure 4.3.a, we schematically represented the divergence of the radiation pattern for the fundamental mode with the black lines.

The reflectivity curve shown in Panel (a) was probed on a circular micropillar having a radius of 1.4 µm. It is constituted by two ($\frac{\lambda}{4}, \frac{\lambda}{4}$) $Al_{0.95}Ga_{0.05}As$/ $Al_{0.10}Ga_{0.90}As$ DBRs, enclosing a $\frac{\lambda}{2}$ $Al_{0.10}Ga_{0.90}As$ spacer, for a resonance wavelength $\lambda \approx 940.5$ nm. There are 18 and 23 layer pairs for the top DBR and for the one in contact with the substrate, respectively.

During the measurement, the incident power on the micropillar was $\approx 400\,\mu W$. The size of the incident collimated beam was adapted to match the radiation pattern of the fundamental mode, upon focalization on the micropillar. The reflected intensity is normalized by the input optical intensity. In Figure 4.3.a, the reflectivity dip associated to the confined mode is clearly visible. The contrast of the reflectivity dip is around 80%. Since the losses from the top mirror are the same as the ones for the bottom mirror (due to the asymmetry in the layer pair number between the two mirrors), this high contrast value shows the good mode matching of the incident laser with the fundamental cavity mode [211]. The oscillations that are visible in the optical stop band outside the mode arise from Fabry-Perot interferences in the optical set-up. By measuring the FWHM of the optical resonance, we find an optical quality factor of 8500 for this micropillar.

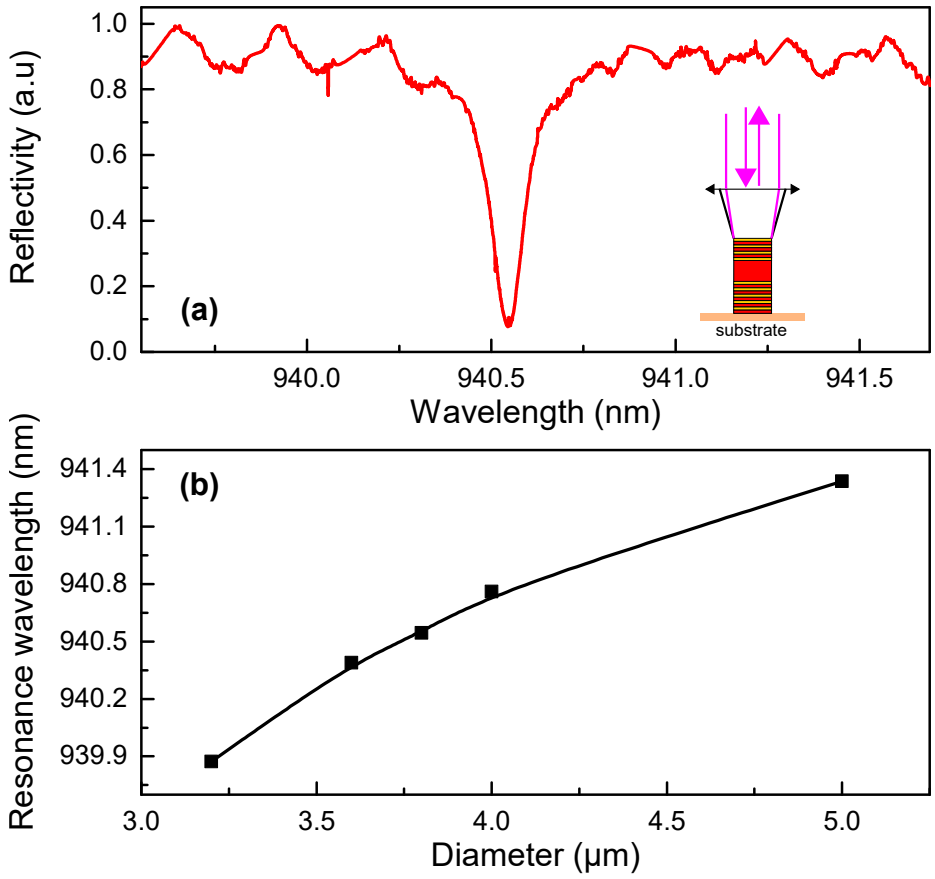

Figure 4.3 – **(a)**: Measured normalized reflectivity on a micropillar. The diameter of the resonator was 3.8 µm. The inset schematically shows the incident and reflected laser fields on the micropillar (violet lines). The incoming beam is focalized by a lens. In the micropillar diagram, the red regions indicate the GaAs rich layers, and the yellow ones the AlAs rich ones. The black lines schematically indicate the free space radiation pattern divergence of the fundamental optical mode. **(b)**: Measured evolution of the optical resonance wavelength as a function of the micropillar diameter. The black line is a guide to the eye connecting the measured resonance wavelengths.

In Panel (b) of Figure 4.3, we plot the evolution of the resonance wavelength for the fundamental optical mode as a function of radius. This curve experimentally shows the dependence predicted in Figure 4.2, that is, the resonance energy is blue-shifted when the radius is decreased. This is accompanied by a decrease in the optical quality factor. Indeed, when the radius is reduced, the intensity of the confined optical field increases at the lateral surfaces of the micropillar. The fabrication defects present on the sides will therefore induce optical losses [212].

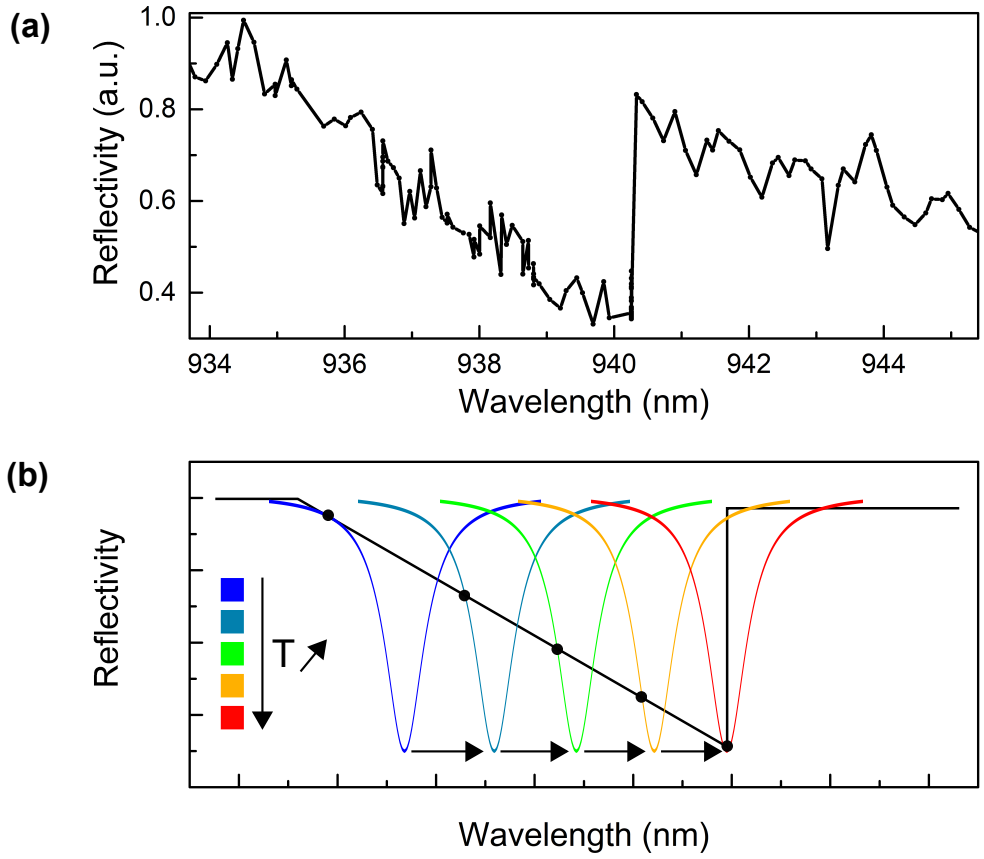

Figure 4.4 – **(a)**: Measured thermo-optic effect on a micropillar. The triangular shape of the reflectivity dip, associated to the micropillar optical resonance, is clearly visible. **(b)**: Schematic diagram of the thermo-optic effect on the optical resonance frequency of a micropillar. The color legend of the reflectivity curves indicates the red shift of the optical mode when the laser wavelength is progressively increased. The black triangular reflectivity dip indicates the observed shape of the probed reflectivity, as shown in Panel (a).

The reflectivity curve obtained on a micropillar can strongly depend on the intensity of the intracavity optical field [213]. In particular, at sufficiently high optical powers, light absorption induces heating inside the sample. This rise in temperature results in a change of the materials optical indices of refraction. Naturally, this will affect the resonance frequency of confined optical modes. This thermo-optic effect will induce a triangular shape of the reflectivity curve when the optical reflectivity is probed with a laser scanning towards the long wavelength direction. This is what we show in Panel (a) of Figure 4.4, where we plot the measured reflectivity curve on a micropillar with a radius of 3.2 µm. The power of the laser was ≈ 5 mW. The trian-

gular shape of the reflectivity curve is clearly visible. The width of the asymmetric reflectivity dip is much larger than the FWHM of the Lorentzian reflectivity obtained at low optical powers.

This effect can be understood by considering the following picture, described schematically in Figure 4.4.b [147]. The high power laser scans the optical resonance by moving towards long wavelengths. When light starts to couple in the cavity mode, shown by the blue low power reflectivity curve, an increase in the refractive indices occurs, due to the temperature rise of the resonator [147]. As a consequence, the optical resonance frequency of the micropillar is red-shifted. By spectrally moving the laser further towards low energies (black points in the figure), we couple an increasing quantity of optical power to the system, and the reflectivity curve is more and more red shifted. Eventually, we reach a point where maximal optical power is coupled to the resonator. In this case, the reflectivity curve cannot red shift anymore. An increase in the wavelength decreases the optical power coupled to the mode. The reflectivity curve abruptly blue shifts back to its initial position (blue curve), and the probed reflectivity is 100%. This gives the curve its triangular shape. Therefore, we can red-shift the resonance wavelength of the fundamental optical mode by sufficiently increasing the intracavity optical power in a micropillar, through this thermo-optic effect.

In this section, we have presented the optical characterization of micropillars through reflectivity experiments, evidencing the effects of light absorption on the resonance frequency of the micropillars. We will take advantage of this experimental method to characterize the optical properties of the studied resonators.

4.2 Confinement of light and acoustic phonons in micropillars

In this section, we present the structures that we have investigated by Raman scattering spectroscopy. We will also describe the set-up that we have implemented for probing anti-Stokes spectra.

4.2.1 Optical micropillars embedding acoustic resonators

The sample that we studied by Raman scattering spectroscopy in this chapter is fabricated from a planar topological nanocavity embedded between two optical DBRs. The localized acoustic state is confined at the interface between DBRs in different topological phases, as described in Section 3.3. For the first phononic DBR, the layer thicknesses are 9.3 nm for GaAs and 8.9 nm for AlAs. For the second mirror, the thicknesses are 8.0 nm for the GaAs and 10.7 nm for AlAs layers, respectively. Each acoustic DBR contains 16 layer pairs. The acoustic system plays the role of an effective 2λ spacer for an optical resonator, constituted by two $(\frac{\lambda}{4}, \frac{\lambda}{4})$ $Al_{0.95}Ga_{0.05}As$/ $Al_{0.10}Ga_{0.90}As$ DBRs. The optical mirror in contact with the substrate is made of 18 layer pairs. The top mirror contains only 14 layer pairs. For the optical mirrors, the layer thicknesses are 69.2 nm and 81.1 nm for the $Al_{0.10}Ga_{0.90}As$ and the $Al_{0.95}Ga_{0.05}As$ layers, respectively. The structure has been fabricated by MBE on a (001) substrate, with a thickness gradient, as for the samples described in the previous chapter. The

acoustic cavity is designed to confine a phononic mode at a nominal frequency of $\approx 300\,\mathrm{GHz}$.

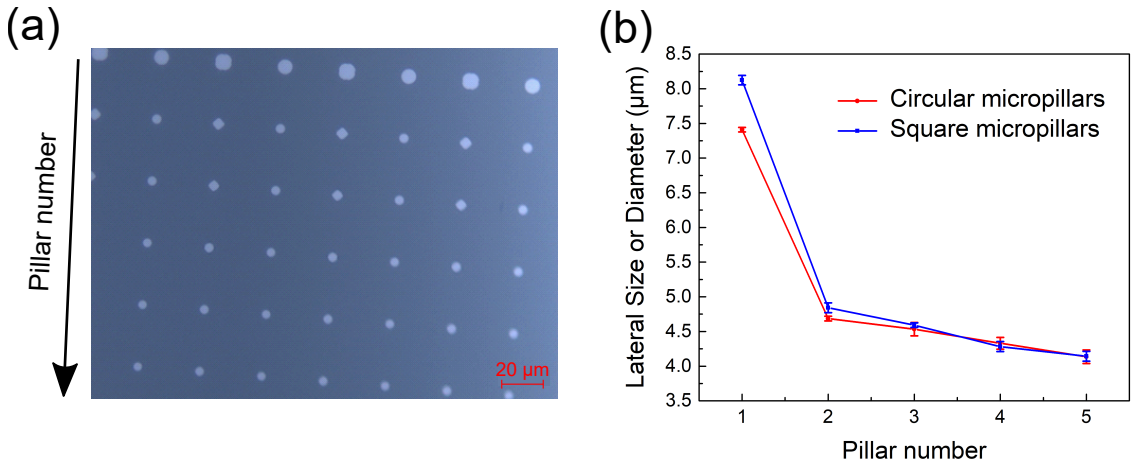

Figure 4.5 – **(a)**: Detailed view of the fabricated sample. The picture was taken with an optical microscope after the lift-off process (see Figure 4.6). The vertical rows of micropillars are clearly visible, with alternating square and circular resonators. When moving in the vertical direction, the lateral dimensions decrease. **(b)**: Evolution of the micropillar lateral dimensions, for both square (blue) and circular (red) resonators, obtained from the picture shown in Panel (a). The error bars indicate the spread in the measured lateral sizes.

From this planar structure micropillar resonators have been etched. This was carried out by Abdelmounaim Harouri and Isabelle Sagnes in the clean room facilities of the C2N/CNRS. The sample presents micropillars with square and circular sections, that are arranged in periodic arrays. Each array contains alternating rows of square and circular micropillars, with decreasing lateral sizes. This can be seen in Panel (a) of Figure 4.5, where we show a detailed view of one of these arrays. From this picture, we measured the average dimensions of the fabricated microresonators. The results are shown in Panel (b) of Figure 4.5.

The fabrication process is illustrated in Figure 4.6. The top part of the planar cavity was covered with a thin film of SiN_4. A positive photoresist was spin coated on the sample. An optical lithography was then carried out. The photoresist was exposed UV light through a patterned optical mask, which defined the lateral sizes and shapes of the micropillars. The photoresist was then developped (Panel (a) in Figure 4.6). A layer of Nickel was deposited on the photoresist (Panel (b)). After the lift-off of the remaining photoresist (Panel (c)), a dry etching was carried out, leaving only the areas that were protected by the Nickel hard mask (Panel (d)).

The lateral dimensions of the resonators are of few micrometers. The acoustic wavelengths in the GaAs and AlAs layers, for frequencies around 300 GHz, are in the range of few tens of nm. Hence, the lateral dimensions of the fabricated micropillars are much larger than the characteristic wavelength of the studied acoustic cavity. Therefore we will consider that the acoustic topological resonator embedded inside the micropillar acts as a planar structure.

Furthermore, the acoustic system behaves as an effective spacer inside the micropillars. Therefore, the micropillar presents a discrete set of optical resonances, as described in the previous section.

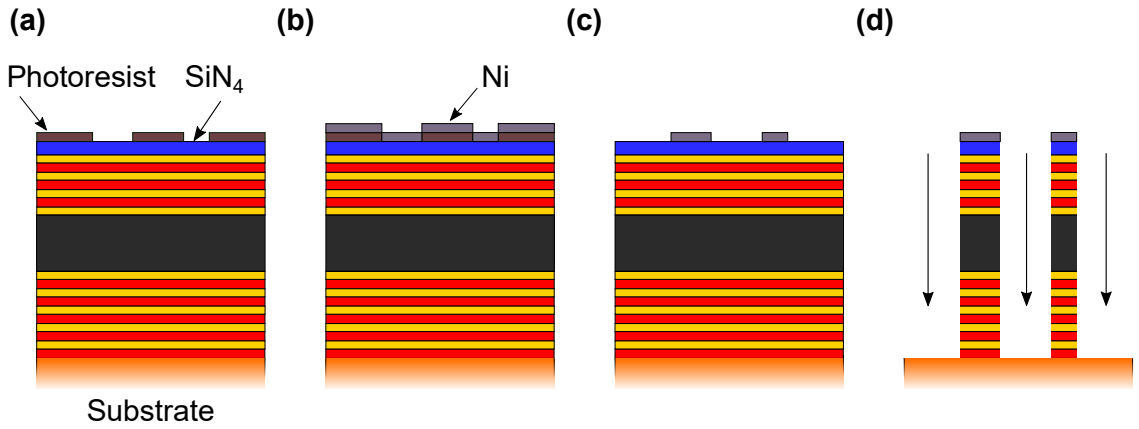

Figure 4.6 – Micropillar fabrication process from a planar cavity. The DBRs correspond to the optical mirrors. The black spacer is the acoustic resonator. **(a)**: Development of the spin-coated photoresist, after the exposition to UV light.**(b)**: Deposition of Ni metal film on the planar structure. **(c)**: Lift-off of the remaining photoresist.**(d)**: Dry etching of micropillars.

4.2.2 Optical probing of micropillars acoustic properties

In the previous section, we described the fabrication process of micropillars embedding an acoustic resonator. We present the experimental set-up that we implemented in order to perform Raman scattering measurements on these systems. The experiment is performed by measuring the anti-Stokes Raman spectra at normal incidence and at room temperature.

A micropillar does not have a continuum of optical modes as is the case for a planar optical cavity (see Section 2.2 in Chapter 2) that can be accessed by varying the incidence angle. Therefore, we chose to perform an experiment aiming to excite the micropillar and collect the Raman signals from the same fundamental optical mode, as illustrated in Figure 4.7. Both the incident and the scattered beams are normal to the surface of the micropillar, as schematically shown in the inset to Figure 4.7. In the case of the sample studied here, the optical mode enables the coupling of the input laser and the collection of the Raman signal shifted by 350 GHz from the laser line. Indeed, the optical quality factor of the planar cavity embedding the acoustic resonator (prior to the etching) is of the order of 1000, corresponding to a FWHM of $\approx$ 350 GHz. The optical quality factor of a micropillar is usually lower than the one of the corresponding optical planar cavity [208, 212]. Therefore, it is possible to simultaneously couple the laser and probe the Raman response through the same mode. Notice however that the micropillars studied here have a rather large lateral dimension. For example, most of the results presented in the next section have been obtained on micropillars having a lateral size of $\approx 8\,\mu$m. According to the plot in Panel (a) of Figure 4.2, the resonance energies of higher order modes are shifted from the one of the fundamental mode by ≈ 1 meV. This corresponds to a frequency shift of $\approx$ 250 GHz. Therefore, the anti-Stokes Raman signal can in principle couple to higher order optical modes. Nevertheless, we will consider this simplified picture where the incident laser and Raman scattered signals couple through the same optical mode.

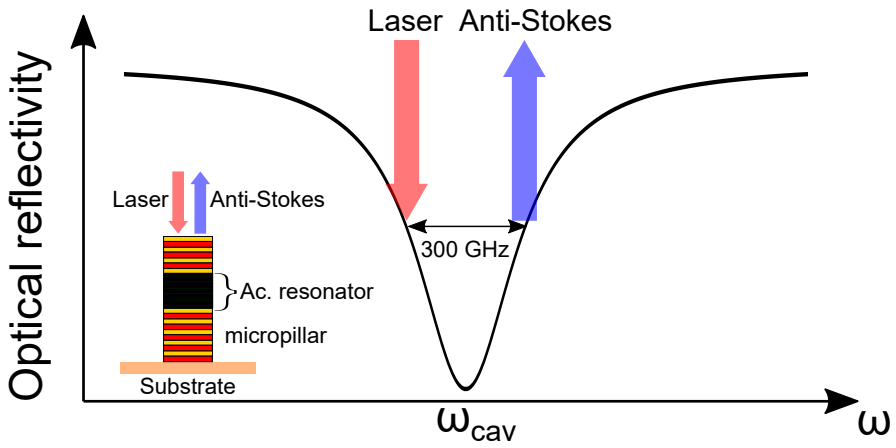

Figure 4.7 – Principle of Raman scattering measurement through the fundamental optical mode of the micropillar. The incident laser and the anti-Stokes signals both couple to the fundamental optical mode. ω_{cav} indicates the optical resonance frequency of the optical mode. The inset to the figure shows a schematic representation of the incident laser beam and the collected Raman signals. The micropillar structure is schematically shown in the inset.

The schematic diagram of the experimental set-up is shown in Figure 4.8. The incident laser is represented by a red beam. We used a tunable CW NIR Ti:Sapph laser (SolsTiS M-Squared). The laser is connected to a wavelength meter (W5-5 HighFinesse GmbH), as before (see Figure 3.1, in Section 3.1), which is not shown here for clarity. The laser beam is focalized on the sample with a lens of focal length 11 mm. With the collimated incident laser beam size, we estimated that the light spot on the sample has a diameter of $\approx 15\,\mu$m, which is larger than the diameter of the measured micropillars. Therefore, the coupling of the laser beam to the optical modes of the studied resonators will be not optimal. The scattered light and the reflected laser beam are then collimated by the same lens and focalized into the double spectrometer for measuring the anti-Stokes spectra.

The sample is kept in a cryostat, in order to avoid any oxidation of the AlAs rich layers contained in the micropillars. The cryostat is fixed on an X-Y translation stage (Newport M-406) that allows to position the laser spot on the micropillars with a resolution lower than 100 nm. This alignment is also carried out using the imaging system represented in the bottom right of Figure 4.8. The represented beam splitter can be slided on the path of the reflected beam in order to image the sample surface.

The experiment has been designed so that it can be also used to perform reflectivity measurements. In this case, the intensity of the input laser is measured with a photodetector. A mirror, represented by a dashed line in Figure 4.8, is added in order to measure the intensity of the reflected laser with another photodetector. We then plot the reflected light intensity from the micropillar (normalized by the incident laser power) as a function of wavelength. The latter is measured with the wavelength meter.

As explained in the previous chapter (Section 3.1), filtering the stray light coming from the excitation laser is essential for performing Raman scattering measurements. A major source of stray light in this configuration is the reflection of the laser on the micropillar. In the previous experiments on planar cavities, the direct reflection was

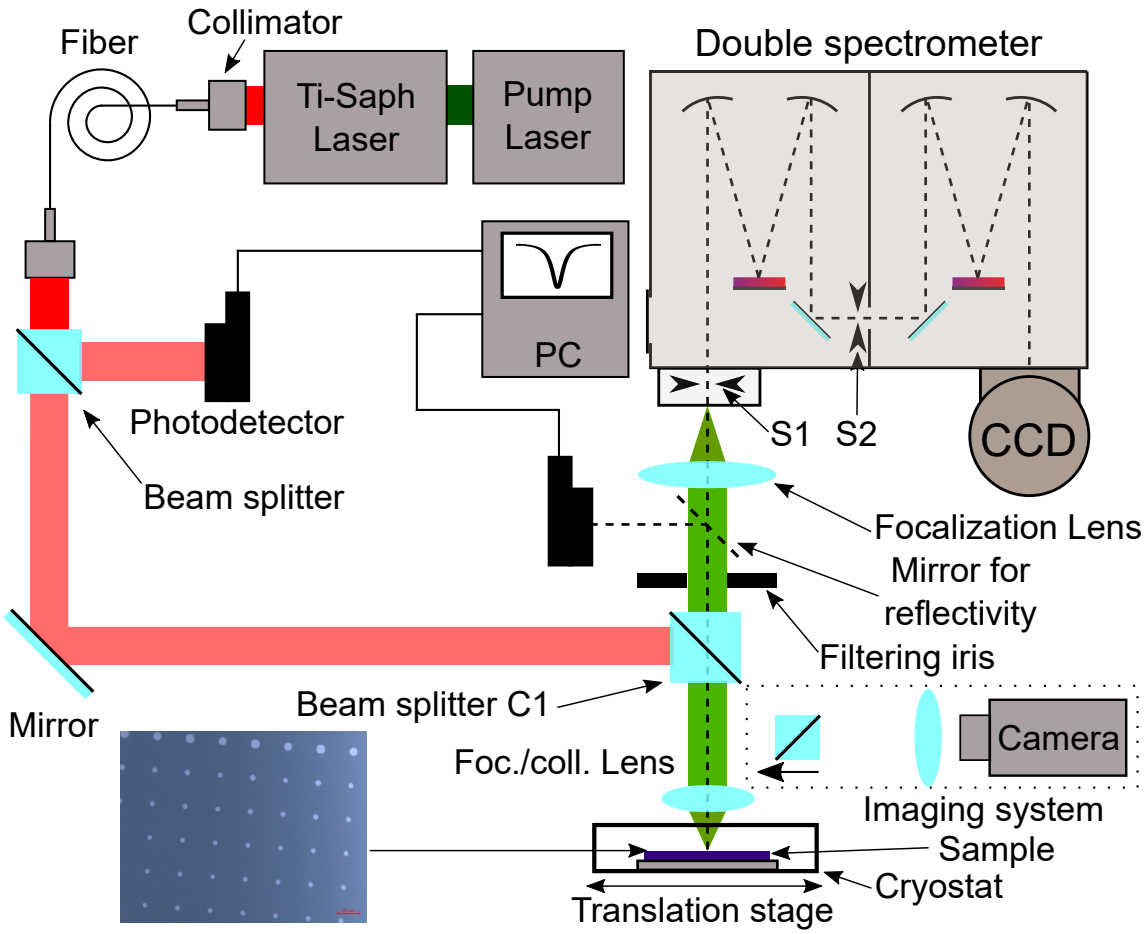

Figure 4.8 – Raman scattering experiment diagram at normal incidence on micropillars. The excitation beam is represented in red. The focalization of the incident laser and the collection of the scattered light occur through the same lens. The superposition of inelastically scattered light and reflected laser light is represented in green. The dashed line in the spectrometer represents the path of the light on the gratings and the mirrors. Under real experimental conditions, the highlighted iris is closed in order to spatially filter out part of the stray light induced by the laser. The sample is inside a vacuum chamber. The Figure shows a picture of an array of micropillars, obtained with an optical microscope. The set-up can also be used to perform reflectivity measurements. In this case a mirror, represented by a dashed line, is added to collect the reflected laser light from the sample.

spatially filtered by taking advantage of the small incidence angle (see Figure 3.1, in Section 3.1). This strategy cannot be implemented in the current experimental configuration, since in this case both the reflected laser beam and the Raman signals propagate in normal direction with respect to the micropillar surface.

The reflected laser beam intensity does not present a constant spatial profile. In Figure 4.9.a, we show the image of the reflected laser spot, recorded with an infrared camera that was positioned behind the beam splitter where the filtering iris is represented in Figure 4.8. In the real experiment, this corresponds to a distance of $\approx 1.5\,\mathrm{m}$ from the sample. We observe that the intensity of the reflected laser spot is maximal in circular rings. The black lines schematically indicate the regions where the laser intensity is minimal. This shape is visible only when the laser spot is positioned on top of a micropillar. We therefore interpret it as a diffraction pattern, originating from the fact that the laser spot at the surface of the sample is larger than the size of the micropillar, similar to an Airy pattern obtained for a circular aperture.

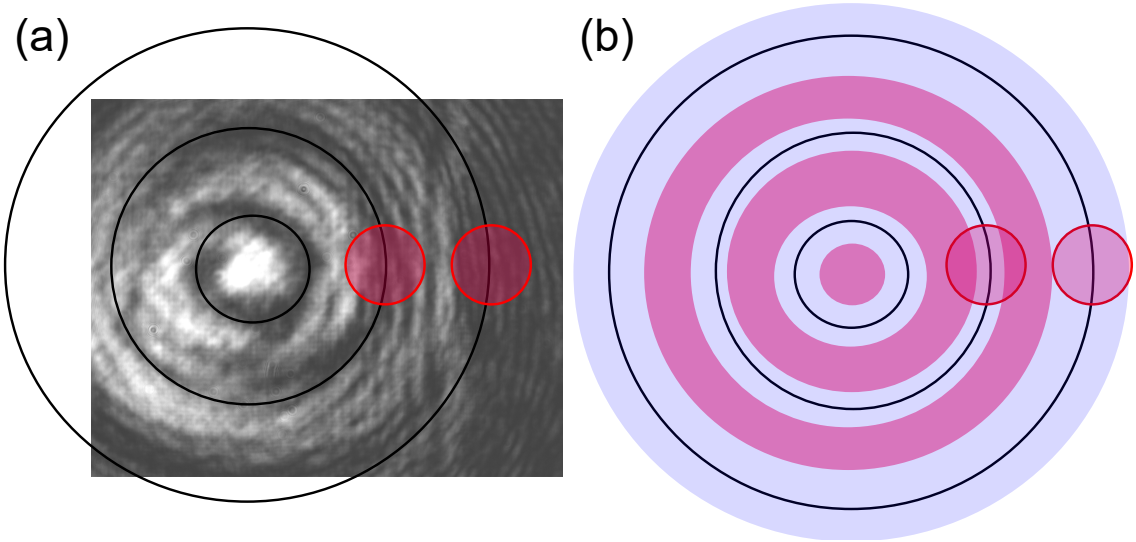

Figure 4.9 – **(a)**: Recorded image of the reflected spot on a micropillar. The image dimensions are 6.656×5.325 mm. The black circles highlight the minima observed in the reflected spot. The red circles mark spatial areas selected by the filtering iris, for which Raman spectra have been successfully probed. **(b)**: Schematic diagram showing the distribution of the diffracted laser (pink) and Raman (blue) fields for the light spot shown in Panel (a). The optical mode containing the Raman signals should have a Gaussian spatial profile, but we represented it uniformly for simplicity. The red circles indicate the same positions as in the recorded image.

In contrast, the Raman signals couple to the free space from the micropillar. We suppose that they do not couple to the micropillar higher order modes. In this case, the Raman scattering signals propagates in the free space with a Gaussian-like spatial profile, given by the fundamental optical mode of the micropillar. The radial modulation observed in Figure 4.9.a is not present for the Raman signals. We schematically represented these considerations in Figure 4.9.b. Therefore, in order to maximally suppress the light coming from the reflected laser, we use a filtering iris on the collection path of the experiment, schematically represented in Figure 4.8. The iris is mounted on translation stages so that it can be precisely positioned on the optical path. By closing it, we can select different parts of the spot that we probe

with the spectrometer. By choosing spatial regions where the diffracted laser light is minimal, we are able to measure Raman spectra on the micropillars. For example, in Panel (a), we have represented two red circles indicating two selected positions of the iris for which we were successfully able to probe the Raman response of the microstructure for this laser spot. The red circles are reproduced in Panel (b) for clarity. By placing the iris between the two red circles, the Raman spectra are no visible, since they are completely covered by the laser stray light.

The experimental set-up presented in this section allowed us to measure Raman scattering spectra of an topological acoustic nanocavity embedded in a micropillar. In the next section, we will describe the results obtained on these systems.

4.3 Raman scattering in micropillars

As explained in the previous section, in these experiments the incident laser and the scattered Raman signals couple to the discrete set of optical modes of the micropillar. Measuring the reflectivity curve of the studied structure is therefore essential to identify the resonance wavelengths of the modes. In Figure 4.10, we show an example obtained on a square micropillar with $\approx 8\,\mu m$ sides. The latter has the biggest lateral size found in one array row, as shown on the right side of Figure 4.10. We see a Lorentzian dip in the optical stop band, associated to the fundamental optical mode. The resonance wavelength is $\approx 892.3\,nm$. The laser spot is larger than the size of the micropillar. Therefore, the mode matching of the incident field with the confined optical mode is not optimized. As a consequence, the contrast of the reflectivity dip is 65%, which is lower than the value measured for the reflectivity curve shown in Figure 4.3.a.

In Figure 4.11.a we show the measured Raman spectrum on a square micropillar. The latter also has a lateral size of $\approx 8\,\mu m$, but the optical resonance wavelength of the fundamental mode is at 911.6 nm. The measured Raman spectrum was obtained by setting the incident laser wavelength at resonance with the optical mode, with an input power of $\approx 15\,mW$ measured just before the beam splitter C_1 in Figure 4.8. The Raman curve is normalized by the laser power and by the integration time. The negative frequency shift indicates that this plot corresponds to an anti-Stokes spectrum. Three distinct Raman peaks are visible.

In Figure 4.11.b we plot the Raman spectrum obtained on the corresponding planar topological structure. This spectrum was obtained on an area of the sample which has not been etched during the fabrication process. The wavelength of the laser is the same as for the spectrum in Panel (a). Numerical simulations based on the photoelastic model for the one-dimensional structure show that the main Raman peak is associated to the confined acoustic mode (not represented here). Its spectral position matches the nominal resonance frequency of the acoustic mode ($\approx 300\,GHz$, that is $\approx 1.2\,meV$).

All the features of the spectrum probed on the planar structure are also visible in the one obtained on the square micropillar, in which the acoustic structure behaves as a planar phononic resonator. In particular, the Raman peak associated to the confined mode is visible in the measurement performed on the microstructure. This result shows that it is possible to probe the confined acoustic mode on these three-dimensional optical resonators.

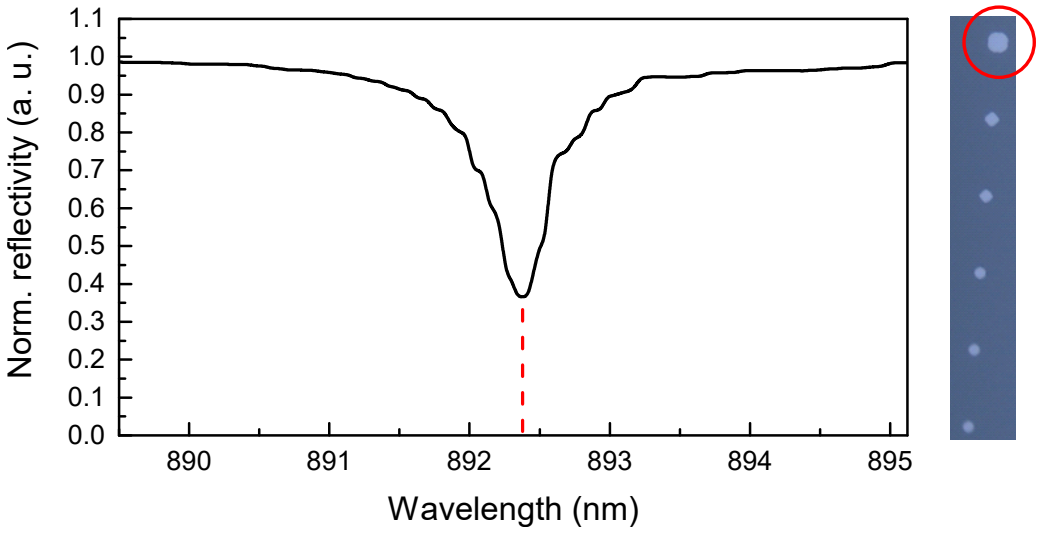

Figure 4.10 – Reflectivity curve obtained on a square micropillar of ≈ 8 µm side. On the right part of the figure, the red circle indicates a micropillar having this lateral dimension in the sample picture shown in Figure 4.5. The dashed red line marks the resonance wavelength of the micropillar. The power of the incident laser is 3 mW.

The obtained spectra are very similar, and no particular feature associated to three-dimensional confinement of the optical mode is visible. We could expect that [113, 214], since the spatial profile of the three-dimensionally confined optical mode in a micropillar presents more Fourier components than the one-dimensional confined field in a planar structure. The localized mode can be seen as a superposition of several plane waves with k vectors oriented in different directions. This could render more mechanical modes Raman active. The confinement effects of light might become more apparent by decreasing the dimensions of the system, since the experimental results presented in Figure 4.11.a have been obtained on a micropillar with a rather large lateral size.

The second measurement that we performed consisted in studying the evolution of the Raman spectra intensity when probing different circular micropillars with the same lateral size (7.5 µm diameter). As explained before, the resonance frequency of the confined optical mode depends on the position on the surface of the sample, since the latter was grown with a thickness gradient. The characterized microresonators in this experiment are evenly spaced. The measurement was carried out for micropillars presenting resonance wavelength around 892 nm. The Raman scattering results are represented as a color map in Panel (a) of Figure 4.12. In total, 12 circular micropillars were studied.

The corresponding reflectivity curves were also measured. They are plotted as a color map in Figure 4.12.b. Each pillar was labeled by a number, as indicated by the vertical coordinates of the two panels. Notice however that the reflectivity characterization was carried out only for one out of two micropillars. The contrast for the reflectivity curves is around 60%.

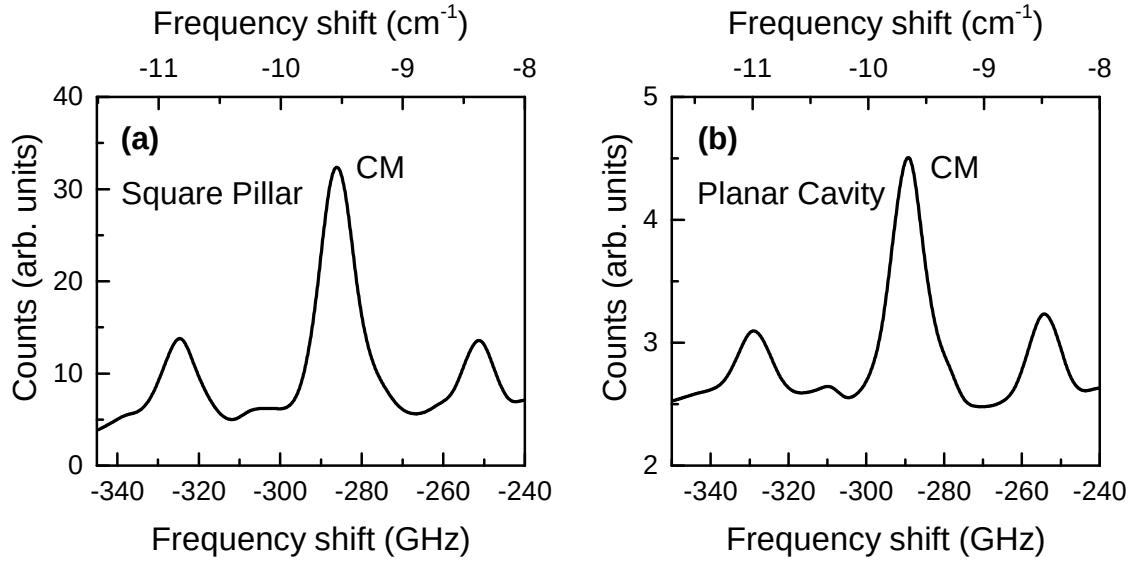

Figure 4.11 – Raman scattering spectra probed on a square micropillar (Panel **(a)**) and on the planar acoustic resonator (Panel **(b)**). The label CM indicates the Raman peak associated to the confined acoustic mode in the topological structure.

The blue regions in Panel (b) correspond to the reflectivity dips associated to the confined optical modes. The dashed red line is a guide to the eye showing the evolution of the resonance wavelength. By moving on the surface of the sample, the resonance wavelength evolves approximately linearly.

The black line in Panel (b) indicates the spectral position of the laser line used for all the Raman scattering measurements, corresponding to an optical wavelength of 892.4 nm. Its power was kept constant for all the probed Raman spectra (≈ 5.7 mW). The vertical blue line indicates the spectral position of the Raman peak associated to the confined mode.

Panel (c) shows the Raman spectrum measured on the eighth micropillar (indicated by the horizontal green line in Panel (a)). In the spectra, we show only two of the three Raman peaks visible in Figure 4.11. This is due to the fact that in this measurement the stray light was very intense at the frequency shifts where the third Raman peak is located. The right Raman peak shown here corresponds to the one generated by the confined acoustic state.

We compare the evolution of the reflectivity curve and of the Raman spectrum as a function of pillar number. We observe that, when the fundamental optical mode is spectrally located far from both the excitation laser line and the Raman signals, the intensity of the Raman peaks is weak. This can be seen for example for the first micropillar (on the bottom of both plots). We observe that by progressively approaching the cavity mode resonance wavelength to the laser line and to the Raman signals (Panel (b)), the intensity of the Raman signals progressively increases. It reaches a maximum for the micropillar where the laser line is resonant with the fundamental confined optical mode and where the Raman signals can couple, too. This is indicated by the green horizontal lines in both panels. This clearly demonstrates the strong dependence of the measured Raman intensities on the detuning of

the fundamental optical mode wavelength with respect to the laser line and to the probed Raman signals.

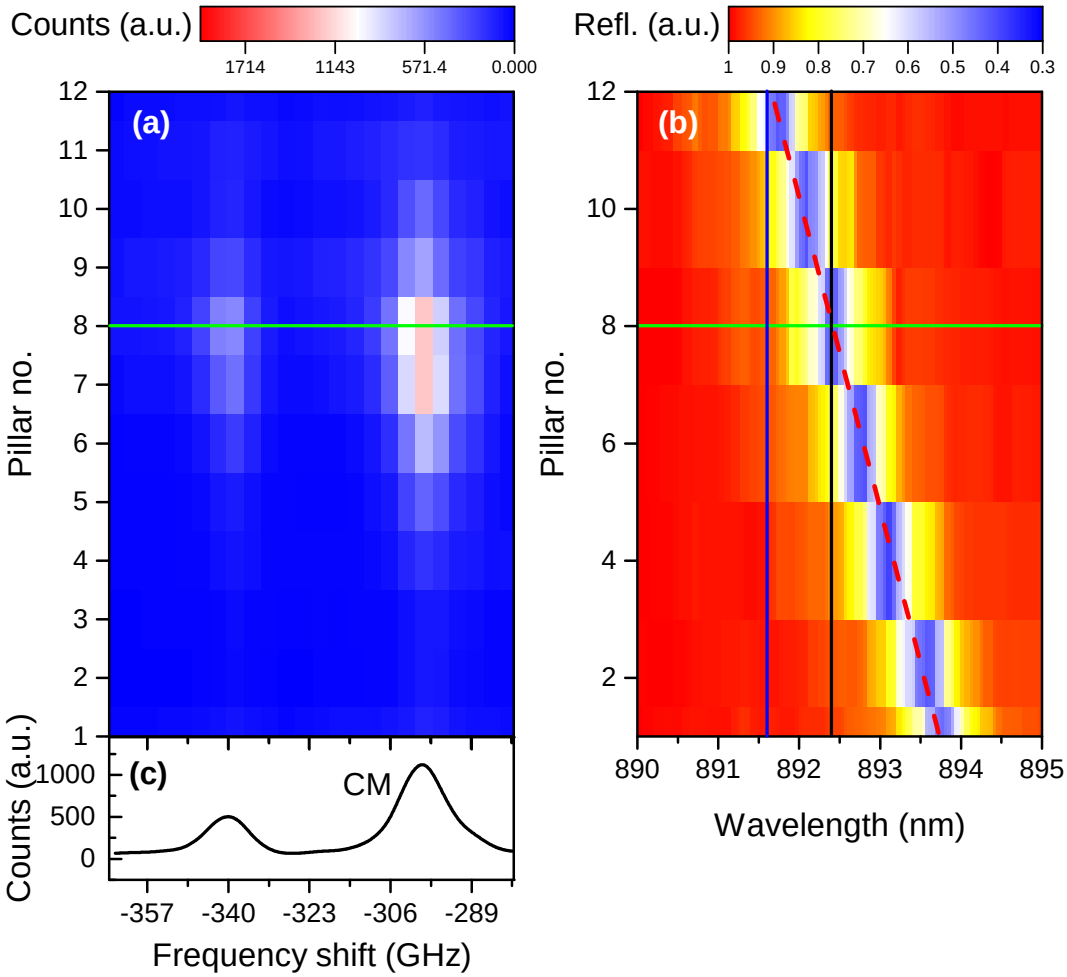

Figure 4.12 – **(a)**: Color map showing the evolution of the Raman spectra as a function of pillar number (see main text).**(b)**: Color map of the measured reflectivity curves as a function of pillar number. By moving on the surface of the sample, we change the optical resonance frequency. The vertical black line shows the spectral position of the laser. The blue line shows the position of the Raman signals shifted by a frequency of $\approx 300\,\mathrm{GHz}$. The horizontal green line in both plots indicates the micropillar for which we measured maximal Raman intensities. The diagonal dashed red line is a guide to the eye showing the evolution of the mode resonance wavelength. **(c)**: measured Raman spectrum on pillar 8. The label CM indicates the Raman peak associated to the confined acoustic mode.

In Section 4.1.2 of this chapter, we have seen that the optical resonance wavelengths of micropillars can be red-shifted by increasing the temperature of the micropillar. This can be carried out by increasing the intracavity optical power. According to the results shown in Figure 4.12 this effect will have an impact on the intensity of the Raman signals.

We have probed Raman spectra when the excitation laser is blue detuned with respect to the fundamental mode, as represented in the left inset to Figure 4.13. The measurement was carried out on a square micropillar with a lateral size of $4.5\,\mu\mathrm{m}$. A

typical measurement is shown in the right panel of Figure 4.13, where the cavity mode Raman peak is highlighted in grey. We then progressively increased the intensity of the incident laser. For each optical power, we measured the intensity of the Raman signal. This was carried out by finding the area under the Raman peak associated to the confined acoustic mode. This value was normalized by the incident optical power. The result is shown with the blue circles in Figure 4.13. We observe that when we increase the power of the incident laser, the normalized Raman intensity decreases. By way of comparison, we performed the same experiment on the planar cavity. In this case, the intensity of the Raman signals increases linearly, as expected from a spontaneous Raman scattering process [105]. Therefore, the normalized Raman intensity probed on the planar structure is almost constant with incident power (blue crosses).

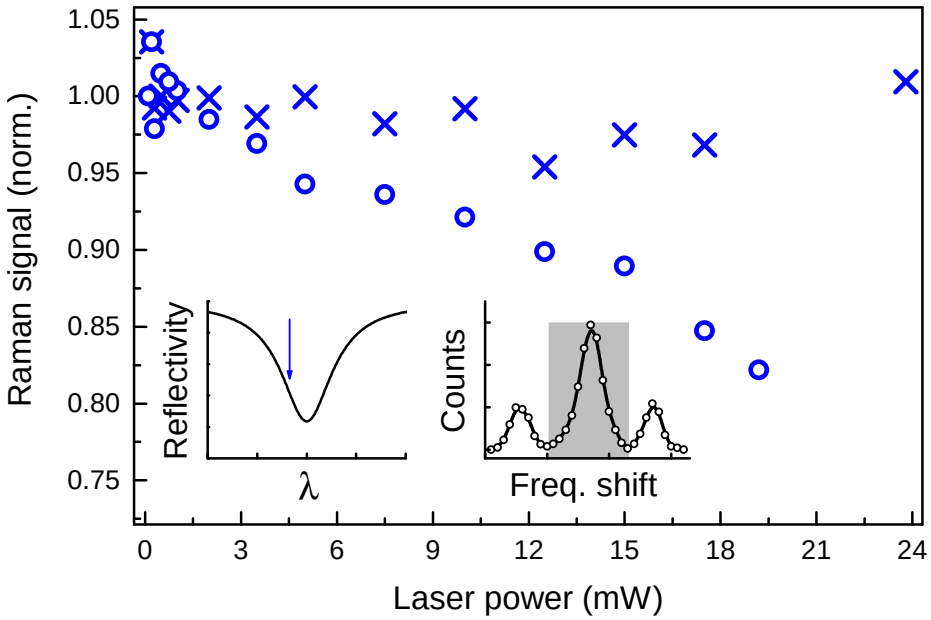

Figure 4.13 – Evolution of the Raman intensities on a planar cavity and on a micropillar as a function of incident power. The crosses indicate the normalized Raman intensities measured on the planar cavity. The circles shown the same measurement, but performed on a micropillar. The laser was set blue-detuned from the optical resonance, as indicated in the left inset to the figure. The right inset shows a typical Raman spectrum, where the Raman peak associated to the confined mode is highlighted.

We interpret this result by considering that for both the micropillar and the planar cavity, the increase of the laser power is accompanied by an increase of the optical intracavity power. This induces a heating of the sample through light absorption. However, in the planar system, the structure is large and heat can be dissipated more easily than in the case of a micropillar. Therefore, the temperature inside the three-dimensional resonator increases more than in the case of the planar cavity, due to its finite lateral dimensions. As explained in the previous section, in this case the

resonance wavelength of the optical mode red-shifts when the power of the laser is increased. In contrast with the case of the planar cavity, the coupling of the fundamental mode to the involved optical fields decreases, leading to an overall decrease in the intensity of the probed Raman signals. This constitutes a first experimental result where the behavior of these three-dimensional optical resonators is distinct with respect to their planar counterpart.

4.4 Conclusion

In this section, we have presented first Raman scattering experimental results obtained on nanophononic cavities embedded in micropillars. We first presented theoretical and numerical models that describe the three-dimensional confinement of light in these systems. After having recalled the fabrication process of these structures, we presented the experimental set-up that allowed us to perform Raman scattering measurements in an anti-Stokes configuration.

These first experimental results allowed to demonstrate that it is possible to probe the acoustic properties of the nanophononic resonator embedded in the micropillar through Raman scattering spectroscopy. This constituted a technical challenge, since in the experimental configuration of the set-up, the reflected laser and the Raman signals present a strong spatial overlap. Filtering the stray-light is therefore more difficult here than in the case of the planar optical structures.

We then performed experimental measurements where we have varied the coupling of the cavity mode with the laser line and the Raman signals. We have seen that by changing this coupling, we induce strong variations in the intensities of the Raman peaks. We then performed a Raman scattering measurement where we have varied the intensity of the incident laser in order to increase the temperature inside the resonator. This leads to a decrease of the Raman scattering intensities normalized by the incident power, caused by the red-shifting of the cavity mode. This behavior has not been observed on the planar structure, since heat is dissipated more efficiently in this case. This constitutes a first experimental result where the three dimensional shape of the micropillar induces a different behavior than its planar counterpart.

The confinement of light in micropillars has not lead for the moment to the observation of a distinct behavior in the Raman activity of the mechanical modes inside the topological structure. However, an effect of the three dimensional localization of light might be visible if the lateral dimensions of the micropillars are sufficiently decreased. Furthermore, by making the micropillar lateral dimensions comparable to the periodicity of the acoustic resonator, we can expect to observe the effects of a three-dimensional confinement of the mechanical modes. In particular, this can be done by decreasing the resonance frequency of the confined acoustic mode. This is what we carry out in the next chapter, where we numerically investigate the interactions between light and three-dimensionally confined mechanical modes at 20 GHz.

Chapter 5

Micropillars as optomechanical resonators

Layered planar systems have demonstrated to be powerful platforms for controlling the propagation of waves, both in optics and in nanophononics. Furthermore, these periodic media enable the simultaneous localization of light and mechanical vibrations in the same structure.

Throughout this manuscript, we have seen that by enclosing an acoustic cavity between two optical DBRs, we can realize a system that confines NIR photons and sub-THz acoustic phonons. As long as the periodicity of the acoustic system is small with respect to the optical wavelength, the acoustic nanocavity plays the role of an effective optical spacer. If the overall length L_{tot} of the acoustic cavity matches the optical resonance condition for an optical Fabry-Perot cavity ($L_{tot} = p\lambda/2$, with p an integer), the confined acoustic mode interacts with an enhanced optical field. This was the case for the experiments carried out on the adiabatic and topological nanocavities, as presented in Chapter 3, in order to facilitate the characterization of the acoustic resonators through Raman scattering spectroscopy.

In the systems presented above, it is clear that the confined phononic modes' properties are solely determined by the design of the acoustic resonator, since the optical mirrors do not play any role in its localization. In other words, these systems can be considered as being constituted by an acoustic resonator embedded inside an optical cavity. Therefore, the acoustic properties of the phononic cavity such as its resonance frequency or its quality factor can be tuned, to a certain extent, independently from the optical parameters.

Further investigations on the optical and mechanical properties of GaAs/AlAs layered systems demonstrated that it is possible to design cavities in such a way that an optical and a mechanical mode are *simultaneously* confined by the same structure. In particular, it was shown that a GaAs/AlAs planar optical microcavity optimized to confine a mode in the NIR range is automatically optimized to localize an acoustic mode at a frequencies of $\approx 20\,\mathrm{GHz}$ [56]. This is due to the intrinsic properties of the used semiconductor materials.

As for the topological cavity embedded in an optical one, it is possible to fabricate micropillar resonators out of these planar systems. Notice however that, in contrast to the results presented in Chapter 4, we will have to consider here both the three-dimensional localization of an optical and a mechanical mode inside the micropillar.

The simultaneous three-dimensional confinement of light and sound in these systems is particularly relevant in cavity optomechanics. Indeed, this could lead to the development of three-dimensional optomechanical resonators operating at very high mechanical frequencies. Their optomechanical properties could be investigated through Brownian motion experiments, and their mechanical motion could be manipulated through optical forces, as presented in Chapter 2 (see Section 2.4). Finally, these structures enable the integration of other systems such as quantum wells or quantum dots. This would enable the possibility to explore the interactions of an electronic excitation with an optical mode and a mechanical mode that are simultaneously confined.

As we have seen in Chapter 4, the optical behavior of micropillars has been extensively studied in the context of photonics and optoelectronics. In this Chapter we investigate the mechanical and optomechanical properties of DBR-based GaAs/AlAs micropillars by perfoming numerical simulations. The Chapter is organized as follows:

- In Section 5.1 we will first recall the experimental results that have shown the simultaneous confinement of light and mechanical vibrations in one-dimensional optical microcavities. We will then describe the measurements, obtained through pump-probe coherent phonon generation and detection, that have evidenced the optomechanical properties of micropillars.
- In Section 5.2, we will compare the optical and mechanical properties of GaAs/AlAs micropillars through numerical simulations.
- In Section 5.3 we will provide an explanation of the confinement mechanisms in a micropillar. In particular, we will compare this system to a simplified resonator, made of a single GaAs cylinder.
- In Section 5.4 we will investigate the main mechanical and optomechanical parameters of micropillars through finite element simulations. We will relate their dependence as a function of design parameters to the confinement mechanisms described in the previous section.
- Finally, we will conclude by summarizing the main results described in this Chapter.

5.1 Towards three-dimensional confinement

The three-dimensional optomechanical confinement in micropillar structures was first envisioned through theoretical considerations and experimental results obtained on planar systems. In this section we present the main mechanisms leading to the simultaneous confinement of an optical and a mechanical mode in one dimension. We then discuss the experimental results demonstrating acoustic confinement in three dimensions observed in micropillars resonators.

5.1.1 Simultaneous confinement of light and sound in planar cavities

The comparison between the intrinsic optical and mechanical properties of GaAs and AlAs allows to rethink the simultaneous confinement of photons and phonons in

planar Fabry-Perot designs [56]. We consider for example an optical cavity, designed to confine an optical mode at a frequency f_0^{opt}, constituted by two $(\frac{\lambda}{4}, \frac{\lambda}{4})$ DBRs enclosing a GaAs $\frac{\lambda}{2}$ spacer. It has been evidenced that this structure also confines a mechanical mode due to two peculiar properties of the GaAs/AlAs material combination. Two "coincidences" in the mechanical and optical parameters lead to this simultaneous localization. The first one is the fact that:

$$\frac{c_{AlAs}}{c_{GaAs}} \approx \frac{v_{AlAs}}{v_{GaAs}} \approx 1.2 \tag{5.1}$$

where c_{AlAs} and c_{GaAs} are the speeds of light, whereas v_{AlAs} and v_{GaAs} are the speed of longitudinal acoustic phonons in the two materials. Let us now consider the longitudinal mechanical mode with a frequency $f_0^{ac} = f_0^{opt} \times \frac{v_{GaAs}}{c_{GaAs}}$ in the structure described above. In the GaAs layers, this mode has the same wavelength as the confined optical mode. Furthermore, due to Equation 5.1, the mechanical mode also has the same wavelength as the confined optical mode in the AlAs layers. Therefore, the two optical mirrors designed to operate as $(\frac{\lambda}{4}, \frac{\lambda}{4})$ DBRs at an optical resonance frequency f_0^{opt} also behave as $(\frac{\lambda}{4}, \frac{\lambda}{4})$ acoustic DBRs for an acoustic wave with a frequency f_0^{ac}. Additionally, the GaAs spacer can also be considered as a $\frac{\lambda}{2}$ layer for the considered mechanical mode. Consequently, the presented optical cavity is automatically optimized to operate as an acoustic Fabry-Perot cavity.

In Figure 5.1 we show the simulated optical and mechanical behavior of such a system, each dielectric mirror being constituted by 18 layer pairs. As illustrated in Figure 5.1.a, the structure confines an optical mode at $f_0^{opt} = 326\,\text{THz}$ (corresponding to a wavelength of $\approx 920\,\text{nm}$). By computing the acoustic reflectivity, we find that the system also localizes a mechanical mode at a resonance frequency $f_0^{ac} \approx 18.3\,\text{GHz}$. This is evidenced by the dip in the stop band in Figure 5.1.b.

The second "coincidence" corresponds to the fact that:

$$Z_{opt} \approx Z_{ac} \approx 0.83 \tag{5.2}$$

where Z_{opt} and Z_{ac} are the optical and acoustic impedance contrasts, respectively. Z_{opt} is defined as $\frac{n_{AlAs}}{n_{GaAs}}$, where n_{AlAs} and n_{GaAs} are the optical indices of refraction in the respective materials. Z_{ac} is defined as $\frac{\rho_{AlAs} v_{AlAs}}{\rho_{GaAs} v_{GaAs}}$, with ρ and v the densities and the speeds of acoustic longitudinal phonons. As already mentioned in Chapter 1 (see Section 1.3), the reflectivity of a DBR is given by $R \approx 1 - 4Z^{2N}$, where Z is the acoustic or optical impedance contrast of the two materials, and N is the number of GaAs/AlAs layer pairs in the structure. Due to Equation 5.2, the optical reflectivity of the DBRs is equal to their acoustic reflectivity. Therefore, the confined mechanical and optical modes decay in the same way in the mirrors. This is shown in Figure 5.1.c. Therefore, a standard GaAs/AlAs Fabry-Perot resonator not only simultaneously confines an optical mode and a mechanical mode, but also their spatial profiles overlap perfectly. This will lead to strong optomechanical interactions between the two fields.

Notice that this "double coincidence" associated to the GaAs/AlAs material combination is not only limited to Fabry-Perot systems. A planar acoustic cavity that is resonant at 20 GHz and that is based on another design (e.g. the adiabatic or topological cavities, presented in Chapter 3) would also optically confine a photonic mode in the NIR. The simultaneous localization of light and sound in these systems is therefore more general than the Fabry-Perot structure presented here, and paves the way toward the design of other optomechanical systems.

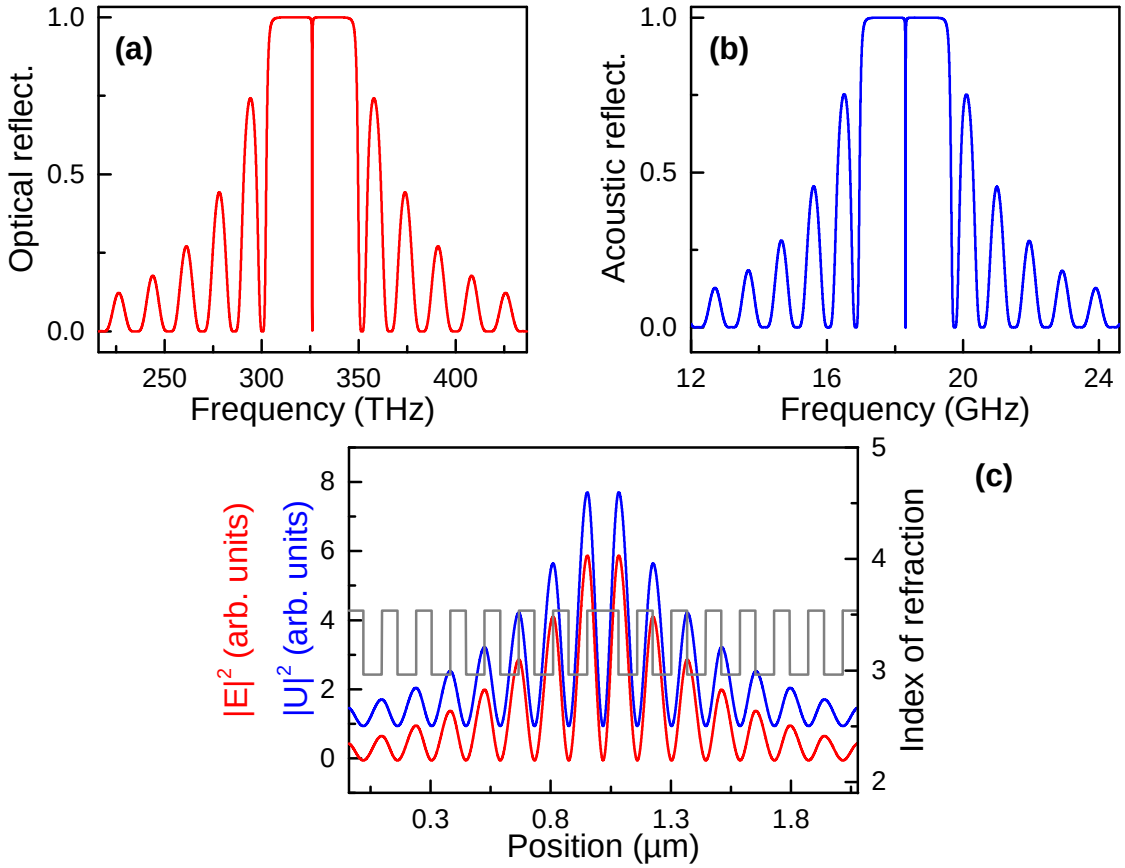

Figure 5.1 – **(a)**: Simulated optical reflectivity curve of a planar GaAs/AlAs Fabry-Perot cavity. The sharp dip in the stop band shows the confinement of an acoustic mode at a frequency of 18.3 GHz. **(b)**: Simulated acoustic reflectivity of the same cavity. The dip in the stop band corresponds to the confinement of an optical mode at a frequency of 326 THz, i.e. a wavelength of $\approx$ 920 nm. **(c)**: Spatial profiles of the confined optical (red curve) and mechanical (blue curve) modes in the considered structure. The profile of the acoustic mode has been translated vertically for clarity. The grey curve shows the dependence of the indices of refraction as a function of position in the cavity.

Putting in evidence the acoustic confinement properties of a planar optical cavity operating in the NIR range is technically difficult by Raman scattering spectroscopy. Indeed, a Raman peak located at a frequency shift of 20 GHz from the laser line is difficult to resolve. Furthermore, stray-light rejection in this frequency shift range also becomes a major challenge. Nevertheless, these experiments have been successfully carried out by implementing spectral filtering techniques to improve the resolution of the set-up and the stray light rejection [215, 216].

Coherent pump-probe phonon generation and detection have demonstrated to be an efficient way to experimentally demonstrate the acoustic confinement properties of planar systems, not only for its fundamental confined mode at a resonance frequency of ≈ 20 GHz, but also for higher order harmonics [56]. A brief presentation of this technique has been carried out in Section 2.3 of Chapter 2. Through this method, it was possible to follow the dynamics of the coherently generated acoustic phonons and to provide first values of the coupling strength between the confined optical and mechanical modes. It was shown that this interaction was essentially mediated through strong photoelastic effects at the considered wavelength (≈ 870 nm). It was expressed as an optomechanical coupling factor $g_{om} = 83\,\mathrm{Trad\,nm^{-1}}$, at the reduction point where the displacement is maximal [56].

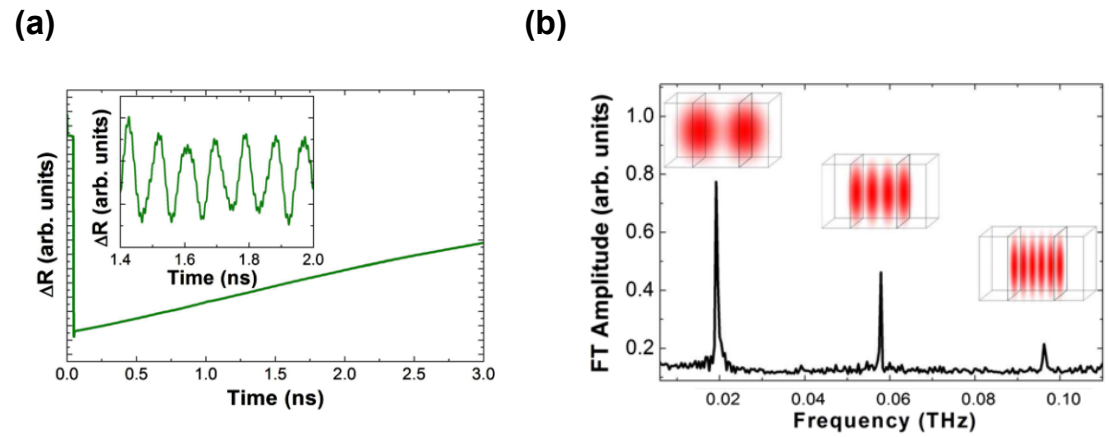

Figure 5.2 – Experimental Pump-probe results obtained on a planar Fabry-Perot cavity. Images reproduced from [56]. **(a)**: Measured differential reflectivity time trace recorded during the experiment. The inset shows a detailed view of the same temporal evolution filtered to display only frequency components > 10 GHz. **(b)**: Fourier transform amplitude of the measured temporal trace shown in Panel (a). The insets show the displacement profiles of the confined acoustic modes corresponding to the measured peaks at ≈ 20 GHz, ≈ 60 GHz and ≈ 100 GHz in the Fourier transform.

The simultaneous localization of photons and phonons, and their strong interaction in planar nanocavities has been shown experimentally. Optomechanical experiments often rely on the interactions between a single mechanical mode with one optical mode. In this context, it is therefore necessary to confine both fields in the three directions of space.

The next step was therefore to demonstrate a full three-dimensional confinement of these modes when planar Fabry-Perot cavities are etched into micropillars. This was successfully carried out, in the frame of a collaboration between our team and the

group of Alejandro Fainstein, at the Centro Atómico Bariloche & Instituto Balseiro in Argentina.

5.1.2 Opto-phononic micropillars

Planar GaAs/AlAs nanocavities allow the fabrication of three-dimensional optomechanical resonators. In this case, we obtain systems where optical and mechanical modes are confined in both the vertical and radial directions. Optomechanical resonators capable of three-dimensionally confining NIR photons and phonons in the GHz range are particularly relevant for:

- High frequency optomechanical experiments. As already mentioned in Chapter 2 (see Section 2.4.3), optomechanical systems with high mechanical resonance frequencies are particularly interesting for the preparation of a mechanical mode in its quantum ground state. We can consider for example a mechanical system resonating at a frequency of 18 GHz, as it is the case of the micropillars studied here. At a temperature of 4.2 K, accessible with usual liquid helium cryostats, the average number of phonons in the confined mode is already $\bar{n} \approx 3.9$ (obtained with the Bose-Einstein distribution). An average phonon occupation number $\bar{n} \leq 1$ could be obtained by further cooling the system at $T \leq 1.4$ K. Alternatively, optomechanical sideband cooling techniques could be implemented to easily reach this regime.

- Interactions between confined acoustic phonons and excitonic systems. GaAs/AlAs micropillars are used in cavity QED applications, where electronic excitations confined in quantum dots or quantum wells are coupled to a localized optical mode. Acoustic phonons propagating in these solid state systems also interact with the confined electronic excitations. If this interaction could be controlled, this would allow to use acoustic phonons as an additional knob to engineer the coupling of quantum wells or quantum dots with their solid state environment.

The first experimental technique used to put in evidence the three-dimensional mechanical confinement in micropillars was pump-probe coherent phonon generation and detection [58]. Similarly to the work carried out on planar cavities described in the previous section, it was possible to probe the existence of a fundamental confined mechanical mode at a resonance frequency of ≈ 20 GHz and its higher order harmonics (Figure 5.3.b). Furthermore, a dependence of the optomechanical coupling strength as a function of the device's lateral dimensions was observed (Figure 5.3.d). This confirmed the existence of lateral confinement effects on the localized mechanical modes. Finally, by following the temporal differential reflectivity traces for different lateral sizes (Figure 5.3.c), it was possible to give estimations of the confinement lifetimes for the considered phonons [58]. These results are in contrast to the experimental measurements presented in Chapter 4. Indeed, the acoustic resonators presented in the previous chapter were considered to be planar phononic structures. This was due to the fact that the characteristic wavelengths of mechanical modes having resonance frequencies around 300 GHz are very small with respect to the micrometric lateral dimensions of the characterized resonators.

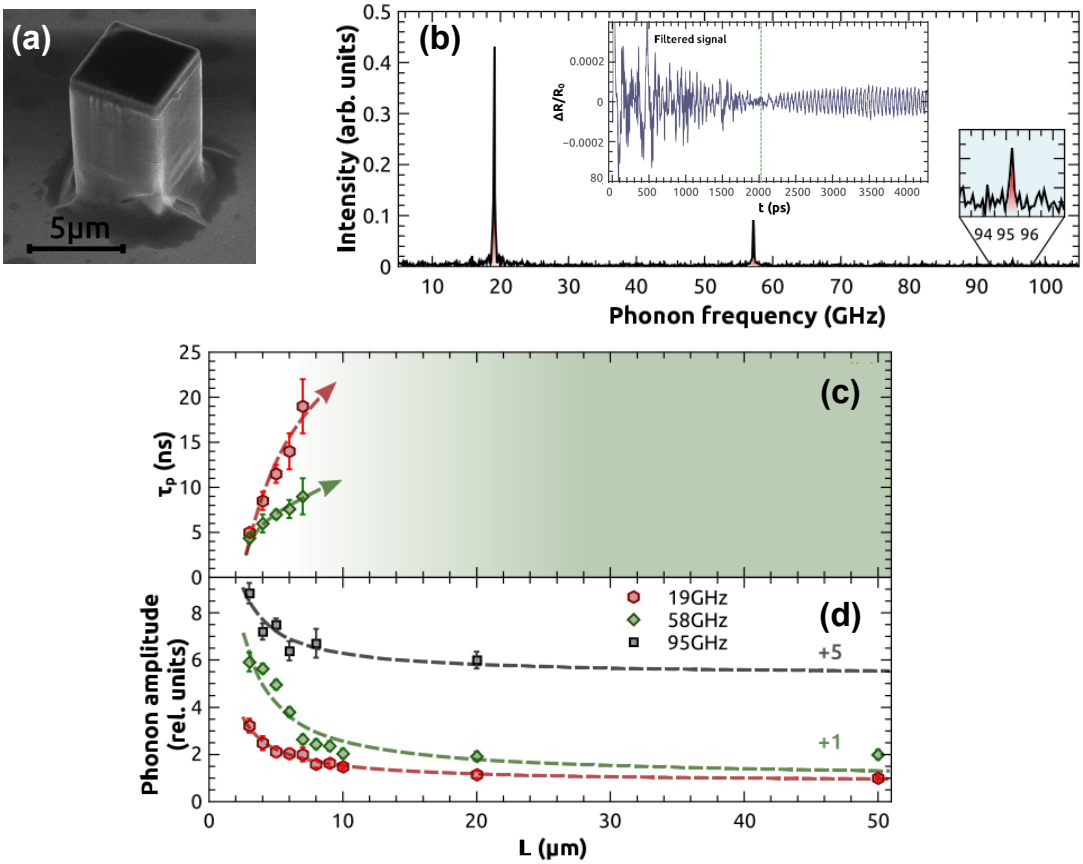

Figure 5.3 – Experimental Pump-probe results obtained on micropillars. Images reproduced from [58]. The presented data was obtained in the frame of a collaboration between our group and the team of Alejandro Fainstein, at the Centro Atómico Bariloche & Instituto Balseiro in Argentina. **(a)**: SEM image of a typical GaAs/AlAs square micropillar characterized in this work. **(b)**: Fourier transform amplitude of the experimental differential reflectivity time trace measured on a micropillar (lateral size $L = 5\,\mu\text{m}$). The peak at $\approx 19\,\text{GHz}$ corresponds to the fundamental confined acoustic mode. Inset: measured time trace, filtered to show components with frequencies between $> 5\,\text{GHz}$ and $< 100\,\text{GHz}$ **(c)**: Evolution of mechanical lifetimes for the $L = 19\,\text{GHz}$ and $L = 58\,\text{GHz}$ confined acoustic modes as a function of the micropillar lateral size L. **(d)**: Mechanical response intensity as a function of pillar size for the three probed mechanical modes.

Experimental measurements demonstrated the full confinement of mechanical modes in micropillars and their optomechanical properties. Understanding the mechanisms that lead to the localization of phonons in these systems is therefore necessary. Numerical simulations relying on the finite element method are particularly useful for that. Furthermore, they allow to quantify the confinement properties of micropillars, since optical and mechanical quality factors can be determined. Finally, the strength of the optomechanical interactions, expressed as vacuum optomechanical coupling factors, can also be calculated. We present our results in the following sections of this chapter.

5.2 Micropillar optical and mechanical confinement, a comparison

The optical confinement properties of GaAs/AlAs micropillars have already been discussed in Chapter 4. As explained before, an intuitive picture to understand the confinement mechanisms of an optical mode in a micropillar is to consider that the system behaves as an optical Fabry-Perot resonator in the vertical direction. Due to the high contrast between the indices of refractions of the semiconductor materials and vacuum, the system also behaves as an optical waveguide in the radial direction, leading to a full three dimensional confinement of an optical mode.

The three dimensional mechanical confinement in a micropillar could be thought of in the same way: the two optical DBRs of the micropillar also behave as acoustic mirrors in the vertical direction as explained in Section 5.1. In the radial direction, the structure would also behave as an "acoustic waveguide", leading to a radial confinement. This is due to the fact that high frequency acoustic phonons cannot propagate in vacuum. They are therefore totally reflected at the vacuum/semiconductor material interfaces.

Since the confinement mechanisms invoked above are quite similar for both fields, we expect to have similar behaviors for the confined optical and mechanical modes. We will see that it is indeed the case, but that differences also exist. The first step of this numerical study is therefore to compare the mechanical behavior of a micropillar with its optical one. In particular a comparison in the spatial profiles of the confined mechanical and optical modes is instructive to understand the similarities and differences between the two fields.

5.2.1 Spatial profile of confined modes

As mentioned throughout this Manuscript, the numerical calculations of the mechanical and optical behavior of a one-dimensional system such as a planar cavity are possible through transfer matrix simulations. The situation is quite different in the case of a three dimensional micropillar. In this case, the confined optical and mechanical states cannot be found through standard transfer matrix calculations. Semi-analytical models can be found in the literature for the study of the mechanical behavior of these resonators [217]. However, the detailed description of the mechanical eigenmodes and of the corresponding optomechanical coupling factors was not carried out. In this work we have chosen to use FEM simulations (COMSOL, Structural Mechanics Mod-

ule, Eigenfrequency study) to compute the eigensolutions and the spatial profiles of the confined modes.

Consider a micropillar such as the one schematically represented in Figure 5.4.a. It is constitued by two $(\frac{\lambda}{4}, \frac{\lambda}{4})$ optical DBRs made of 10 GaAs/AlAs layers pairs enclosing a $\frac{\lambda}{2}$ GaAs spacer. The radius of the micropillar is 1.51 µm. The width of the spacer is 130 nm. By taking the limit case of a planar cavity, i.e. by considering only a vertical confinement, we can estimate that both the mechanical and confined optical modes have a wavelength of ≈ 260 nm, corresponding to resonance frequencies of ≈ 323 THz and of ≈ 18.2 GHz for the optical and mechanical mode, respectively.

The micropillars simulated in this work have rotational symmetry. Furthermore, we consider that both the optical and mechanical properties of GaAs and AlAs are isotropic. Such assumptions allow us to simplify the modeling of the structure, assuming a 2D axisymmetric system described in cylindrical coordinates.

Figures 5.4.b and 5.4.c correspond to the simulated spatial profile of the confined optical and mechanical modes, respectively. The calculations were carried out for a system without substrate. The plotted physical quantities are $\left|\overrightarrow{E}(r,z)\right|^2$ and $|\overrightarrow{u}(r,z)|^2$ in the (O; $\vec{r}$; $\vec{z}$) plane, and normalized to the respective maxima of the considered fields. In both cases, the z axis corresponds to the revolution axis of the micropillar.

For the optical mode (Figure 5.4.b), we find again what was described in Chapter 4: we observe a vertical modulation of $\left|\overrightarrow{E}\right|^2$, due to the vertical confinement of the field by the two DBRs. The mode presents a minimum at the center of the spacer, due to the choice of a $\frac{\lambda}{2}$ GaAs spacer. The smooth Bessel function distribution of the electric field intensity in the radial direction is characteristic of the optical field's lateral confinement observed in cylindrical micropillars.

We now compare the mechanical and optical behavior of a micropillar. Notice that the confined acoustic mode (Figure 5.4.c) presents analogies with the optical one. Also in this case we observe a vertical confinement of the mode with an exponential decay of the envelope of $|\overrightarrow{u}(r,z)|^2$ along the z direction. The two DBRs are playing the role of $(\frac{\lambda}{4}, \frac{\lambda}{4})$ acoustic mirrors. The considered stop-band for the fundamental confined phononic mode is the one associated to the first zone edge acoustic minigap. Therefore, the $(\frac{\lambda}{4}, \frac{\lambda}{4})$ geometry optimizes the confinement of the acoustic mode in the vertical direction, since it maximizes the span of the considered acoustic minigap, as explained in Section 1.3 of Chapter 1. The zone center acoustic minigaps used in Chapter 3 to confine acoustic modes are closed in the systems considered here.

The localized acoustic mode inside the micropillar also presents a "slow" Bessel-like envelope in the radial direction, due to the lateral confinement of the phonons, in a similar way as for the optical mode.

Nevertheless, in contrast to what is observed for the optical field, the confined mechanical mode also presents a "fast" modulation in the radial direction. This difference in the spatial profiles of the optical and mechanical modes is highlighted in the bottom parts of Panel (b) and Panel (c). Detailed views of the two confined modes are plotted, corresponding to the regions marked by the dashed magenta rectangles in the micropillars. In the detailed view of Panel (c), antinodes in the displacement pattern are clearly visible and their intensity decays both in the vertical and radial directions when moving away from the spacer center.

The existence of these antinodes is independent of the number of layer pairs in the top and bottom DBRs. In Figure 5.5, we show the spatial profile of the confined

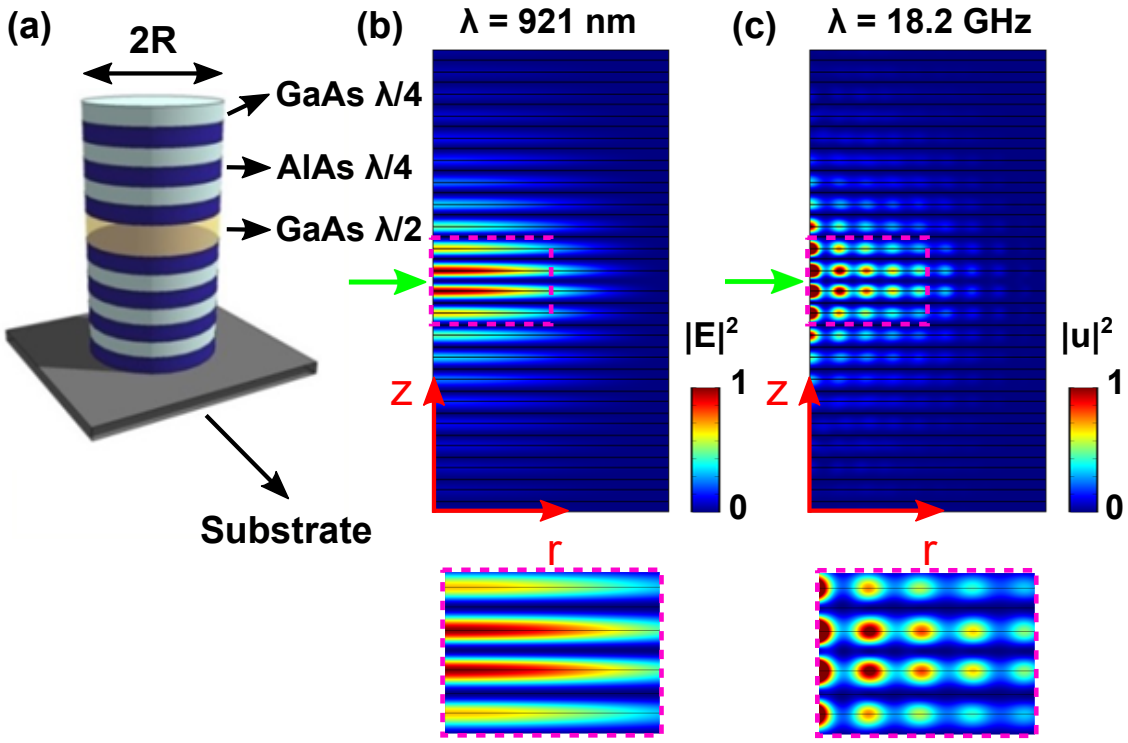

Figure 5.4 – **(a)**: Diagram of a cylindrical micropillar cavity on a substrate, formed by two DBRs enclosing a spacer. **(b)**: Normalized modulus square of the electric field in a micropillar. The structure is constituted by two optical DBRs each with 10 GaAs/AlAs layer pairs enclosing a $\lambda/2$ spacer. The resonance wavelength is 921 nm. Bottom part of the panel: detailed view of the confined optical mode in the micropillar region marked by a dashed magenta square. **(c)**: Normalized modulus square of the displacement field in the same micropillar as **(b)**. The mechanical resonance frequency is 18.2 GHz. Bottom part of the panel: detailed view of the confined mechanical mode in the micropillar region marked by a dashed magenta square. The green arrows in **(b)** and **(c)** indicate the position of the spacer.

acoustic modes for three micropillars, where we have varied the number of layer pairs N for the top and bottom DBRs. The considered structures have the same radius. We observe in Figure 5.5.a and 5.5.b, that the spatial profiles of the mechanical modes are almost the same when we drastically changed the number of layer pairs.

Notice that by decreasing this parameter below $N = 6$, the mechanical mode profile starts to be altered. This is shown in Figure 5.5.c, where the spatial profile of the confined mode is plotted for $N = 4$. By comparing it to Figure 5.5.b, we notice in particular that the displacement amplitudes at the top and bottom interfaces between the micropillar and vacuum increase (indicated by black arrows in the two panels). This is understood by considering that, as in the case of planar acoustic cavities, the phonons are less and less confined in the vertical direction. The air/sample interfaces play a more and more important role in the interference build up of the acoustic mode, leading to its deformation.

The fast radial modulation of the confined acoustic mode presented in this section is characteristic of the mechanical confinement in GaAs/AlAs micropillars. It constitutes a clear distinction between the optical and mechanical behavior of this optomechanical resonator. Other differences have been noted between the two fields, in particular the dependence of their eigenfrequencies as a function of the micropillar radius, as explained in the next section. We will see that these differences are related to the finite lateral size of the structure, and to the existence of the Poisson's ratio, a mechanical parameter that couples the motion of the micropillar in the vertical direction with the one in the radial direction.

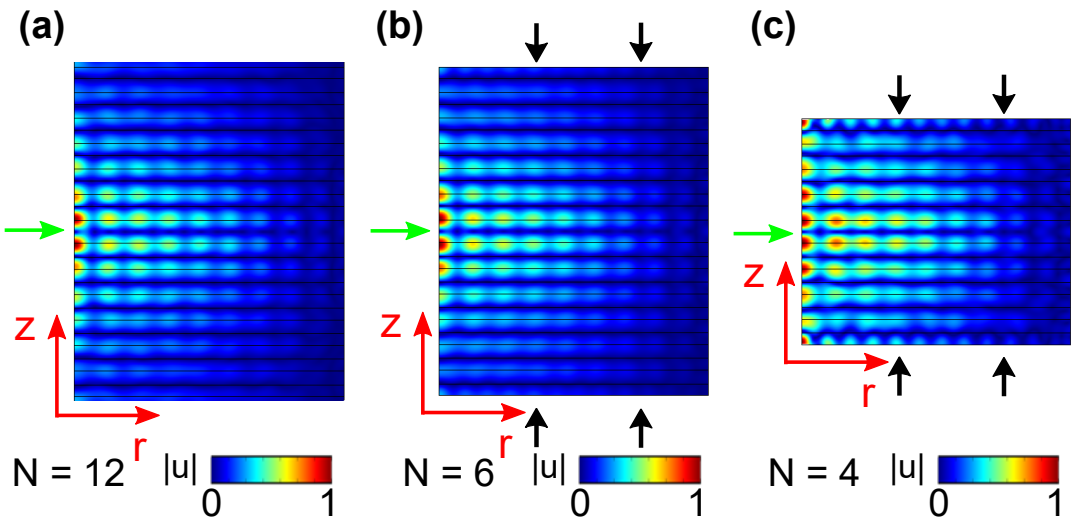

Figure 5.5 – Spatial profiles of the confined mechanical mode as a function of pair number. The plotted quantities in the color maps are the normalized displacement modulus. N is the number of GaAs/AlAs layer pairs in the top and bottom DBRs. From Panel **(a)** to Panel **(c)**, the number of layer pairs is decreased from $N = 12$ to $N = 4$. The green arrows indicate the position of the spacer. In Panel **(b)** and Panel **(c)**, the full structures are plotted in the vertical direction. The top and bottom GaAs/vacuum interfaces are indicated by the black arrows. Panel **(a)** is a detailed view of the micropillar around the spacer (top and bottom interface not visible), where the spacer and 6 layer pairs for the top and bottom DBR are visible.

5.2.2 Eigenfrequencies as a function of radius

In DBR-based micropillars, analogous confinement mechanisms for photons and phonons occur in the vertical direction. However important distinctions can be noted, such as the presence of a "fast" modulation observed in the radial direction for the spatial profile of the mechanical mode. The second major difference that can be noted when comparing the two confined modes is the dependence of their eigenfrequencies on the radius of the micropillar. This dependence is shown in Figure 5.6.a for the fundamental confined optical mode. As already mentioned in Chapter 4, we observe that by decreasing the radius of the system we smoothly increase the eigenfrequency of the optical eigenmode.

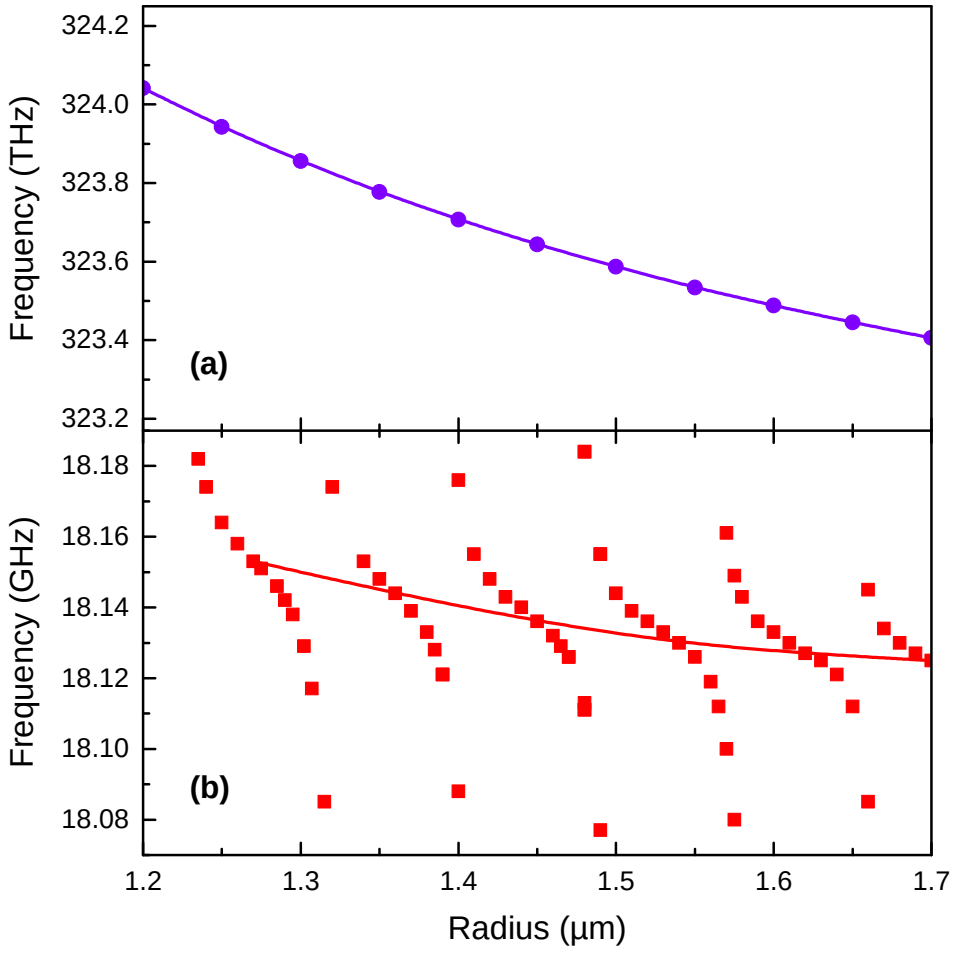

Figure 5.6 – **(a)**: Fundamental confined optical mode eigenfrequency as a function of the micropillar radius. **(b)**: Fundamental confined mechanical mode eigenfrequency as a function of radius. The red line connects the eingenfrequencies located at the centre of the successive branches.

The dependence of the mechanical mode eigenfrequency is dramatically different, as shown in Figure 5.6.b. Indeed, if also in this case an overall increasing of the mechanical eigenfrequency occurs when the radius of the micropillar decreases (indi-

cated by the continuous red curve), this variation is not smooth as in the case of the optical mode. In contrast, we observe a series of branches, suggesting the presence of successive anticrossings, separated by a period of $\approx 100\,\text{nm}$. In each branch, between two consecutive anticrossings, the resonance frequency of the confined mode strongly depends on the radius of the micropillar. We have represented here their variation over a frequency span of 100 MHz.

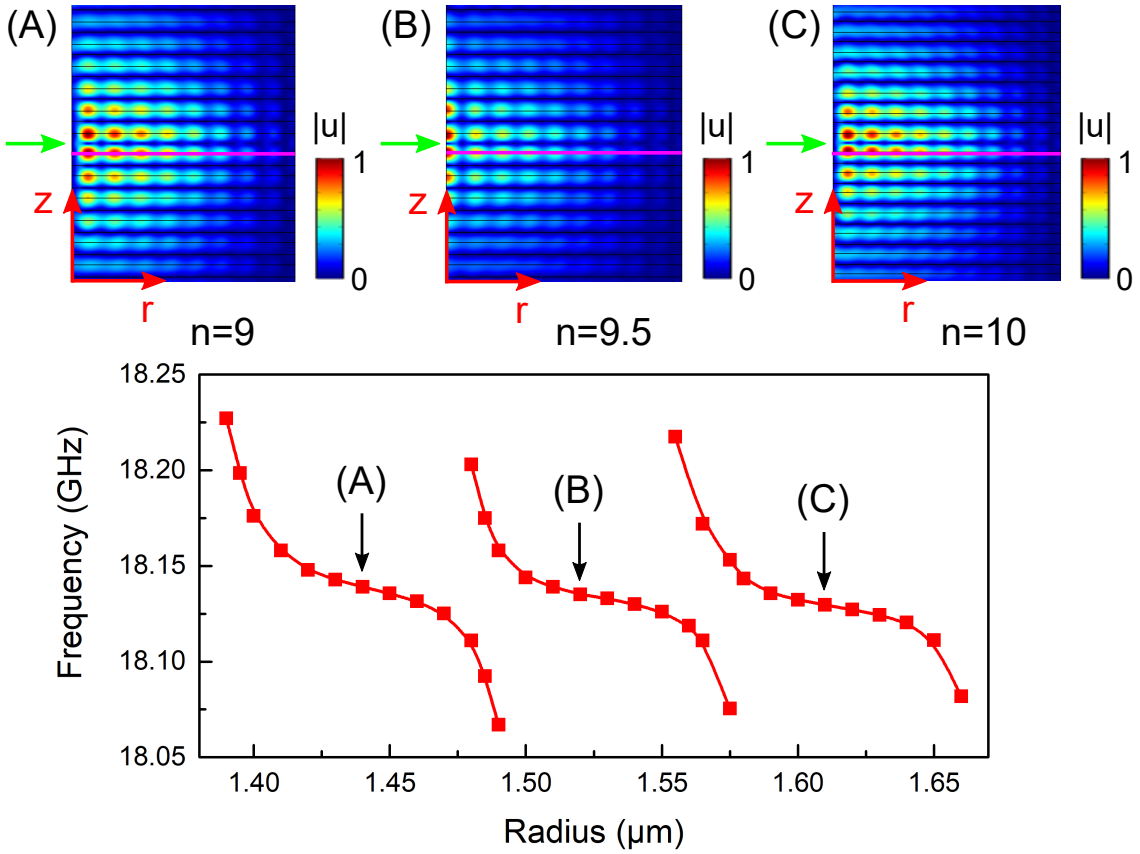

Figure 5.7 – Confined mechanical mode profile as a function of the micropillar radius. Bottom part of the figure: detailed view of the mechanical mode eigenfrequency dependence as a function of R. Top part of the figure: spatial profiles of the confined mechanical mode, for three different radii. The value n corresponds to the number of antinodes present along the radial direction of the pillar. The magenta segments indicate the line along which we counted the number of nodes. The green arrows indicate the position of the spacer. The radii are marked by (A), (B) and (C) in the bottom part of the figure, and the corresponding labels are indicated next to the represented spatial profiles.

This sequence of avoided crossings is due to the coupling of different mechanical degrees of freedom, as we will see in the next section. It is accompanied by an evolution of the spatial profile of the confined mechanical mode. This variation is shown in Figure 5.7. In the bottom part of the figure, we show a detailed view of the confined mechanical mode eigenfrequency dependence as a function of the micropillar radius. In the top part of the figure, we show the spatial profiles of the confined modes calculated for three different radii. These radii are located at the center of

three consecutive branches, as indicated in the bottom part of the figure by the arrows (A), (B) and (C).

From Figure 5.7 we can see that the number of antinodes n in the spatial profiles increases when the radius of the system is increased. To show that, we count their number in the radial direction, along the lines indicated by the magenta segments in the spatial profiles. They correspond to a GaAs spacer/AlAs interface, where the antinodes' intensities are maximal. The values of n are indicated below each spatial profile. From these simulations, we can see that the number of antinodes in the radial direction changes by one half every time we move from one branch to the next. We stress the fact that the number of nodes in the confined mechanical mode can be well studied when we choose three radii values located at the center of the successive branches. By moving away from these central regions, we observe in our calculations that the confined mode has a spatial profile which keeps the mechanical energy localized at the center of the micropillar, with more and more complex shapes.

The presence of the fast radial modulation in the spatial profile of the confined acoustic mode marks a clear distinction between the mechanical and optical behaviors of a micropillar. This difference is confirmed when comparing the dependence of the optical and mechanical resonance frequencies of the confined modes as a function of the system radius. For the mechanical mode we observe successive anticrossings, that are absent in the smooth dependence of the optical eigenfrequencies. Their existence is accompanied by an increase in the number of antinodes along the radial direction when raising R. The presence of anticrossings suggests the existence of coupling mechanisms between displacements along different directions and elastic boundary conditions that are absent in the optical case.

5.3 Mechanical confinement mechanisms in micropillars

In the former sections, we highlighted major differences between the mechanical and optical properties of a micropillar. In this section, we investigate the origin of these differences through FEM simulations. In particular, we have studied the effect of the Poisson's ratio on the mechanical properties of a micropillar. In order to understand the origin of the effects mentioned before, we propose a simplified model: a uniform GaAs cylinder of height $2H$ and diameter $2R$, surrounded by vacuum (Figure 5.8). We take $2H = 130\,\text{nm}$, corresponding to the thickness of the micropillar GaAs spacer considered in the previous sections.

The choice of such a simplification is motivated by considering that a simple GaAs cylinder also behaves as a three-dimensional acoustic cavity. Indeed, for this system, the confinement mechanism in the radial direction at $r = R$ is the same as the one of the micropillar more complex case. In the vertical direction, at $Z = 0$ and $Z = 2H$ acoustic phonons also undergo total reflection. Therefore, in this simplified model, the top and bottom interfaces behave as perfect acoustic mirrors.

The advantage of this simplified model is that it allows to understand the effect of the Poisson's ratio, the parameter responsible for the coupling between different mechanical degrees of freedom. In particular, we show that it is this coupling that induces the generation of the fast radial modulation observed in the micropillars and the anticrossings observed in Figure 5.6.b.

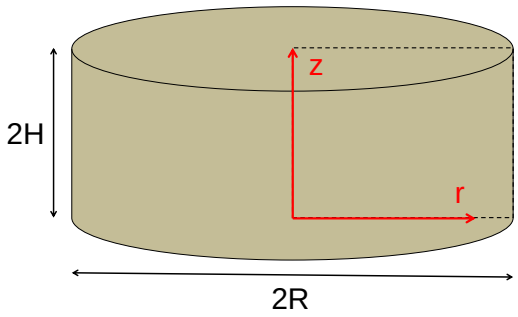

Figure 5.8 – GaAs cylinder. No substrate is present. The dashed rectangle corresponds to one section of the cylinder across the (O; $\vec{r}$; $\vec{z}$) plane.

In linear elasticity, the stress and the strain tensors are linked through the generalized Hooke's law (with Einstein notation) $\sigma_{ij} = C_{ijkl}\eta_{kl}$. σ_{ij} and η_{kl} correspond to the components of the stress and the strain tensor, respectively. C_{ijkl} are the components of the stiffness tensor. In general, the stiffness tensor contains 21 independent components. Considering an isotropic material, the stiffness tensor simplifies and relates the stress to the strain component with the following relation:

$$\eta_{ij} = \frac{1+\nu}{E} \times \sigma_{ij} - \frac{\nu}{E} \times \delta_{ij}\sigma_{kk} \tag{5.3}$$

E is the Young modulus, δ_{ij} the Kronecker delta and ν is the Poisson's ratio. The latter parameter describes the normal strain η_{ii} induced in the direction i when a stress σ_{jj} is applied in an orthogonal direction. We illustrate this by considering the 2 dimensional tensile testing represented in Figure 5.9. The deformation of the tensile specimen is expressed in cartesian coordinates.

In this simple case the only stress component different from 0 (in the central part of the sample) is the vertical component σ_{33}. Applying Equation 5.3, we find that the two strain components $\eta_{ij} \neq 0$ are $\eta_{11} = \frac{\sigma_{11}}{E}$ and $\eta_{22} = -\frac{\sigma_{11}\times\nu}{E}$, represented in Figure 5.9. In the expression of η_{22} the Poisson's ratio quantifies the horizontal contraction induced by uniaxial vertical tensile stress.

In the case of the cylinder represented in Figure 5.8, the Poisson ratio establishes a coupling between vertical and radial mechanical degrees of freedom. To understand the role of this parameter, we consider two limit cases. The first one is a "decoupled" cylinder, where we set the Poisson's ratio $\nu = 0$. We then consider a second case where $\nu = 0.31$, the real value of the Poisson's ratio in GaAs.

In both situations, the considered cylinder is surrounded by vacuum. We therefore apply a free boundary condition to all the GaAs/vacuum interfaces. In terms of stress components, such boundary conditions correspond to:

$$\begin{aligned} &\sigma_{zz} = \sigma_{z\phi} = \sigma_{zr} = 0 \ at \ Z = 0 \ and \ z = 2H \\ &\sigma_{rr} = \sigma_{z\phi} = \sigma_{zr} = 0 \ at \ r = R \end{aligned} \tag{5.4}$$

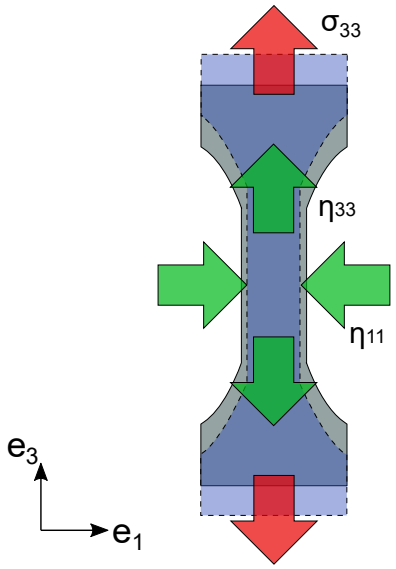

Figure 5.9 – Tensile testing diagram. Tensile specimen before (grey) and while σ_{11} is applied (blue). The red arrows indicate the stress component σ_{11}. The green arrows correspond to the strain components η_{11} and η_{33} in the central part of the sample.

We first consider the case $\nu = 0$. It is possible to analytically solve the elastic wave equation by seeking a solution only confined in the vertical direction. This solution that we call the "vertical decoupled mode" has the following displacement components:

$$\begin{aligned} u_r^k(r,z,\phi) &= u_\phi^k(r,z,\phi) = 0 \\ u_z^k(r,z,\phi) &= A_0 \times cos(kz) \end{aligned} \tag{5.5}$$

where k is the vertical wavenumber, and A_0 is an arbitrary amplitude. In order to comply with the free boundary conditions at $Z = 0$ *and* $z = 2H$, i.e. maximum displacement amplitude at these boundaries, the vertical wavenumber satisfies $k \times 2H = \pi\,[2\pi]$. This solution is also the one found for an infinite planar structure (i.e. cylindrical plate with an infinite radius).

It is also possible to solve the same problem for a purely radial displacement. We call this mode the "radial decoupled mode" and the displacement field in the structure has the following components:

$$\begin{aligned} u_z^q(r,z,\phi) &= u_\phi^k(r,z,\phi) = 0 \\ u_r^q(r,z,\phi) &= B_0 \times J_1(qr) \end{aligned} \tag{5.6}$$

where q is the radial wavenumber, B_0 is an arbitrary amplitude, and J_1 designates the Bessel function of the first kind. The discrete values of q can be determined so that the mode complies with the free boundary conditions at $r = R$. These solutions are also valid for the case of an infinite cylinder. The first 3 values of q are given below:

order of q	value of q
1	1.8412/R
2	5.3314/R
3	8.5363/R

The two types of solutions for $\nu = 0$ are shown in Figure 5.10. The leftmost simulations in Panel (a) and Panel (b) correspond to the fundamental vertical and radial modes, respectively. Also in this case we used an FEM approach to find their spatial profiles. The two considered decoupled modes have similar eigenfrequencies for $R = 75\,\text{nm}$, equal to $\approx 15.5\,\text{GHz}$.

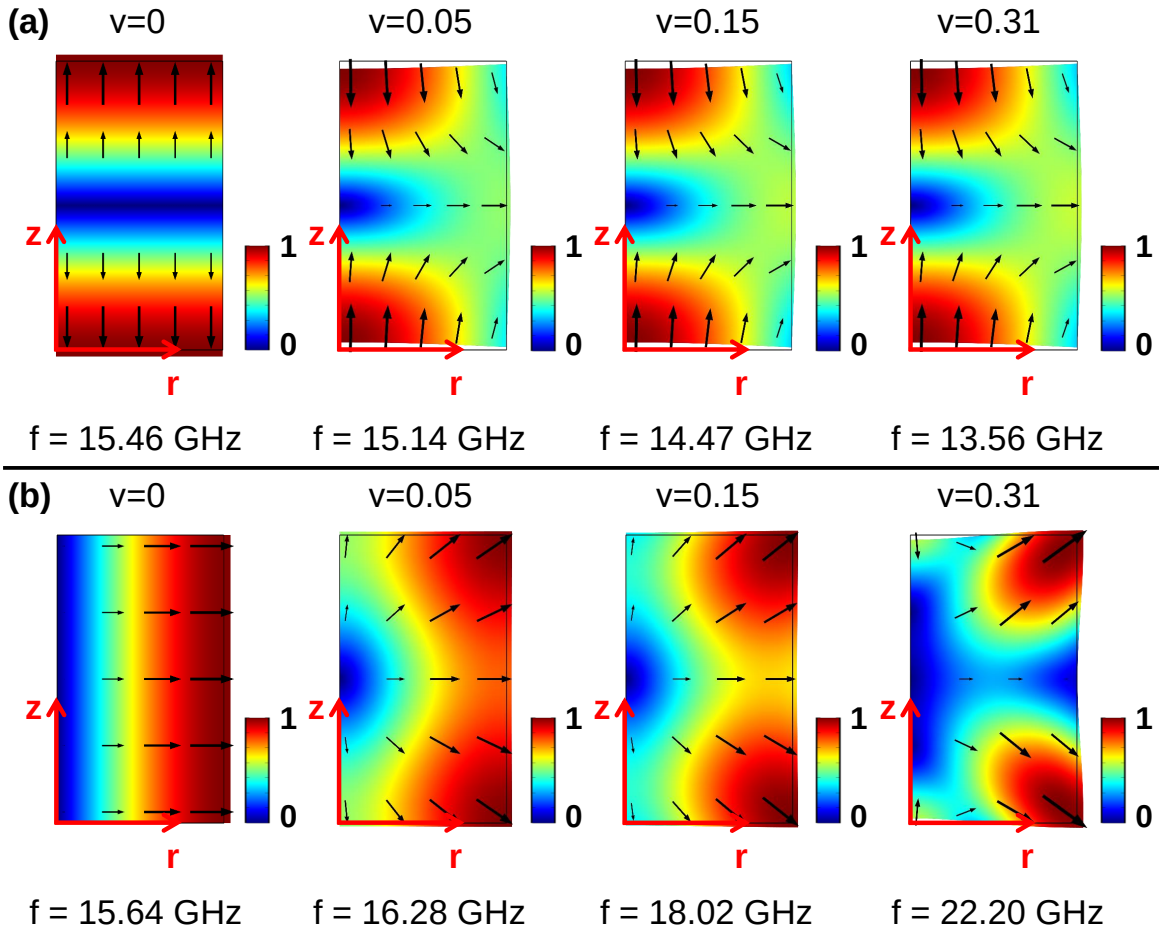

Figure 5.10 – Evolution of the mode spatial profiles when increasing the Poisson's ratio ν (from left to right), for a cylinder with $R = 75.3\,\text{nm}$ and $2H = 130\,\text{nm}$. Panels **(a)** and **(b)** show the evolution of the vertical and radial-like modes, respectively. The color scale corresponds to the normalized modulus of total displacement. The arrows indicate the calculated displacement direction and intensity at different points in the cylinder. The z axis corresponds to the revolution axis of the system. The value of ν used for each simulation is indicated on top of every plot. The calculated eigenfrequencies are reported on the bottom.

We then progressively increase the value of the Poisson's ratio up to $\nu = 0.31$, the real value for GaAs. As shown in Panel (a) and Panel (b) of Figure 5.10, we observe a progressive modification of the two modes spatial profiles showing simultaneously vertical and radial components. Indeed, a Poisson's ratio different from 0 implies that a vertical stress simultaneously coexists with a non-zero radial strain component, leading to a mode mixing between the two decoupled modes. As we can see in the

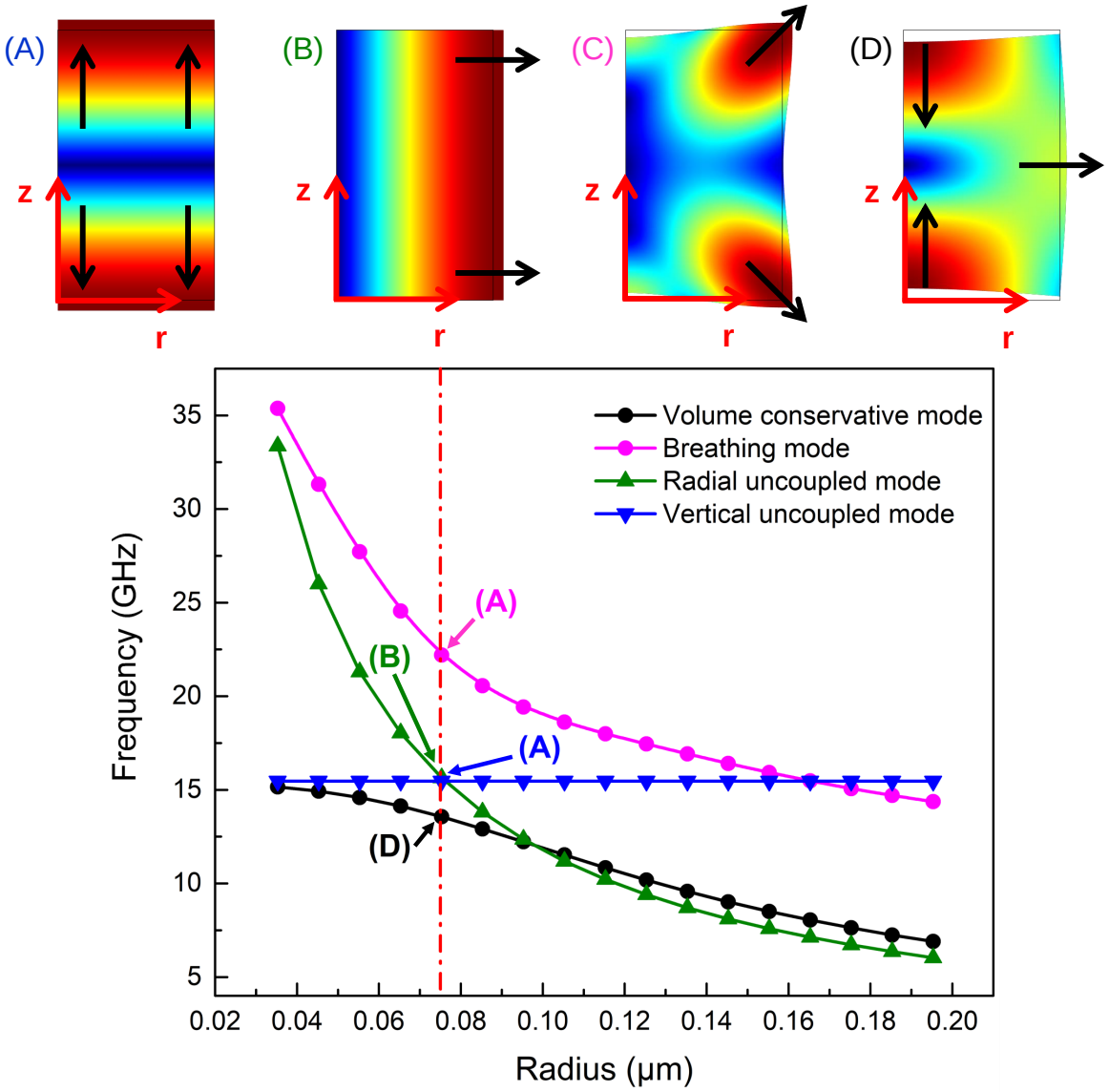

Figure 5.11 – Eigenfrequencies of the decoupled (triangle symbols) and coupled modes (circle symbols) as a function of the GaAs cylinder's radius. The blue and the green curves indicate the eigenfrequency dependence of the vertical and radial decoupled modes ($\nu = 0$), respectively. The magenta and the black dependences correspond to the breathing and the volume conservative modes ($\nu = 0.31$), respectively. The spatial profiles of the considered modes are shown in the top part of the figure (FEM simulations) for $R = 75.3\,\mathrm{nm}$, as shown by the arrows in the graph. This radius value is marked by a vertical dashed line in the plot. The color scale indicates the modulus of displacement. The black arrows schematically show the direction of the displacement.

evolution of the spatial profile of the two modes, antinodes appear at the air/vacuum interfaces, satisfying the boundary conditions in both the vertical and the radial directions. For the mode that was initially confined purely in the vertical direction the eigenfrequency decreases when the Poisson's ratio increases (Figure 5.10.a). In the case of the mechanical mode with displacement components in the radial direction when $\nu = 0$, the eigenfrequency increases (Figure 5.10.b). For the low frequency coupled mode (Figure 5.10, rightmost plot in Panel (a)), we have a "volume conservative mode", since a compression in the vertical direction is accompanied by an expansion of the cylinder in the radial one. For the high frequency coupled mode (Figure 5.10, rightmost plot in Panel (b)), we find a "breathing mode", where a vertical expansion is accompanied by a radial expansion.

The role played by the Poisson's ratio in coupling different degrees of freedom is confirmed when studying the dependence of the mechanical eigenfrequencies of the coupled and decoupled modes as a function of the radius. We will focus here on the vertical and radial decoupled modes ($\nu = 0$), and on the coupled modes obtained with $\nu = 0.31$.

We first consider the case $\nu = 0$. The vertical decoupled mode eigenfrequency as a function of the cylinder's radius is represented by the blue curve in Figure 5.11. The resonance frequency of this mode does not depend on the radius of the cylinder, since it is only affected by the height of the cylinder $2H$.

The variation of the fundamental radial decoupled mode eigenfrequency ($\nu = 0$) is represented by the green curve in the same figure. In this case, when we increase the radius of the cylinder the mechanical eigenfrequencies decrease. These values are independent from the height of the considered system.

We now consider $\nu = 0.31$. The eigenfrequencies of the coupled modes are shown by the magenta curve for the breathing mode, and by the black curve for the volume conservative mode. A clear anticrossing is present between the two curves for a radius of $\approx 75\,\mathrm{nm}$, marked by the vertical dashed line, where the two decoupled modes ($\nu = 0$) are degenerate. The spatial profiles of the modes calculated for this radius are shown in the top part of Figure 5.11. The labels (A) and (B) indicate the profiles of the decoupled modes, whereas the coupled modes are marked by the labels (C) for the breathing mode, and (D) for the volume conservative mode. Their eigenfrequencies are indicated in the graph of Figure 5.11. Far from the anticrossing, the coupled mechanical modes spatial profiles and eigenfrequencies tend to replicate the ones of the decoupled modes. This further confirms the role played by the Poisson's ratio in coupling the vertical and the radial modes found for $\nu = 0$.

We now move to the case of a micropillar. Notice that the two considered systems are not completely equivalent. In particular, in a micropillar the edges of the GaAs spacer are not free in the vertical direction, as in the case of the GaAs cylinder. The continuity of stress and displacement components apply at the interface between the GaAs spacer and the surrounding AlAs layers. Naturally, these boundary conditions will have a significant effect on the spatial profile of the confined mechanical mode. Nevertheless, the coupling mechanisms due to the Poisson's ratio that we have described before for a cylinder also occur in the more complex case of a GaAs/AlAs micropillar.

We start our analysis by considering $\nu = 0$ for both GaAs and AlAs. We find a mode that is confined purely in the vertical direction, due to the presence of the two DBRs. This is analogous to the vertically confined mode in the GaAs cylinder

(top left part of Figure 5.10.a). The spatial profile of this mode, represented by the normalized displacement modulus, is shown in Figure 5.12.a. The only stress components $\sigma_{ij} \neq 0$ induced by this mechanical vibration are the vertical ones (σ_{zz}). They are shown in Figure 5.12.b. When we progressively increase the Poisson's ratio for both materials, the existence of $\sigma_{zz} \neq 0$ implies a gradual modification of the confined mode where both vertical and radial strain components are simultaneously present. Such a confined mode complies with the vertical confinement induced by the acoustic mirrors and the sample/vacuum boundary conditions, leading to the generation of antinodes as observed in Figure 5.4.c in the displacement pattern. By extending the reasoning carried out for the case of the GaAs cylinder, the effect of the Poisson's ratio is to induce a coupling between the vertically confined mode and successive mechanical modes with a dominant radial component.

As in the case of the GaAs cylinder, the coupling between radial and vertical displacements induced by the Poisson's ratios also explains the existence of anticrossings in the variation of the mechanical eigenfrequencies as a function of the micropillar radius. The black and magenta curves shown in Figure 5.11 correspond to half branches in the dependence shown in Figure 5.6.b.

In Figure 5.7, we have seen that the number of antinodes increases when we increase the radius R. According to the discussion carried out in this section, we can understand this as an effect of the Poisson's ratio. Indeed, this parameter couples the vertically confined mode to the successive radial-like vibrating modes of the micropillar, as evidenced by the sequence of anticrossings observed in Figure 5.6.b. This leads to the increasing of the antinodes number observed in our simulations.

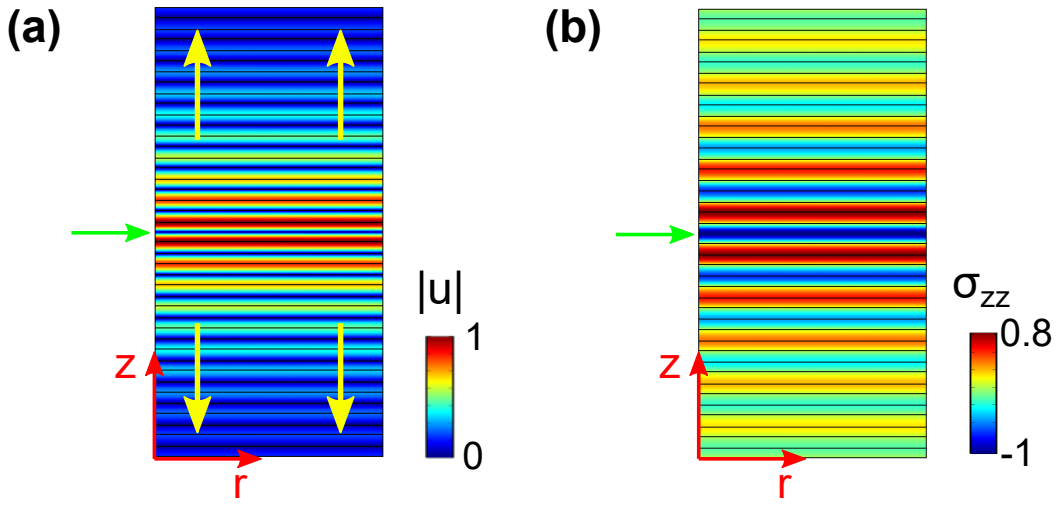

Figure 5.12 – Spatial profile of the decoupled vertical mode in a micropillar. The Poisson's ratio is set to 0 for both GaAs and AlAs. In both panels the green arrows show the position of the spacer.**(a)**: The color map shows the modulus of normalized total displacement. The yellow arrows show the direction of displacement.**(b)**:The color map shows the normalized vertical stress component σ_{zz}

In this section, we used FEM simulations to provide a description of the mechanisms that lead to the confinement of an acoustic mode in a GaAs/AlAs micropillar. In particular, we have evidenced the fact that it is the coupling of different mechanical degrees of freedom, induced by the materials Poisson's ratios, that explains the

generation of the antinodes in the spatial profile of the confined mode inside a micropillar. Furthermore, this also leads to the generation of the successive anticrossings observed in the dependence of the mechanical eigenfrequencies as a function of the resonator radius. In the next section, we will take advantage of the developed models to calculate some relevant optomechanical parameters.

5.4 Optomechanical properties of micropillars

In this section, we perform numerical simulations to calculate the mechanical quality factor and the vacuum optomechanical coupling factor g_0. These parameters are particularly relevant for optomechanical experiments such as Brownian motion measurements or optomechanical sideband cooling (see Section 2.4.3 in Chapter 2). We study their evolution when we change design parameters of the micropillar.

5.4.1 Mechanical quality factor

The results discussed in the previous sections have shown that the mechanical behavior of an AlAs/GaAs micropillar depends on its geometry. For example, the confined mode eigenfrequency and spatial profile vary with the structure's lateral dimensions. As a consequence, the way in which the mechanical energy is stored and dissipated depends on the design parameters of the micropillar. This dissipation is quantified by the mechanical quality factor $\mathrm{Q_m}$. This parameter describes how well the resonator is isolated from its environment, since it corresponds to the quantity of mechanical energy that is lost *per* cycle of oscillation.

In this section, we investigate the effect of two design parameters, the radius of the micropillar and the number of AlAs/GaAs layer pairs in the DBRs, through our FEM models. We start this discussion by addressing the dependence of $\mathrm{Q_m}$ with the radius of the micropillar over one branch of the dependence shown in Figure 5.6.b. The number of GaAs/AlAs layer pairs in the top and bottom DBRs are called N_{top} and N_{bot}, respectively. In this study, we have considered two structures: one with $N_{top} = N_{bot} = N = 10$ and the other one $N_{top} = N_{bot} = N = 20$.

A detailed view of the considered branch is shown in Figure 5.13.a for radii around 1.53 µm. The values of the mechanical eigenfrequencies are almost unaffected by the number N of GaAs/AlAs layers in the top and bottom DBRs. In this dependence, we can consider three different regions: a central one where the mechanical eigenfrequencies weakly depend on the radius of the micropillar, and two others, located at the edges of the branch, where the resonance frequencies strongly depend on this parameter.

In order to calculate the value of the mechanical quality factor over the branch plotted in Figure 5.13.a, we introduced dissipation of mechanical energy into the GaAs substrate by introducing perfectly matched layers (PMLs) domains. This is represented in Figure 5.14, where we show the implemented FEM model. No other dissipation channels are considered. The value of $\mathrm{Q_m}$ can be calculated considering that $Q_m = \frac{Re(\omega_m)}{2Im(\omega_m)}$, where ω_m is the complex eigenfrequency found in the presence of mechanical losses (the values plotted in Figure 5.13.a correspond to the real part of the eigenfrequencies).

We calculated the dependence of the mechanical quality factor of a micropillar as a function of its radius for $N = 10$ and $N = 20$. The results are shown in Figure 5.13.b and Figure 5.13.c for the two considered structures. In the case of $N = 10$, a minimum of the mechanical quality factor is reached when we consider mechanical modes in the central part of the dependence, where the eigenfrequencies weakly depend on the lateral size of the resonator. The value of Q_m increases for the modes located on the edges of the branch. The situation is opposite in the case of $N = 20$: in this case a maximum of the quality factor is reached in the regions where the eigenfrequencies weakly depend on the radius.

We can explain the behavior of the mechanical quality factor in the two considered cases by studying the way in which the mechanical energy is stored inside the resonator. In particular, we can calculate the fraction of energy stored in the radial direction α with the following equation:

$$\alpha = \frac{E_{mech}^{radial}}{E_{mech}} = \frac{\int_{pillar} \frac{1}{2} \times \omega^2 \left|u_r(r,\phi,z)\right|^2 \times \rho \times \mathrm{d}V}{\int_{pillar} \frac{1}{2} \times \omega^2 \|\overrightarrow{u}(r,\phi,z)\|^2 \times \rho \times \mathrm{d}V} \tag{5.7}$$

where E_{mech} is the total stored mechanical energy of the mode, E_{mech}^{radial} is the mechanical energy stored in the radial direction, ω is the mode eigenfrequency, ρ the mass density, $\|\overrightarrow{u}\|$ is the norm of total displacement, and $|u_r|$ is the modulus of radial displacement in the micropillar. We determined the value of α by implementing Equation 5.7 in our numerical model, and we calculated its dependence over the considered branch for the two structures with $N = 10$ and $N = 20$, as shown in Figure 5.13.d.

The result of these calculations shows that over one branch, we can clearly distinguish two regions for both $N = 10$ and $N = 20$. At the center of the branch, where the eigenfrequencies are weakly dependent on the micropillar radius, we observe that the mechanical energy is mainly stored in the vertical direction. This region is marked in grey in all panels of Figure 5.13. When we move far away from the anticrossings, into the regions where the eigenfrequencies strongly depend on R, the fraction of radial energy increases progressively. The mechanical mode therefore acquires an increasing radial character, similarly to what is observed for the simplified model of a GaAs cylinder. We marked in white those radii intervals.

We can now explain the behavior of the mechanical quality factors for $N = 10$ and $N = 20$ by considering independently the coupling to the substrate of the vertical and radial components of the confined mode.

For a purely vertical confined mode such as the one represented in Figure 5.12, the mechanical quality factor is determined by the acoustic reflectivity of the DBR connected to the GaAs substrate (i.e. bottom DBR). In contrast, in the case of mechanical modes having important radial components, the mechanical quality factor is less sensitive to the reflectivity of the DBRs. In the case of $N = 10$, the quality factor of the vertically confined mode is very low, due to the few number of GaAs/AlAs layer pairs. Eventually, the quality factor of this mode is lower than of the decoupled radial mode. As a consequence, the vertical-like modes represented in the grey region of Figure 5.13.c have a lower mechanical quality factor than the modes with a mixed vertical-radial spatial profile, represented in the white regions of the plots.

The situation is the opposite in the case of $N = 20$. The quality factor of the vertical decoupled mode is higher than the value of the radial mode. In this case, we

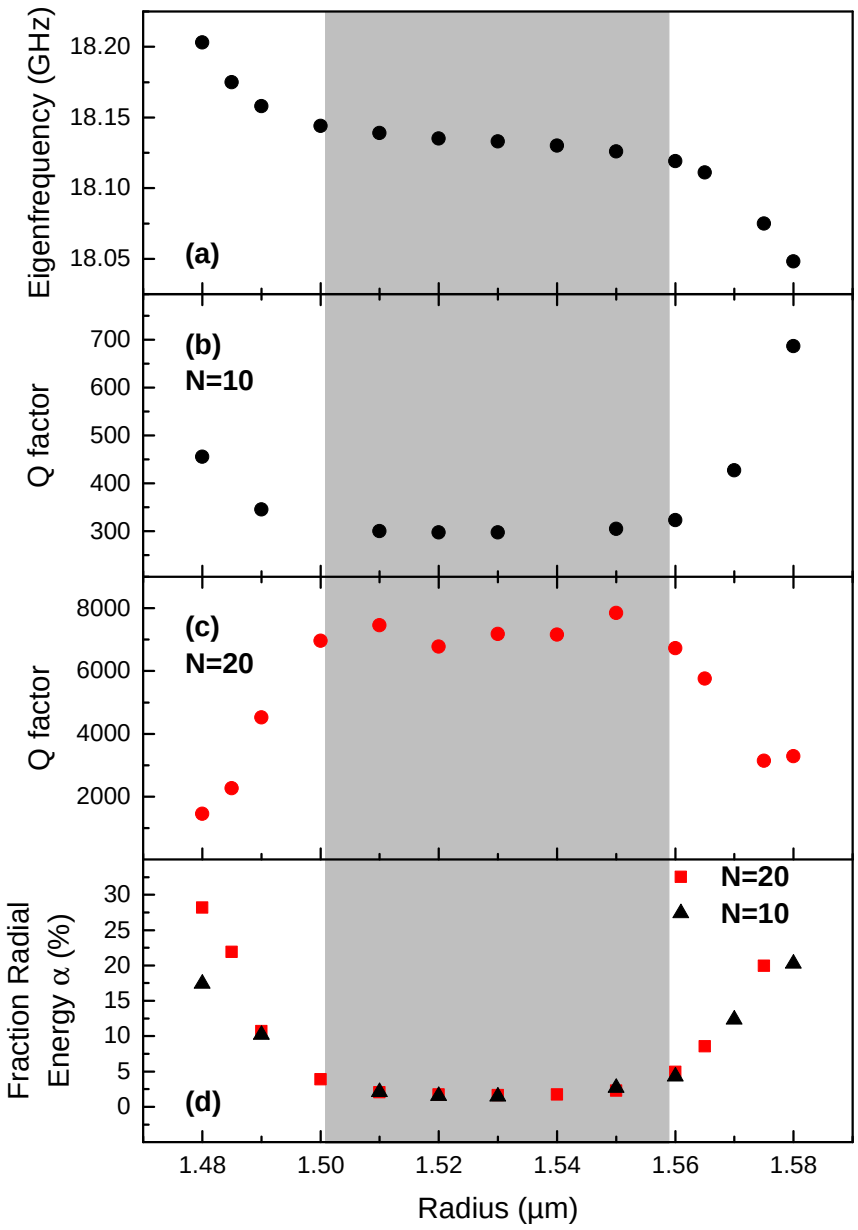

Figure 5.13 – **(a)**: Detailed view of the considered branch showing the fundamental mechanical mode eigenfrequency as a function of radius, with $N = 20$. **(b)**: Mechanical quality factor dependence as a function of radius over the branch plotted in Panel (a), for a micropillar with $N = 10$ for the top and bottom DBRs. **(c)**: Mechanical quality factor as a function of radius, for a micropillar with $N = 20$. **(d)**: Mechanical radial energy fraction α stored in the fundamental confined mode as a function of the radius of the micropillar, for $N = 10$ (black triangles) and $N = 20$ (red squares). In all panels the grey region indicates the radius interval where the mechanical energy is stored mainly in the vertical direction. White regions indicate the radii intervals where α increases.

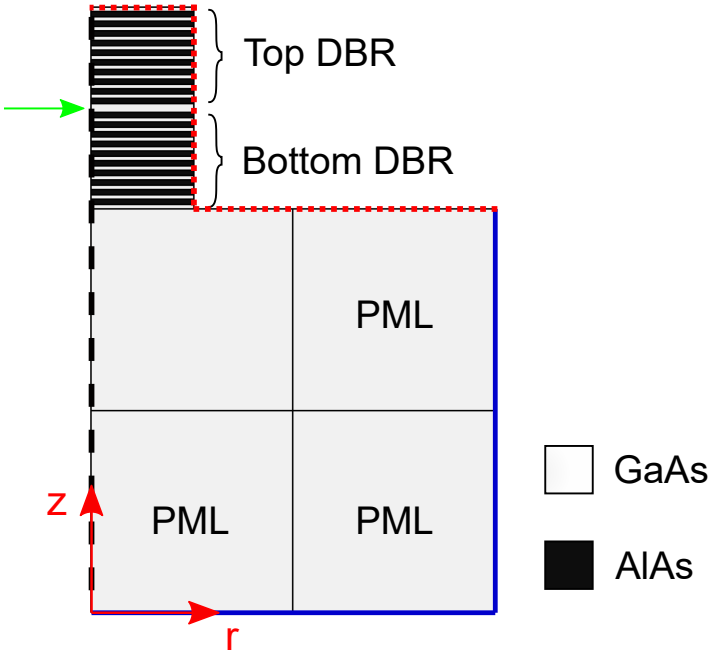

Figure 5.14 – Diagram of the FEM model used to calculate the mechanical quality factors of a micropillar. The colors correspond to the materials as indicated by the legend. The green arrow marks the position of the spacer. Perfectly matched layers, implemented to account for mechanical energy dissipation through the substrate, are specified. The top and bottom DBRs are also indicated. For the structure represented here, N_{top} and N_{bot} are both equal to $N = 10$. The black dashed line indicates the revolution axis of the structure, along z. The solid blue lines show the fixed constraint (i.e. zero displacement) boundary conditions applied to the perfectly matched layers. The dotted red lines indicate the free stress boundary conditions applied to the micropillar and to the substrate.

therefore observe maximal values of the mechanical quality factor in the grey region of Figure 5.13.d, where the modes are mainly vertical.

In both cases we observe that the calculated Q_m strongly depends on the radius of the system. Changes by a factor of 4 are observed for a change in R of approximately 50 nm. Therefore, the dependence of the mechanical quality factor as a function of the radius of the micropillar is dramatically affected by the spatial profile of the considered confined mode.

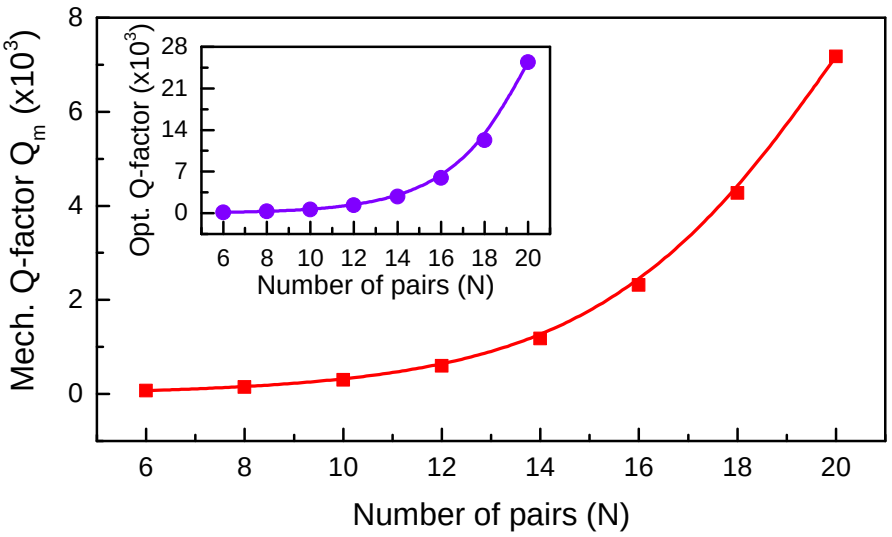

Figure 5.15 – Mechanical quality factor as a function of pair number N for the top and bottom DBRs. The inset corresponds to the same dependence for the optical quality factor. For both curves the micropillar radius is kept constant and is equal to 1.53 µm.

We then studied the dependence of Q_m when N ($N_{top} = N_{bot} = N$) is increased (Figure 5.15), for a given value of the radius. We can compare it to the dependence of the optical quality factor (Q_{opt}) as a function of the same parameter (inset to the figure). For the optical simulations, the micropillar is not in contact with a substrate, but is embedded in air. In both cases, the quality factors increase in a similar way when N is increased. This is due to the fact that by increasing the optical and acoustic reflectivities of the mirrors, the energy losses along the vertical direction are decreased. This behavior is analogous to the one observed in the corresponding planar systems.

Notice however that the dissipation mechanisms through the DBRs are not the same for the two fields. This is due to the fact that the mechanical energy is dissipated through the substrate in our model. Therefore, for the mechanical mode, it is the acoustic mirror connected to the substrate which is determinant for mechanical damping, since it acts as the connecting medium to the substrate. In other words, the mechanical energy can only be released towards the substrate through the bottom DBR. Therefore, it is this part of the micropillar that limits the reached values for the mechanical quality factor.

The minor role played by the top DBR in the acoustic confinement can be illustrated by considering two micropillars with different designs. The first one is modeled

with $N_{top} = N_{bot} = 10$ and the second one with $N_{top} = 6$ and $N_{bot} = 10$. The calculated mechanical quality factors obtained are of 290 and 280, respectively, showing that the value of this parameter is essentially determined by the bottom mirror. Such a behavior is in strong contrast with the case of the confined optical mode, where both DBRs correspond to dissipation channels and play a crucial role in its confinement. As a consequence, the confinement strength of the optical and mechanical modes can be tuned independently by controlling the number of layer pairs in the top mirror.

In the case of $N = 20$, we reach a maximal value for the mechanical quality factor equal to ≈ 8000 for a resonance frequency around 18 GHz. This gives a $Q \cdot f$ product of $\approx 10^{14}$ Hz, which corresponds to an order of magnitude for this figure of merit that is comparable to the ones reported for state-of-the-art optomechanical systems [26].

The numerical simulations described above enabled us to calculate the mechanical quality factors. However, previous experimental and theoretical studies on high frequency acoustic cavities have shown that scattering processes of acoustic phonons into other mechanical modes due to anharmonicity effects, or dissipation mechanisms due to the presence of surface/interface defects can be an important source of mechanical energy losses [89, 147]. Furthermore, other dissipation processes as thermo-elastic effects or viscous damping if the mechanical resonator is surrounded by a fluid such as air can also significantly affect the value of the mechanical quality factor [155]. These effects have not been taken into account in our model, as only dissipation of mechanical energy through the substrate is considered here. Nevertheless, these simulations provide values for Q_m comparable to experimental ones.

In reference [58], phonon lifetimes of confined acoustic modes in micropillars have been experimentally measured. The probed systems were designed for confining modes at comparable wavelengths using the same materials. The number of layer pairs and the lateral dimensions are similar to the case of $N = 20$ considered in this section. The studied micropillars in the experimental work have, however, a square section. The mechanical quality factors that were measured range between 200 and 1000. As shown in Figure 5.13.c, the simulated quality factors reported here range between 2000 and 8000, resulting in orders of magnitude that are compatible with respect to the measured ones.

5.4.2 Optomechanical coupling factor

The simulations presented above allowed to describe the optical and mechanical behavior of micropillars. Through this numerical approach it is possible to calculate the magnitude of the interaction between the fields. In this section, we present the numerical simulations that we performed to calculate the vacuum optomechanical coupling factor g_0. This parameter quantifies the strength of the interaction between the confined mechanical and optical modes, as presented in Chapter 2.

For the systems considered here, the value of g_0 can be separated into two contributions: the geometrical coupling factor g_0^{geom} and the photoelastic coupling factor g_0^{photo}. The first term quantifies the optomechanical coupling related to the change of the microcavity shape and dimensions. The second term accounts for the change of the micropillar optical resonance frequency due to local changes of the indices of refraction. These variations are caused by the photoelastic effect.

In the framework of these calculations we have left aside the geometrical coupling factor contribution and focused only on the photoelastic one. Additionally, we

consider only the photoelastic contributions in the GaAs layers. This hypothesis is justified by considering that the photoelastic effect inside a material presents a resonant behavior when approaching an electronic transition of the system. As in the case of the calculations performed for the Raman scattering cross section of planar structures, we neglect the photoelastic effect in the AlAs.

The method implemented in our FEM model to calculate the g_0 has been developed in collaboration with the group of Ivan Favero, at the Laboratoire Matériaux et de Phénomènes Quantiques. It can be summarized as following:

- We first calculate the confined optical mode in a micropillar where no mechanical strain is present. We find an unperturbed angular eigenfrequency ω_0.

- We simulate the spatial profile of the confined mechanical mode in the micropillar. We denote the mechanical eigenfrequency Ω_m. We calculate the mechanical energy stored in the micropillar E_{mech}. We can then determine the zero point fluctuation x_{zpf} as:

$$x_{zpf} = \frac{x_{max}}{2}\sqrt{\frac{\hbar\Omega_m}{2E_{mech}}} \tag{5.8}$$

  The x_{max} parameter corresponds to the displacement at the considered reduction point. The reduction point in these calculations is the point having maximal displacement intensity, located at the interface between the GaAs spacer and an AlAs layer, at $r = 0$.

- We then determine the new eigenfrequency of the confined optical mode, after having perturbed the permittivity tensor components of the GaAs layers through the photoelastic effect, with the spatial profile of the calculated mechanical mode. The g_{om} is described by the change in frequency induced by a differential displacement of the reduction point, as $\frac{\partial\omega}{\partial x_{max}}$. Therefore, in order to numerically implement this differential calculation, we normalize the spatial profile of the mechanical field so that we consider small mechanical displacements. We denote the new optical eigenfrequency $\omega_{perturb}$, that is affected by the normalized displacement field. The optomechanical coupling factor is calculated as $g_{om} = \frac{|\omega_0 - \omega_{perturb}|}{x_{max}}$, where x_{max} is the normalized displacement at the reduction point (i.e. the point of maximal displacement). The vacuum optomechanical coupling factor can then be determined simply by calculating $g_0 = g_{om} \times x_{zpf}$.

In our model, the only components of the photoelastic tensor affecting the GaAs dielectric tensor are p_{11} and p_{12}.[1] The values of these two parameters can be found in the literature for a wavelength of 920 nm, and are $p_{11} = 0.276$ and $p_{12} = 0.305$ [218]. The shear strain components reach maximal values that are of the same order of magnitude as the normal ones. However, the photoelastic constant p_{44} is one order of magnitude smaller than p_{11} and p_{12} in GaAs, for optical wavelengths of ≈ 920 nm [111]. We will neglect their contribution. In this case, the dielectric tensor of GaAs is diagonal. Its components can be expressed as (see Equation 2.9 in Chapter 2):

[1] We have expressed here the photoelastic constants in contracted notation. The photoelastic components p_{ijkl} become p_{ij}, with 11→1, 22→2, 33→3, 32→4, 31→5 and 21→6. The indices 1, 2 and 3 indicate here the radial, azimutal and height coordinates, respectively.

$$\begin{aligned}\epsilon_{11} &= (1/n^2 + p_{11}\eta_{11} + p_{12}\eta_{33})^{-1} \\ \epsilon_{22} &= (1/n^2 + p_{12}\eta_{11} + p_{12}\eta_{33})^{-1} \\ \epsilon_{22} &= (1/n^2 + p_{12}\eta_{11} + p_{11}\eta_{33})^{-1}\end{aligned} \tag{5.9}$$

In Figure 5.16, we report the values of g_0 calculated for a micropillar constituted by a 10 periods DBR on each side. The calculation was carried out over the branch shown in Figure 5.13. As in the case of the calculations of the mechanical quality factor, the variation of the confined mode spatial profile also leads to strong changes in the value of g_0, since it affects its spatial overlap with the localized optical mode. The maximal values for the calculated g_0 are reached for the mechanical states located in the grey region of the plot, where the displacement is mainly vertical. For such modes, the value of the g_0 reaches values as high as $1\,\mathrm{Mrad\,s^{-1}}$, which are comparable to values obtained for state-of-the-art optomechanical resonators [20, 25].

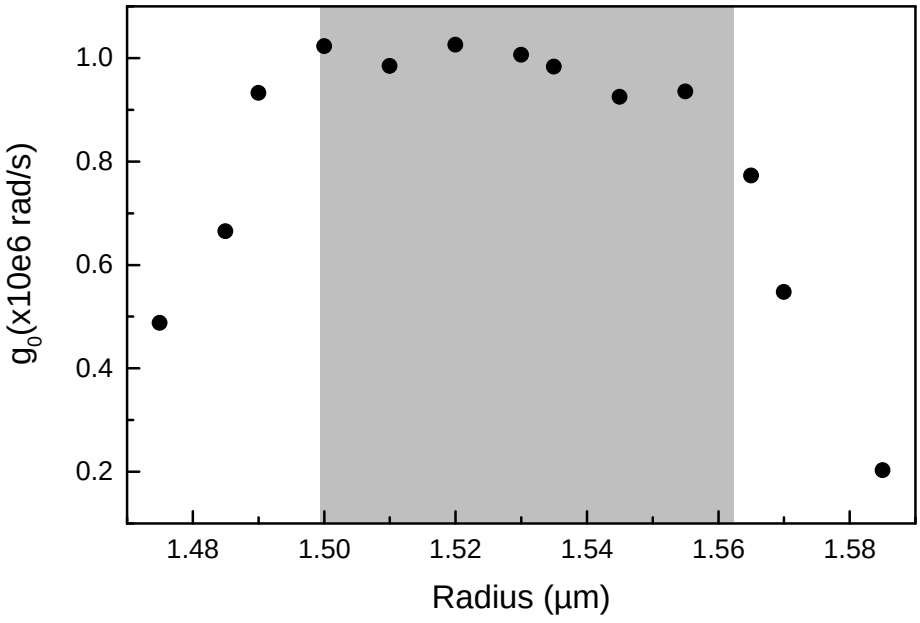

Figure 5.16 – Vacuum optomechanical coupling factor g_0 as a function of radius. The grey region indicates the radii where the mechanical mode is mainly vertical. White regions indicate the intervals where α increases.

The maximal value reached for the g_0 is of the order of $1.025\,\mathrm{Mrad\,s^{-1}}$ for a radius of 1.52 µm. The zero point fluctuation x_{zpf} found for this radius is 0.6325 fm and the effective mass m_{eff} is 1.16 pg.

Despite the strong radial modulation observed in the spatial profile of the confined mechanical mode, the acoustic field still presents a large spatial overlap with the localized optical mode, resulting in large vacuum optomechanical coupling factors. However, we can see in Figure 5.16, that the value of this parameter strongly varies with the radius of the micropillar. Indeed, the g_0 drops by one order of magnitude

over a variation of 50 nm in the radius of the micropillar. The value of the vacuum optomechanical coupling factor in reference [58] was estimated to be in the MHz range. This well corresponds to the calculated values in the central part of the plot.

5.4.3 Local optomechanical properties of micropillars

The calculation of the confined mechanical and optical mode profiles allowed to determine *global* mechanical, optical, and optomechanical parameters. Indeed, the mechanical and optical quality factors correspond to scalar values describing the overall micropillar energy losses. The vacuum optomechanical coupling factor quantifies the global interaction strength between the confined optical and mechanical modes. Although these parameters are particularly relevant for experiments as Brownian motion measurements or sideband optomechanical cooling, other situations require a *local* description of the field distributions that are involved.

This is quite clear in solid-state cavity quantum electrodynamics. We can consider the coupling between a confined optical mode and an excitonic system such as a quantum well or a quantum dot embedded inside the micropillar spacer [54, 205]. In order to get maximal interaction between the excitonic system and the optical mode, the electronic transition must be resonant with the optical field, and the emitter must be located in the regions of maximal electric field intensity $\left|\vec{E}\right|$ [54].

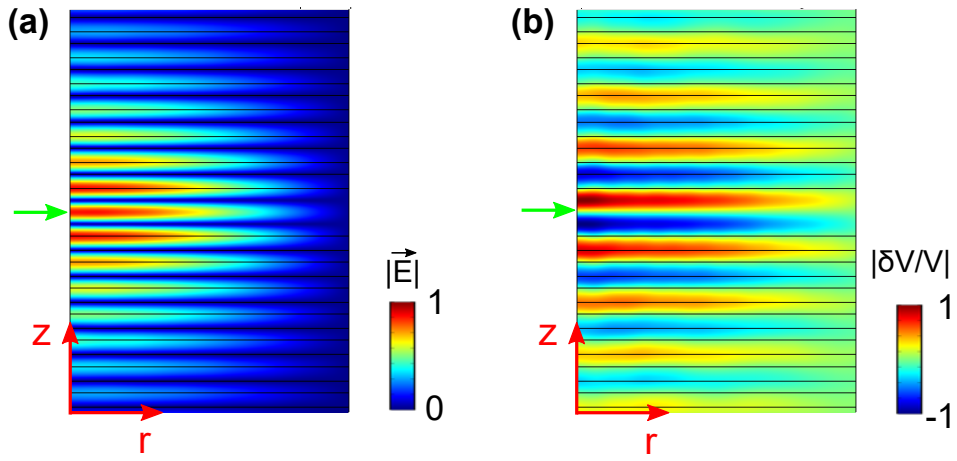

Figure 5.17 – Spatial profiles of the confined optical (Panel **(a)**) and mechanical modes (Panel **(b)**) in a micropillar. The optical resonance wavelength is 925 nm. The mechanical resonance frequency is 18.1 GHz. The plots are detailed views where the λ spacer and 6 layer pairs of the top and bottom mirrors are visible.

We can consider a structure where an excitonic system would be engineered to interact simultaneously with a confined photonic and phononic mode. In this case, we can expect that the emission properties will be modified not only by the confinement of an optical field, but also by the presence of a confined acoustic mode.

Acoustic phonons can couple to electronic transitions through deformation potential, as we have seen in Chapter 2. We can take advantage of this interaction in order to couple an excitonic system to the confined mechanical mode. This was carried out for example in the work reported by Munsch et al. [219], where a quantum dot was coupled to the mechanical motion of nanowire resonator, with mechanical resonance

frequencies in the MHz range. The local strength of this interaction is proportional to the mechanical mode volumetric strain. To maximize the coupling of a quantum emitter such as a quantum dot with the confined mechanical mode through this effect, the two-level system should therefore be placed at the maximum of the $\Delta V/V$ field. In Figure 5.17, we show the spatial profiles of the electric field (Panel (a)) and of the volumetric strain (Panel (b)) for the confined optical and mechanical mode inside a micropillar. The simulated structure corresponds to a λ spacer embedded between two $(\frac{\lambda}{4}, \frac{\lambda}{4})$ optical DBRs, with 12 GaAs/AlAs layer pairs. In Figure 5.17.a, we can see that the optical field presents a maximum in the middle of the spacer, indicated by the green arrow. The spatial profile of the volumetric strain is shown in Panel (b) of Figure 5.17. It is determined by the vertical and radial strain components of the confined acoustic mode. The distribution of these strain components inside the micropillar blurs the radial modulation discussed in the previous sections. As a consequence, the antinodes observed for the displacement field (see Figure 5.4) are not observed for the volumetric strain. Additionnally, this field distribution presents a node at the center of spacer.

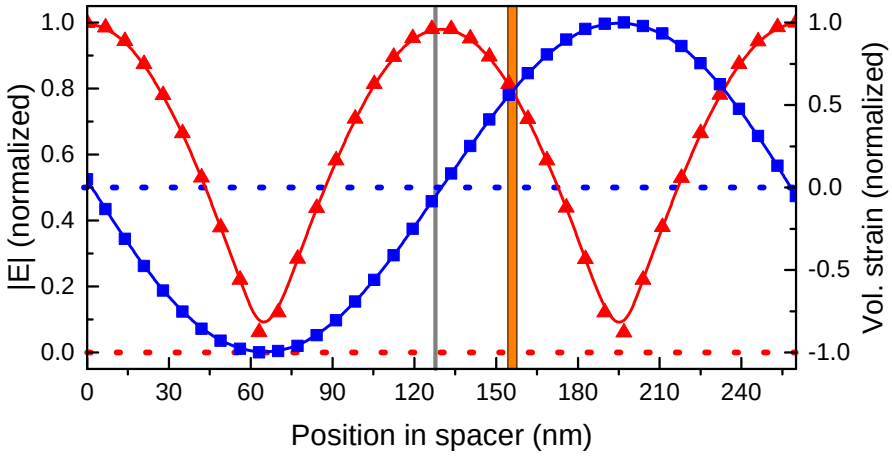

Figure 5.18 – Spatial profiles of the confined modes inside a λ spacer . The fields are plotted along z, at $r = 0$. The red curve shows the normalized electric field modulus (left axis). The blue curve corresponds to the normalized volumetric strain (right axis). The dashed horizontal red and blue lines indicate the origins for the electric field modulus and for the volumetric strain, respectively. The vertical grey line marks the center of the spacer, where the quantum emitter is placed to get maximal interaction with the confined electric field. The orange area shows a position where the quantum emitter would interact simultaneously with the confined optical and mechanical modes.

From these spatial profiles, it is clear that by placing a quantum emitter such as a quantum dot at the center of the micropillar (both in the vertical and radial direction), the system is located at the maximum of the electric field, but at the minimum of the volumetric strain profile. The quantum dot would not couple to the confined mechanical mode. The quantity $\Delta V/V$ presents a maximum at the sides of the λ spacer. It is therefore not possible in this optomechanical resonator to simultaneously maximize the interactions of a semiconductor quantum dot with the confined optical and mechanical modes. An optimized situation, where the quantum

dot would interact with both the confined optical and mechanical mode has to be found. This can be carried out by shifting the position of the quantum dot along the z direction. In Figure 5.18, we show the spatial profiles of the confined optical field (red curve) and of the volumetric strain (blue curve) for the confined mechanical mode inside the spacer along z. The fields are shown for $r = 0$, the radial coordinate for which both fields present maximal intensities. The fields have been normalized by their maximal value. The vertical orange area indicates a position inside the spacer where the magnitude of both normalized fields have equal magnitude. We conclude that this would be an optimal position where to locate a quantum emitter that simultaneously interacts with a confined optical and mechanical mode.

As explained before, current fabrication techniques allow to deterministically position a quantum emitter such as an InGaAs quantum dot at the local maximum of the electric field [118, 220, 221]. By using the same fabrication techniques, it would be therefore possible to precisely place a quantum dot inside the GaAs spacer in such a way that it could interact simultaneously with both the confined optical and mechanical modes. By measuring the photoluminescence spectrum of this quantum emitter that couples to the confined optical mode, it would be possible to demonstrate that its emission properties can also be engineered by controlling its surrounding acoustic environment. Additionally, the simultaneous coupling of a quantum dot with a confined mechanical and optical modes would be a first step toward the realization of strongly coupled atom-cavity-mechanics systems. This would allow the implementation of enhanced optomechanical cooling schemes due to the presence of the two-level system [222].

5.5 Conclusion

In this chapter we have studied the simultaneous confinement of photons and high frequency phonons in GaAs/AlAs micropillars. We have recalled the experimental results that demonstrated the co-localization of an optical and a mechanical mode in planar systems and three dimensional resonators. We performed numerical simulations through the finite element method, that enabled us to study the properties of the confined mechanical mode. We have seen that while the confinement mechanisms which lead to the localization of an acoustic mode are similar to the ones for its optical counterpart, the spatial profile of the two fields and the dependence of their resonance frequencies as a function of the radius of the micropillar present significant differences. We have explained these differences by considering the effect of the Poisson's ratio on the acoustic behavior of a micropillar. This mechanical parameters couples the vertically confined mode to the radial modes, as we have illustrated on a simplified GaAs cylinder model. This leads to the generation of anticrossings in the dependence of the mechanical eigenfrequencies as a function of the micropillar radius. Furthermore, it induces the presence of a fast radial modulation in the displacement field of the confined acoustic mode.

We have then studied the dependence of the mechanical quality factor and of the optomechanical coupling rate as a function of design parameters of the optomechanical resonator. They have shown a strong dependence on the radial dimension of the system. This can be related to the evolution of the mechanical mode profile when this parameter is varied.

Additionally, we have investigated the potential of micropillars as optomechanical resonators. We have shown that by increasing the number of layer pairs in the DBRs, high mechanical and optical quality factors can be reached. This is particularly relevant for optomechanical experiments such as sideband cooling. Furthermore, these simulations demonstrated that the vacuum optomechanical factor and the $Q \cdot f$ product in micropillars can reach values as high as $1\,\mathrm{Mrad\,s^{-1}}$ and 10^{14} Hz, respectively, which are comparable to the values reported for state-of-the-art optomechanical systems.

Finally, in the last section, we provided a qualitative description of the simultaneous interaction of a quantum dot with a confined optical and mechanical mode. By positioning the quantum dot in a region of the spacer where it would interact with both the mechanical and the optical confined mode, we could measure the modification of the emission properties of a quantum emitter, due to the engineering of its phononic environment.

Conclusions

The engineering of mechanical vibrations at the nanoscale has nowadays become a mature field of research, and the number of systems aiming to control phonon dynamics in the hypersonic range has significantly diversified. In particular, this allowed the development of nanostructured systems enabling the confinement of high frequency mechanical vibrations. These resonant structures play a central role in nanophononics, for example in the development of high frequency acoustic devices, such as phonon filters, acoustic monochromatic detectors, or SASERs. Additionally, the development of high frequency mechanical resonators has become particularly relevant in other fields of research, such as cavity optomechanics. In this thesis, we have investigated novel nanophononic structures that localize mechanical vibrations in the hypersonic range, and we have studied their interactions with confined optical fields. The general purpose of this work was also to progressively move from opto-phononic systems that confine light and mechanical vibrations in a planar geometry, to resonators that simultaneously localize both fields in the three dimensions of space.

One-dimensional acoustic superlattices are well known in nanophononics, and have nowadays become an essential tool for the manipulation of high frequency mechanical vibrations. In particular, they allow the creation of acoustic minigaps in their phononic band diagrams, that is, frequency intervals for which mechanical waves cannot propagate. Acoustic superlattices enable the fabrication of Fabry-Perot cavities, which have nowadays become the canonical resonator in layered nanophononic systems.

Our first research line consisted in further exploring the physical mechanisms that can be used for confining longitudinal acoustic phonons. We studied these novel confinement strategies in nanophononic layered platforms, for mechanical waves at resonance frequencies around 350 GHz. This work was presented in Chapter 3 of the manuscript. These designs where inspired from band engineering confinement methods that have been implemented in photonics. The resonators were experimentally studied through high resolution cavity-enhanced Raman scattering spectroscopy. This technique is well adapted for measuring the acoustic properties of nanophononic cavities operating in the few hundreds of GHz frequency range.

The first one-dimensional confinement strategy that we have implemented is based on the local engineering of band structures in an acoustic periodic medium. This was carried out by progressively changing the layer thicknesses of a GaAs/AlAs superlattice. In this way, we adiabatically bend the local acoustic band diagram of the structure. This enables the creation of a "phononic quantum well", in which the state is smoothly localized.

In optics, the adiabatic localization of photons enabled the fabrication of three dimensional optical resonators with improved quality factors with respect to traditional photonic Fabry-Perot designs. In a similar way, the progressive confinement

of an acoustic state studied in this thesis could lead to the development of future nanophononic three-dimensional resonators with enhanced confinement properties.

The Raman scattering spectra obtained on a one-dimensional adiabatic cavity embedded in an optical resonator clearly demonstrate the existence of the designed confined state. Furthermore, the experimental data is perfectly reproduced by numerical simulations based on a photoelastic model. This allowed us to identify the origin of all the Raman features present the measured spectra. We also numerically investigated the impact of the adiabatic transformation magnitude on the spatial profile of the confined modes, and on their mechanical quality factors. We demonstrated that in the presented adiabatic cavity, the energy, the spatial profile, and the Raman activity of the confined modes can be tailored by controlling the design of the artificial phononic potential.

A possible way to implement such adiabatic localization in three dimensional resonators would be to fabricate micropillar structures that confine mechanical modes in all directions of space, from adiabatic nanophononic planar cavities. We could then study the effect of the adiabatic design on the mechanical quality factors of the confined mechanical modes, and compare it to the confinement properties of standard Fabry-Perot based micropillars.

The second confinement strategy that we have proposed is the localization of interface states by taking advantage of the topological phases of acoustic superlattices. The topological properties of a nanophononic layered structure are described in its acoustic band diagram by the Zak phases, that is, the topological invariants associated to the represented bands. It is possible to change the topological phase of an acoustic superlattice by band inversion, i.e. by inverting the symmetry properties of the mechanical modes bounding a given acoustic minigap. This is carried out by closing and reopening the considered forbidden frequency interval. In this work, we have implemented band inversion by changing the relative thicknesses of the GaAs and AlAs layers in the superlattice unit cell. By concatening two DBRs in different topological phases, we create a confined state that is localized at the interface between the two structures. We have carried out Raman scattering measurements on topological acoustic nanocavities embedded in optical resonators. The obtained spectra clearly demonstrate the presence of an interface state inside the acoustic cavity. The topological resonators presented in this work constitutes a first experimental demonstration of the use of topological phases for the development of nanophononic systems. Other designs could be implemented for the study of confined acoustic states based on topological invariants. In optics, photonic structures have been fabricated in order to generate topologically protected edge states by coupling series of micropillar resonators [223]. These structures have been developed in close analogy to the Su-Schrieffer–Heeger (SSH) model, which was originally proposed to understand the physics of electrons in polyacetylene [224]. This model could be readily applied to high frequency acoustic systems, since nanophononic structures constituted by several evanescently coupled resonators can be implemented to simulate long chains of atoms [173]. Therefore, layered nanophononic systems could be used for the further development of topologically engineered interface and edge states operating in the hypersonic range, that are robust against fabrication defects.

Based on the planar structures studied in Chapter 3, we fabricated micropillar resonators with micrometric lateral sizes, that allow to confine optical modes in the three dimensions of space. The spacers of these photonic resonators are constituted by

topological nanophononic cavities that are resonant at frequencies around 300 GHz. Due to the small wavelength of the confined mechanical modes with respect to the micropillar lateral dimensions, the acoustic cavities could still be considered as planar nanophononic systems. The presentation of these opto-phononic platforms and of the experimental results obtained on these structures was carried out in Chapter 4.

The finite lateral dimensions of the considered cavities lead to the creation of a discrete set of optical resonances. This effect needs to be taken into account in order to optically probe the acoustic properties of the embedded nanophononic resonators. We have developed an experimental set-up that allows to couple the incident laser and to collect the Raman scattered signals through the same confined optical mode. The measurement of the inelastically scattered light generated by the acoustic confined mode is here experimentally challenging, since the laser light that is reflected by the micropillar spatially overlaps with the Raman signals, and is an intense source of stray light. By implementing optical filtering techniques, we were able to probe the acoustic confinement properties of nanophononic resonators embedded in micropillars. The intensity of the measured Raman spectra strongly depends on the detuning of the fundamental optical mode wavelength with respect to the laser line and to the probed Raman signals. Furthermore, the magnitude of the probed Raman peaks presents a nonlinear behavior with respect to the laser incident power. We have interpreted this result in terms of thermo-optic effects that shift the optical cavity resonance frequency when the intensity of the intracavity field is increased. We experimentally showed that this effect is enhanced in micropillar resonators with respect to planar structures, since their micrometric lateral dimensions prevents efficient heat dissipation. This observation constitutes a first experimental result where micropillar cavities present a distinctly different behavior with respect of their one-dimensional counterpart, in the context of probing the acoustic properties of nanophononic structures.

The acoustic resonators studied in Chapter 4 enable the localization of optical fields in the three directions of space. However, the characterized systems were still considered to behave as planar structures for confined mechanical vibrations, at 300 GHz. In order to get the simultaneous three dimensional localization of photons and phonons in micropillars, one possible strategy is to decrease the resonance frequencies of the confined acoustic modes. It has been shown that a GaAs/AlAs DBR-based Fabry-Perot resonator designed to confine an optical mode in the NIR range is automatically optimized for the localization of a mechanical mode at resonance frequencies around 20 GHz. This is due to the intrinsic acoustic and optical properties of GaAs and AlAs semiconductor materials. By fabricating micropillars out of these planar opto-phononic resonators, we can obtain a system in which the acoustic mode and the optical field are simultaneously three-dimensionally confined. This was recently demonstrated through pump-probe coherent phonon generation and detection measurements.

The experimental results obtained on these three dimensional optomechanical resonators motivated the numerical modeling of these systems, that was presented in Chapter 5 of this manuscript. Such theoretical study of the optical, mechanical, and optomechanical behavior of micropillars was carried out by performing simulations based on the finite element method.

We have first compared the behaviors of the confined optical and mechanical modes inside a micropillar. Both fields present a vertical confinement, due to the presence of the GaAs/AlAs DBRs, which play the role of acoustic and optical mirrors. In the

radial direction, a micropillar acts as an acoustic and as an optical waveguide, leading to the full localization of both fields inside the resonator. However, when considering the confined mechanical mode spatial profile, we noticed a strong radial modulation of the displacement field. In contrast, this modulation is not observed in the spatial profile of the confined optical mode. Furthermore, the dependence of the mechanical eigenfrequencies on the micropillar radius presents a series of anticrossings, which are absent when considering the same dependence for the optical confined mode.

We have explained these particular features of the confined mechanical mode by considering the effect of the Poisson's ratio, starting from a simplified model, that is, a GaAs cylinder. In particular, this parameter couples different mechanical degrees of freedom, in this case the vertical strain components to the radial ones. This leads to the generation of the anticrossings in the micropillar mechanical eigenfrequencies dependence, and induces the radial modulation observed in the displacement fields of the confined phononic mode. Furthermore, due to the coupling of the radial and vertical mechanical degrees of freedom, the spatial profiles of the confined acoustic mode strongly depends on the micropillar radius. This dependence entails the fast changes observed in the values of the mechanical quality factor and of the vacuum optomechanical coupling factor as a function of the micropillar lateral dimensions.

The numerical simulations presented in this manuscript show that micropillars are a promising platform in the context of high frequency cavity optomechanics. Indeed, these resonators work at unprecedented high mechanical frequencies (around 18 GHz) with respect to state-of-the art optomechanical systems, and with high values for the quality factors (greater than 10^3 in the considered DBR configurations) and for the $Q \cdot f$ products ($\approx 10^{14}$ Hz). In addition, they can provide very high optomechanical coupling factors (of the order of 10^6 rad/s). This numerical description of the micropillar opto-phononic properties is also relevant for optimizing the coupling of quantum emitters, such as InGaAs quantum dots, to the confined mechanical and optical modes. This would pave the way toward the study of hybrid cavity optomechanical systems coupled to excitonic two-level systems.

So far, the only experimental technique that allowed to put in evidence the confinement of mechanical modes in micropillars at resonance frequencies around 20 GHz are pump-probe experiments. This method relies on the impulsive generation of coherent mechanical waves inside the considered structures. Experimental techniques based on the measurement of micropillars thermal fluctuations, such as Brownian motion experiments or Raman scattering spectroscopy, have not been successfully implemented for this purpose. This is highly desirable in the context of cavity optomechanics, where mechanical modes are usually probed in this regime.

The Raman scattering experiments performed on micropillars embedding acoustic resonators have shown that it is possible to probe confined mechanical modes at resonance frequencies around 300 GHz. By improving our current experimental set-up, in particular by implementing better stray light filtering techniques, it might be possible to approach resonance frequencies around 20 GHz. Therefore, the three-dimensionally confined acoustic modes discussed in Chapter 5 could be probed through Raman scattering spectroscopy measurements. This would constitute a step forward toward the implementation of Brownian motion measurements on these optomechanical resonators.

Brownian motion experiments would be a very powerful tool for characterizing the mechanical and optomechanical properties of GaAs/AlAs micropillars. Indeed,

this experimental technique is widely used in cavity optomechanics to measure the phononic population of confined mechanical modes, and to monitor the effects of optical forces on the mechanical motion of optomechanical resonators. Nevertheless, implementing Brownian motion measurement schemes working at the required NIR optical wavelengths and tens of GHz acoustic frequencies is challenging. The high mechanical resonance frequency of the considered mechanical mode implies the use of detection lines with large bandwidths. Reaching a sufficiently high sensitivity is in these conditions technically difficult, in particular for optical signals in the near infrared range.

One way to overcome these experimental challenges could be to lower the temperature of the optomechanical resonator. Despite the fact that the average phononic population in the confined mode would decrease, this could lead to an overall increase in the intensity of the Brownian motion signals. In particular, this is due to the fact that the mechanical quality factor of the micropillar would be enhanced. This behavior has been observed in other GaAs based optomechanical resonators, such as microdisks [147]. Increasing the mechanical quality factor would "sharpen" the Brownian motion spectrum, facilitating its measurement over the noise background of the detection line. Furthermore, it has been shown that, close to the electronic transitions of the GaAs layers, the photoelastic constant p_{12} presents a resonant behavior [159]. This enhancement of the photoelastic effect is even stronger at low temperatures. By measuring the micropillar optomechanical response in these conditions, it could be possible to probe the Brownian motion of a micropillar with a sufficiently high signal to noise ratio. This would enable the study of high frequency optomechanical resonators with large optomechanical coupling factors, facilitating the preparation of a mechanical oscillator in its ground state.

The work presented in this thesis offers multiple perspectives for the control of acoustic phonon dynamics in the GHz-THz range. Through the control of the interactions between phonons and other excitations, the engineering of optophononic resonators could have an impact in novel applications in solid state physics, including optomechanics and quantum technologies.

Bibliography

[1] N. W. Ashcroft and N. D. Mermin. *Solid State Physics*. Brooks Cole, 1976.

[2] P. Y. Yu and M. Cardona. *Fundamentals of Semiconductors: Physics and Materials Properties*. Springer, 2010.

[3] B. Jalali and S. Fathpour. Silicon photonics. *Journal of Lightwave Technology*, 24(12):4600–4615, 2006.

[4] Michael Riordan, Lillian Hoddeson, and Conyers Herring. The invention of the transistor. *Rev. Mod. Phys.*, 71:S336–S345, Mar 1999.

[5] Martin Maldovan. Sound and heat revolutions in phononics. *Nature*, 503:209–217, Nov 2013. Review Article.

[6] Sebastian Volz, Jose Ordonez-Miranda, Andrey Shchepetov, Mika Prunnila, Jouni Ahopelto, Thomas Pezeril, Gwenaelle Vaudel, Vitaly Gusev, Pascal Ruello, Eva M. Weig, Martin Schubert, Mike Hettich, Martin Grossman, Thomas Dekorsy, Francesc Alzina, Bartlomiej Graczykowski, Emigdio Chavez-Angel, J. Sebastian Reparaz, Markus R. Wagner, Clivia M. Sotomayor-Torres, Shiyun Xiong, Sanghamitra Neogi, and Davide Donadio. Nanophononics: state of the art and perspectives. *The European Physical Journal B*, 89(1):15, 2016.

[7] Nianbei Li, Jie Ren, Lei Wang, Gang Zhang, Peter Hänggi, and Baowen Li. Colloquium: Phononics: Manipulating heat flow with electronic analogs and beyond. *Rev. Mod. Phys.*, 84:1045–1066, Jul 2012.

[8] Thorne Lay, Hiroo Kanamori, Charles J. Ammon, Meredith Nettles, Steven N. Ward, Richard C. Aster, Susan L. Beck, Susan L. Bilek, Michael R. Brudzinski, Rhett Butler, Heather R. DeShon, Göran Ekström, Kenji Satake, and Stuart Sipkin. The Great Sumatra-Andaman Earthquake of 26 December 2004. *Science*, 308(5725):1127–1133, 2005.

[9] T. T. Trang Nghiêm and Pierre-Olivier Chapuis. Phononic thermal resistance due to a finite periodic array of nano-scatterers. *Journal of Applied Physics*, 120(4):044305, 2016.

[10] Alexander A. Balandin. Nanophononics: Phonon engineering in nanostructures and nanodevices. *Journal of Nanoscience and Nanotechnology*, 5(7):1015–1022, 2005.

[11] Eric Pop. Energy dissipation and transport in nanoscale devices. *Nano Research*, 3(3):147–169, 2010.

[12] Zhong Yan, Guanxiong Liu, Javed M. Khan, and Alexander a. Balandin. Graphene quilts for thermal management of high-power GaN transistors. *Nature Communications*, 3(May):827, 2012.

[13] Paulina Hołuj, Christoph Euler, Benjamin Balke, Ute Kolb, Gregor Fiedler, Mathis M. Müller, Tino Jaeger, Emigdio Chávez Angel, Peter Kratzer, and Gerhard Jakob. Reduced thermal conductivity of tinisn/hfnisn superlattices. *Phys. Rev. B*, 92:125436, Sep 2015.

[14] P. E. Hopkins, C. M. Reinke, M. F. Su, R. H. Olsson, E. A. Shaner, Z. C. Leseman, J. R. Serrano, L. M. Phinney, and I. El-Kady. Reduction in the thermal conductivity of single crystalline silicon by phononic crystal patterning. *Nano Letters*, 11(1):107–112, 2011. PMID: 21105717.

[15] Bruce L. Davis and Mahmoud I. Hussein. Nanophononic metamaterial: Thermal conductivity reduction by local resonance. *Phys. Rev. Lett.*, 112:055505, Feb 2014.

[16] Masako Tanaka. An industrial and applied review of new MEMS devices features. *Microelectronic Engineering*, 84(5):1341 – 1344, 2007. Proceedings of the 32nd International Conference on Micro- and Nano-Engineering.

[17] K. L. Ekinci and M. L. Roukes. Nanoelectromechanical systems. *Review of Scientific Instruments*, 76(6):061101, 2005.

[18] D. Rugar, R. Budakian, H. J. Mamin, and B. W. Chui. Single spin detection by magnetic resonance force microscopy. *Nature*, 430:329 EP –, Jul 2004.

[19] J. Chaste, A. Eichler, J. Moser, G. Ceballos, R. Rurali, and A. Bachtold. A nanomechanical mass sensor with yoctogram resolution. *Nature Nanotechnology*, 7:301 EP –, Apr 2012.

[20] Markus Aspelmeyer, Tobias J. Kippenberg, and Florian Marquardt. Cavity optomechanics. *Rev. Mod. Phys.*, 86:1391–1452, Dec 2014.

[21] Michael Metcalfe. Applications of cavity optomechanics. *Applied Physics Reviews*, 1(3):031105, 2014.

[22] S. Bose, K. Jacobs, and P. L. Knight. Preparation of nonclassical states in cavities with a moving mirror. *Phys. Rev. A*, 56:4175–4186, Nov 1997.

[23] K. Børkje, A. Nunnenkamp, and S. M. Girvin. Proposal for entangling remote micromechanical oscillators via optical measurements. *Phys. Rev. Lett.*, 107:123601, Sep 2011.

[24] J. Chan, T. P. M. Alegre, Amir H. Safavi-Naeini, Jeff T. Hill, Alex Krause, Simon Gröblacher, Markus Aspelmeyer, and Oskar Painter. Laser cooling of a nanomechanical oscillator into its quantum ground state. *Nature*, 478:89–92, Oct 2011.

[25] Jasper Chan, Amir H. Safavi-Naeini, Jeff T. Hill, Seán Meenehan, and Oskar Painter. Optimized optomechanical crystal cavity with acoustic radiation shield. *Applied Physics Letters*, 101(8):081115, 2012.

[26] D. T. Nguyen, C. Baker, W. Hease, S. Sejil, P. Senellart, A. Lemaître, S. Ducci, G. Leo, and I. Favero. Ultrahigh Q-frequency product for optomechanical disk resonators with a mechanical shield. *Applied Physics Letters*, 103(24):241112, 2013.

[27] A. Barfuss, J. Teissier, E. Neu, A. Nunnenkamp, and P. Maletinsky. Strong mechanical driving of a single electron spin. *Nature Physics*, 11:820 EP –, Aug 2015.

[28] Martin V. Gustafsson, Thomas Aref, Anton Frisk Kockum, Maria K. Ekström, Göran Johansson, and Per Delsing. Propagating phonons coupled to an artificial atom. *Science*, 346(6206):207–211, 2014.

[29] R. P. G. McNeil, M. Kataoka, C. J. B. Ford, C. H. W. Barnes, D. Anderson, G. A. C. Jones, I. Farrer, and D. A. Ritchie. On-demand single-electron transfer between distant quantum dots. *Nature*, 477:439 EP –, Sep 2011.

[30] A. Fainstein, B. Jusserand, and V. Thierry-Mieg. Raman scattering enhancement by optical confinement in a semiconductor planar microcavity. *Physical Review Letters*, 75(20):3764–3767, 1995.

[31] T. J. Kippenberg and K. J. Vahala. Cavity optomechanics: Back-action at the mesoscale. *Science*, 321(5893):1172–1176, 2008.

[32] C. Mechri, P. Ruello, and V. Gusev. Confined coherent acoustic modes in a tubular nanoporous alumina film probed by picosecond acoustics methods. *New Journal of Physics*, 14(2):023048, 2012.

[33] Vincent Juvé, Aurélien Crut, Paolo Maioli, Michel Pellarin, Michel Broyer, Natalia Del Fatti, and Fabrice Vallée. Probing elasticity at the nanoscale: Terahertz acoustic vibration of small metal nanoparticles. *Nano Letters*, 10(5):1853–1858, 2010.

[34] Alexey M. Lomonosov, Adil Ayouch, Pascal Ruello, Gwenaelle Vaudel, Mikhail R. Baklanov, Patrick Verdonck, Larry Zhao, and Vitalyi E. Gusev. Nanoscale Noncontact Subsurface Investigations of Mechanical and Optical Properties of Nanoporous Low-k Material Thin Film. *ACS Nano*, 6(2):1410–1415, 2012. PMID: 22211667.

[35] B. C. Daly, K. Kang, Y. Wang, and David G. Cahill. Picosecond ultrasonic measurements of attenuation of longitudinal acoustic phonons in silicon. *Phys. Rev. B*, 80:174112, Nov 2009.

[36] Fernando Pérez-Cota, Richard J. Smith, Emilia Moradi, Leonel Marques, Kevin F. Webb, and Matt Clark. High resolution 3D imaging of living cells with sub-optical wavelength phonons. *Scientific Reports*, 6:39326, Dec 2016.

[37] Bertrand Audoin, Clément Rossignol, Nikolay Chigarev, Mathieu Ducousso, Guillaume Forget, Fabien Guillemot, and Marie-Christine Durrieu. Picosecond acoustics in vegetal cells: non invasive in vitro measurements at a sub-cell scale. *Physics Procedia*, 3(1):323 – 331, 2010. International Congress on Ultrasonics, Santiago de Chile, January 2009.

[38] Norberto Daniel Lanzillotti Kimura. *Acoustic phonon dynamics in nanometric multilayers*. Theses, Université Pierre et Marie Curie - Paris VI, May 2009.

[39] M. Cardona and G. Güntherodt. *Light Scattering in Solids V: Superlattices and Other Microstructures*. Springer, 1989.

[40] V. Villafane, P. Soubelet, A. E. Bruchhausen, N. D. Lanzillotti-Kimura, B. Jusserand, A. Lemaître, and A. Fainstein. Slow light and slow acoustic phonons in optophononic resonators. *Physical Review B - Condensed Matter and Materials Physics*, 94(20):1–10, 2016.

[41] A. Soukiassian, W. Tian, D. A. Tenne, X. X. Xi, D. G. Schlom, N. D. Lanzillotti-Kimura, A. Bruchhausen, A. Fainstein, H. P. Sun, X. Q. Pan, A. Cros, and A. Cantarero. Acoustic bragg mirrors and cavities made using piezoelectric oxides. *Applied Physics Letters*, 90(4):042909, 2007.

[42] M. Trigo, A. Bruchhausen, A. Fainstein, B. Jusserand, and V. Thierry-Mieg. Confinement of acoustical vibrations in a semiconductor planar phonon cavity. *Phys. Rev. Lett.*, 89:227402, Nov 2002.

[43] A. Huynh, B. Perrin, N. D. Lanzillotti-Kimura, B. Jusserand, A. Fainstein, and A. Lemaître. Subterahertz monochromatic acoustic wave propagation using semiconductor superlattices as transducers. *Phys. Rev. B*, 78:233302, Dec 2008.

[44] T. Czerniuk, C. Brüggemann, J. Tepper, S. Brodbeck, C. Schneider, M. Kamp, S. Höfling, B. A. Glavin, D. R. Yakovlev, A. V. Akimov, and M. Bayer. Lasing from active optomechanical resonators. *Nature Communications*, 5:4038 EP –, Jul 2014. Article.

[45] C. Brüggemann, A. V. Akimov, A. V. Scherbakov, M. Bombeck, C. Schneider, S. Höfling, A. Forchel, D. R. Yakovlev, and M. Bayer. Laser mode feeding by shaking quantum dots in a planar microcavity. *Nature Photonics*, 6:30–34, Nov 2011.

[46] W. Maryam, A. V. Akimov, R. P. Campion, and A. J. Kent. Dynamics of a vertical cavity quantum cascade phonon laser structure. *Nature Communications*, 4:2184 EP –, Jul 2013.

[47] A. J. Kent, R. N. Kini, N. M. Stanton, M. Henini, B. A. Glavin, V. A. Kochelap, and T. L. Linnik. Acoustic Phonon Emission from a Weakly Coupled Superlattice under Vertical Electron Transport: Observation of Phonon Resonance. *Phys. Rev. Lett.*, 96:215504, Jun 2006.

[48] M. F. Pascual Winter, G. Rozas, B. Jusserand, B. Perrin, A. Fainstein, P. O. Vaccaro, and S. Saravanan. Selective optical generation of a coherent acoustic nanocavity mode. *AIP Conference Proceedings*, 893(JUNE):965–966, 2007.

[49] Ling Lu, John D. Joannopoulos, and Marin Soljacic. Topological photonics. *Nature Photonics*, 8:821–829, Oct 2014. Review Article.

[50] Cheng He, Xu Ni, Hao Ge, Xiao-Chen Sun, Yan-Bin Chen, Ming-Hui Lu, Xiao-Ping Liu, and Yan-Feng Chen. Acoustic topological insulator and robust one-way sound transport. *Nature Physics*, 2005(20032092):2005–2007, 2016.

[51] Christian Brendel, Vittorio Peano, Oskar Painter, and Florian Marquardt. Snowflake phononic topological insulator at the nanoscale. *Phys. Rev. B*, 97:020102, Jan 2018.

[52] B. Gayral, J. M. Gérard, B. Legrand, E. Costard, and V. Thierry-Mieg. Optical study of gaas/alas pillar microcavities with elliptical cross section. *Applied Physics Letters*, 72(12):1421–1423, 1998.

[53] F. Albert, C. Hopfmann, A. Eberspächer, F. Arnold, M. Emmerling, C. Schneider, S. Höfling, A. Forchel, M. Kamp, J. Wiersig, and S. Reitzenstein. Directional whispering gallery mode emission from limaçon-shaped electrically pumped quantum dot micropillar lasers. *Applied Physics Letters*, 101(2):021116, 2012.

[54] O. Gazzano, S. Michaelis de Vasconcellos, C. Arnold, A. Nowak, E. Galopin, I. Sagnes, L. Lanco, A. Lemaître, and P. Senellart. Bright solid-state sources of indistinguishable single photons. *Nature Communications*, 4:1425, Feb 2013.

[55] Marta Galbiati, Lydie Ferrier, Dmitry D. Solnyshkov, Dimitrii Tanese, Esther Wertz, Alberto Amo, Marco Abbarchi, Pascale Senellart, Isabelle Sagnes, Aristide Lemaître, Elisabeth Galopin, Guillaume Malpuech, and Jacqueline Bloch. Polariton condensation in photonic molecules. *Phys. Rev. Lett.*, 108:126403, Mar 2012.

[56] A. Fainstein, N. D. Lanzillotti-Kimura, B. Jusserand, and B. Perrin. Strong optical-mechanical coupling in a vertical gaas/alas microcavity for subterahertz phonons and near-infrared light. *Phys. Rev. Lett.*, 110:037403, Jan 2013.

[57] Juan Restrepo, Ivan Favero, and Cristiano Ciuti. Fully coupled hybrid cavity optomechanics: Quantum interferences and correlations. *Phys. Rev. A*, 95:023832, Feb 2017.

[58] S. Anguiano, A. E. Bruchhausen, B. Jusserand, I. Favero, F. R. Lamberti, L. Lanco, I. Sagnes, A. Lemaître, N. D. Lanzillotti-Kimura, P. Senellart, and A. Fainstein. Micropillar resonators for optomechanics in the extremely high 19–95-GHz frequency range. *Phys. Rev. Lett.*, 118:263901, Jun 2017.

[59] J. D. Joannopoulos, S. G. Johnson, J. N. Jn Winn, and R. D. Meade. *Photonic crystals: molding the flow of light*. Princeton University Press, 2008.

[60] E. Yablonovitch. Inhibited spontaneous emission in solid-state physics and electronics. *Phys. Rev. Lett.*, 58:2059–2062, May 1987.

[61] K. Sakoda. *Optical Properties of Photonic Crystals*. Springer, 2001.

[62] H. A. Macleod. *Thin-Film Optical Filters*. Taylor & Francis, 2010.

[63] J. L. Jewell, J. P. Harbison, A. Scherer, Y. H. Lee, and L. T. Florez. Vertical-cavity surface-emitting lasers: Design, growth, fabrication, characterization. *IEEE Journal of Quantum Electronics*, 27(6):1332–1346, 1991.

[64] J. Rarity and C. Weisbuch, editors. *Microcavities and Photonic Bandgaps: Physics and Applications*. Springer, 1996.

[65] C. Weisbuch, M. Nishioka, A. Ishikawa, and Y. Arakawa. Observation of the coupled exciton-photon mode splitting in a semiconductor quantum microcavity. *Phys. Rev. Lett.*, 69:3314–3317, Dec 1992.

[66] J. M. Gérard, B. Sermage, B. Gayral, B. Legrand, E. Costard, and V. Thierry-Mieg. Enhanced spontaneous emission by quantum boxes in a monolithic optical microcavity. *Phys. Rev. Lett.*, 81:1110–1113, Aug 1998.

[67] V. Narayanamurti, H. L. Störmer, M. A. Chin, A. C. Gossard, and W. Wiegmann. Selective transmission of high-frequency phonons by a superlattice: The "dielectric" phonon filter. *Phys. Rev. Lett.*, 43:2012–2016, Dec 1979.

[68] C. Colvard, R. Merlin, M. V. Klein, and A. C. Gossard. Observation of folded acoustic phonons in a semiconductor superlattice. *Phys. Rev. Lett.*, 45:298–301, Jul 1980.

[69] M Cardona and R. Merlin. *Light Scattering in Solids IX: Novel Materials and Techniques*, volume 108. Springer-Verlag, Berlin Heidelberg, topics app edition, 2007.

[70] M. S. Kushwaha, P. Halevi, L. Dobrzynski, and B. Djafari-Rouhani. Acoustic band structure of periodic elastic composites. *Phys. Rev. Lett.*, 71:2022–2025, Sep 1993.

[71] E. N. Economou and M. Sigalas. Stop bands for elastic waves in periodic composite materials. *The Journal of the Acoustical Society of America*, 95(4):1734–1740, 1994.

[72] R. Martínez-Sala, J. Sancho, J. V. Sánchez, V. Gómez, J. Llinares, and F. Meseguer. Sound attenuation by sculpture. *Nature*, 378:241, Nov 1995.

[73] F. Cervera, L. Sanchis, J. V. Sánchez-Pérez, R. Martínez-Sala, C. Rubio, F. Meseguer, C. López, D. Caballero, and J. Sánchez-Dehesa. Refractive acoustic devices for airborne sound. *Phys. Rev. Lett.*, 88:023902, Dec 2001.

[74] S. Yang, J. H. Page, Z. Liu, M. L. Cowan, C. T. Chan, and P. Sheng. Ultrasound tunneling through 3D phononic crystals. *Phys. Rev. Lett.*, 88:104301, Feb 2002.

[75] S. Benchabane, A. Khelif, J.-Y. Rauch, L. Robert, and V. Laude. Evidence for complete surface wave band gap in a piezoelectric phononic crystal. *Phys. Rev. E*, 73:065601, Jun 2006.

[76] T. Gorishnyy, C. K. Ullal, M. Maldovan, G. Fytas, and E. L. Thomas. Hypersonic phononic crystals. *Phys. Rev. Lett.*, 94:115501, Mar 2005.

[77] A. Huynh, N. D. Lanzillotti-Kimura, B. Jusserand, B. Perrin, A. Fainstein, M. F. Pascual-Winter, E. Peronne, and A. Lemaître. Subterahertz phonon dynamics in acoustic nanocavities. *Phys. Rev. Lett.*, 97:115502, Sep 2006.

[78] P. A. Deymier. *Acoustic Metamaterials and Phononic Crystals: 173 (Springer Series in Solid-State Sciences)*. Springer-Verlag, 2013.

[79] R. H. Olsson III and I. El-Kady. Microfabricated phononic crystal devices and applications. *Measurement Science and Technology*, 20(1):012002, 2009.

[80] A. Khelif, A. Choujaa, S. Benchabane, B. Djafari-Rouhani, and V. Laude. Guiding and bending of acoustic waves in highly confined phononic crystal waveguides. *Applied Physics Letters*, 84(22):4400–4402, 2004.

[81] S. Yang, J. H. Page, Z. Liu, M. L. Cowan, C. T. Chan, and P. Sheng. Focusing of sound in a 3D phononic crystal. *Phys. Rev. Lett.*, 93:024301, Jul 2004.

[82] B. Graczykowski, A. El Sachat, J. S. Reparaz, M. Sledzinska, M. R. Wagner, E. Chavez-Angel, Y. Wu, S. Volz, F. Alzina, and C. M. Sotomayor Torres. Thermal conductivity and air-mediated losses in periodic porous silicon membranes at high temperatures. *Nature Communications*, 8(1):415, 2017.

[83] M. Maldovan and E. L. Thomas. Simultaneous localization of photons and phonons in two-dimensional periodic structures. *Applied Physics Letters*, 88(25):251907, 2006.

[84] N. D. Lanzillotti-Kimura, A. Fainstein, A. Huynh, B. Perrin, B. Jusserand, A. Miard, and A. Lemaître. Coherent generation of acoustic phonons in an optical microcavity. *Phys. Rev. Lett.*, 99:217405, Nov 2007.

[85] I. E. Psarobas, N. Papanikolaou, N. Stefanou, B. Djafari-Rouhani, B. Bonello, and V. Laude. Enhanced acousto-optic interactions in a one-dimensional phoxonic cavity. *Phys. Rev. B*, 82:174303, Nov 2010.

[86] Alexander G. Krause, Martin Winger, Tim D. Blasius, Qiang Lin, and Oskar Painter. A high-resolution microchip optomechanical accelerometer. *Nature Photonics*, 6:768–772, Oct 2012.

[87] A. H. Safavi-Naeini, T. P. Mayer Alegre, J. Chan, M. Eichenfield, M. Winger, Q. Lin, J. T. Hill, D. E. Chang, and O. Painter. Electromagnetically induced transparency and slow light with optomechanics. *Nature*, 472:69–73, Mar 2011.

[88] John Orton and Tom Foxon. *Molecular Beam Epitaxy: A Short History*. Oxford University Press, 2015.

[89] G. Rozas, M. F. Pascual Winter, B. Jusserand, A. Fainstein, B. Perrin, E. Semenova, and A. Lemaître. Lifetime of THz acoustic nanocavity modes. *Phys. Rev. Lett.*, 102:015502, Jan 2009.

[90] P. Giannozzi, S. de Gironcoli, P. Pavone, and S. Baroni. Ab initio calculation of phonon dispersions in semiconductors. *Phys. Rev. B*, 43:7231–7242, Mar 1991.

[91] H.-Y. Hao and H. J. Maris. Study of phonon dispersion in silicon and germanium at long wavelengths using picosecond ultrasonics. *Phys. Rev. Lett.*, 84:5556–5559, Jun 2000.

[92] H.-Y. Hao and H. J. Maris. Dispersion of the long-wavelength phonons in Ge, Si, GaAs, quartz, and sapphire. *Phys. Rev. B*, 63:224301, May 2001.

[93] R. Legrand, A. Huynh, S. Vincent, B. Perrin, and A. Lemaître. Device for acoustic pulse echo experiments in the subterahertz range. *Phys. Rev. B*, 95:014304, Jan 2017.

[94] Jean-claude Toledano. *Physique des électrons dans les solides*. Cours de l'Ecole Polytechnique, 1993.

[95] C. Colvard, T. A. Gant, M. V. Klein, R. Merlin, R. Fischer, H. Morkoc, and A. C. Gossard. Folded acoustic and quantized optic phonons in (GaAl)As superlattices. *Phys. Rev. B*, 31:2080–2091, Feb 1985.

[96] C. Rossignol. *Etude Théorique et numérique d'expériences d'acoustique picoseconde*. PhD thesis, Université Pierre et Marie Curie, 2000.

[97] B. Jusserand, D. Paquet, F. Mollot, F. Alexandre, and G. Le Roux. Influence of the supercell structure on the folded acoustical Raman line intensities in superlattices. *Phys. Rev. B*, 35:2808–2817, Feb 1987.

[98] Martin A. Afromowitz. Refractive index of $Ga_{1-x}Al_xAs$. *Solid State Communications*, 15(1):59 – 63, 1974.

[99] N. D. Lanzillotti-Kimura, a. Fainstein, C. a. Balseiro, and B. Jusserand. Phonon engineering with acoustic nanocavities: Theoretical considerations on phonon molecules, band structures, and acoustic Bloch oscillations. *Physical Review B - Condensed Matter and Materials Physics*, 75(2):1–11, 2007.

[100] Giovanna Panzarini, Lucio Claudio Andreani, A. Armitage, D. Baxter, M. S. Skolnick, V. N. Astratov, J. S. Roberts, Alexey V. Kavokin, Maria R. Vladimirova, and M. A. Kaliteevski. Exciton-light coupling in single and coupled semiconductor microcavities: Polariton dispersion and polarization splitting. *Physical Review B*, 59(7):5082–5089, 1999.

[101] H. T. Grahn, H. J. Maris, J. Tauc, and B. Abeles. Time-resolved study of vibrations of $a-Ge:H/a-Si:H$ multilayers. *Phys. Rev. B*, 38:6066–6074, Sep 1988.

[102] Wei Chen, Yu Lu, Humphrey J. Maris, and Gang Xiao. Picosecond ultrasonic study of localized phonon surface modes in Al/Ag superlattices. *Phys. Rev. B*, 50:14506–14515, Nov 1994.

[103] N. D. Lanzillotti-Kimura, A. Fainstein, B. Perrin, B. Jusserand, A. Soukiassian, X. X. Xi, and D. G. Schlom. Enhancement and inhibition of coherent phonon emission of a Ni film in a $BaTiO_3/SrTiO_3$ cavity. *Phys. Rev. Lett.*, 104:187402, May 2010.

[104] V. Villafañe, A. E. Bruchhausen, B. Jusserand, P. Senellart, A. Lemaître, and A. Fainstein. Confinement of gigahertz sound and light in Tamm plasmon resonators. *Phys. Rev. B*, 92:165308, Oct 2015.

[105] Robert W. Boyd. *Nonlinear Optics, Third Edition*. Academic Press, 2008.

[106] H Kuzmany. *Solid-state spectroscopy : an introduction*. Springer, Heidelberg New York, 2009.

[107] Jianjun He, Bahram Djafari-Rouhani, and Jacques Sapriel. Theory of light scattering by longitudinal-acoustic phonons in superlattices. *Physical Review B*, 37(8):4086–4098, 1988.

[108] Benchabane Sarah. *Guidage et filtrage des ondes dans les cristaux phononiques.* PhD thesis, Université de Franche-Comté, 2006.

[109] M. Bass, E. W. V. Stryland, D. Williams, and W. Wolfe. *Handbook of Optics, Vol. 2: Devices, Measurements, and Properties, Second Edition.* McGraw-Hill Professional, 1994.

[110] Robert E. Newnham. *Properties of Materials: Anisotropy, Symmetry, Structure.* Oxford University Press, 2005.

[111] Bahram Djafari-Rouhani, Said El-Jallal, and Yan Pennec. Phoxonic crystals and cavity optomechanics. *Comptes Rendus Physique*, 17(5):555 – 564, 2016. Phononic crystals / Cristaux phononiques.

[112] Adnen Mlayah, Jean-Roch Huntzinger, and Nicolas Large. Raman-Brillouin light scattering in low-dimensional systems: Photoelastic model versus quantum model. *Phys. Rev. B*, 75:245303, Jun 2007.

[113] William Hayes and Rodney Loudon. *Scattering of Light by Crystals (Dover Science Books).* Dover Publications, 2004.

[114] Bachelier G. *Propriétés optiques de nano-structures métalliques et semi-conductrices.* PhD thesis, Université Paul Sabatier, 2004.

[115] P. V. Santos, L. Ley, J. Mebert, and O. Koblinger. Frequency gaps for acoustic phonons in $a-Si:H/a-SiN_x$: H superlattices. *Phys. Rev. B*, 36:4858–4867, Sep 1987.

[116] R. Loudon. Theory of the first-order Raman effect in crystals. *Proceedings of the Royal Society of London A: Mathematical, Physical and Engineering Sciences*, 275(1361):218–232, 1963.

[117] A. Kastler. Atomes à I'lntérieur d'un Interféromètre Perot-Fabry. *Applied Optics*, 1(1):17, 1962.

[118] A. Dousse, L. Lanco, J. Suffczyński, E. Semenova, A. Miard, A. Lemaître, I. Sagnes, C. Roblin, J. Bloch, and P. Senellart. Controlled light-matter coupling for a single quantum dot embedded in a pillar microcavity using far-field optical lithography. *Phys. Rev. Lett.*, 101:267404, Dec 2008.

[119] T. E. Sale. *Vertical Cavity Surface Emitting Lasers.* Research Studies Press LTD., 1995.

[120] A. Dousse. *Deterministic cavity-quantum dot coupling and fabrication of an ultrabright source of entangled photon pairs.* PhD thesis, Université Paris Diderot, 2010.

[121] N. D. Lanzillotti-Kimura, A. Fainstein, B. Jusserand, and A. Lemaître. Resonant Raman scattering of nanocavity-confined acoustic phonons. *Physical Review B*, 79(035404):1141–1142, 2009.

[122] A. Fainstein, B. Jusserand, and V. Thierry-Mieg. Raman efficiency in a planar microcavity. *Physical Review B*, 53(20):R13287—-R13290, 1996.

[123] A. Fainstein, B. Jusserand, and V. Thierry-Mieg. Raman scattering enhancement by optical confinement in a semiconductor planar microcavity. *Phys. Rev. Lett.*, 75:3764–3767, Nov 1995.

[124] A. Fainstein, M. Trigo, D. Oliva, B. Jusserand, T. Freixanet, and V. Thierry-Mieg. Standing optical phonons in finite semiconductor superlattices studied by resonant Raman scattering in a double microcavity. *Phys. Rev. Lett.*, 86:3411–3414, Apr 2001.

[125] A. Fainstein and Bernard Jusserand. Performance of semiconductor planar microcavities for Raman-scattering enhancement. *Phys. Rev. B*, 57:2402–2406, Jan 1998.

[126] C. Thomsen, H. T. Grahn, H. J. Maris, and J. Tauc. Surface generation and detection of phonons by picosecond light pulses. *Phys. Rev. B*, 34:4129–4138, Sep 1986.

[127] C. Thomsen, J. Strait, Z. Vardeny, H. J. Maris, J. Tauc, and J. J. Hauser. Coherent phonon generation and detection by picosecond light pulses. *Phys. Rev. Lett.*, 53:989–992, Sep 1984.

[128] Pascal Ruello and Vitalyi E. Gusev. Physical mechanisms of coherent acoustic phonons generation by ultrafast laser action. *Ultrasonics*, 56:21–35, 2015.

[129] N. D. Lanzillotti-Kimura, A. Fainstein, and B. Jusserand. Towards GHz-THz cavity optomechanics in DBR-based semiconductor resonators. *Ultrasonics*, 56:80–89, 2015.

[130] Ivan Favero and Khaled Karrai. Optomechanics of deformable optical cavities. *Nature Photonics*, 3(4):201–205, 2009.

[131] O. Arcizet, P.-F. Cohadon, T. Briant, M. Pinard, and A. Heidmann. Radiation-pressure cooling and optomechanical instability of a micromirror. *Nature*, 444:71–74, Nov 2006.

[132] Christopher Baker, William Hease, Dac-Trung Nguyen, Alessio Andronico, Sara Ducci, Giuseppe Leo, and Ivan Favero. Photoelastic coupling in gallium arsenide optomechanical disk resonators. *Opt. Express*, 22(12):14072–14086, Jun 2014.

[133] I. Favero, C. Metzger, S. Camerer, D. König, H. Lorenz, J. P. Kotthaus, and K. Karrai. Optical cooling of a micromirror of wavelength size. *Applied Physics Letters*, 90(10), 2007.

[134] Roman Schnabel, Nergis Mavalvala, David E. McClelland, and Ping K. Lam. Quantum metrology for gravitational wave astronomy. *Nature Communications*, 1:121, Nov 2010. Review Article.

[135] Subhadeep Gupta, Kevin L. Moore, Kater W. Murch, and Dan M. Stamper-Kurn. Cavity nonlinear optics at low photon numbers from collective atomic motion. *Phys. Rev. Lett.*, 99:213601, Nov 2007.

[136] Lu Ding, Christophe Baker, Pascale Senellart, Aristide Lemaitre, Sara Ducci, Giuseppe Leo, and Ivan Favero. High frequency gaas nano-optomechanical disk resonator. *Phys. Rev. Lett.*, 105:263903, Dec 2010.

[137] E. Verhagen, S. Deléglise, S. Weis, A. Schliesser, and T. J. Kippenberg. Quantum-coherent coupling of a mechanical oscillator to an optical cavity mode. *Nature*, 482:63–67, Feb 2012.

[138] Sungkun Hong, Ralf Riedinger, Igor Marinković, Andreas Wallucks, Sebastian G. Hofer, Richard A. Norte, Markus Aspelmeyer, and Simon Gröblacher. Hanbury brown and twiss interferometry of single phonons from an optomechanical resonator. *Science*, 358(6360):203–206, 2017.

[139] Matt Eichenfield, Jasper Chan, Ryan M Camacho, Kerry J Vahala, and Oskar Painter. Optomechanical crystals. *Nature*, 462(7269):78–82, 2009.

[140] E. Gavartin, R. Braive, I. Sagnes, O. Arcizet, A. Beveratos, T. J. Kippenberg, and I. Robert-Philip. Optomechanical coupling in a two-dimensional photonic crystal defect cavity. *Phys. Rev. Lett.*, 106:203902, May 2011.

[141] J. D. Thompson, B. M. Zwickl, A. M. Jayich, Florian Marquardt, S. M. Girvin, and J. G. E. Harris. Strong dispersive coupling of a high-finesse cavity to a micromechanical membrane. *Nature*, 452:72–75, Mar 2008.

[142] X Sun, J Zheng, M Poot, C W Wong, and H X Tang. Femtogram doubly clamped nanomechanical resonators embedded in a high-Q two-dimensional photonic crystal nanocavity. *Nano Letters*, 12(5):2299–2305, 2012. PMID: 22471420.

[143] Simon Gröblacher, Klemens Hammerer, Michael R. Vanner, and Markus Aspelmeyer. Observation of strong coupling between a micromechanical resonator and an optical cavity field. *Nature*, 460:724–727, Aug 2009.

[144] S. Sebastian, I. Favero, D. Hunger, P. Paulitschke, J. Reichel, K. Karrai, and E. Weig. Cavity nano-optomechanics: a nanomechanical system in a high finesse optical cavity, 2010.

[145] A. V. Oppenheim and G. C. Verghese. *Introduction to Communication, Control and Signal Processing*. Massachusetts Institute of Technology: MIT OpenCouseWare, Spring 2010.

[146] Viktor Tsvirkun. *Optomechanics in hybrid fully-integrated two-dimensional photonic crystal resonators*. PhD thesis, 2015.

[147] William Hease. *Gallium Arsenide optomechanical disks approaching the quantum regime*. PhD thesis, Université Paris Diderot, 2016.

[148] Constanze Metzger, Ivan Favero, Alexander Ortlieb, and Khaled Karrai. Optical self cooling of a deformable Fabry-Perot cavity in the classical limit. *Phys. Rev. B*, 78:035309, Jul 2008.

[149] T.J. Kippenberg and K.J. Vahala. Cavity opto-mechanics. *Opt. Express*, 15(25):17172–17205, Dec 2007.

[150] Florian Marquardt, Joe P. Chen, A. A. Clerk, and S. M. Girvin. Quantum theory of cavity-assisted sideband cooling of mechanical motion. *Phys. Rev. Lett.*, 99:093902, Aug 2007.

[151] A. Schliesser, P. Del'Haye, N. Nooshi, K. J. Vahala, and T. J. Kippenberg. Radiation pressure cooling of a micromechanical oscillator using dynamical backaction. *Phys. Rev. Lett.*, 97:243905, Dec 2006.

[152] R. W. Peterson, T. P. Purdy, N. S. Kampel, R. W. Andrews, P.-L. Yu, K. W. Lehnert, and C. A. Regal. Laser cooling of a micromechanical membrane to the quantum backaction limit. *Phys. Rev. Lett.*, 116:063601, Feb 2016.

[153] A. D. O'Connell, M. Hofheinz, M. Ansmann, Radoslaw C. Bialczak, M. Lenander, Erik Lucero, M. Neeley, D. Sank, H. Wang, M. Weides, J. Wenner, John M. Martinis, and A. N. Cleland. Quantum ground state and single-phonon control of a mechanical resonator. *Nature*, 464:697–703, Mar 2010.

[154] J D Teufel, T Donner, Dale Li, J W Harlow, M S Allman, K Cicak, A J Sirois, J D Whittaker, K W Lehnert, and R W Simmonds. Sideband cooling of micromechanical motion to the quantum ground state. *Nature*, 475(7356):359–63, 2011.

[155] E. Gil-Santos, C. Baker, D. T. Nguyen, W. Hease, C. Gomez, A. Lemaître, S. Ducci, G. Leo, and I. Favero. High-frequency nano-optomechanical disk resonators in liquids. *Nature Nanotechnology*, 10:810–816, Aug 2015.

[156] Fenfei Liu, Seyedhamidreza Alaie, Zayd C. Leseman, and Mani Hossein-Zadeh. Sub-pg mass sensing and measurement with an optomechanical oscillator. *Opt. Express*, 21(17):19555–19567, Aug 2013.

[157] K. L. Ekinci, Y. T. Yang, and M. L. Roukes. Ultimate limits to inertial mass sensing based upon nanoelectromechanical systems. *Journal of Applied Physics*, 95(5):2682–2689, 2004.

[158] Y. W. Hu, Y. F. Xiao, Y. C. Liu, and Q. Gong. Optomechanical sensing with on-chip microcavities. *Frontiers of Physics*, 8(5):475–490, Oct 2013.

[159] B. Jusserand, A. N. Poddubny, A. V. Poshakinskiy, A. Fainstein, and A. Lemaitre. Polariton resonances for ultrastrong coupling cavity optomechanics in GaAs/AlAs multiple quantum wells. *Phys. Rev. Lett.*, 115:267402, Dec 2015.

[160] M. Lermer, N. Gregersen, F. Dunzer, S. Reitzenstein, S. Höfling, J. Mørk, L. Worschech, M. Kamp, and A. Forchel. Bloch-wave engineering of quantum dot micropillars for cavity quantum electrodynamics experiments. *Phys. Rev. Lett.*, 108:057402, Jan 2012.

[161] Kerry J Vahala. Optical microcavities. *Nature*, 424(August):839–846, 2003.

[162] Susumu Noda, Masayuki Fujita, and Takashi Asano. Spontaneous-emission control by photonic crystals and nanocavities. *Nature Photonics*, 1(8):449–458, 2007.

[163] O. Painter. Two-Dimensional Photonic Band-Gap Defect Mode Laser. *Science*, 284(5421):1819–1821, 1999.

[164] M. Palamaru and Ph Lalanne. Photonic crystal waveguides: Out-of-plane losses and adiabatic modal conversion. *Applied Physics Letters*, 78(11):1466–1468, 2001.

[165] P. Lalanne and J. P. Hugonin. Bloch-wave engineering for high-Q, small-V microcavities. *IEEE Journal of Quantum Electronics*, 39(11):1430–1438, Nov 2003.

[166] Bong-Shik Song, Susumu Noda, Takashi Asano, and Yoshihiro Akahane. Ultra-high-Q photonic double-heterostructure nanocavity. *Nat Mater*, 4(3):207–210, March 2005.

[167] Ryuichi Ohta, Yasutomo Ota, Masahiro Nomura, Naoto Kumagai, Satomi Ishida, Satoshi Iwamoto, and Yasuhiko Arakawa. Strong coupling between a photonic crystal nanobeam cavity and a single quantum dot. *Applied Physics Letters*, 98(17):173104, 2011.

[168] P. Velha, E. Picard, T. Charvolin, E. Hadji, J. C. Rodier, P. Lalanne, and D. Peyrade. Ultra-High Q/V Fabry-Perot microcavity on SOI substrate. *Opt. Express*, 15(24):16090–16096, Nov 2007.

[169] Yinan Zhang and Marko Lončar. Submicrometer diameter micropillar cavities with high quality factor and ultrasmall mode volume. *Opt. Lett.*, 34(7):902–904, Apr 2009.

[170] Guillaume Malpuech and Alexey Kavokin. Picosecond beats in coherent optical spectra of semiconductor heterostructures: photonic Bloch and exciton-polariton oscillations. *Semiconductor Science and Technology*, 16(3):R1, 2001.

[171] N. D. Lanzillotti-Kimura, A. Fainstein, C. A. Balseiro, and B. Jusserand. Phonon engineering with acoustic nanocavities: Theoretical considerations on phonon molecules, band structures, and acoustic Bloch oscillations. *Phys. Rev. B*, 75:024301, Jan 2007.

[172] N. D. Lanzillotti Kimura, A. Fainstein, and B. Jusserand. Phonon Bloch oscillations in acoustic-cavity structures. *Phys. Rev. B*, 71:041305, Jan 2005.

[173] N. D. Lanzillotti-Kimura, A. Fainstein, B. Perrin, B. Jusserand, O. Mauguin, L. Largeau, and A. Lemaître. Bloch oscillations of THz acoustic phonons in coupled nanocavity structures. *Phys. Rev. Lett.*, 104:197402, May 2010.

[174] M. M. de Lima, Yu. A. Kosevich, P. V. Santos, and A. Cantarero. Surface acoustic Bloch oscillations, the Wannier-Stark ladder, and Landau-Zener tunneling in a solid. *Phys. Rev. Lett.*, 104:165502, Apr 2010.

[175] F. R. Lamberti, Q. Yao, L. Lanco, D. T. Nguyen, M. Esmann, A. Fainstein, P. Sesin, S. Anguiano, V. Villafa ne, A. Bruchhausen, P. Senellart, I. Favero, and N. D. Lanzillotti-Kimura. Optomechanical properties of GaAs/AlAs micropillar resonators operating in the 18 GHz range. *Opt. Express*, 25(20):24437–24447, Oct 2017.

[176] M Giehler, T Ruf, M Cardona, and K Ploog. Interference effects in acoustic-phonon Raman scattering from GaAs/AlAs mirror-plane superlattices. *Physical Review B*, 55(11):7124–7129, 1997.

[177] Adnen Mlayah, Jean Roch Huntzinger, and Nicolas Large. Raman-Brillouin light scattering in low-dimensional systems: Photoelastic model versus quantum model. *Physical Review B - Condensed Matter and Materials Physics*, 75(24):1–10, 2007.

[178] F. Duncan M. Haldane. Nobel lecture: Topological quantum matter. *Rev. Mod. Phys.*, 89:040502, Oct 2017.

[179] David Tong. Lectures on the quantum Hall effect. 2016.

[180] B. Andrei Bernevig, Taylor L. Hughes, and Shou-Cheng Zhang. Quantum spin Hall effect and topological phase transition in HgTe quantum wells. *Science*, 314(5806):1757–1761, 2006.

[181] C. L. Kane and E. J. Mele. Quantum spin Hall effect in graphene. *Phys. Rev. Lett.*, 95:226801, Nov 2005.

[182] M. Z. Hasan and C. L. Kane. Colloquium: Topological insulators. *Rev. Mod. Phys.*, 82:3045–3067, Nov 2010.

[183] Yuanbo Zhang, Yan-Wen Tan, Horst L. Stormer, and Philip Kim. Experimental observation of the quantum Hall effect and Berry's phase in graphene. *Nature*, 438:201–204, Nov 2005.

[184] W. P. Su, J. R. Schrieffer, and A. J. Heeger. Solitons in polyacetylene. *Physical Review Letters*, 42(25):1698–1701, 1979.

[185] Alan J. Heeger. Nobel lecture: Semiconducting and metallic polymers: The fourth generation of polymeric materials. *Rev. Mod. Phys.*, 73:681–700, Sep 2001.

[186] Zheng Wang, Yidong Chong, J. D. Joannopoulos, and Marin Soljacic. Observation of unidirectional backscattering-immune topological electromagnetic states. *Nature*, 461:772–775, Oct 2009.

[187] F. D. M. Haldane and S. Raghu. Possible realization of directional optical waveguides in photonic crystals with broken time-reversal symmetry. *Phys. Rev. Lett.*, 100:013904, Jan 2008.

[188] M. Hafezi, S. Mittal, J. Fan, A. Migdall, and J. M. Taylor. Imaging topological edge states in silicon photonics. *Nature Photonics*, 7:1001–1005, Oct 2013.

[189] Pai Wang, Ling Lu, and Katia Bertoldi. Topological phononic crystals with one-way elastic edge waves. *Phys. Rev. Lett.*, 115:104302, Sep 2015.

[190] Zhaoju Yang, Fei Gao, Xihang Shi, Xiao Lin, Zhen Gao, Yidong Chong, and Baile Zhang. Topological acoustics. *Phys. Rev. Lett.*, 114:114301, Mar 2015.

[191] Yao-Ting Wang, Pi-Gang Luan, and Shuang Zhang. Coriolis force induced topological order for classical mechanical vibrations. *New Journal of Physics*, 17(7):073031, 2015.

[192] Meng Xiao, Guancong Ma, Zhiyu Yang, Ping Sheng, Z. Q. Zhang, and C. T. Chan. Geometric phase and band inversion in periodic acoustic systems. *Nature Physics*, 11(3):240–244, 2015.

[193] Meng Xiao, Z. Q. Zhang, and C. T. Chan. Surface impedance and bulk band geometric phases in one-dimensional systems. *Physical Review X*, 4(2):1–12, 2014.

[194] J Zak. Berry's Phase for Energy Bands in Solids given the adiabatic form. *Physical Review Letters*, 62(23):2747–2750, 1989.

[195] R. D. King-Smith and David Vanderbilt. Theory of polarization of crystalline solids. *Phys. Rev. B*, 47:1651–1654, Jan 1993.

[196] M. V. Berry. Quantal phase factors accompanying adiabatic changes. *Proceedings of the Royal Society of London A: Mathematical, Physical and Engineering Sciences*, 392(1802):45–57, 1984.

[197] János K. Asbóth, László Oroszlány, and András Pályi. A Short Course on Topological Insulators. *Lecture Notes in Physics*, 919, 2015.

[198] Alexey Kavokin, Ivan Shelykh, and Guillaume Malpuech. Optical Tamm states for the fabrication of polariton lasers. *Applied Physics Letters*, 87(26):261105, 2005.

[199] Olivier Gazzano. *Sources brillantes de photons uniques indiscernables et demonstration d'une porte logique quantique*. PhD thesis, Université Paris Diderot, 2013.

[200] Stefan Alewander Maier. *Plasmonics: fundamentals and applications*. Springer, 2007.

[201] Gerald Bastard. *Wave mechanical applied to semiconductor heterostructures*. Editions de Physique„ Les Ulis Cedex, France, 1990.

[202] F. Maucher, T. Pohl, S. Skupin, and W. Krolikowski. Self-organization of light in optical media with competing nonlinearities. *Phys. Rev. Lett.*, 116:163902, Apr 2016.

[203] T. Rivera, F. R. Ladan, A. Izraël, R. Azoulay, R. Kuszelewicz, and J. L. Oudar. Reduced threshold all-optical bistability in etched quantum well microresonators. *Applied Physics Letters*, 64(7):869–871, 1994.

[204] T. Jacqmin, I. Carusotto, I. Sagnes, M. Abbarchi, D. D. Solnyshkov, G. Malpuech, E. Galopin, A. Lemaître, J. Bloch, and A. Amo. Direct observation of Dirac cones and a flatband in a honeycomb lattice for polaritons. *Phys. Rev. Lett.*, 112:116402, Mar 2014.

[205] Daniele Bajoni, Pascale Senellart, Esther Wertz, Isabelle Sagnes, Audrey Miard, Aristide Lemaître, and Jacqueline Bloch. Polariton laser using single micropillar GaAs−GaAlAs semiconductor cavities. *Phys. Rev. Lett.*, 100:047401, Jan 2008.

[206] V. Giesz, N. Somaschi, G. Hornecker, T. Grange, B. Reznychenko, L. De Santis, J. Demory, C. Gomez, I. Sagnes, A. Lemaître, O. Krebs, N. D. Lanzillotti-Kimura, L. Lanco, A. Auffeves, and P. Senellart. Coherent manipulation of a solid-state artificial atom with few photons. *Nature Communications*, 7:11986, Jun 2016.

[207] N. Somaschi, V. Giesz, L. De Santis, J. C. Loredo, M. P. Almeida, G. Hornecker, S. L. Portalupi, T. Grange, C. Antón, J. Demory, C. Gómez, I. Sagnes, N. D. Lanzillotti-Kimura, A. Lemaítre, A. Auffeves, A. G. White, L. Lanco, and P. Senellart. Near-optimal single-photon sources in the solid state. *Nature Photonics*, 10:340–345, Mar 2016.

[208] B. Gayral. *Modification du taux d'émission spontanée de boîtes quantiques dans des microcavités optiques*. PhD thesis, Université Pierre et Marie Curie, 2000.

[209] D. Marcuse. *Theory of Dielectric Optical Waveguides (Quantum electronics–principles and applications)*. Academic Press Inc, 1974.

[210] M. Kern. *Introduction à la méthode des éléments finis*. Cours de l'Ecole Nationale Supérieure des Mines de Paris, 2004.

[211] P. Hilaire, C. Antón, C. Kessler, A. Harouri, A. Lemaître, I. Sagnes, P. Senellart, and L. Lanco. Accurate measurement of a 96% input coupling into a cavity using polarization tomography. arXiv:1802.09862, 2018.

[212] T. Rivera, J.-P. Debray, J. M. Gérard, B. Legrand, L. Manin-Ferlazzo, and J. L. Oudar. Optical losses in plasma-etched AlGaAs microresonators using reflection spectroscopy. *Applied Physics Letters*, 74(7):911–913, 1999.

[213] Christophe Arnold, Vivien Loo, Aristide Lemaître, Isabelle Sagnes, Olivier Krebs, Paul Voisin, Pascale Senellart, and Loïc Lanco. Optical bistability in a quantum dots/micropillar device with a quality factor exceeding 200 000. *Applied Physics Letters*, 100(11):111111, 2012.

[214] M. Cazayous, J. Groenen, J. R. Huntzinger, A. Mlayah, and O. G. Schmidt. Spatial correlations and Raman scattering interferences in self-assembled quantum dot multilayers. *Phys. Rev. B*, 64:033306, Jun 2001.

[215] S. Anguiano, G. Rozas, A. E. Bruchhausen, A. Fainstein, B. Jusserand, P. Senellart, and A. Lemaître. Spectra of mechanical cavity modes in distributed bragg reflector based vertical gaas resonators. *Phys. Rev. B*, 90:045314, Jul 2014.

[216] G. Rozas, B. Jusserand, and A. Fainstein. Fabry-Pérot-multichannel spectrometer tandem for ultra-high resolution raman spectroscopy. *Review of Scientific Instruments*, 85(1):013103, 2014.

[217] Daniel Garcia-Sanchez, Samuel Déleglise, Jean-Louis Thomas, Paola Atkinson, Camille Lagoin, and Bernard Perrin. Acoustic confinement in superlattice cavities. *Phys. Rev. A*, 94:033813, Sep 2016.

[218] P. Renosi and J.S. Apriel. Acousto-optics of semiconductor crystals and superlattices in resonance conditions. *Ultrasonics*, 31(5):327 – 332, 1993. Special Issue Acousto Optics/Imaging.

[219] Mathieu Munsch, Andreas V. Kuhlmann, Davide Cadeddu, Jean-Michel Gérard, Julien Claudon, Martino Poggio, and Richard J. Warburton. Resonant driving of a single photon emitter embedded in a mechanical oscillator. *Nature Communications*, 8(1):76, 2017.

[220] Yu-Ming He, Jin Liu, Sebastian Maier, Monika Emmerling, Stefan Gerhardt, Marcelo Davanço, Kartik Srinivasan, Christian Schneider, and Sven Höfling. Deterministic implementation of a bright, on-demand single-photon source with near-unity indistinguishability via quantum dot imaging. *Optica*, 4(7):802–808, Jul 2017.

[221] M. Gschrey, A. Thoma, P. Schnauber, M. Seifried, R. Schmidt, B. Wohlfeil, L. Krüger, J.-H. Schulze, T. Heindel, S. Burger, F. Schmidt, A. Strittmatter, S. Rodt, and S. Reitzenstein. Highly indistinguishable photons from deterministic quantum-dot microlenses utilizing three-dimensional in situ electron-beam lithography. *Nature Communications*, 6:7662 EP –, Jul 2015. Article.

[222] Juan Restrepo, Cristiano Ciuti, and Ivan Favero. Single-polariton optomechanics. *Phys. Rev. Lett.*, 112:013601, Jan 2014.

[223] P. St-Jean, V. Goblot, E. Galopin, A. Lemaître, T. Ozawa, L. Le Gratiet, I. Sagnes, J. Bloch, and A. Amo. Lasing in topological edge states of a one-dimensional lattice. *Nature Photonics*, 11(10):651–656, 2017.

[224] W. P. Su, J. R. Schrieffer, and A. J. Heeger. Solitons in polyacetylene. *Phys. Rev. Lett.*, 42:1698–1701, Jun 1979.